

An Investigation into the Effects of Submergence Depth,
Speed and Hull Length-to-Diameter Ratio on the Near-
Surface Operation of Conventional Submarines

Edward Dawson
B.E. Naval Architecture (Hons)

Submitted in fulfilment of the
requirements for the Degree of
Master of Philosophy

University of Tasmania
November 2014

STATEMENT OF ORIGINALITY

This thesis contains no material which has been accepted for a degree or diploma by the University or any other institution, except by way of background information and duly acknowledged in the thesis, and to the best of my knowledge and belief no material previously published or written by another person except where due acknowledgement is made in the text of the thesis, nor does the thesis contain any material that infringes copyright.

A handwritten signature in black ink, appearing to read 'Edward Dawson', with a long horizontal flourish extending to the right.

Edward Dawson

November 2014

AUTHORITY OF ACCESS

This thesis may be made available for loan and limited copying and communication in accordance with the Copyright Act 1968.

A handwritten signature in black ink, appearing to read 'Edward Dawson', with a long horizontal flourish extending to the right.

Edward Dawson

November 2014

ABSTRACT

The strategic requirement for naval submarines to operate in near surface and littoral environments continues to increase as they are more frequently employed to support joint force missions. The operational workload for helmsmen and the risk to mission safety and success are significantly increased due to the interaction between the submarine and the free-surface. This thesis reports on an experimental investigation into the effects of submergence depth, speed of advance and length-to-diameter ratio on the interaction between a streamlined axisymmetric body and the free-surface when travelling in a near-surface condition.

A broad review of the existing literature indicates that little work has been published to date on the effects of length-to-diameter on the near-surface performance of streamlined axisymmetric bodies. Furthermore, there is little or no experimental data available describing the vertical force and moment that act on a shallowly submerged body moving beneath the free-surface. Nonetheless, there is evidence to confirm that the requirement for submarine near-surface operation is significant and that a well-founded understanding of submarine near-surface performance is needed.

A model scale experimental program was conducted to measure and observe the resistance, lift force, trimming moment and wave field generated by a series of submerged bodies of revolution moving at constant forward speed. The Joubert conventional submarine geometry was tested in its bare hull configuration in three length-to-diameter ratio formats: 7.30, 8.50 and 9.50. The three geometries possess the same maximum diameter. The models were tested at velocities that correspond to a Froude number range of 0.10 to 0.50 inclusive and at centreline submergence depths of between 1 and 3.5 hull diameters.

The results of the experiment indicate that the wave resistance, lift force and trimming moment all vary periodically with speed and are directly influenced by the wavelength of the free-surface wave field generated by the submerged body. The steady-state wave field itself is a direct function of the submerged body's length-to-diameter ratio and speed of advance (Froude number). The magnitude of the forces and trimming moment were found to diminish exponentially with an increase in submergence depth. Considering the submergence depths and speeds experienced by naval submarines when conducting near-surface operations, it is concluded that the effect of wave resistance is a secondary issue and that the vertical lift force is of the greatest operational significance. Based on the test results of the three Joubert hull geometries, it was observed that for near-surface operation a larger length-to-diameter ratio is preferable for achieving minimum resistance and vertical plane motion (lower relative lift force and trimming moment).

An evaluation of the SHIPFLOW 4.7 potential flow software program was completed using the experimentally measured data in conjunction with additional published experimental and numerical wave resistance data. Good correlation was observed for the predictions of lift force and trimming moment. Mixed results were achieved when comparing the numerically predicted and experimentally measured wave resistance. Nonetheless, it is concluded that the potential flow method offers an inexpensive and suitable approach to evaluating the near-surface performance of submarine type geometries.

ACKNOWLEDGEMENTS

There are many people who I wish to thank for the generous contributions and kind support which they offered to me during the time I undertook this research project. I am sincerely grateful.

Thank you to my academic supervisors Professor Dev Ranmuthugala and Associate Professor Paul Brandner. Thank you also to Dr Martin Renilson for his supervision at the start of the program and to Brendon Anderson for sponsoring the project.

As part of this research I have had the good fortune to work with several accomplished undergraduate students: Samuel Wilson-Haffenden, Sean Van-Steel, Damien Neulist, Dean Fletcher and Nick Johnson. Thank you for your commitment, consideration and for the long hours of work. I wish you every success in your future endeavours.

Thank you to the sponsoring organisations who have kindly supported this research: The Australian Defence Science and Technology Organisation, The Australian Maritime College and Graduate Research Office (University of Tasmania) and BMT Design Services Australia Pty. Ltd.

Thank you to the dedicated staff of the AMC Towing Tank: Dr Gregor Macfarlane, Dr Jonathan Duffy, Kirk Meyer, Liam and Drew Honeychurch, Peter Tomic, Tim Lillienthal and Shaun Denehey.

Thank you to Andrew Monks and Thomas Knaub of QinetiQ Engineering Services Melbourne: two exceptionally skilled model makers with a great sense of humour.

Thank you to Per Ekblom, Magnus Östberg and the team at FLOWTECH International AB.

Thank you to Dr Tim Gourlay. I have greatly appreciated your support and the technical discussions that we have had from time to time over the course of my research.

Thank you to my mother and father who provided their unwavering support and encouragement. I offer a special thank you to Dr Jeanne Dawson for editing and proof reading this manuscript.

DEDICATION

To Rebekah,

Thank you for standing by me. I'm forever grateful for your love and understanding.
Ad astra per aspera.

With my love,

Edward

TABLE OF CONTENTS

STATEMENT OF ORIGINALITY	I
AUTHORITY OF ACCESS	II
ABSTRACT	III
ACKNOWLEDGEMENTS	IV
TABLE OF CONTENTS	V
NOMENCLATURE	VIII
ABBREVIATIONS AND ACRONYMS	XIII
AXIS SYSTEM AND ORIGIN	XV
1 INTRODUCTION	1
1.1 RESEARCH OBJECTIVES	2
1.2 SCOPE OF WORK	2
1.3 RESEARCH STRATEGY AND DOCUMENT STRUCTURE	3
2 BACKGROUND: SUBMARINE OPERATIONS IN THE LITTORAL	5
2.1 REALISATION OF THE CAPABILITY EDGE	5
2.2 AREA OF OPERATIONS	5
2.3 SUBMARINE HULL SIZE, SHAPE AND ARRANGEMENT	9
2.4 OPERATIONAL SPEED PROFILE	14
2.5 SUMMARY	15
3 LITERATURE REVIEW AND SIGNIFICANT THEORY	16
3.1 THEORETICAL ANALYSIS OF SUBMARINE RESISTANCE, LIFT AND TRIM	16
3.2 EXPERIMENTAL INVESTIGATIONS OF SUBMERGED BODY WAVE RESISTANCE	30
3.3 NUMERICAL INVESTIGATIONS OF SUBMERGED BODY WAVE RESISTANCE, DRAG, LIFT AND TRIMMING MOMENT	45
4 IMPLICATIONS OF SMALL SCALE SUBMARINE MODEL TESTING	69

4.1	SCALE EFFECTS ON SUBMERGED BODY RESISTANCE TESTS	69
4.2	TURBULENCE STIMULATION	70
4.3	FORM FACTOR AND FRICTION COEFFICIENT EXPANSION LINE	77
4.4	STING MOUNT INTERFERENCE EFFECTS	80
4.5	BLOCKAGE AND BOUNDARY INTERACTION	84
5	EXPERIMENTAL INVESTIGATION	86
5.1	EXPERIMENTS AND OBJECTIVES	86
5.2	PHYSICAL MODELS: SUBOFF AND JOUBERT GEOMETRIES	86
5.3	TEST FACILITY AND EQUIPMENT	89
5.4	TESTING PROGRAM	95
5.5	TEST PROCEDURE	97
5.6	DATA PROCESSING	97
5.7	UNCERTAINTY ANALYSIS AND TEST REPEATABILITY	99
6	NUMERICAL INVESTIGATION: SHIPFLOW	104
6.1	SHIPFLOW OVERVIEW AND STRUCTURE	105
6.2	PROBLEM DEFINITION	106
6.3	MODELLING AND PANELISATION	106
6.4	CONVERGENCE CRITERIA	109
6.5	MESH INDEPENDENCE	109
6.6	BOUNDARY AND INITIAL CONDITIONS	111
6.7	CALCULATION OF THE PARAMETER SOLUTIONS	111
7	EXPERIMENT RESULTS	113
7.1	EFFECTS OF SUBMERSION DEPTH AND SPEED ON TOTAL RESISTANCE COEFFICIENT	113
7.2	EFFECT OF LENGTH-TO-DIAMETER ON TOTAL RESISTANCE COEFFICIENT	117
7.3	VERTICAL PLANE FORCE AND MOMENT	120
8	NUMERICAL RESULTS	146

8.1	BASELINE STUDY OF A $L/D = 5.00$ PROLATE SPHEROID	146
8.2	SHIPFLOW WAVE RESISTANCE FOR SERIES 58 MODEL 4166	149
8.3	SHIPFLOW JOUBERT LENGTH-TO-DIAMETER SIMULATIONS	152
9	CONCLUDING REMARKS AND RECOMMENDATIONS	167
9.1	CONCLUDING REMARKS	167
9.2	RECOMMENDATIONS FOR EXTENDING THIS RESEARCH	170
	REFERENCES	171
APPENDIX A	BOUNDARY LAYER TRANSITION INVESTIGATION	177
APPENDIX B	LOAD CELL AND WAVE PROBE CALIBRATION	184
APPENDIX C	UNCERTAINTY ANALYSIS	185
APPENDIX D	SUBOFF RESISTANCE COEFFICIENT DATA	192
APPENDIX E	SHIPFLOW RUN FILES	195
	RESEARCH PUBLICATIONS	198

NOMENCLATURE

A	Aft (subscript)
A_{MS}	Section area at midships [m ²]
C_F	Frictional resistance coefficient
C_L	Lift force coefficient $C_L = \frac{F_z}{0.5\rho \cdot U^2 \cdot S}$
C_M	Trimming moment coefficient $C_M = \frac{M}{0.5\rho \cdot U^2 \cdot S \cdot L}$
C_P	Pressure coefficient $C_P = 1 - \left(\frac{U}{U_\infty}\right)^2$
C_p	Prismatic coefficient
C_R	Residuary resistance coefficient $C_R = C_T - C_F$
C_T	Total resistance coefficient $C_T = \frac{R_T}{0.5\rho \cdot U^2 \cdot S}$
C_W	Wave resistance coefficient $C_W = \frac{R_W}{0.5\rho \cdot U^2 \cdot S}$
D	Hull diameter (beam) [m]
D_B	Sting base diameter [m]
d_s	Sting diameter [m]
D_S	Sting flare diameter [m]
EHP_T	Total effective horsepower
EHP_{Tmin}	Minimum total effective horsepower
F	Forward (Subscript)
f_0	Limiting depth [m]
Fr	Froude Number based on characteristic length $Fr = \frac{U}{\sqrt{g \cdot L}}$
F_x	Surge force [N]

F_Y	Sway force [N]
F_Z	Lift force [N]
g	Gravitational acceleration (constant = 9.81 m/s ²)
H	Streamlined body or submarine hull height [m]
h	Submergence depth of centreline axis to still free-surface [m]
H^*	Non-dimensional submergence depth $H^* = \frac{h}{D}$
H_W	Wave height [m]
k	Form factor (1 + k)
k	Height of surface protuberance (roughness element) [m]
K	Roll moment [N-m]
k	Wave component interaction index
k_{crit1}	Critical height of roughness element (lower threshold) [m]
k_{crit2}	Critical height of roughness element (upper threshold) [m]
k_F	Form coefficient L/D Length to diameter ratio
L	Hull length [m]
L/D	Length-to-diameter ratio
L_a	Length of aft section [m]
L_f	Length of forward section [m]
L_M	Truncated model length [m]
L_{pmb}	Length of parallel mid-body section [m]
L_S	Sting flare length [m]
l_s	Sting length [m]
m	Location of maximum cross-section
M	Trimming moment [N-m]
MS	Midships (Subscript)
N	Number or index of wave interaction

N	Yaw moment [N-m]
n_a	Aft section index
n_f	Forward section index
N_P	Number of panels
p	Pressure [Pa]
p	Roll velocity [rad/s]
P_E	Effective power
q	Pitch velocity [rad/s]
r	Yaw velocity [rad/s]
r_0	Non-dimensional nose radius
r_1	Non-dimensional tail radius
$Re_{k\,crit}$	Critical Reynolds number based on the roughness height (k) at which transition occurs
Re_k	Reynolds Number based on characteristic roughness element height (k)
Re_L	Reynolds Number based on characteristic length $Re_L = \frac{U \cdot L}{\nu}$
$Re_{x\,crit}$	Critical Reynolds number based on the point of transition from the leading edge (x)
R_{Form}	Form resistance [N]
$R_{Friction}$	Friction resistance [N]
$R_{Viscous}$	Viscous resistance [N]
R_W	Wave resistance [N]
S	Wetted surface area [m ²]
u	Body velocity component in the longitudinal (x axis) direction [m/s]
U	Uncertainty estimate
U	Velocity [m/s]
U_∞	Far field (free-stream) velocity [m/s]

v	Body velocity component in the transverse (y axis) direction [m/s]
V	Wave velocity [m/s]
w	Body velocity component in the vertical (z axis) direction [m/s]
W	Tank width [m]
x	Distance from a specified datum in the direction of the longitudinal axis [m]
x	Principal longitudinal coordinate
X_a	Aft profile (run) longitudinal coordinate [m]
X_f	Forward profile (entrance) longitudinal coordinate [m]
y	Principal transverse coordinate
Y_a	Aft profile (run) radial coordinate [m]
Y_f	Forward profile (entrance) radial coordinate [m]
z	Model centerline stand-off distance [m]
z	Principal vertical coordinate
z	Wave system wave component separation distance [m]
∇	Gradient operator
Φ	Velocity potential
∂	Partial derivative
μ	Statistical mean
α	Pitch angle [rad]
β	Drift angle [rad]
δ	Rudder angle [rad]
ΔC_F	Frictional resistance coefficient adjustment factor
δp	Sail plane angle [deg]
δr	Rudder angle [deg]
δs	Stern plane angle [deg]

θ	Angle between the direction of travel and the wave crest vector normal
λ	Wavelength [m]
ν	Kinematic viscosity [m ² /s]
π	Pi (constant)
ρ	Water density [kg/m ³]
σ	Statistical standard deviation
ψ	Yaw angle [rad]

ABBREVIATIONS AND ACRONYMS

AIP	Air Independent Propulsion
AMC	Australian Maritime College
AO	Area of operation
ASW	Anti-Submarine Warfare
AUV	Autonomous underwater vehicle
BEM	Boundary Element Method
CFD	Computational Fluid Dynamics
DARPA	Defense Advanced Research Projects Agency
EW	Electronic Warfare
GRP	Glass reinforced polymer
HPMM	Horizontal Planar Motion Mechanism
ITTC	International Towing Tank Conference
LOA	Length overall
MS	Midship
PC	Personal computer
PF	Potential flow
SOA	Speed of advance
SS	Conventionally Powered Patrol Submarine
SSB	Conventionally Powered Ballistic Missile Submarine
SSBN	Nuclear Powered Ballistic Missile Submarine
SSG	Conventionally Powered Guided Missile Submarine
SSGN	Nuclear Powered Guided Missile Submarine
SSK	Conventional Powered Submarine
SSN	Nuclear Powered Submarine
TDC	Top dead centre

US	United States
UTAS	University of Tasmania
VLS	Vertical Launch System
VOF	Volume of fluids
WP	Wave Probe
WWI	World War One
WWII	World War Two

AXIS SYSTEM AND ORIGIN

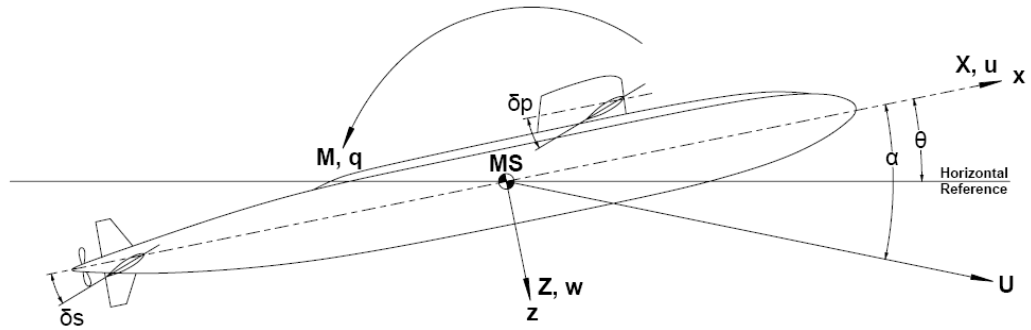


Figure 0-1 Positive direction of vertical plane motion, angles, velocities, forces and moments (adapted from Feldman (1979)). Centre of rotation is at midships.

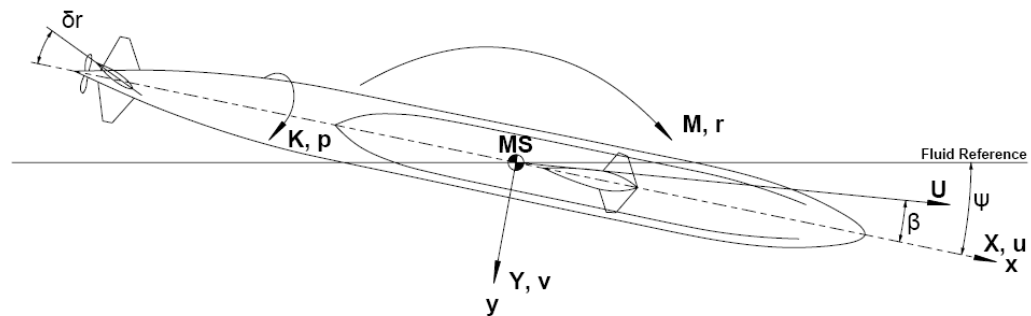


Figure 0-2 Positive direction of horizontal plane motion, angles, velocities, forces and moments (adapted from Feldman (1979)). Centre of rotation is at midships.

1 INTRODUCTION

The strategic requirement to operate naval submarines in the littoral environment and near the ocean's surface continues to increase. For conventionally powered submarines there has always been a need to approach the surface during snorting (power generation) evolutions. For attack submarines in general there is the frequent need to move to periscope depth to conduct surveillance operations and deploy/recover personnel and off-board systems. In each instance the submarine is operating in an inherently unstable condition as it interacts with the ocean's surface.

Submarine manoeuvrability and control become critical when operating in the near-surface environment as there is an elevated risk to both platform and personnel due to the platform and surface interaction. Operational economy and discretion are also strongly influenced by how the submarine performs in the near-surface condition. These performance characteristics are largely influenced by the size, shape and configuration of the submarine and the speed and depth at which it is operating. Consequently, a well-founded understanding of near-surface submarine hydrodynamic performance is required to enable platform design evaluation and support the safe and efficient conduct of submarine operations.

The hydrodynamic resistance and vertical lift forces that are experienced by a submarine transiting near the surface differ considerably from those experienced when it is deeply submerged. The interaction of the submarine's dynamic pressure distribution and the finite water column above it results in gravity waves being generated on the free-surface (the air-water interface). The result of this can be summarised as follows:

- a. There is an increase in the submarine's resistance due to the additional energy that is imparted by the submarine to elevate the free-surface; that is, wave-making resistance becomes a significant contributor to the resistance profile. As a result, the submarine's effective speed of advance (SOA) will be reduced for a given power input. Alternatively, an increase in propulsive power and energy usage is required to maintain a given SOA.
- b. An unbalanced vertical pressure distribution across the submarine can occur, which results in a net force-moment couple acting on the submarine to displace and rotate it in the vertical plane. The effect of this couple may require the helmsman to affect a change in the control surfaces to counteract the imbalance and keep the submarine on course.
- c. Depending on the proximity to the free-surface, it is likely that a wake may be generated. This is a visual signature that can betray the submarine's location, size, speed and heading to enemy anti-submarine warfare (ASW) assets.

This research thesis examines, through the use of experimental and numerical methods, the wave resistance, lift force and trimming moment experienced by submarine hull-like bodies when travelling beneath a free-surface. The body's speed of advance, submergence depth and length-to-diameter ratio (L/D) are investigated to identify their effect on resistance, lift force, trimming moment and surface wave generation.

1.1 RESEARCH OBJECTIVES

The aims of the research are to:

- a. investigate the effects of speed, submergence depth and length-to-diameter ratio on the forces and moments generated by a streamlined body travelling in close proximity to the free-surface;
- b. identify the influence of submarine speed, submergence depth and length-to-diameter ratio on submarine generated surface wave characteristics;
- c. investigate the application of potential flow (PF) numerical methods and tools for predicting submarine performance when operating near the free-surface;
- d. quantify the effects of near-surface operations in comparison to deep operations, and identify optimum configurations and conditions for submarine operational speed, depth and length-to-diameter; and
- e. increase the existing scientific body of knowledge related to submarine hydrodynamics and near-surface operation.

1.2 SCOPE OF WORK

The scope of work is summarised below:

- a. Conduct captive model experiments using scale generic submarine models in the Australian Maritime College (AMC) Towing Tank to quantify the axial resistance (drag force), vertical force (lift) and the trimming moment for a submarine operating near the free-surface. Measurements are conducted at a range of forward speeds, submergence depths, and hull configurations (bare hull with a systematic variation of length-to-diameter ratio). The submarine geometries are two configurations of the DARPA SUBOFF nuclear type submarine geometry described by Groves et al. (1989) and three L/D variants of the Joubert conventional type submarine geometry described by Anderson et al. (2012).
- b. Measure and observe submarine generated surface waves for different configurations, speeds, and depths.
- c. Identify an appropriate hull-borne boundary layer transition device for small scale, low speed submarine models tested in the towing tank.
- d. Carry out numerical modelling of the submarine and free-surface interaction for selected speed, depth and hull configurations using a PF solver to obtain forces, moments, and wave patterns.
- e. Compare the PF results against corresponding experimental results.

1.3 RESEARCH STRATEGY AND DOCUMENT STRUCTURE

The research strategy adopted to deliver the research outcomes and objectives comprises the use of the following three interrelated research tools:

- a. Investigation through a detailed literature review to report on the relevant work completed by others, contextualise the need for near-surface submarine operation and support the experiment and numerical based investigations.
- b. Investigation by experiment to observe, measure and record the hydrodynamic forces, moments and generated surface waves experienced by a submerged submarine hull-like body in proximity to the free-surface.
- c. Implementation of a commercially available potential flow numerical simulation tool to investigate its ability to predict the hydrodynamic forces, moments and generated surface waves experienced by a submerged submarine hull-like body travelling beneath a free-surface.

Figure 1-1 presents a diagrammatic view of the research strategy.

The thesis document is structured so as to present the research in a coherent and logical manner. The following provides a description of each of the chapters within this document:

Chapter 1 presents the introduction to the research problem and the method of investigation used in addressing the problem.

Chapter 2 provides a background narrative elaborating on the nature of near-surface submarine operations and the context for the current research.

Chapter 3 provides a literature review of the hydrodynamic phenomena associated with the physical interaction effects experienced by submarines during near-surface operation; and the pertinent experimental and numerical research completed to date.

Chapter 4 presents a discussion of the challenges experienced when conducting small scale, low speed model tests and the methods used to address and manage them.

Chapter 5 describes the experimental setup and methods used to measure and record the forces, moment and free-surface wave profile generated by the interaction of the physical model and the free-surface.

Chapter 6 discusses the potential flow software used to simulate and predict the interaction effects between the submerged body and the free-surface. It provides detail on the modelling and simulation methods used in this research.

Chapter 7 presents the results of the experimental tests. It also includes a discussion of the results in the context of the research thesis: free-surface interaction effects on submarine near-surface operation.

Chapter 8 presents the results of the numerical simulations. It also includes a discussion of the results and the application of the potential flow method to the research problem.

Chapter 9 presents the conclusions drawn from the research and the areas that are considered to need further investigation to address the breadth of the research problem addressed in this thesis.

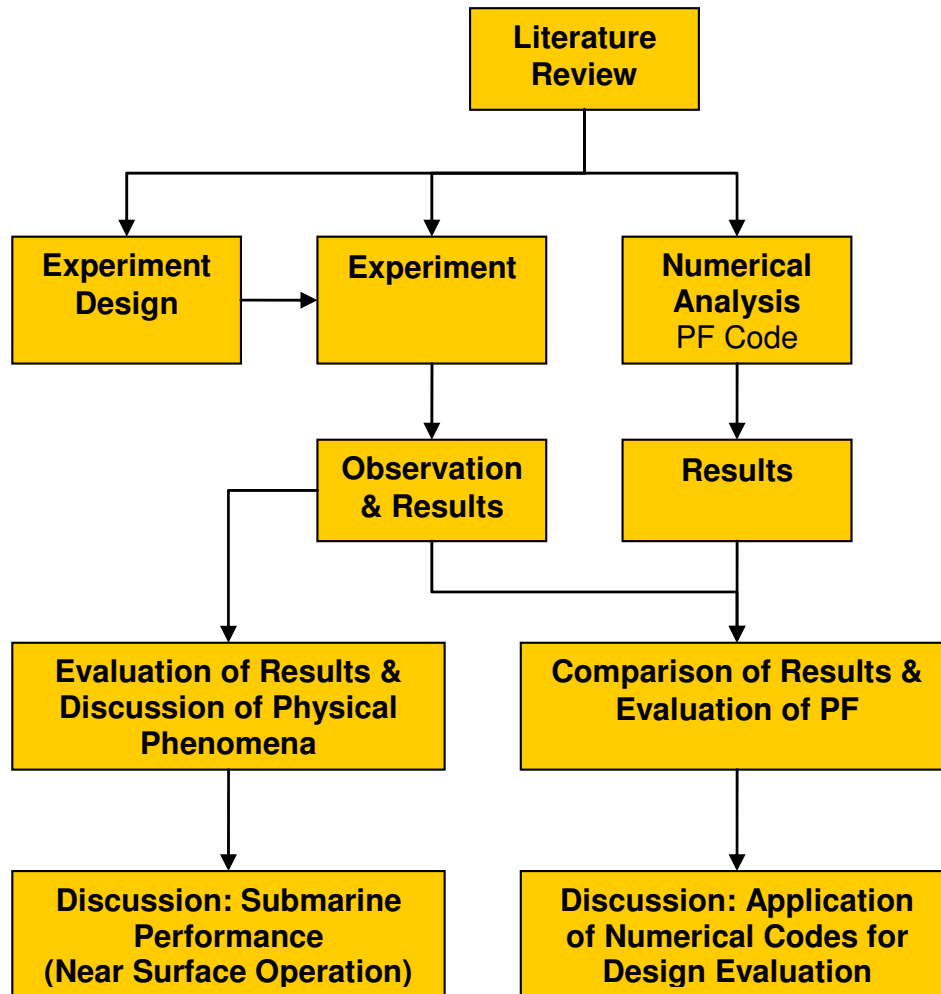


Figure 1-1 Research strategy process flow diagram

2 BACKGROUND: SUBMARINE OPERATIONS IN THE LITTORAL

2.1 REALISATION OF THE CAPABILITY EDGE

The strategic capabilities and importance of the submarine were not fully realised until after the Second World War (WWII). Arguably, it was the United States' use of the submarine during the American Civil War that established the platform as a coastal and inland waterway aggressor. But despite some degree of success during the national conflict, the submarine was still regarded as having limited application in naval combat. Although each of the world's major navies possessed sizable submarine fleets at the beginning of WWI, their effective deployment was hampered by a lack of operational and strategic thinking, limited technology-based capability and an overwhelming prejudice against the evolving submarine doctrine (Polmar, 1963).

As the conflict grew and evolved, so did the submarine and its operational capabilities. The size, shape and speed of submarines began to change in response to their operational shortcomings and emerging requirements. The ocean-going submarine established itself as a threat to all shipping and expanded the range of operation to beyond the confines of coastal waters. This era also saw the development of the submarine as an anti-submarine warfare asset. However, it is important to understand that the smaller conventional submarine was, and is today, an effective littoral patrol and attack platform.

2.1.1 THE ROLE OF THE SUBMARINE

The operational role and technology-based capability of submarines have developed in parallel, starting slowly at first and escalating rapidly through WWI and WWII and continuing today. As a consequence, the technology attributes of a submarine cannot be viewed in isolation from its strategic role as the two are not mutually exclusive. It is common to discuss submarine operational strategy in terms of sea control and sea denial. These strategic approaches can be both defensive and offensive. Several distinct types of submarines now exist and have a unique part to play in many national maritime defence strategies. While the overall size, shape, configuration and performance of these submarine types vary significantly, all modern submarines share the common strategic and tactical advantage of stealth: the element of surprise. A description of the predominant types of submarine and their role in strategic maritime defence operations is presented by Hervey (1994).

2.2 AREA OF OPERATIONS

Throughout the First and Second World Wars a significant number of submarine operations occurred in the littoral waters surrounding the harbours and coastal expanse of allied and enemy territory. During this period the submarine operated on the surface for the majority of its deployment, submerging only just below the surface for torpedo attack and threat evasion purposes. It was largely during WWII and the eventual involvement of the United States and Japan that deep (blue) water submarine operations became commonplace. Submarines began to engage hostile fleets in the Pacific, Indian and Atlantic oceans after having transited from regional or domestic bases. Despite this, the submarine still spent the majority of its time on the surface and had limited efficiency during submerged operation. It was only the development of the snorkel, air independent propulsion (AIP) and, eventually, nuclear propulsion

and self-sustained atmospheric conditioning that allowed submarine operation to transition to beneath the ocean's surface for significant durations (Polmar, 1963).

With the end of WWII and the ensuing nuclear arms race of the Cold War, the world's super powers adopted long range nuclear powered attack and ballistic missile submarines to safeguard their national interests and counteract the East versus West military threat. Many of the submarine operations of this time were conducted in the deep waters off continental Europe and the United States with strategic deployments requiring the submarine to operate submerged for anywhere up to three months at a time. Nonetheless, coastal patrols were still being conducted by many nations using smaller conventionally powered submarines.

It is important to understand that littoral environs are often extremely favourable for submarine operation, especially where traditional ASW sonar detection systems are employed. This is primarily due to the effects of the hydrography: mixing thermal layers resulting in retarded sound propagation as well as signal bottom bounce. Each of these significantly reduces the effectiveness of ASW sonar system (Ristvedt, 1993). In addition, the conventional submarine's size and stealth when operating in a quiet state (advancing at slow speeds on its battery-powered propulsion system) give it a significant tactical advantage against ASW sensors.

2.2.1 NEAR-SURFACE SUBMARINE OPERATIONS

The requirement for submarines to operate near the surface is not unique to conventional (non-nuclear powered) type boats; however, conventional type submarines are required to operate in the near-surface condition on a more frequent basis. The principal operational requirements for the predominant submarine types to operate in close proximity to the free-surface are presented in Table 2-1.

Table 2-1 Operational requirements for submarine near-surface operation by submarine type (submarine type is described in the abbreviation and acronym list) Key: ✓ = Required, ✖ = Not required, O = Required, but not relatively often

Operational Evolution Requiring Shallow Submergence	Conventional		Nuclear		
	SS & SSK	SSG	SSN	SSGN	SSBN
Power generation (snort) & air exchange	✓	✓	✖	✖	✖
Periscope observation	✓	✓	✓	O	O
Communication & electronic warfare	✓	✓	✓	O	O
Deploy or recover swimmers & equipment	✓	✓	✓	✓	O
Deploy or recover off-board systems	✓	✓	✓	O	✖
Search and Rescue	O	O	O	O	O
Strike Warfare	O	O	O	O	O
Leaving/entering a port	✓	✓	✓	✓	✓

Near-surface operation typically requires the submarine to be manoeuvring at low speed and at a depth that provides between only two and five hull diameters separation between the submarine and the ocean's surface. The operation of naval submarines requires the helmsmen to exert significant psychological and physical effort to maintain depth, trim and heading. This effort is increased significantly when the submarine is operating near the surface and at slow speeds.

The primary threat to conventional submarines during transit and patrol is detection by enemy sonar and surface signature detection by thermal, electro-optical and atmospheric sensor systems. For operations where long transit distances are involved the likelihood of detection per unit time on station is greatly increased. Similarly, the tactical implications of the ocean's bathymetry, route choke points and navigation hazards can impact the ability for the submarine to maintain stealth. The effectiveness of modern conventional submarine power generation and storage systems means that operational discretion ratios are in the order of 10 percent. That is, a diesel-electric submarine will spend approximately 10 percent of its time at snort depth to replenish its stored energy levels (Ristvedt, 1993).

On arrival at the area of operation (AO) it is common for the submarine to conduct numerous or sustained surveillance evolutions at periscope depth to acquire electronic warfare (EW) data and gather information on enemy force size and structure (Hervey, 1994). Due to the performance constraints of submarine communications systems, the submarine may be required to operate at periscope depth for prolonged periods in order to transmit tactical information to a command centre (DiOrio, 1995).

The strategic and tactical advantage gained by inserting covert Special Operations forces into a hostile AO is significant. The submarine offers a clandestine platform which can deploy and recover operatives close to coastal areas with a relative level of safety (DiOrio, 1995). However, swimmer release and recovery is conducted primarily at very low speeds and in close proximity to the surface. Swimmers are deployed from either the torpedo tubes, conning tower or from hull-mounted dry deck shelters. Any loss of control resulting in rapid or extreme depth excursion can be fatal to the swimmers or betray the submarine's location and compromise its mission.

The launch of mines, surface-to-air and surface-to-surface weapons often requires the submarine to operate close to the surface. The exact depth of operation will depend on the weapon system and the tactical requirement. However, maintaining course and depth during weapons launch is extremely important to avoid the submarine impacting the store as well as ensuring the store can deploy effectively.

Despite the continued development of AIP systems and the increase in efficiency of conventional diesel generator and battery technology, the conventionally powered submarine is still required to operate at shallow depths to conduct power generation and atmosphere replenishment evolutions (snorting). As operational tempo increases so too does the frequency of snorting. As previously mentioned, the frequency and duration of snorting is determined by the whole-of-submarine power generation, propulsion and resistance system in combination with operational requirements. Any opportunity to increase the submarine's submerged endurance will have a favourable

impact on its ability to conduct operations in a covert manner and capitalise on the advantage of stealth.

In each of the operational scenarios presented here, the submarine will be operating in a near-surface condition where the effects of submarine and free-surface interaction can impact operational performance and discretion. Crook (1994) notes that with the increase in submarine littoral operation there will also be an increase in the duration at which the submarine will be operating at periscope depth and interacting with the ocean surface.

2.2.2 THE FUTURE OF SUBMARINE OPERATIONS

Looking back at the twentieth century, the changes in threat, technology and submarine operational doctrine led to a considerable change in the number and type of submarines in operation. Figure 2-1 illustrates the change in the type and number of submarines operated by the world's navies since 1900. The introduction of the nuclear powered submarine in the 1960's is clearly evident, as is the escalation of submarine fleet size during the Cold War era.

The effects of post-Cold War Russian, British and US nuclear disarmament policies and wholesale cuts to national defence spending are evident in the reduction in the numbers of both conventional and nuclear submarines. However, it is important to recognise that the conventionally powered submarine (SS & SSK) has remained a mainstay of the world's fleets and is now a platform that is within the reach of many nations.

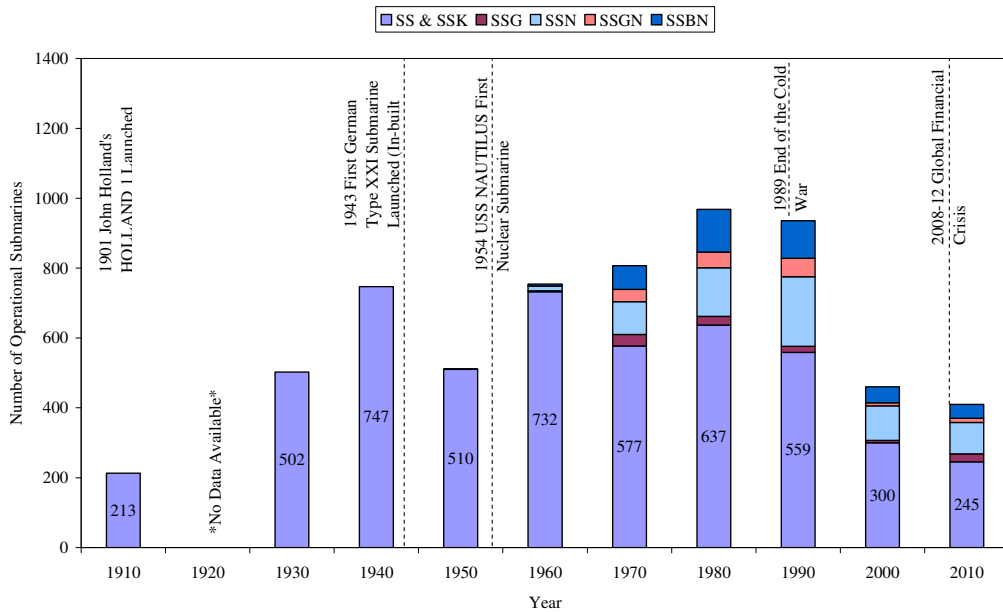


Figure 2-1 Numbers of operational submarines by type since 1910 (Actual number of SS & SSK submarines shown)

With increasing global financial pressures resulting in further cuts to State appropriations and in response to the established asymmetric threat that exists globally, the role of submarines is shifting towards that of a joint force capability component. The modern submarine is now, more than ever, being employed in joint operations as a pre-strike payload delivery system. Whether the payload is Special Operations personnel, unmanned off-board systems or ordnance, the joint forces role is bringing the submarine into the littoral environment and near to the surface on a more frequent basis.

2.3 SUBMARINE HULL SIZE, SHAPE AND ARRANGEMENT

The overall size and geometry of any submarine is the result of a complex design trade-off process where operational, financial and technological requirements and constraints are balanced to deliver a mission-capable platform. At the highest level, the implications of payload, diving depth, speed of advance and endurance drive the submarine's principal dimensions, form characteristics and propulsion and control systems. The hull diameter and length are largely governed by the number of internal decks required and the installed/embarked equipment attributed to habitability systems, communications systems, power generation and propulsion systems and sensor and weapons systems.

From an external viewpoint, the type and number of control surfaces is dependent on the hull's principal dimensions and form characteristics in combination with the prescribed manoeuvrability requirements. The sail's size and location is largely driven by the number and types of masts that are installed and their location within the hull. The shape of the sail is determined mainly by the hydrodynamic, signature and operational performance requirements.

2.3.1 AN OVERVIEW OF SUBMARINE HULL DESIGN EVOLUTION

Submarine hull size, shape and arrangement have changed significantly since the platform's introduction in the late nineteenth century. Up until the mid-1940s submarines would transit on the surface, first under gasoline powered engines, then later in their development under diesel powered engines. They would submerge to only shallow depths for the purposes of attack or evasion and would do so running on electrical energy stored in batteries. These platforms were generally considered as submersible ships rather than true submarines. This was also evident in their external hull shape which possessed many surface ship-like features: a fine bow and stern with a stem, twin propellers, a deck and superstructure with deck-mounted guns and antennae, high length-to-beam ratios and in some instances prominent engine exhaust uptakes. Many of these design attributes were directed at improving the surfaced performance of the submarine. The beam of the submersible was moderate for its length and comprised a round bilge. However, saddles and bilge keels were commonplace to improve the typically poor surface seakeeping performance. The overall length of the submarine was increased from that of the early designs to minimise the effects of wave-making resistance, particularly for trans-ocean fleet submarines (Friedman, 1984). Examples of typical submarine geometries of the early twentieth century are presented in Figure 2-2 and Figure 2-3.

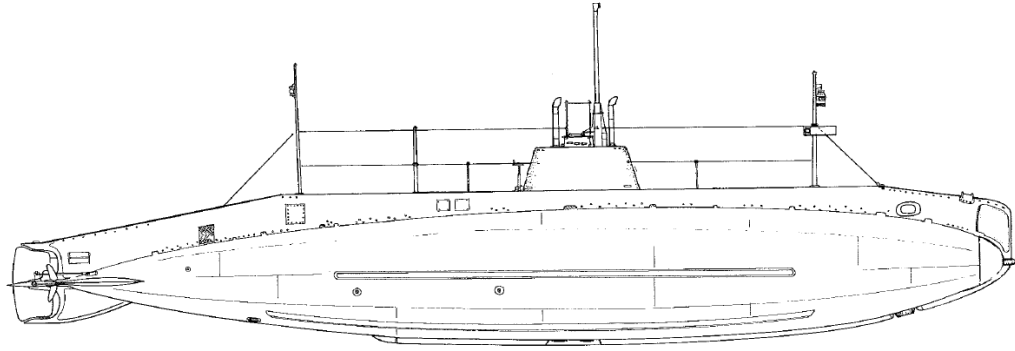


Figure 2-2 Pre-World War I US harbour defence submarine design (C Class) circa 1906. External profile view LOA = 32.10 m; BOA = 4.23 m; $L/D = 7.60$ (Friedman, 1995)

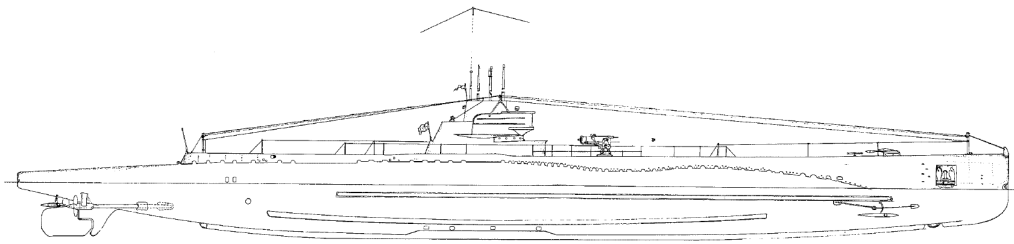


Figure 2-3 World War I US S Class submarine design circa 1920. External profile view LOA = 70.41 m; BOA = 6.65 m; $L/D = 10.60$ (Friedman, 1995)

The submersible ship design attributes remained largely unchanged throughout WWI and well into WWII with little variation among the world's fleets. Similarly, the operational doctrine adopted by submarine commanders relied on predominantly surfaced operation. In 1941 the British developed the Type 271 ASW radar which was effective at detecting surfaced submarines. This new ASW threat drove the required duration of submerged operation upwards. At this time, German submarine performance meant that the boat was required to surface to recharge its batteries every 8-9 hours for a period of approximately 1 hour. This put the submarine at high risk. In response to this risk, the German Navy developed and implemented the snorkel. The snorkel, originally a Dutch innovation, allowed the submarine to run submerged just below the surface and out of the detection range of the radar while replenishing its batteries (Ristvedt, 1993).

In parallel to the introduction of the snorkel, the Walter hydrogen peroxide diesel engine was being developed in Germany. The Walter engine allowed the submarine to run submerged at high speeds or for long durations at low speed without the need to surface or snorkel. However, this technology was not fully embraced by the German Navy and the submarine fleet remained largely powered by conventional diesel engines fitted with a snorkel (Polmar, 1963).

The increase in submerged power generation and propulsion system efficiency and effectiveness led to the design driven transition of the submersible ship to what is now accepted as the submarine. In response to this change in operational capability, the

submarine designers quickly began to optimise the external hull for underwater performance. This resulted in the removal of many external protuberances, a reduction in sail size and the general streamlining of the hull and sail. The German Type XXI submarine represents the embodiment of this design revolution and is itself recognised as the first of the generation of modern conventional submarines (Figure 2-4) (Polmar, 1963).

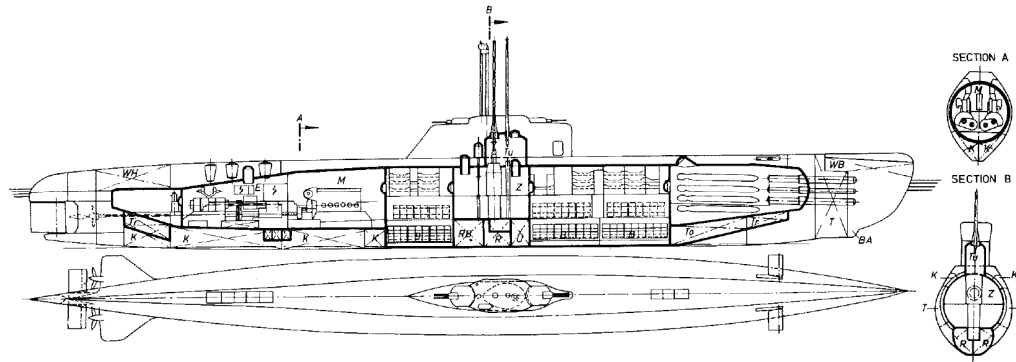


Figure 2-4 World War II German Type XXI Submarine circa 1943. Internal profile view (above) external plan view (below) LOA = 76.70 m; BOA = 8.00 m; $L/D = 9.60$ (Friedman, 1984)

2.3.2 THE REVOLUTION IN HULL DESIGN FOR UNDERWATER PERFORMANCE

Post WWII research into the hydrodynamic performance of the submarine led to further refinements in hull size, shape and arrangement and resulted in the hydrodynamically optimised axisymmetric tear drop hull shape. The US pioneered the design of high speed submarines. It was discovered that the existing hull forms performed poorly at higher speeds and were observed to develop significant trimming moment instability. The result of British and US research and development was an axisymmetric body of revolution that was considerably shorter than existing submarines of comparable volume. This led to greater manoeuvrability and favourable diving performance. The US efforts resulted in development of the USS ALBACORE experimental submarine (Figure 2-5). Combined with a single centrally located propeller, which increased hull propulsive efficiency to 0.90, the ALBACORE was able to make speeds of 33 knots when fully submerged. Later in the platform's development it was fitted with X-form control surfaces. Combined with the agile hull shape, the ALBACORE was capable of significantly higher turn rates than existing submarines. Incidentally, these favourable shape and size characteristics were not so dissimilar to John Holland's *Holland* submarine that was constructed at the turn of the 20th century (Figure 2-6) (Friedman, 1984).

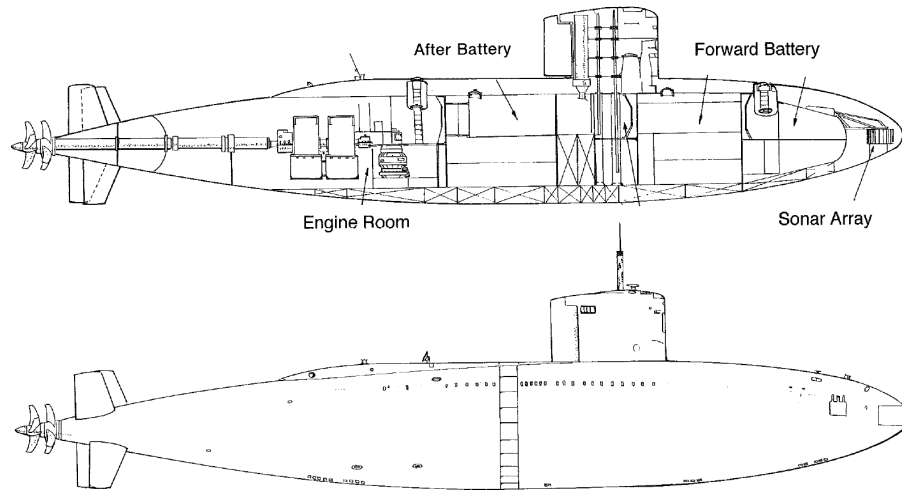


Figure 2-5 USS ALBACORE circa 1968. Internal profile view (above) outboard profile view (below) LOA = 62.10 m; BOA = 8.20 m; $L/D = 7.60$ (Friedman, 1994)

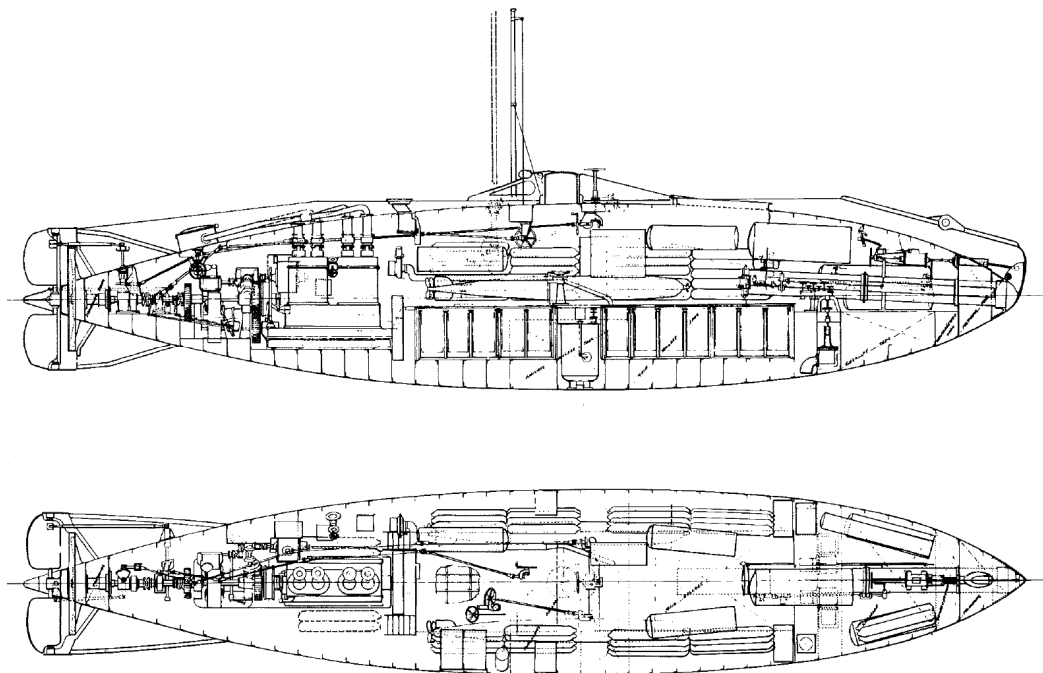
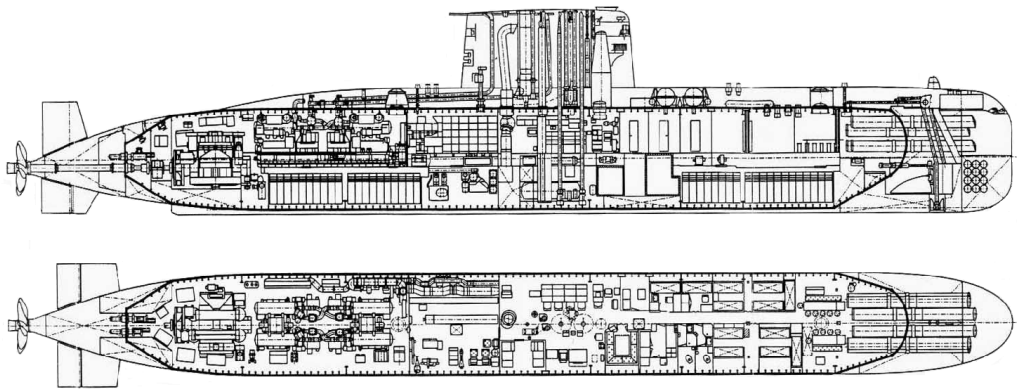


Figure 2-6 John Holland's *Holland* submarine circa 1900. Internal profile view (above) internal plan view (below) LOA = 19.46 m; BOA = 3.58 m; $L/D = 5.43$ (Friedman, 1994)

2.3.3 SUBMARINE LENGTH TO DIAMETER RATIO: IDEAL VERSUS PRACTICAL

In the 1950s researchers in the US identified an optimum length-to-diameter ratio for minimum resistance during deeply submerged operation. Burcher and Rydill (1994) report that the research indicated that an elliptical body of revolution with an L/D of approximately 6.00 is ideal for minimum submerged resistance. However, Friedman (1984) quotes an optimum L/D value of 7.00 which is attributable to the development of the ALBACORE. The experimental study conducted by Gertler (1950) shows that, for the series of geometries tested, a minimum deeply submerged resistance occurs at approximately 6.50. What is important to note, and is done so by Gertler (1950) and Kormilitsin and Khalizev (2001), is that the region of the resistance coefficient curve surrounding the minimum is relatively flat. This means that there is a range of L/D that is suitable for achieving minimal resistance.

The implication of integrating mission payload, powering and propulsion and crew sustainment systems into the idealised elliptical body of revolution means that this shape and form is often impractical for use as a naval submarine hull. As a result, naval submarine hull forms typically have a region of parallel mid-body that is required to accommodate the on-board systems (Burcher and Rydill, 1994). This has been found to be a more efficient approach to recovering internal volume than modifying the bow and stern profiles (Friedman, 1984). This approach to hull design is seen in contemporary conventional and nuclear submarines such as those shown in Figure 2-7 and Figure 2-8 respectively. The introduction of the parallel mid-body results in a submarine with an L/D greater than the ideal value of 6.50.



**Figure 2-7 German Type 209-1400 conventional submarine circa 1971-2008
Internal profile view (above) internal plan view (below) LOA = 61.20 m;
BOA = 6.25 m; L/D = 9.80 (Torkelson, 2005)**

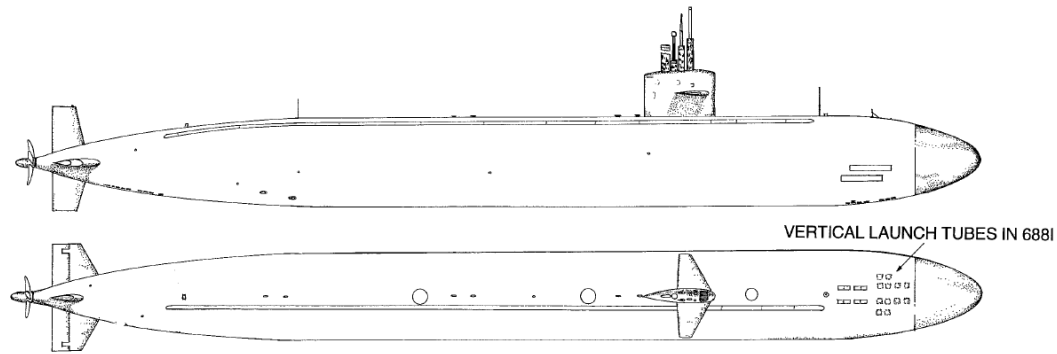


Figure 2-8 US LOS ANGELES (688) Class Nuclear Attack Submarine circa 1972-96. External profile view (above) external plan view (below) LOA = 110.00 m; BOA = 10.00 m; $L/D = 11.00$ (Friedman, 1994)

There are also occasions where the length of the submarine is modified as a result of through-life system upgrades or end-of-life extension modifications. An example of this is the integration of a 6 metre long air independent propulsion plug into the Swedish NÄCKEN Class submarine. This modification resulted in a 12 percent increase in hull length and an increase in L/D ratio from 8.67 to 9.74.

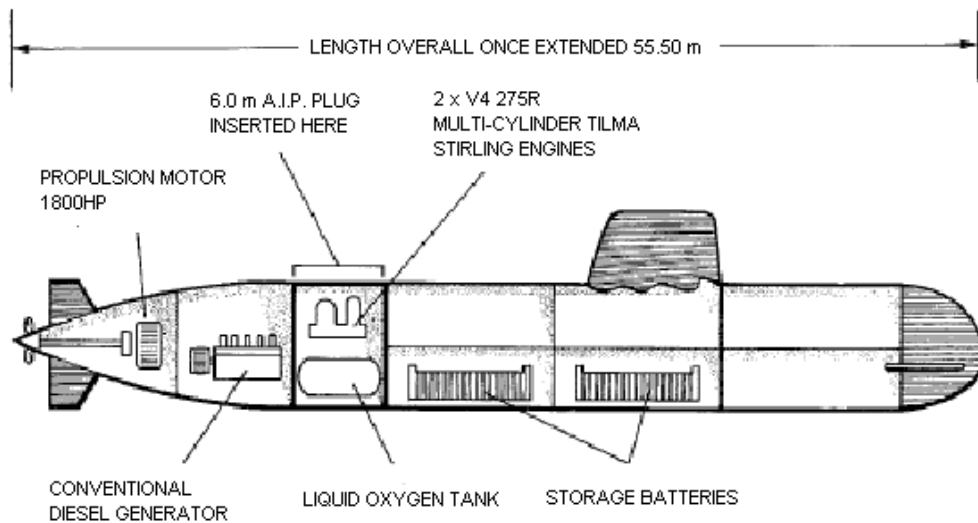


Figure 2-9 NÄCKEN Class Submarine showing 6.0m AIP plug (adapted from (Hervey, 1994))

2.4 OPERATIONAL SPEED PROFILE

The operational speed of modern submarines is a relatively well guarded piece of tactical information. However, it can be estimated that when operating in a near-surface condition and conducting littoral operations the submarine would be advancing at a speed no greater than approximately 15 knots and on average between 5 and 10 knots. Consequently, the equivalent Froude number regime will vary depending on the length of the submarine. A table of equivalent Froude number is given as a guide

to understanding the near-surface operational speed range of modern submarines (Table 2-2).

Table 2-2 Near-surface operational speed and equivalent Froude number based on hull length (L)

Operational Speed [kts]	$L = 60$ m	$L = 80$ m	$L = 100$ m
2	0.042	0.037	0.033
4	0.085	0.073	0.066
6	0.127	0.110	0.099
8	0.170	0.147	0.131
10	0.212	0.184	0.164
12	0.254	0.220	0.197
14	0.297	0.257	0.230

2.5 SUMMARY

Over the past 100 years of naval submarine development the size (length and diameter) and geometry of submarines has changed considerably. Though small or localised changes in on-board technology have indeed had an impact on submarine hull size and shape, the most significant changes can be attributed to the following occurrences:

- a. With the introduction of efficient battery technology, conventionally powered submarines were able to operate submerged for longer durations and as a result, the hull shape moved away from the characteristic WWI-WWII submersible ship configuration towards the contemporary, hydrodynamically tuned, axisymmetric body of revolution.
- b. The development of nuclear power generation and propulsion systems, together with advancements in materials and metallurgy, led to an increase in overall hull size and the creation of the long-range ballistic missile submarine. Consequently, the length-to-diameter ratio increased significantly, notwithstanding the overall increase in hull diameter that was required to accommodate the inter-continental ballistic missile vertical launch systems (VLS).

The capability, performance and economic attributes of the conventional type submarine have ensured its survival through the nuclear age and have positioned it as the submarine of choice for the majority of modern and developing naval powers. The evolution in maritime war-fighting and defence doctrine, largely in response to the changing global threat, has led to the submarine re-emerging as a high-value joint operations platform that is once again operating in the littoral environment.

Historically, the hydrodynamic characteristics of a submarine (resistance, manoeuvrability and acoustic signature) have been optimised for deeply submerged (blue water) operation. However, as littoral (green water) submarine operations become more and more prevalent, there is a justifiable need to identify and understand the effects of depth, speed and L/D on submarine near-surface operational performance.

3 LITERATURE REVIEW AND SIGNIFICANT THEORY

3.1 THEORETICAL ANALYSIS OF SUBMARINE RESISTANCE, LIFT AND TRIM

In order to establish a detailed understanding of the axial and vertical plane hydrodynamic forces and moments experienced by a streamlined body moving in a fluid, it is important to deconstruct the total forces and moments into their component parts. These components and their relative contribution differ for a body moving either fully submerged in a fluid or on or near the fluid's free-surface boundary. Similarly, the relative velocity of the body and fluid will have a significant effect on the type and dominance of the physical phenomena that manifest as a resultant force to resist motion. The following sections provide a detailed theoretical description of the physical phenomena that cause the forces (resistance and lift) and moment (trim) to act on a submerged body with relative motion and in proximity to a free-surface.

3.1.1 CHARACTERISTICS OF SUBMERGED BODY RESISTANCE

For a streamlined body moving at constant velocity in a homogenous viscous (real) fluid domain of infinite size there are two dominant contributors to the body's resistance to motion: friction (tangential shear forces) and form (normal pressure forces) resistance. The contribution of friction and form resistance components is dependent on the size and shape of the body. However, a streamlined body with attached flow will possess predominantly friction resistance (Granville, 1976).

Friction resistance occurs as a result of the fluid's interaction with the body and the establishment of a fluid boundary layer on and around the body's surface. A complex fluid microstructure occurs in the boundary layer and will vary significantly depending on the relative velocity, location along the length of the body and the effects of local pressure gradients. For an attached flow the boundary layer can be either laminar or turbulent with a varying transitional region dividing the two. A detailed description of friction resistance and hull boundary layer formation is presented by Larsson and Raven (2010).

An increase in the relative flow velocity will result in a reduction of the contribution of friction resistance for a constant contact area and surface roughness. This occurs as a result of the boundary layer momentum thickness reducing as velocity and hence Reynolds number increases (Larsson and Raven, 2010). The extension of the laminar boundary layer region will also result in a reduction of friction resistance. This can be achieved by streamlining the fore-body to provide a favourable pressure gradient to delay boundary layer transition (Granville, 1976).

Due to the negligible change in velocity profile in the fluid region outside the boundary layer, this region of the flow field is often assumed to be inviscid, despite the entire fluid region possessing a quasi-uniform viscosity. The topography of typical flow regions for a submerged body is presented in Figure 3-1. Boundary layer separation can occur due to the presence and effects of a negative (adverse) pressure gradient. The separated boundary layer will result in a reduction in the normal pressure acting on the after-body, thereby increasing the pressure differential between the fore and aft sections of the body and increasing the net form resistance (Larsson and Raven, 2010).

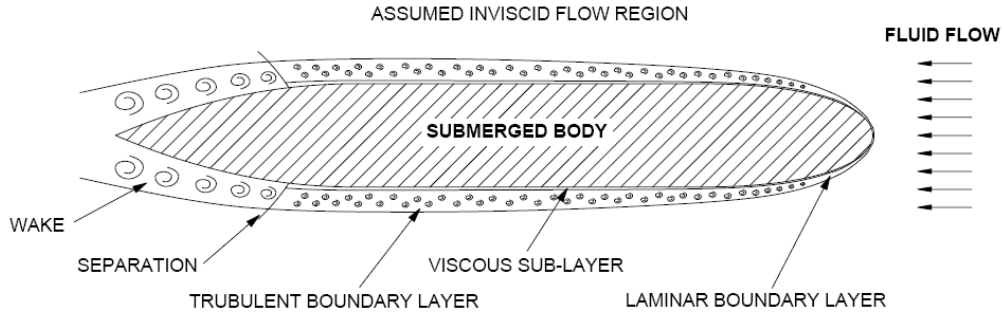


Figure 3-1 General flow topography for a body travelling in an infinite fluid domain (adapted from Larsson and Raven (2010))

Assuming again that a submerged body is travelling in a homogenous and infinite fluid domain, and that hydrostatic pressure is constant (or alternatively non-existent), the motion of the fluid around the three-dimensional body will result in local regions of high and low flow velocity close to the body. The incident flow will diverge about a dividing streamline that stagnates on the leading edge of the body. The flow will then converge again at the trailing edge of the body and continue downstream. These regions of high and low velocity flow result in regions of low and high pressure, respectively. The resultant non-uniform pressure field comprises force components that act normal to the body's surface. It is the net effect of these normal pressures that results in the form resistance (Larsson and Raven, 2010).

If the surrounding fluid was inviscid (ideal) there would be total pressure recovery across the body. That is, there are forces acting on the body in all directions, relative to the body's geometry, and the combined effect of the individual components would result in a net zero force. However, due to the viscous effects of boundary layer flow and separation, as discussed previously, the pressure is not recovered. This results in a force that will act to oppose the body's motion. This phenomenon is best represented in a two-dimensional flow condition as shown in Figure 3-2.

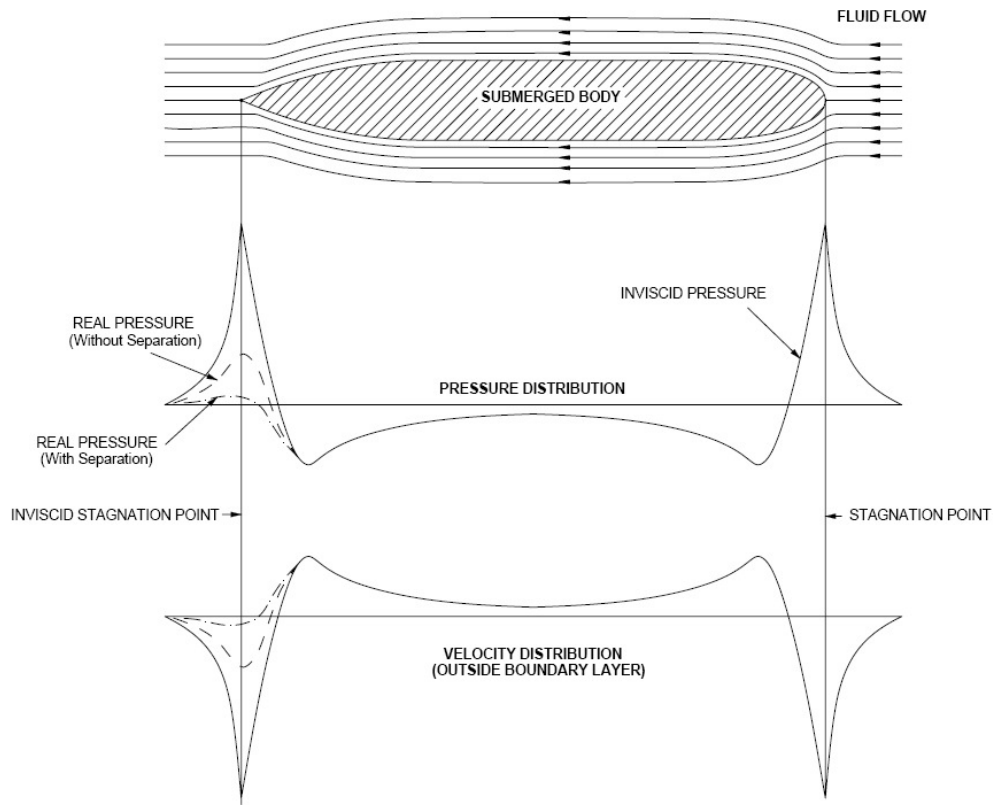


Figure 3-2 Ideal and real two-dimensional flow pressure and velocity distribution around a body travelling in an infinite fluid domain (adapted from Larsson and Raven (2010))

While the two-dimensional case provides an efficient means of representing the pressure effects of accelerated flow around the body, it is not an accurate representation of the three-dimensional flow experienced by a streamlined, axisymmetric body of revolution. Due to the increasing and decreasing diameter of the body over its length, the streamlines diverge and converge not only in a radial direction but also in a circumferential direction. The effect of the combined radial and circumferential divergence of the streamlines across the fore-body results in a thinner boundary layer when compared to the two-dimensional flow condition. In contrast, the convergence of the streamlines in the after-body region results in a thicker boundary layer. As a consequence, the analytical formulations of flat plate flow are not accurate for predicting the boundary layer properties of a body with acute lateral curvature (Larsson and Raven, 2010).

The effect of increasing the relative velocity between the body and the fluid will result in an increase in form resistance. This increase is proportional to the velocity squared. The total resistance of the body is represented by the relationship presented in Equation 3-1 where C_T is the total resistance coefficient for the body.

$$R_T = \frac{1}{2} \rho \cdot C_T \cdot U^2 \cdot S \quad \text{Equation 3-1}$$

The discussion so far has considered the zero incidence condition where the hull is axisymmetric and is travelling with its longitudinal axis parallel to the direction of the fluid flow. Where there is body asymmetry or, more importantly, an angle of incidence between the body and the direction of the flow, the body will be subject to a complex system of flow structures that act to increase the overall resistance and give rise to non-zero lift and/or side forces. Firstly, as the hull takes up an angle of incidence to the flow, the pressure distribution surrounding the hull will shift and become non-symmetrical (Figure 3-3). This is largely due to the cross-flow effect that occurs as the streamlines distort, diverge and converge, around the hull as well as boundary layer separation.

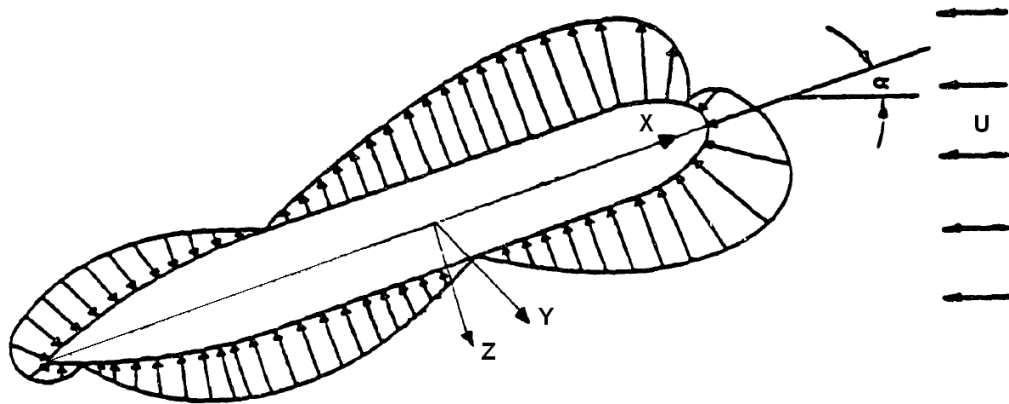


Figure 3-3 The effect of non-zero incidence flow on the pressure distribution surrounding an axisymmetric body travelling with uniform velocity in a fluid (Hickey, 1990)

Further increases in resistance will occur due to the creation of complex vortex structures which form as a result of the asymmetric flow over the hull and its appendages (Figure 3-4). These vortex structures have a strong Reynolds number dependency and as a consequence, will evolve as the relative velocity of the submarine increases.

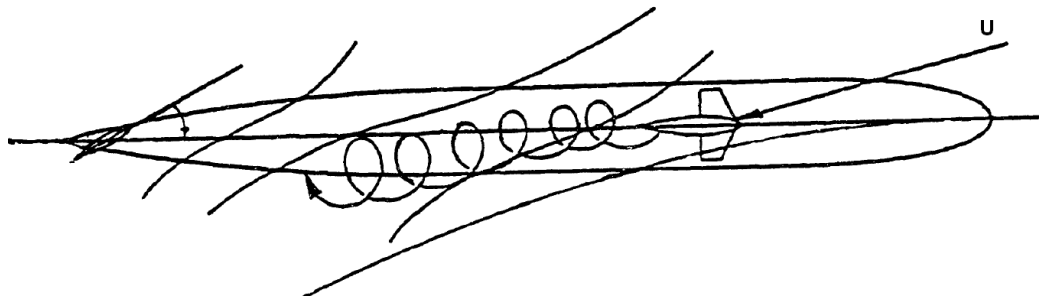


Figure 3-4 The effect of non-zero incidence flow on the formation of hull-borne vortices on a body travelling with uniform velocity in a fluid. Vortices form on the hull, sail and other appendages (Hickey, 1990)

3.1.2 EFFECTS OF HULL GEOMETRY AND APPENDAGES ON SUBMERGED SUBMARINE RESISTANCE

Considering the overall shape of the submerged body, any variation of its three-dimensional form or surface area will result in a change in its resistance-velocity relationship. Research conducted by Gertler (1950) led to the identification of the ideal form of an axisymmetric body of revolution with low resistance at high speeds. The dominant parameter was found to be the ratio of the body's length and diameter. There is a trade-off between the two resistance components that is directly related to these two dimensions. Burcher and Rydill (1994) illustrate the effect of length-to-diameter ratio on each of the resistance components and the total resistance for a body of constant volume (Figure 3-5). It is assumed that the secondary effects of fore-body and after-body shape on resistance are implicit in the representation. Based on the observations made by Gertler (1950) the optimum length-to-diameter ratio is approximately 6.00.

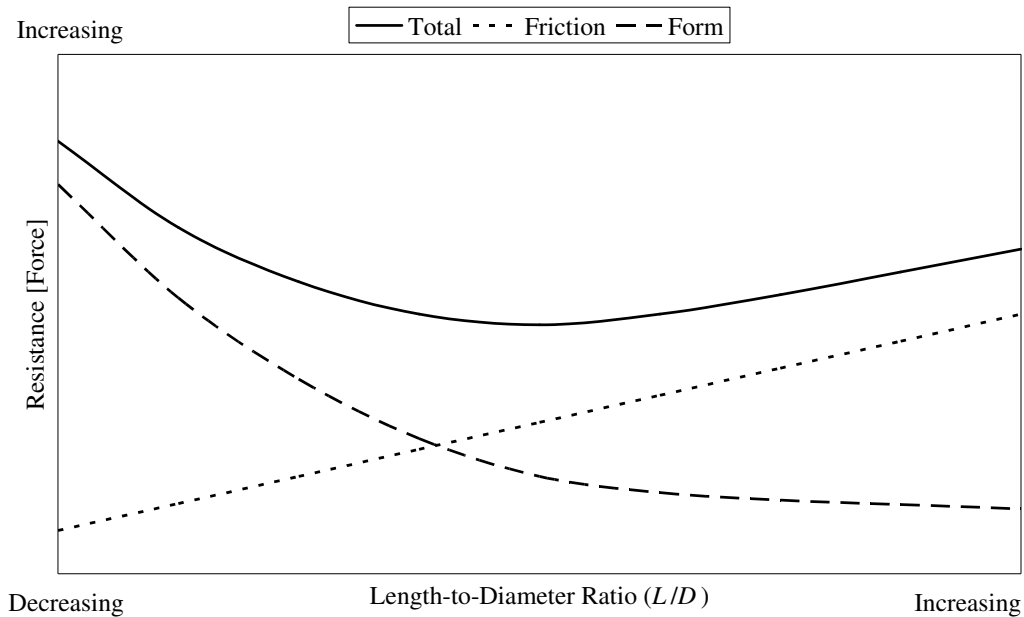


Figure 3-5 Effect of length to diameter ratio on streamlined body resistance (constant volume) in an infinite fluid domain at constant velocity (adapted from Burcher and Rydill (1994))

Kormilitsin and Khalizev (2001) provide a more detailed discussion on the effects of a submarine hull's length, beam and height relationships on propulsive performance and controllability. When considering the resistance acting on a streamlined axisymmetric bare hull, Kormilitsin and Khalizev (2001) report that the friction resistance coefficient accounts for around 50 to 60 percent of the total resistance. Considering the relationship of total viscous resistance presented in Equation 3-2, the form resistance can be described in terms of the friction resistance component with the aid of a non-dimensional coefficient (k_f) (Equation 3-3).

$$R_{Viscous} = R_{Friction} + R_{Form} \quad \text{Equation 3-2}$$

$$R_{Form} = k_F \cdot R_{Friction} \quad \text{Equation 3-3}$$

Based on the relationship of k_F with respect to the hull's length-to-diameter and its height-to-beam ratio shown in Figure 3-6, it is apparent that the form resistance is in the order of 10 to 25 percent of the friction resistance for hulls with $6 \leq L/D \leq 10$, with k_F decreasing with increasing L/D . For hulls with $10 \leq L/D \leq 20$ the form resistance reduces asymptotically to between 5 and 10 percent of the friction resistance. Kormilitsin and Khalizev (2001) suggest that a reduction in form resistance can be achieved by elongating the hull to an L/D of approximately 14. However, the resultant increase in length and wetted surface area leads to an increase in friction resistance. This behaviour is in agreement with that presented by Burcher and Rydill (1994) (Figure 3-5).

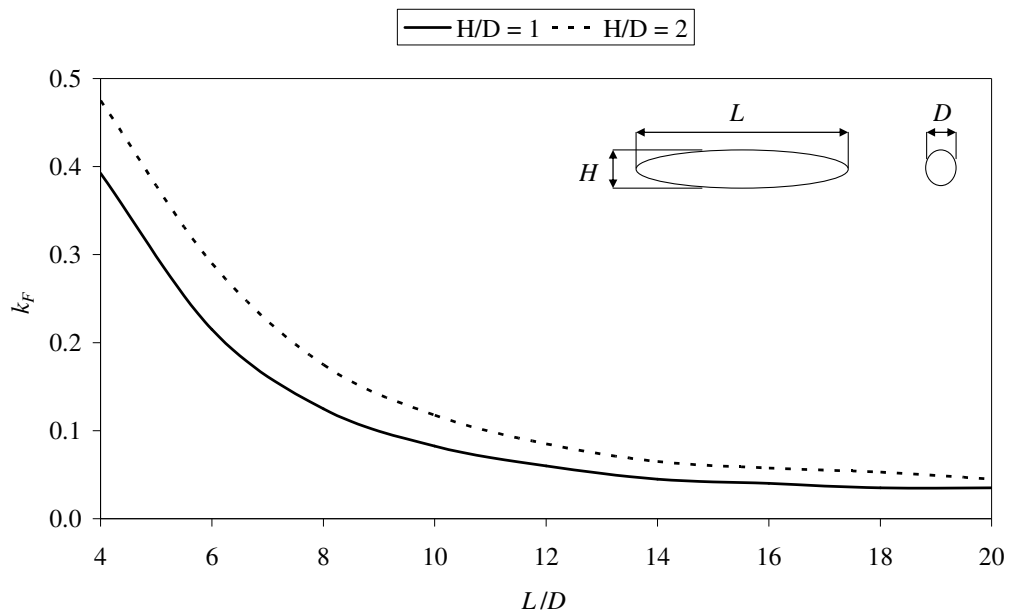


Figure 3-6 Droblenkov's k_F design curves for streamlined bodies of revolution with respect to length-to-diameter and height-to-beam ratio (adapted from Kormilitsin and Khalizev (2001))

A quantitative representation of the relationship between the total viscous resistance and the friction and form components is presented by Kormilitsin and Khalizev (2001) and is reproduced here in Figure 3-7. The relationship is based on geometries of equivalent displacement (constant volume). A local minimum of viscous resistance can be observed at an L/D of approximately 6.00. However, the region surrounding the minimum ($6 \leq L/D \leq 12$) is relatively flat with only slight variations in resistance with the change in L/D . Consequently, a range of L/D hull forms can be considered to possess favourable deeply submerged resistance characteristics.

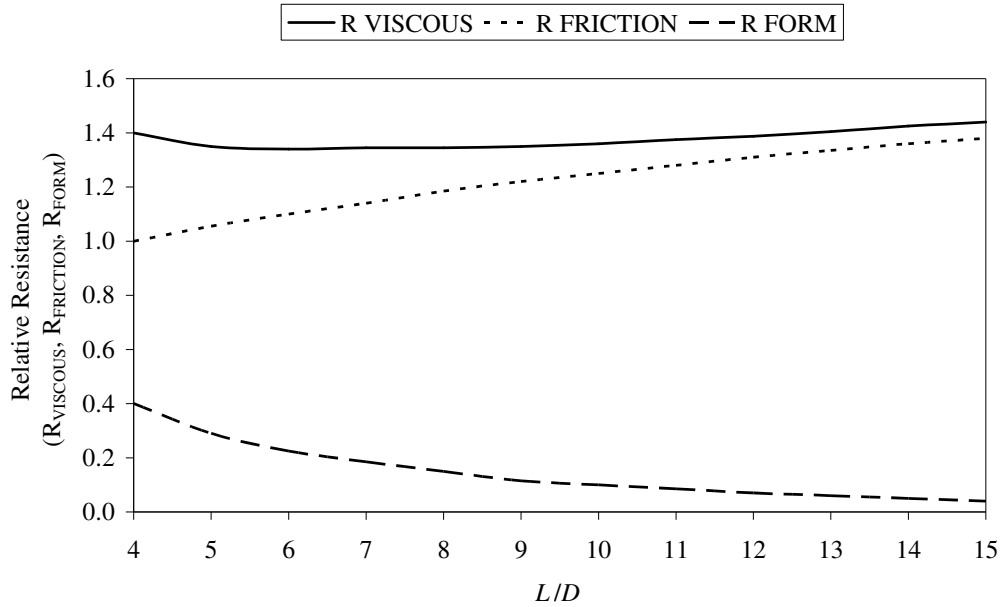


Figure 3-7 Deeply submerged submarine relative resistance (viscous resistance and its friction and form components) as a function of length-to-diameter ratio (adapted from Kormilitsin and Khalizev (2001))

As the hull cross-section shape tends away from a circular profile towards an oval profile (height-to-beam ratio > 1), as is commonly found with conventional submarine hull shapes, there is a tendency for the optimum L/D value to decrease. This behaviour is based on forms with comparable relative wetted surface area (Kormilitsin and Khalizev, 2001).

Kormilitsin and Khalizev (2001) add that form resistance is sensitive to the fullness of the hull (its prismatic coefficient) and the shape of its forward and aft ends. The experimental investigations conducted by Gertler (1950), discussed here in section 3.2.2, agree with this assertion. The reason for the interdependency is that, as stated previously, the form resistance is the manifestation of the effects of the non-uniform pressure field acting on the body. Rapid changes in section shape give rise to pressure gradients, either favourable (positive) or adverse (negative), and a net form resistance. Hull shapes of elliptical form and without any parallel mid-body are shown to possess the most favourable pressure gradient distribution and hence form resistance when compared to a parabolic form or elliptical form with parallel mid-body (Figure 3-8) (Kormilitsin and Khalizev, 2001). Unfortunately, purely elliptical forms are generally impractical for use as the basis of a naval submarine hull.

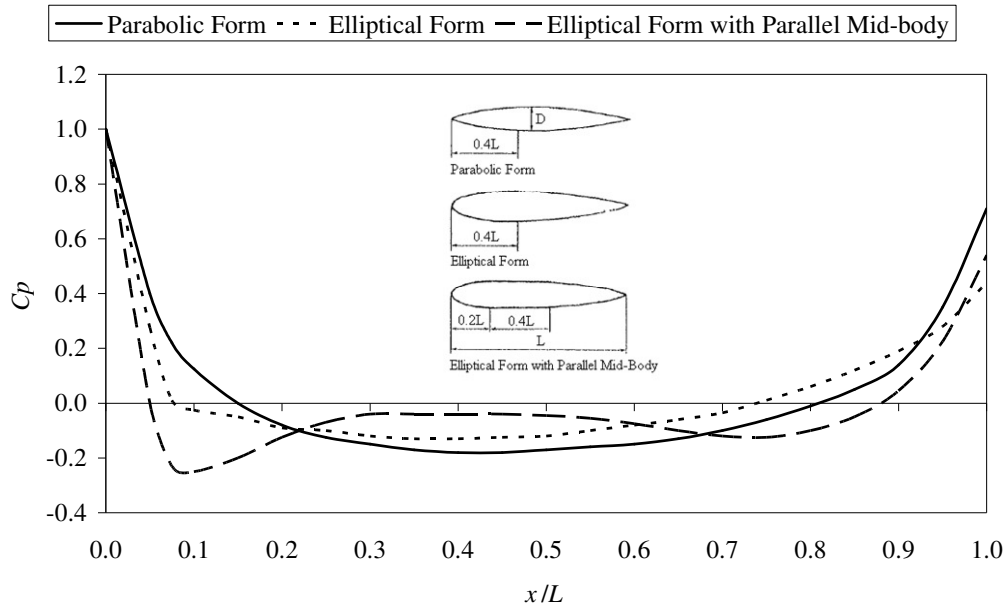


Figure 3-8 Effect of form and parallel mid-body on the longitudinal distribution of pressure gradient (adapted from Kormilitsin and Khalizev (2001))

The total resistance of a deeply submerged axisymmetric body of revolution can be assumed to be the sum of the aforementioned viscous components: friction and form resistance. The addition of any appendages and protuberances to the streamlined body will increase the total resistance. While each appendage and protuberance will possess its own friction and form resistance component, their interaction with the streamlined hull gives rise to more complex three-dimensional flow behaviour that contributes to the resistance quota. Some appendages will be subject to phenomena such as vortex shedding and induced resistance. Burcher and Rydill (1994) provide an indication of the ‘resistfulness’ of common submarine appendages (Table 3-1). Kormilitsin and Khalizev (2001) note that the resistance of an appendage is sensitive to the way it interacts with the bare hull. Where appendages intersect the hull, such as control surfaces and sails (bridge fins), the geometry of their intersection should be faired or blended in a manner that reduces the interaction effects.

Table 3-1 Indication of ‘resistfulness’ of submarine appendages and protuberances for a generic submarine configuration (Burcher and Rydill, 1994)

Component	$\frac{\Delta P_E}{\text{Total } P_E} (\%) = A$	$\frac{\Delta \text{Area}}{\text{Total Area}} (\%) = B$	Resistfulness = A/B
Hull	68.50	84.33	0.81
Bridge Fin	7.87	8.05	0.98
Stern Planes	7.71	3.28	2.35
Bow Planes	3.54	0.58	6.14
Upper Rudder	5.34	1.64	3.26
Lower Rudder	1.81	1.11	1.63
Sonar Fairing	2.88	0.16	18.03
Ballast Keel	6.05	6.10	0.99

3.1.3 CHARACTERISTICS OF FREE-SURFACED INDUCED RESISTANCE

The introduction of the free-surface boundary adds complexity to the resistance characteristics of a body moving in what becomes a two-phase flow condition. While friction and form resistance still provide a significant contribution to the total resistance quota, there are several new components that have varying levels of effect. The most dominant type, and the subject of this research, is wave making resistance.

By virtue of the submarine’s motion through the water, a pressure field is established around the external surfaces of the hull. Often referred to as the distribution of total pressure, the behaviour of the pressure field is generally similar among streamlined bodies of revolution and is comparable to those shown in Figure 3-8. In a deeply submerged condition the pressure field solely influences the body’s viscous resistance components. However, as the body approaches the free-surface the pressure field interacts with the non-rigid boundary and, depending on its relative magnitude, will generate a series of surface disturbances. The resultant disturbances or gravity waves will develop into a travelling wave field at the free-surface.

When the wave field has become fully developed it will travel with a phase velocity equal to that of the body’s velocity. For a deep water environment with the body travelling on the free-surface, the wave field closely resembles that of the Kelvin wave pattern with a composition of both transverse and divergent waves. More accurately, the wave pattern of a streamlined body moving on or near the free-surface is the combination of several wave patterns. A finite amount of energy is required to generate these systems of surface disturbance. This energy must be contributed by the body for it to sustain a constant forward speed (van Manen and van Oossanen, 1988).

The travelling wave system is the combination of several wave systems that occur at points along the length of the body and is highly dependent on the body’s size, form and speed. It is well understood that there are five discrete contributors to the overall wave field and that these occur at the locations of relative maximum and minimum total pressure (Larsson and Raven, 2010).

The five components are:

- a. The Bernoulli wave that occurs at the bow. This system decays rapidly ahead and astern of the body and is not considered to radiate energy.
- b. The bow wave that occurs coincident with the high pressure region at the leading edge and originates with a wave crest.
- c. The forward shoulder wave that originates in the region of low pressure that occurs as the body's girth increases. This wave system originates with a wave trough.
- d. The aft shoulder wave that occurs in the region of low pressure that exists where the body's girth begins to reduce. Like the forward shoulder wave, the system originates with a wave trough.
- e. The stern wave that occurs coincident with the high pressure region at the trailing edge. Like the bow wave, the stern wave originates with a wave crest.

The wave system of a simple wedge-shaped body is presented in Figure 3-9 below.

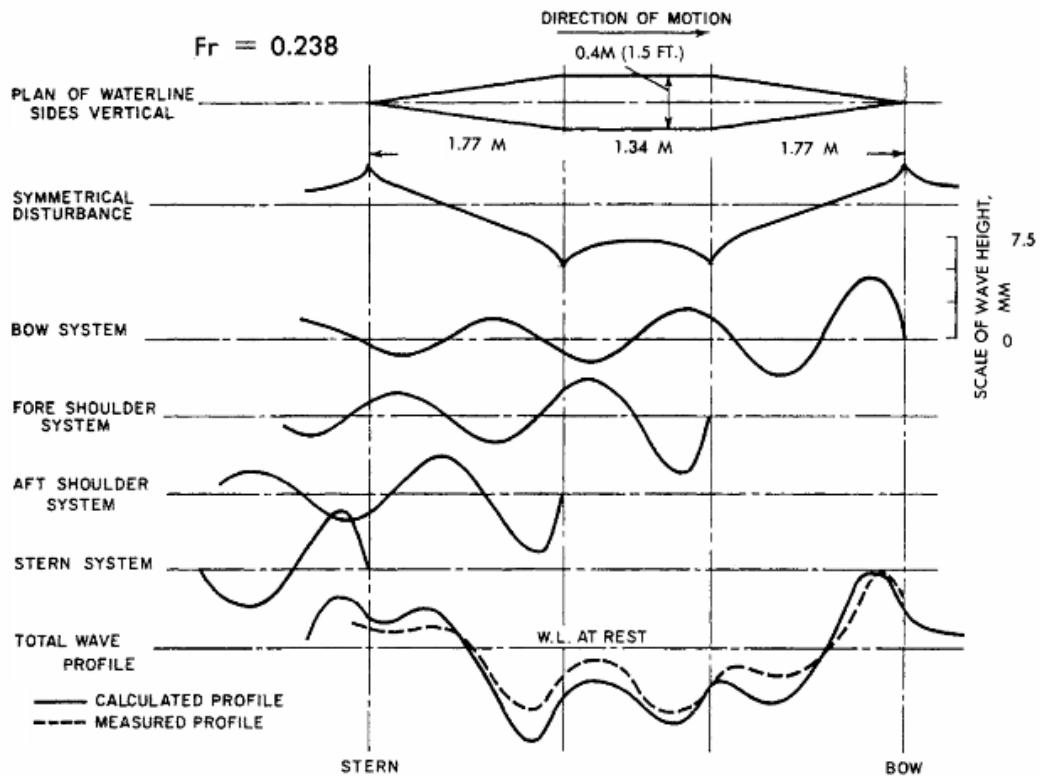


Figure 3-9 The wave system components and their interaction for a wedge-shaped body travelling at $Fr = 0.238$ (van Manen and van Oossanen, 1988).

As the body moves at a steady velocity the wave systems interact with one another in either a constructive or destructive way as the generated surface elevations coincide. The wavelength of the surface waves can be approximated to a free wave travelling at the same velocity. In this instance it is the velocity of the moving body. The transverse waves propagate with their crest normal to the direction in which the body is moving. In a deep water condition, the wavelength of the transverse waves can be determined using Equation 3-4, whereas the wavelength of the divergent waves can be determined using Equation 3-5. In Equation 3-5 the angle theta (θ) is the angle between the body's direction of travel and the vector normal to the crest of the divergent wave (van Manen and van Oossanen, 1988).

$$\lambda = 2 \cdot \pi \cdot \frac{V^2}{g} \quad \text{Equation 3-4}$$

$$\lambda' = 2 \cdot \pi \cdot \frac{V^2}{g} \cdot \cos^2 \theta \quad \text{Equation 3-5}$$

As the body's velocity changes, so too do the wavelengths of the bow, stern and shoulder wave systems. Depending on their length and the phase difference between these systems, constructive interaction can occur where the crests of two or more waves coincide. Conversely, destructive interaction can occur where a crest from one wave system coincides with a trough of another. Wave interaction typically only occurs for the transverse components of the wave systems (Larsson and Raven, 2010).

The velocities or Froude numbers at which these in-phase and 180 degree out-of-phase interactions occur is approximated by the relationship presented in Equation 3-6. Constructive interaction occurs for positive even integer values of N , while destructive interaction occurs for positive odd integer values on N (Rawson & Tupper, 2001).

$$\frac{V^2}{0.9L} = \frac{g}{N \cdot \pi} \quad \text{Equation 3-6}$$

Using Equation 3-6 the Froude number at which these fundamental interactions occur were calculated assuming a body length (L) of unity. This data is presented in Table 3-2. The constructive and destructive interaction of the wave systems results in a periodically varying increase in the wave resistance experienced by the body. Where two wave components interact in a constructive manner, the wave elevation increases and results in an increase in the energy imparted to the surrounding fluid by the body. At low speeds the waves generated by the body are vanishingly small and the total resistance is predominantly viscous. At high speeds (Froude numbers much greater than approximately 0.50) the wavelength of the wave systems becomes much longer than the body length and the interference phenomenon ceases to occur and the coefficient of wave resistance (C_w) diminishes (Larsson and Raven, 2010). This relief in additional resistance at high speed is not readily experienced by naval submarines as these speeds far exceed those currently attainable or considered operationally practical.

Table 3-2 Froude number where constructive and destructive interaction occurs between two wave systems

<i>N</i>	<i>Fr</i>	Interaction Type
1	0.54	Constructive
2	0.38	Destructive
3	0.31	Constructive
4	0.27	Destructive
5	0.24	Constructive
6	0.22	Destructive

An alternative method of predicting the speeds at which constructive interference occurs was developed by Baker and Kent (1919) and is based on the z-method. This method considers only the interaction of the body's bow and aft shoulder wave systems which are separated by the wave-making distance (*z*). Baker and Kent (1919) were able to redefine the z-method with respect to the body's prismatic coefficient. A modified version of Baker and Kent's formulation, which combines the wave dispersion relation, is presented by Larsson and Raven (2010). In this instance the Froude number at which constructive interaction occurs can be calculated using Equation 3-7 for *k* = 1, 2 and 3. However, this adaptation of the z-method does not provide the Froude number at which the peak wave resistance occurs (approximately *Fr* = 0.50).

$$Fr = \sqrt{\frac{C_p}{2\pi(k + 0.25)}} \quad \text{Equation 3-7}$$

Using Equation 3-7 the Froude numbers at which constructive interaction occurs were calculated for a range of prismatic coefficients from 0.50 to 1.00. The results are presented in Table 3-3.

Table 3-3 Froude number where constructive interaction occurs based on body prismatic coefficient

<i>k</i>	<i>C_p</i> = 0.50	<i>C_p</i> = 0.60	<i>C_p</i> = 0.70	<i>C_p</i> = 0.80	<i>C_p</i> = 0.90	<i>C_p</i> = 1.00
1	0.25	0.28	0.30	0.32	0.34	0.36
2	0.19	0.21	0.22	0.24	0.25	0.27
3	0.16	0.17	0.19	0.20	0.21	0.22

When comparing the method presented by Rawson and Tupper (2001) (Equation 3-6) with that modified z-method presented by Larsson and Raven (2011) (Equation 3-7) it could be surmised that Equation 3-6 is representative of a body with a prismatic coefficient of approximately 0.80. Rawson and Tupper (2001) report that the increase in wave resistance that occurs when *N* = 3 (*Fr* = 0.31) is significantly influenced by the prismatic coefficient of the body to which it is related. The overall significance of predicting the speeds at which the different wave interactions occurs is that it can guide the selection of body form characteristics, particularly length and prismatic

coefficient, to achieve minimum wave resistance at specific operational speeds. It is evident that the near-surface operational speed range (Table 2-2) coincides with the region where wave making and wave resistance have a significant effect on a submerged body's resistance performance.

3.1.4 LIFT FORCE AND TRIMMING MOMENT

Near-surface operation of a submarine is inherently an asymmetric problem, whereas operation in a deep water condition is assumed to be symmetric. This is due to the interaction between the submerged body and the flexible free-surface boundary which gives rise to a vertical lift force and trimming moment (Griffin, 2002). A vertical plane force and moment occur due to the interaction effect that exists when the body's hydrodynamic pressure field generates free-surface waves, which in turn generate a non-uniform hydrostatic pressure distribution surrounding the body (Figure 3-10).

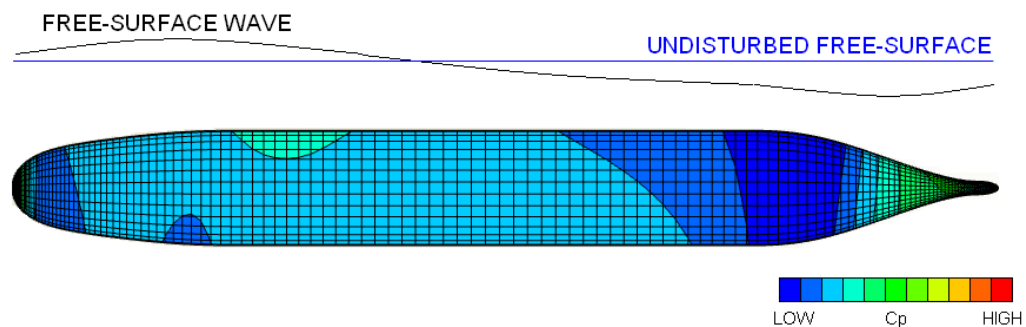


Figure 3-10 The non-uniform pressure distribution occurring on a submerged body and the resultant wave system (surface disturbance) due to the interaction between the body and the free-surface boundary.

The resultant direction and magnitude of the vertical force and moment that occur due to the net asymmetric pressure distribution are known to vary with speed and submergence depth. Investigations into the forces and moments acting on submerged bodies of revolution using numerical methods conducted by Doctors and Beck (1987) and Crook (1994) have indicated several important behavioural characteristics. These are:

- a. At low Froude numbers the submerged body experiences a lift force that draws it towards the free surface. The non-dimensional lift force coefficient increases to a peak value in the region of $Fr = 0.40$, after which it reduces and transitions to a force pulling the body away from the free-surface. The transition occurs in the region of $Fr = 0.60$.
- b. At low Froude numbers the interaction between the body and the free-surface typically results in a pressure distribution that causes a bow down trimming moment to occur. This causes the aft end of the body to move towards the free-surface. As the speed increases, the direction of the moment will change such that the body possesses a bow up trimming moment. This behaviour is periodic and is dependent on the speed at which the body is travelling.

These effects are illustrated in Figure 3-11 below.

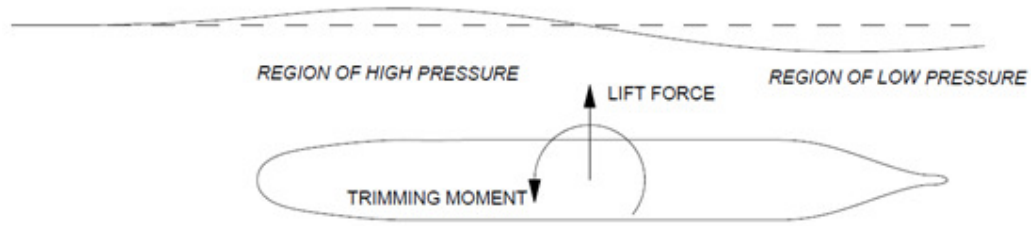


Figure 3-11 Representation of the vertical force and moment couple that occurs when the submerged body is interacting with the free-surface (the direction of the force and moment shown above is typical of low speed operation)

Similar to the wave making resistance, the vertical force and moment behavioural characteristics are largely dependent on the geometric arrangement of the body as well as its speed and submergence depth. More detailed observations have been made by researchers using potential flow based numerical methods. A discussion of their observations is included in Section 3.3.

3.1.5 SUMMARY

The forces and moments acting on a deeply submerged axisymmetric body in relative motion with the surrounding fluid originate predominantly from viscous effects and comprise tangential (friction resistance) and normal pressure (form resistance) components. Discounting surface roughness, the magnitude of the resistance force is principally influenced by the relative speed of the body and its geometric form, in particular its length-to-diameter ratio and prismatic coefficient. Investigations into the drag performance of deeply submerged streamlined bodies have shown that the ideal geometric form comprises an elliptical shape with a length-to-diameter ratio of 6.00. However, this ideal hydrodynamic configuration is not effective for use as the basis of a naval submarine hull as it does not provide adequate internal volume to accommodate the platform's payload.

When the axisymmetric body is moving parallel with and in proximity to a free-surface boundary it will induce a surface wave system that travels with a phase velocity equal to the speed of the body. The surface wave system comprises five discrete wave components and occurs as a result of the body's flow induced pressure field disturbing the flexible free-surface boundary. Interaction between the four hull-borne wave components leads to wave interference effects that are dependent on the speed and length of the body. The interference of the wave systems can be constructive or destructive as their crests and troughs coincide. Positive interaction results in increased wave resistance, whereas destructive interference minimises the wave resistance. The interference phenomenon varies periodically with speed up to a Froude number of approximately 0.50, after which the wavelengths of the hull-borne waves become too long to cause interaction effects.

An asymmetric normal pressure field will occur on the body due to the change in elevation of the nearby free-surface boundary. The asymmetric normal pressure distribution results in a vertical force and moment couple acting on the body to

displace and rotate it in the vertical plane. At Froude numbers below approximately 0.60 there is a tendency for the body to experience a lifting force that pushes it towards the free-surface. Beyond $Fr = 0.60$ the lift force acts to push the body away from the surface. A trimming moment occurs in combination with the lift force. The direction of the trimming moment changes periodically with speed and typically initiates with a bow down trim at low speeds ($Fr < 0.30$). As speed increases this will change and possibly oscillate between bow up and bow down before becoming predominantly bow up at higher speeds ($Fr > 0.35$).

3.2 EXPERIMENTAL INVESTIGATIONS OF SUBMERGED BODY WAVE RESISTANCE

The results of experimental investigations into the wave resistance of submerged bodies have been presented by several authors, the majority of which was published in the first half of the twentieth century. Of these endeavours, perhaps the most relevant is the work of Weinblum et al. (1950) and Gertler (1950). Incidentally, these authors' work preceded some of the most significant changes in submarine hull shape design. In combination with other technological developments, the change in hull shape resulted in an increase in sustained operating speed, endurance, depth of submergence and sensor performance. To date, however, little experimental work has been published showing the effects of length-to-diameter on the near-surface performance of submerged bodies.

To characterise the near-surface performance of a submerged body or submarine it is useful to relate its submergence depth to one of its dimensional parameters. To this end, the submergence depth of an axisymmetric body's longitudinal centreline below the still waterline (h) is non-dimensionalised with its maximum diameter (D), resulting in the relationship presented in Equation 3-8 and illustrated in Figure 3-12. This relationship is used exclusively in the work presented in this thesis.

$$H^* = \frac{h}{D} \quad \text{Equation 3-8}$$

A similar relationship is also presented by Hoerner (1965) where the centreline submergence depth is non-dimensionalised with either overall body length or maximum hull diameter.

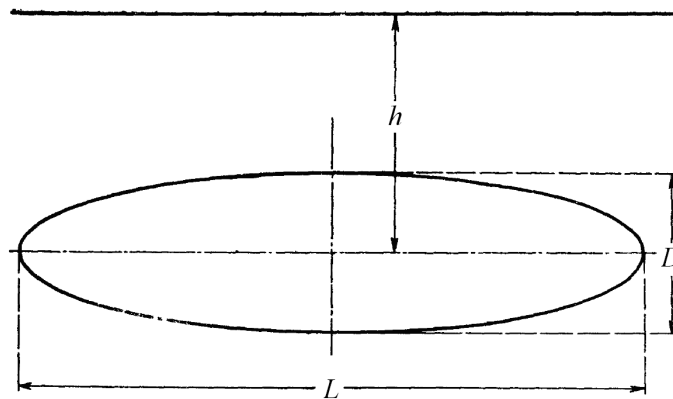


Figure 3-12 Dimensional characteristics of immersed body of revolution

3.2.1 WAVE RESISTANCE OF IMMERSED BODIES OF REVOLUTION (WEINBLUM ET AL., 1950)

In their study, Weinblum et al. (1950) investigated the effects of submergence depth, speed of advance and body shape on the wave resistance characteristics of a series of axisymmetric bodies of revolution. Physical experiments were completed at the Prussian Research Institute for Water Engineering and Shipbuilding with the results first published in 1936. The nature of the research conducted was a compromise between theoretical and applied. The geometries of the bodies of revolution were selected in order to make comparison between the experiment results and the theoretical calculation method proposed by Havelock (1919), Havelock (1931a) and Havelock (1931b). Four models were tested in the experiment, each having a length-to-diameter ratio of 8.00.

Experiments were conducted at length base Froude numbers of between, nominally, $Fr = 0.20$ and 0.50 and at centreline submergence depths of zero ($H^* = 0.00$) to six body radii ($H^* = 3.00$) inclusive. The model principal dimensions and model centreline section shapes are presented in Table 3-4 and Figure 3-13, Figure 3-14, Figure 3-15 and Figure 3-16 respectively.

Table 3-4 Principal dimensions of models tested (Weinblum et al., 1950)

Model Number	Length [m]	Length to Diameter (L/D)	Volume [m^3]	Wetted Surface [m^2]	Prismatic Coefficient (C_p)
1242	4	8.00	0.429	4.26	0.546
1257	4	8.00	0.628	5.46	0.800
1286	4	8.00	0.524	4.94	0.667
1242 & 1257 Blend	4	8.00	0.528	4.86	0.673

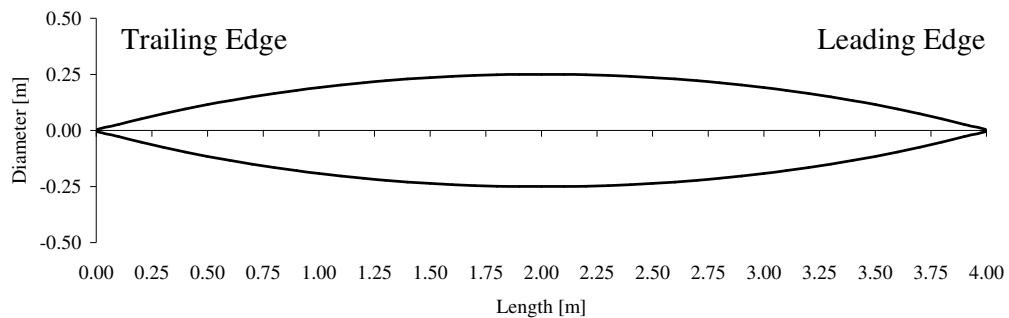


Figure 3-13 Centreline profile of Model 1242 ($C_p = 0.546$)

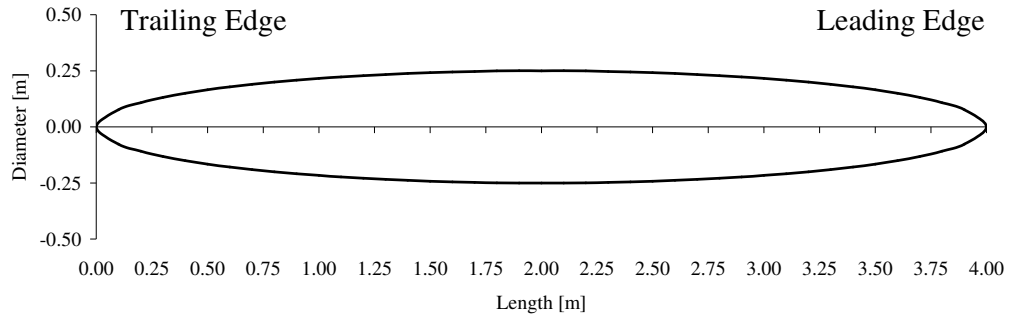


Figure 3-14 Centreline profile of Model 1286 ($C_p = 0.667$)

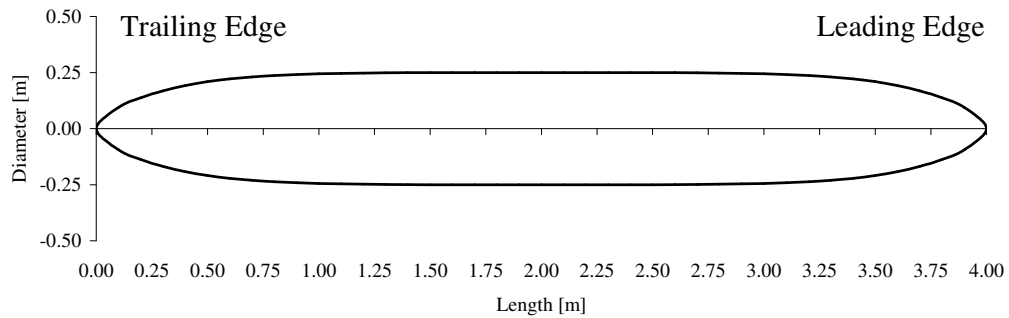


Figure 3-15 Centreline profile of Model 1257 ($C_p = 0.800$)

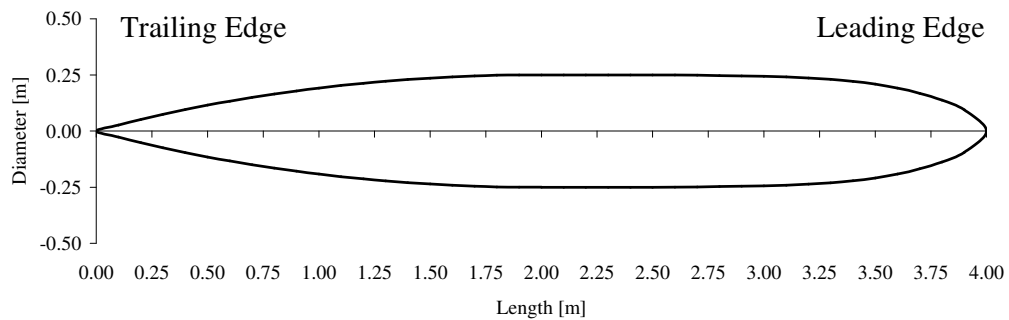


Figure 3-16 Centreline profile of Model 1242 & 1257 Blend ($C_p = 0.673$)

Weinblum et al. (1950) made several fundamental observations based on the results of their experiment. These observations were that wave making and its effect on submerged body resistance is dependent upon the speed of advance of the submerged body and its depth relative to the free-surface. A hump and hollow response similar to that exhibited by surface ships was observed for the total resistance with respect to Froude number. Weinblum et al. (1950) suggest that these hump and hollow features are more pronounced than for those commonly observed for surface ships. Consequently, the region of optimum resistance, the hollow, is relatively narrow and its location varies with Froude number. The magnitude and location of these features, relative to Froude number, are strongly dependent on the submerged body's geometry, in particular its prismatic coefficient.

The hump and hollow effect that occurs as a result of wave making is clearly identifiable in the residual resistance coefficient of model 1257 and to a lesser extent blended model 1242 & 1257 (Figure 3-17). Model 1242 does not exhibit the same periodically varying resistance trend as can be observed for the remaining models. In comparison to the other models, Model 1242 resembles a parabolic form, possesses no parallel mid-body section and has the lowest prismatic coefficient. Nonetheless, the free-surface interaction effect quickly diminishes as submergence depth is increased for all models.

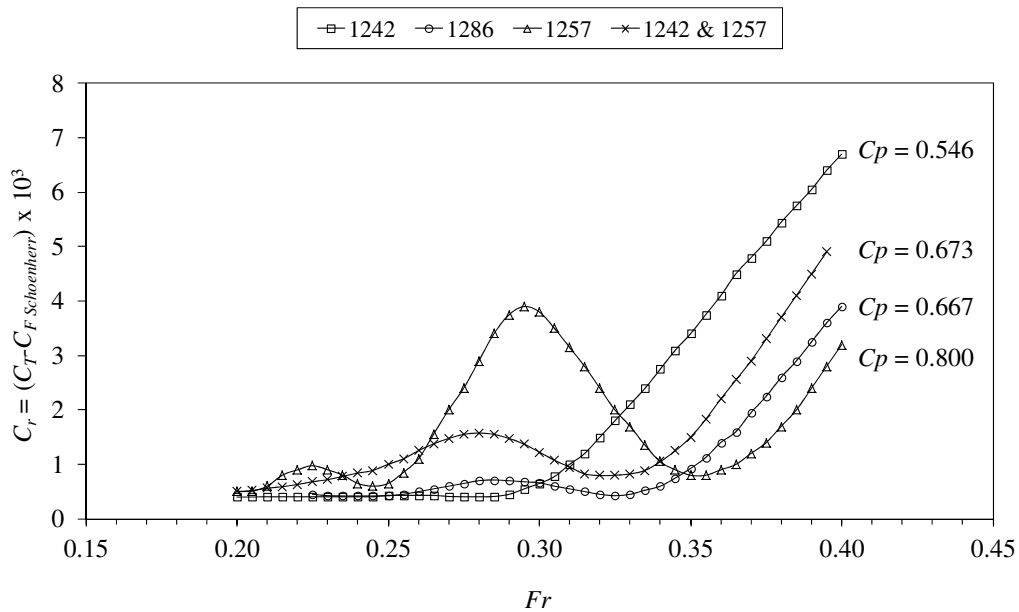


Figure 3-17 Residual resistance coefficient for models 1242, 1286, 1257 and 1242&1257 at $H^* = 1.00$. Adapted from Weinblum et al. (1950)

It can be inferred that the lack of the hump and hollow feature in the residual resistance coefficient of model 1242 is due to the nature of its dynamic pressure distribution, in particular the lack of forward and aft shoulder low pressure regions. As a result, the interaction between the forward and aft high pressure regions and the mid-body low pressure region do lead to constructive reinforcement in the lower Froude number range ($Fr < 0.35$).

Of the four bodies that were tested, it was observed that the location of the first hollow occurred at a higher Froude number ($Fr \approx 0.355$) for a full-bodied geometry (higher prismatic coefficient) while the finer geometries progressively had a minimum wave resistance at lower Froude numbers ($Fr \approx 0.325$). Despite these observations, Weinblum et al. (1950) warn that due to the myriad of possible body geometries it is difficult to make generalised statements regarding the relationship between body geometry and wave resistance.

Perhaps the most important theorisation made by Weinblum et al. (1950) is the relationship between the Froude number and the limiting depth of immersion (the depth at which wave resistance becomes negligible). Weinblum et al. (1950) theorised that the limiting depth of a submerged body can be determined by equating the length

of a body-generated free two-dimensional wave to 1.33 times the limiting depth (f_0) where the wavelength (λ) is a direct function of body length (L) and Froude number (Fr). Or in other terms, the limiting depth is equal to 0.75 times the wavelength generated by a body travelling beneath the surface at a specific Froude number (Equation 3-9). The rationale supporting this theorem is that at the limiting depth the amplitude of the resultant free two-dimensional wave is in the order of 1 percent of the surface amplitude and can therefore be discounted.

$$f_0 = 0.75\lambda \quad \text{Equation 3-9}$$

The wavelength of the free two-dimensional wave can be represented in terms of Froude number and body length as presented in Equation 3-10.

$$\lambda = 2 \cdot \pi \cdot Fr^2 \cdot L \quad \text{Equation 3-10}$$

This theoretical behaviour was observed by Weinblum et al. (1950) to agree with the results of their experiments. However, they consider this approach to be better used as an approximate criterion. To determine a specific body's limiting depth it is necessary to consider its actual geometry. The limiting depth to speed relationship for a body of length equal to unity ($L = 1.00$) is presented in Figure 3-18.

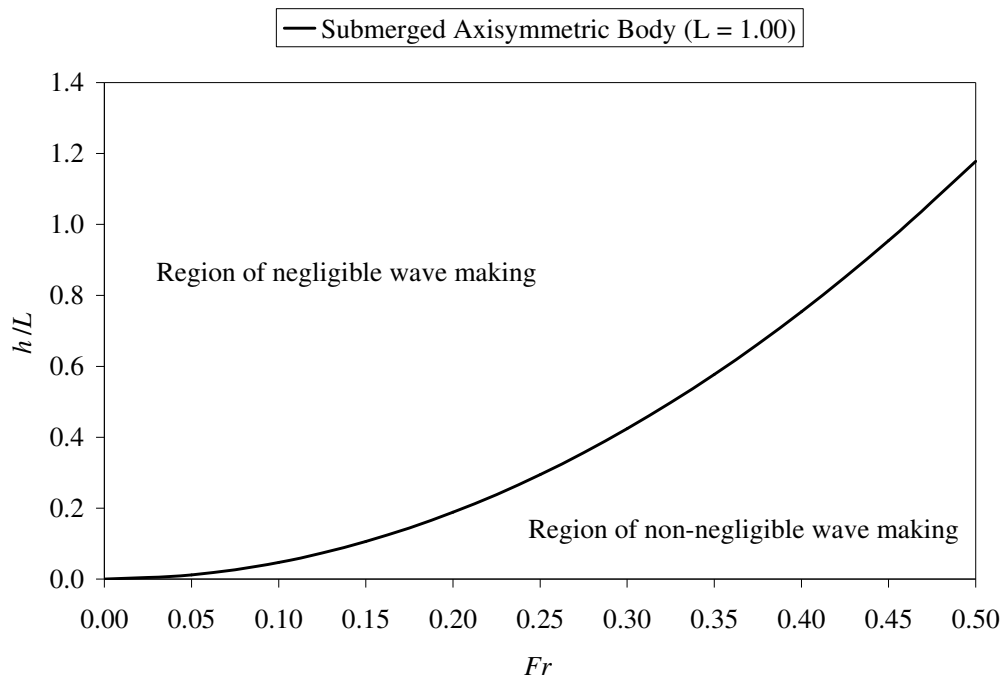


Figure 3-18 Critical submergence depth versus Froude number as theorised by Weinblum et al. (1950)

Hoerner (1965) reports on the theoretical and experimental work of Weinblum et al. (1950) and several other authors and concludes that the effect of wave making can be neglected at submergence depth-to-diameter ratios of 5 ($H^* = 5.00$) and beyond.

Given the findings of Weinblum et al. (1950), this is something of a gross generalisation and is only relevant when considering arbitrarily shaped streamlined bodies travelling at any Froude number. Through their research Weinblum et al. (1950) have shown that operation at low Froude numbers will result in a shallower critical submergence depth.

With regard to the theoretical wave resistance prediction method proposed by Havelock (1919, 1931a and 1931b), the experiments were shown to compare satisfactorily with the results calculated using this analytical method. However, while the magnitude of the resistance curve is close to the experimental result, there is a definite lag between the experimentally observed and the calculated location of the second resistance hump. At the very least, the experiments show that Havelock's theoretical method provided a reliable indication of the resistance curve for a variation of body geometry with changing Froude number (Weinblum et al., 1950).

3.2.2 RESISTANCE PERFORMANCE OF HIGH-SPEED SUBMARINE HULL SHAPES (GERTLER, 1950)

An extensive experimental program was conducted by Gertler (1950) to investigate the effect of body geometry on the minimum resistance of a systematic series of streamlined bodies of revolution. The objective of the investigation was to develop general criteria that could be used to guide the designer towards hull shapes that would result in low-resistance or, conversely, high-speed submarine designs. Consequently, the majority of experiments conducted by Gertler (1950) were done in a deep-water condition. However, of the 24 models tested, four were tested in a near-surface (snorkelling) condition to gain insight into the selection of an optimum form for shallowly submerged operation.

The experimental program conducted by Gertler (1950) comprised 24 different nine foot long model geometries that together formed the Series 58 family. The geometries were developed using a sixth-degree polynomial function. The following non-dimensional geometric parameters were varied across the series:

- a. Prismatic coefficient (C_p)
- b. Location of maximum cross-section (m)
- c. Non-dimensional nose radius (r_o)
- d. Non-dimensional tail radius (r_t)
- e. Fineness (length-to-diameter) ratio (L/D)

The four models tested at snorkelling depths were of identical length and length-to-diameter ratio but were of different prismatic coefficient as indicated in Table 3-5. The section profiles of the four models are presented in Figure 3-19 through Figure 3-22. As the investigation was focused on high-speed submarine operation, the majority of the models were tested at Froude numbers of 0.10 up to 1.80. However, as Gertler (1950) indicates, even in 1950 it was unlikely that near-surface submarine operations would be conducted at high speed.

Table 3-5 Principal dimensions of models tested (Gertler, 1950)

Model Number	Length [m]	Length to Diameter (L/D)	Volume [m ³]	Wetted Surface [m ²]	Prismatic Coefficient (C _p)
4157	2.743	7.00	0.215	2.615	0.65
4164	2.743	7.00	0.182	2.349	0.55
4165	2.743	7.00	0.199	2.491	0.60
4166	2.743	7.00	0.232	2.733	0.70

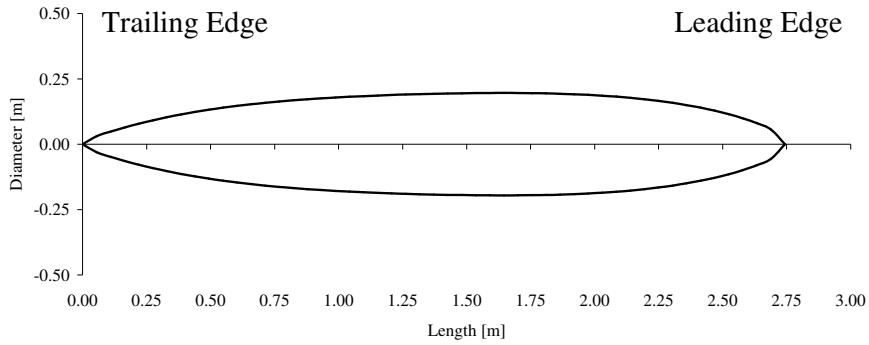


Figure 3-19 Centreline profile of Model 4157 (C_p = 0.65)

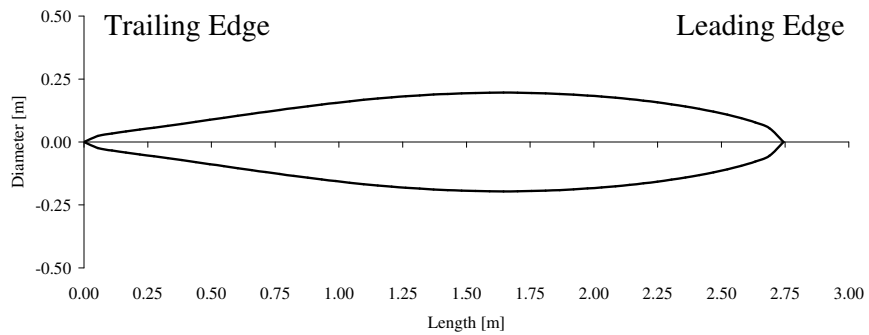


Figure 3-20 Centreline profile of Model 4164 (C_p = 0.55)

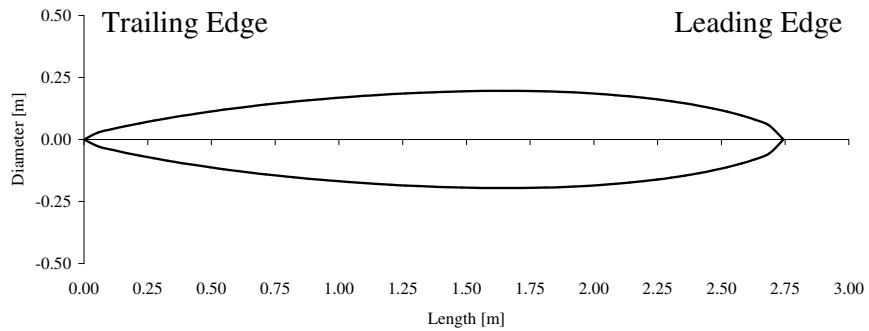


Figure 3-21 Centreline profile of Model 4165 (C_p = 0.60)

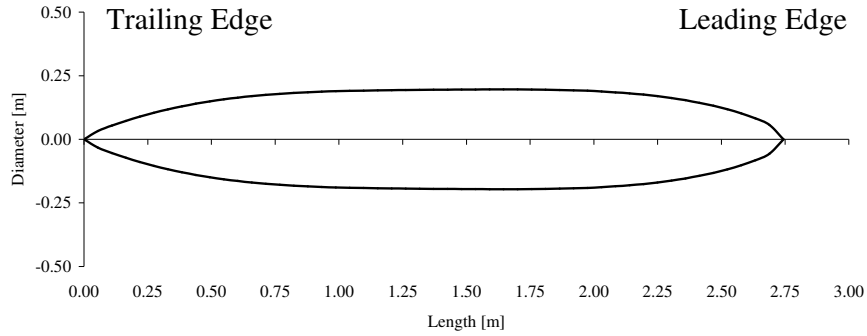


Figure 3-22 Centreline profile of Model 4166 ($C_p = 0.70$)

As a result of the extensive test program, Gertler (1950) was able to draw several conclusions about the effect of the aforementioned geometric parameters on submarine resistance. While many of the observations pertain to the deeply submerged condition, Gertler (1950) also noted some implications of geometry on near-surface resistance performance. To articulate the relative performance of the various models, Gertler (1950) presents the results in the form of merit curves for a full-scale (60,000 cubic feet) submarine. The data is presented with the principal geometric parameter as the abscissa and the normalised total effective horsepower (EHP_T/EHP_{Tmin}) as the ordinate. The total effective horsepower of the submarine is directly related to its residuary and frictional resistance as indicated in Equation 3-11. In this case, the value of 1.689 accounts for the conversion of the velocity (U) when knots are used, while the value of 550 accounts for the conversion of foot-pound per second to horsepower.

$$EHP_T = (C_R + C_F + \Delta C_F) \cdot \frac{\rho U^3 S}{2} \cdot \frac{(1.689)^3}{550} \quad \text{Equation 3-11}$$

Based on the results of the deep submergence tests, Gertler (1950) identified that a length-to-diameter ratio of 6.50 resulted in the minimum effective horsepower (relative to the Series 58 models tested). This result represents the bare hull condition. By accounting for the increase in resistance due to the addition of control surfaces, done so using an empirical approach, Gertler (1950) found that the local minimum effective horsepower shifts to a length-to-diameter ratio of approximately 7.00. It is important to note that the difference in the total resistance for an $L/D = 6.50$ and that of the $L/D = 10.00$ (model 4159) geometry is in the order of 7.5 percent.

With regard to the influence of the body's prismatic coefficient, Gertler (1950) identified that the minimum submerged resistance occurs at approximately $C_p = 0.60$. While this minimum is consistent for both the $L/D = 7.00$ and $L/D = 5.00$ model geometries, the rate of departure from the minimum differs considerably between the two curves (Figure 3-23). Gertler (1950) surmises that this behaviour is likely to be due to the presence of a substantial amount of form drag attributed to the $L/D = 5.00$ geometry. The addition of control surfaces was not observed to shift the optimum value of C_p . Within the range of models tested by Gertler (1950) none of the remaining geometric parameters was found to have any significant effect on the minimum resistance of the model. However, Gertler (1950) does indicate that bodies

that possess parallel mid-body or very full after-bodies will likely generate greater total resistance than those of Series 58. This agrees with Kormilitsin and Khalizev's (2001) statement that the prismatic coefficient is a critical design parameter as it affects the body's form resistance. Based on theoretical calculations of form drag, the optimum prismatic coefficient for a submarine hull without parallel mid-body and with an L/D of between 7.00 and 8.00 is $C_p = 0.60$.

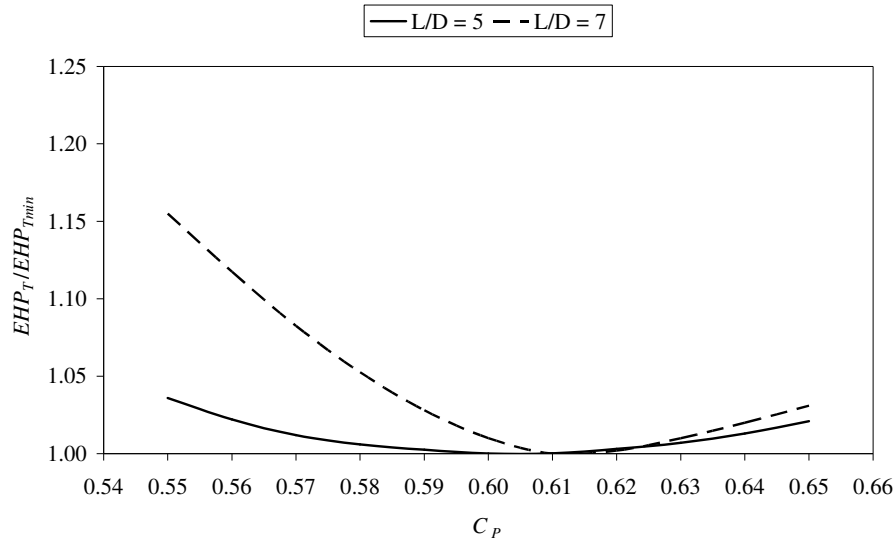
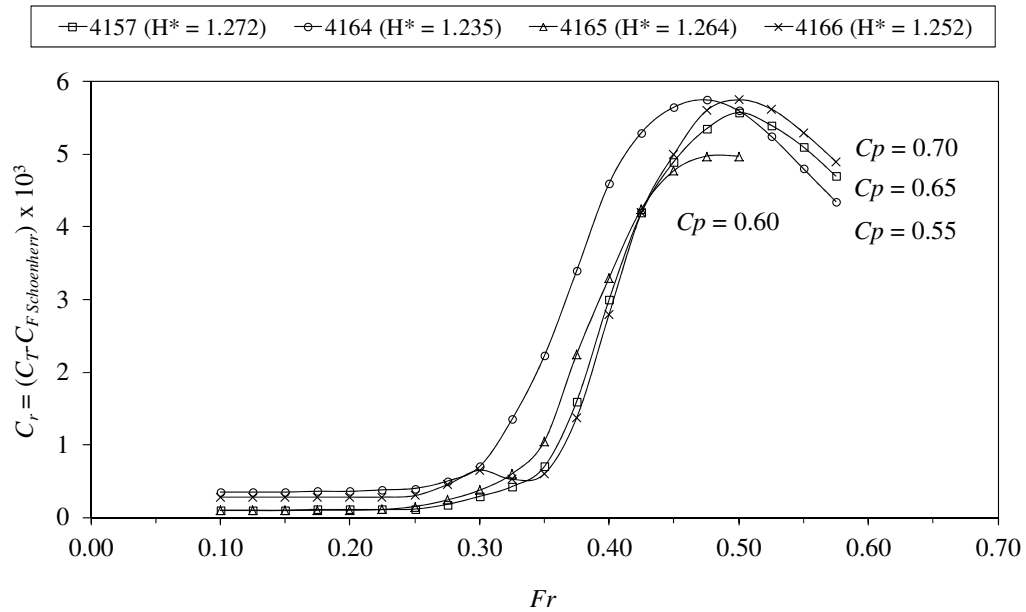


Figure 3-23 Effect of prismatic coefficient on relative propulsive performance of the Series 58 models with length-to-diameter ratio of $L/D = 5.00$ and $L/D = 7.00$
Adapted from Gertler (1950)

Based on the results of the tests conducted at snorkelling depth, Gertler (1950) concludes that the effect of varying the geometrical parameters is more prominent. In particular, the prismatic coefficient at which the minimum (or optimum) resistance occurs varies with Froude number. At Froude numbers below $Fr = 0.265$ the minimum resistance is attributed to a body with a prismatic coefficient tending towards the optimum deep submergence value of $C_p = 0.60$. Within the range $0.31 \leq Fr \leq 0.40$ the minimum resistance occurs at $C_p \approx 0.65$. At Froude numbers above 0.40 Gertler (1950) observed the optimum C_p to shift back towards the optimum deep water value.

The residual resistance coefficient for the four streamlined bodies tested at snorkelling depths are presented in Figure 3-24 for the shallowest test depths. Gertler (1950) determined the residual resistance coefficient by subtracting corresponding values along the Schoenherr friction coefficient line from the values of total resistance coefficient determined directly from the experiment. While the non-dimensional depths are not consistent among the models, they are considered close enough to compare the residuary resistance characteristics of the models. It is apparent that the model with a prismatic coefficient of $C_p = 0.70$ (model 4166) possesses the characteristic hump and hollow in the region of $Fr = 0.30$, while the remaining models do not. Unfortunately, the print quality of the publication from which the results data was digitised does not support high fidelity reproduction. Nonetheless, this behaviour agrees with the observations made of the results presented by Weinblum et al. (1950).

Like Weinblum et al. (1950), Gertler (1950) observed that the residual resistance reduces monotonically with an increase in submergence depth.



**Figure 3-24 Residual resistance coefficient for models 4157, 4164, 4165 and 4166
Adapted from Gertler (1950)**

Based on his observations and additional corrections for an appended submarine body and assuming a full scale snorkelling speed of no greater than 12 knots, Gertler (1950) concludes that an ideal hull form would possess the following geometric characteristics:

- a length to diameter ratio (L/D) of 7.00;
- a prismatic coefficient (C_p) of 0.61;
- a non-dimensional nose radius (r_0) of 0.5;
- a non-dimensional tail radius (r_l) of 0.1; and
- a maximum section at 36% aft of the nose.

3.2.3 ON THE EXPERIMENTAL DETERMINATION OF THE RESISTANCE COMPONENTS OF A SUBMERGED SPHEROID (FARELL AND GÜVEN, 1973)

Farell and Güven (1973) report on their experimental investigation into the wave resistance of a 5:1 spheroid body. Unlike previous researchers who had also investigated the effects of free-surface interaction on shallowly submerged axisymmetric bodies of revolution, Farell and Güven (1973) extended the scope of their experiments to focus on the effects of free-surface interaction on the viscous resistance component of the body's total resistance and not on the total resistance alone. Farell and Güven (1973) used wake survey measurement techniques to determine the viscous resistance of the shallowly submerged spheroid. In addition to this, they made resistance (drag force) measurements of the model in the towing tank in a deeply submerged condition as well as in a wind tunnel. The viscous drag of the spheroid was measured in the wind tunnel using wake measurements similar to those used in the towing tank.

The premise upon which Farell and Güven (1973) based their research is that determining the resistance components of a body travelling on or near a free-surface is not trivial and cannot be done accurately using the standardised correlation line and form factor method. Farell and Güven (1973) cite the assertion of Landweber (1951), Wu (1963), Key (1965) and Tzou (1969) that a body's viscous resistance will vary significantly with Froude number.

The 5:1 spheroid model tested by Farell and Güven (1973) in the Iowa Institute of Hydraulic Research towing tank had an overall length of 5 feet (1.524m) with a corresponding maximum diameter of 1 foot (0.305m). The towing tank dimensions reported by Farell and Güven (1973) are a total tank length of 300 feet (91 m), overall width of 10 feet (3.048m) and a depth of 10 feet (3.048m). The model was tested across a range of Froude numbers from $0.30 \leq Fr \leq 0.45$ and at submergence depths equivalent to $H^* = 0.79$, $H^* = 3.75$ and $H^* = 4.75$.

Similar to the results obtained by their predecessors, such as Weinblum et al. (1950), Farell and Güven (1973) observed a significantly increased total resistance at the shallowest submergence depth ($H^* = 0.79$) in comparison to the two deeper submergence depths (Figure 3-25). However, their comparison between the total resistance of the spheroid at $H^* = 3.75$ and $H^* = 4.75$ indicated that the interaction effect (wave making) was not negligible for the $H^* = 3.75$ submergence depth at Froude numbers of $Fr \geq 0.37$. This was illustrated by the upward trend in the resistance coefficient curve. Nonetheless, Farell and Güven (1973) conclude that negligible wave resistance was experienced by the spheroid at the $H^* = 4.75$ depth for the range of speeds tested.

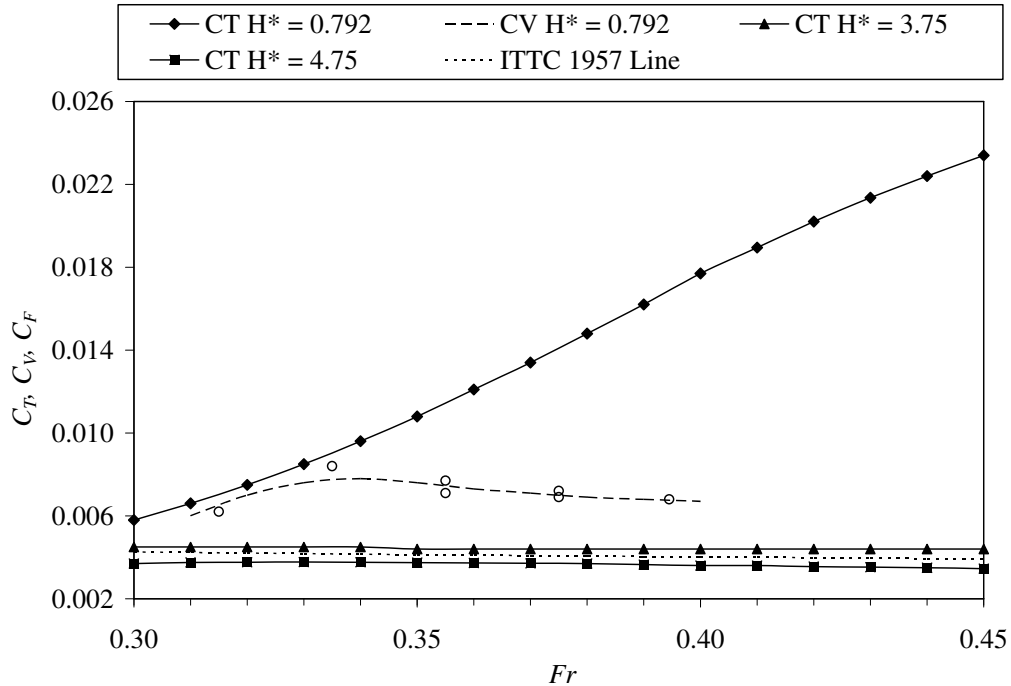


Figure 3-25 Influence of the free-surface interaction on a submerged spheroid's viscous resistance: comparison between the viscous and total resistance measured at $H^* = 0.792$ (adapted from Farell and Güven, 1973)

As a result of their rigorous investigation, Farell and Güven (1973) were able to make several additional observations of significance. Despite possible influences from their experimental setup, Farell and Güven (1973) conclude that the free-surface interaction has a significant influence on the viscous flow region surrounding the spheroid. The result of this is a significant increase in the viscous resistance component when compared to a deeply submerged condition. The results of both the towing tank wake surveys and the wind tunnel tests support this assertion as they show that at the shallow submergence depth ($H^* = 0.79$) the measured viscous resistance coefficient is significantly higher than the spheroid's total resistance coefficient measured at $H^* = 3.75$ and $H^* = 4.75$.

Farell and Güven (1973) observed that there was a significant increase (>100 percent) in the viscous resistance measured for the spheroid positioned near the wind tunnel wall (at a stand-off distance approximately equal to $H^* = 0.79$) when compared to that measured for the spheroid positioned along the axis of the tunnel. While this result cannot be directly compared to the behaviour of the spheroid moving beneath a flexible free-surface boundary that does not have its own viscous boundary layer, Farell and Güven (1973) do present wind tunnel flow visualisation images that illustrate the influence of the interaction of the spheroid with a boundary on the spheroid's wake field and pressure distribution (Figure 3-26). Farell and Güven (1973) state that as the spheroid approaches the free-surface boundary, the interaction between the two increases the divergence of the streamlines around the stern region of the body. This results in both a reduction in pressure and boundary layer separation occurring earlier. Together, these effects can account for a large increase in resistance.

Farrel and Güven (1973) note that this phenomenon is not experienced by surface ships, despite their interaction with the free-surface and the production of waves, quite simply because the hull breaks the surface and does not act as a submerged flow boundary.

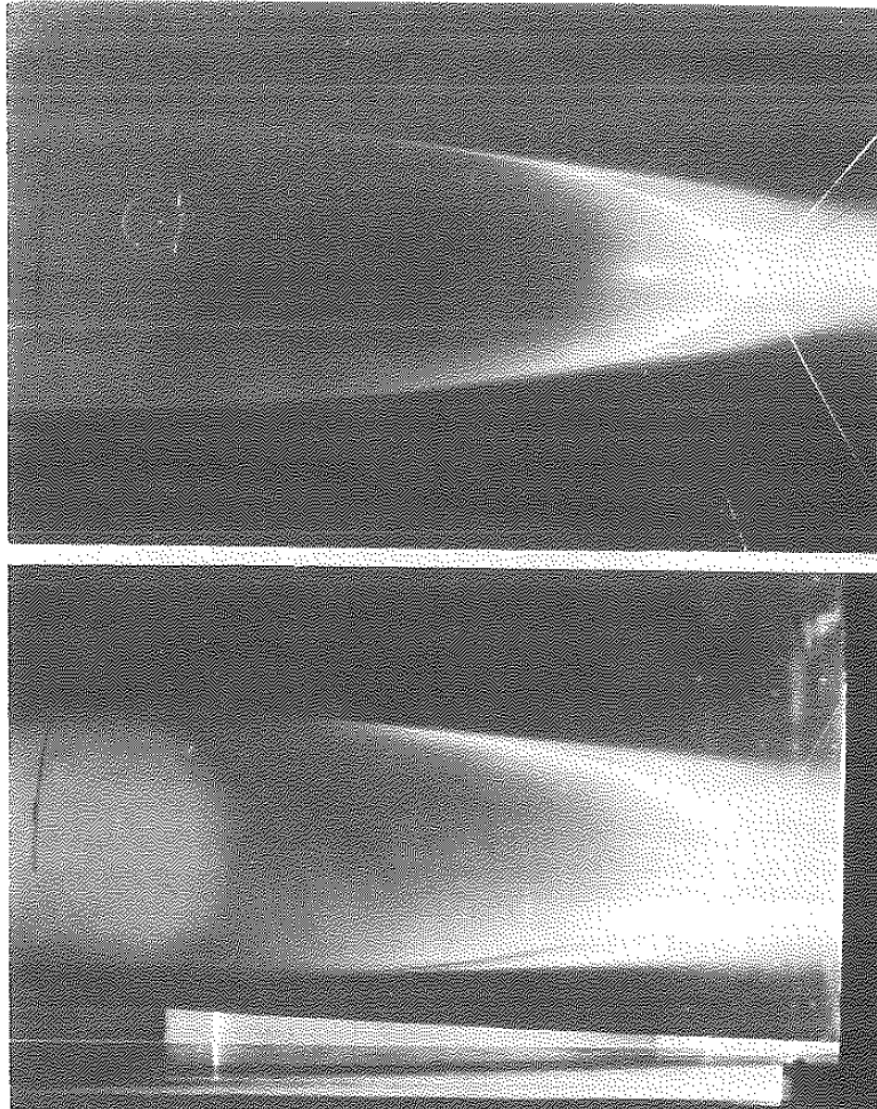


Figure 3-26 Wind tunnel flow visualisation of the wake behind the spheroid when located on the centreline of the tunnel (top) and near the tunnel floor (bottom) (Farell and Güven, 1973)

A comparison of the total resistance coefficient curve at the $H^* = 4.75$ submergence depth against the 1957 ITTC ship-model correlation line indicated a distinct decrease in the resistance coefficient at the lower Froude numbers. Farell and Güven (1973) conclude that this is due to the presence of laminar regions in the boundary layer caused by a reduction in the effectiveness of the boundary layer transition device. The results presented in Figure 3-25 show that the transition device becomes ineffective for Froude numbers less than approximately $Fr = 0.31$.

Farell and Güven (1973) quite importantly conclude that the viscous resistance of a submerged streamlined body moving beneath the free surface is much larger than for the same body moving in a deeply submerged condition and that it varies with Froude number. As a result, the conventional approach of separating the resistance components from the total measured resistance becomes ineffectual. This is an issue that was perhaps overlooked or dismissed in the results presented by other authors up to the time of Farell and Güven's (1973) article. Furthermore, Farell and Güven (1973) suggest that the wave resistance of a shallowly submerged body should be determined from direct surface profile measurements or by subtracting the viscous resistance, measured by wake survey, from the total measured resistance.

3.2.4 HULL SHAPE DESIGN OPTIMISATION OF A SNORKELLING VEHICLE (ALVAREZ ET AL., 2009)

In their work to optimise the hydrodynamic performance of an autonomous underwater vehicle (AUV), Alvarez et al. (2009) conducted both experimental resistance tests and equivalent numerical simulations using a non-linear potential flow method to predict the wave resistance of the vehicle. The approach used by Alvarez et al. (2009) was to implement a simulated annealing optimisation technique to obtain a minimum wave resistance for a fixed submergence depth and submerged body volume across a limited speed range. The geometry of an existing AUV, known as the Cormorán, was used as the starting point of the optimisation study (referred to by Alvarez et al. (2009) as the *Original* hull geometry). By seeking the minimum total resistance Alvarez et al. (2009) were able to derive an optimised AUV body geometry (referred to as the *Optimized* hull geometry).

In their formulation of total resistance, Alvarez et al. (2009) summate the frictional, form and wave resistance components using the empirical method presented by van Manen and van Oossanen (1988) and Hendrix et al. (2001) for friction resistance and form factor, respectively. The wave resistance component was predicted using a potential flow method with a non-linear free-surface boundary condition. Alvarez et al. (2009) conducted a series of experiments in the model ship basin at the University of Trieste to measure the total axial resistance of the Original and Optimized models and validate their numerical predictions. The experimental models were tested at a scale of 1:2 (half size). The principal dimensions and centreline profiles of the full-scale Original and Optimized geometries are presented in Table 3-6 and Figure 3-27 and Figure 3-28, respectively.

Table 3-6 Principal dimensions of models tested (Alvarez et al., 2009)

Model	Length [m]	Length to Diameter (L/D)	Volume [m ³]	Wetted Surface [m ²]	Prismatic Coefficient (C_p)
Original	1.42	8.875	0.0245	0.63	0.858
Optimized	1.49	7.842	0.0245	0.62	0.580

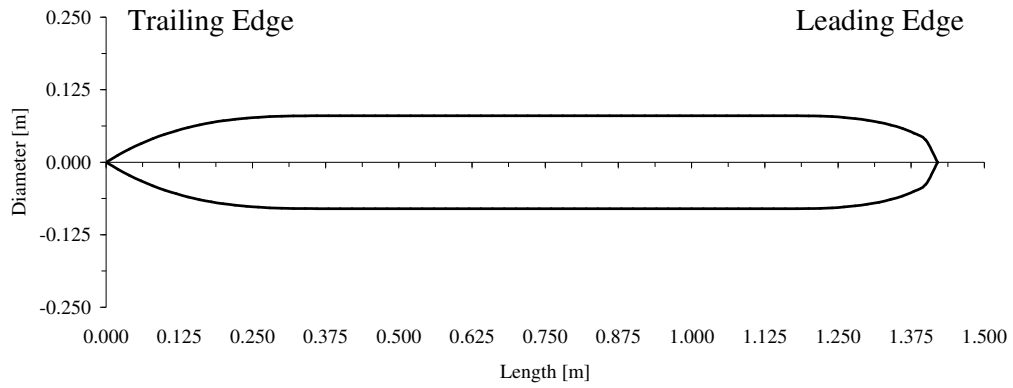


Figure 3-27 Centreline profile of Original model ($L/D = 8.875$, $C_p = 0.858$)

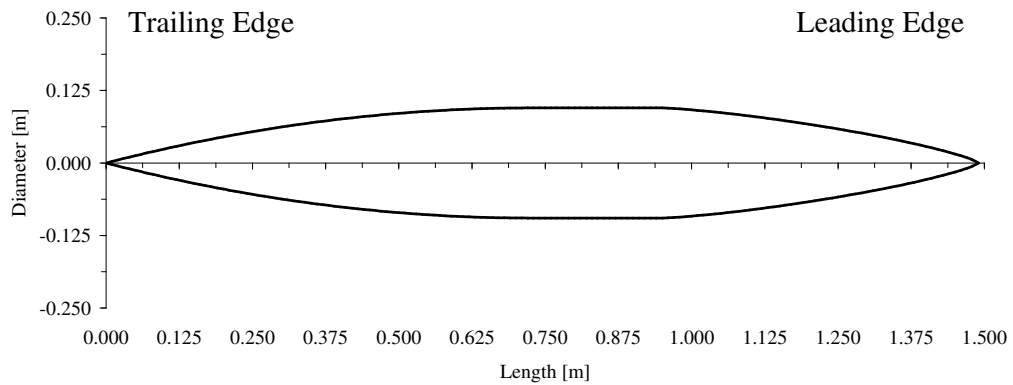


Figure 3-28 Centreline profile of Optimized model ($L/D = 7.842$, $C_p = 0.580$)

The models were tested at a draft of 0.05 metres and at forward speeds of 0.5 to 1.05 m/s in 0.05 m/s increments. The resultant non-dimensional speeds and depths for the two models are presented in Table 3-7.

Table 3-7 Non-dimensional speeds and submergence depths tested by Alvarez et al. (2009)

Model	Lower Froude Number (Fr)	Upper Froude Number (Fr)	Non-Dimensional Submergence Depth (H^*)
Original	0.189	0.398	1.125
Optimized	0.185	0.388	1.026

Alvarez et al. (2009) present the results of their numerical prediction of wave making resistance for the Original and Optimized geometries (Figure 3-29). The results show that while the Optimized hull geometry generates lower wave making resistance in the speed range of interest ($0.26 \leq Fr \leq 0.30$) the Original hull performs better at the higher speed range of $0.335 \leq Fr \leq 0.375$. This behaviour agrees with the observations made by Weinblum et al. (1950), where geometries with higher prismatic coefficients generate relatively lower wave resistance at higher Froude numbers due to the

interaction effects of the body generated free-surface wave systems. It is important to consider that the Optimised hull shape was obtained with a reduction in the length-to-diameter ratio and prismatic coefficient while taking a form that is comparable to the parabolic hull shape presented by Kormilitsin and Khalizev (2001) and model 1242 tested by Weinblum et al. (1950).

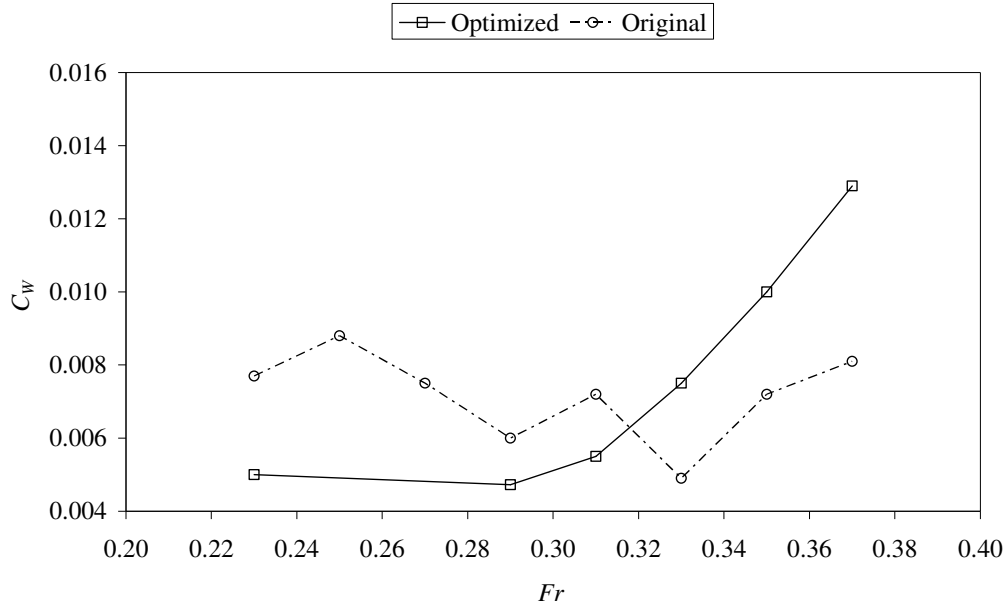


Figure 3-29 Wave resistance coefficient versus Froude number of the Original and Optimized AUV hull geometries tested by Alvarez et al. (2009)

3.3 NUMERICAL INVESTIGATIONS OF SUBMERGED BODY WAVE RESISTANCE, DRAG, LIFT AND TRIMMING MOMENT

Although fluid viscosity is known to have an effect on the decay of free-surface waves and while viscosity is fundamental to form and friction resistance, the formation of surface waves and wave resistance is a direct function of the fluid's weight. Consequently, it is considered appropriate to use potential (inviscid) flow theory to address the wave making problem (Kostyukov, 1959). Investigation into the wave making characteristics of a submerged body using potential flow theorisations are considered to have begun in the early twentieth century with the work of Lamb (1913). Lamb's work focussed on the evaluation of the free-surface wave motion generated by a shallowly submerged cylinder in a fluid domain of infinite depth. The outcomes of Lamb's research are considered by subsequent researchers to have been only the first step in what has become an established approach to calculating the free-surface disturbance due to its interaction with a submerged body (Farell, 1973).

Subsequent work by Havelock established results for the approximation of the wave resistance of a sphere (Havelock, 1917), for prolate and oblate spheroids (Havelock, 1931a), and for an ellipsoid (Havelock, 1931b). In these works Havelock used distributed parallel doublets to describe the body and determine a solution that satisfied the body boundary conditions. Havelock (1931a) produced results for five different body shapes ranging from an oblate sphere with an x/y axis ratio (L/D) of

0.80 through to a prolate spheroid with an x/y ratio (L/D) of 5.00. Calculations were performed with the body's longitudinal axis of rotation submerged at a non-dimensional depth of $H^* = 1.00$. Perhaps the only insightful result of Havelock's analyses related to the wave making characteristics of bodies of revolution was that there is a reduction in wave resistance at the lower speeds for the geometries of greater length. Havelock's results also show aspects of the periodic behaviour observed experimentally by Weinblum et al. (1950) and Gertler (1950); however, more recent work, most notably by Farell (1973) and Doctors and Beck (1987), has shown that these early results were not accurate and did not adequately capture the wave resistance at low Froude numbers.

As a result of continued research in this area and the application of potential flow and boundary element methods (BEM) to this problem, the shortcomings of Havelock's method have since been overcome. While the earlier uses of potential flow theory focussed on wave resistance, subsequent work using BEM have enabled the prediction of drag, lift, and trimming moment as well. While the phenomenon of free-surface waves is non-linear, most of the approximation methods developed so far treat the boundary in a linearised manner. The following sections provide a review of the outcomes of specific work conducted to date and its application to submarine near-surface performance modelling.

3.3.1 WATER FORCES ON SUBMERGED BODIES IN MOTION (WIGLEY, 1953)

Of the many authors that have reported on the results of potential flow theory investigations into the forces and moments acting on a submerged axisymmetric body of revolution moving near the free-surface, Wigley (1953) provides perhaps the most concise yet insightful account. Wigley (1953) presents the results of his numerical approximations of the wave resistance, lift force and pitching (trimming) moment acting on a submerged spheroid. In his investigation Wigley (1953) uses an adaptation of the distributed source method established by Havelock to calculate the wave resistance, lift force coefficient and trimming moment coefficient.

Wigley (1953) presents the results of his calculations of the wave resistance, lift force and trimming moment for a slender spheroid with a length-to-diameter ratio of 20 ($D/L = 0.05$). The analyses were completed for a range of submergence depths from $h/L = 0.05$ to $h/L = 1.00$ inclusive and for a range of length Froude number from $Fr = 0.0$ to $Fr = 5.0$ inclusive. The equivalent non-dimensional depth based on hull diameter for the slender ellipsoid geometry analysed by Wigley (1953) ranges from $H^* = 1.00$ to $H^* = 20.00$ inclusive.

Based on the results of his calculations, Wigley (1953) observed that the wave resistance characteristic of the submerged spheroid bore close resemblance to that of surface craft (Figure 3-30). The wave resistance coefficient possesses a hump and hollow shape with the first peak at $Fr = 0.30$ and the second, larger peak at $Fr = 0.50$. Wigley (1953) also observed that the effect of the free-surface on the wave resistance gradually decreases with increasing submergence depth and becomes negligible at a depth-to-length ratio of 0.50 ($H^* = 10.00$) (Figure 3-31). This is a significantly deeper submergence depth than that observed by Weinblum et al. (1950) or Gertler (1950), where the free-surface effect was considered to become negligible at $H^* \approx 3.00$.

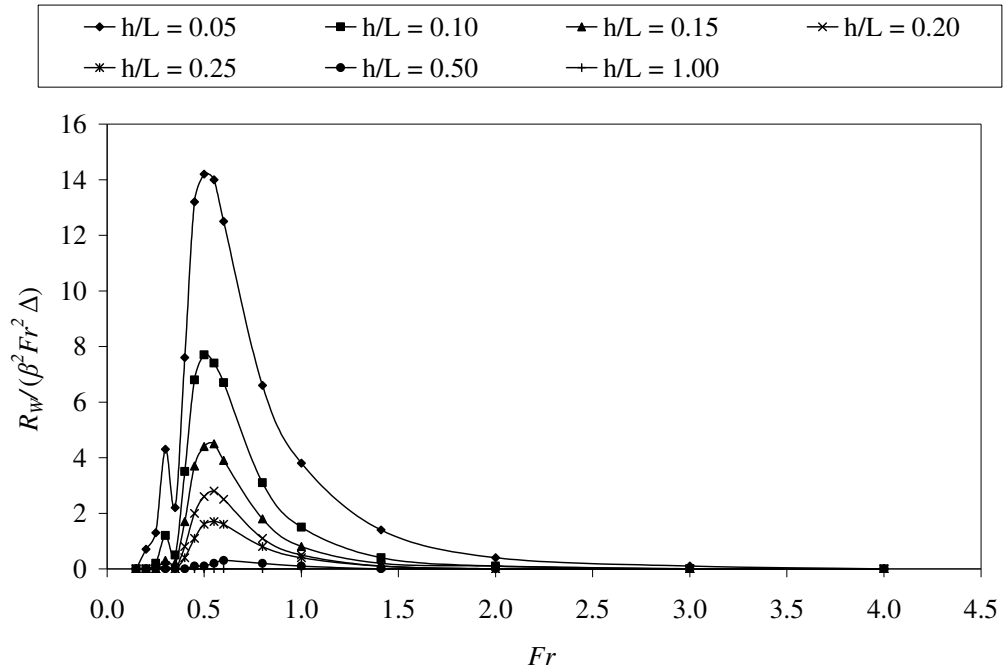


Figure 3-30 Wave making resistance coefficient for a spheroid calculated using a distributed source method (Wigley, 1953)

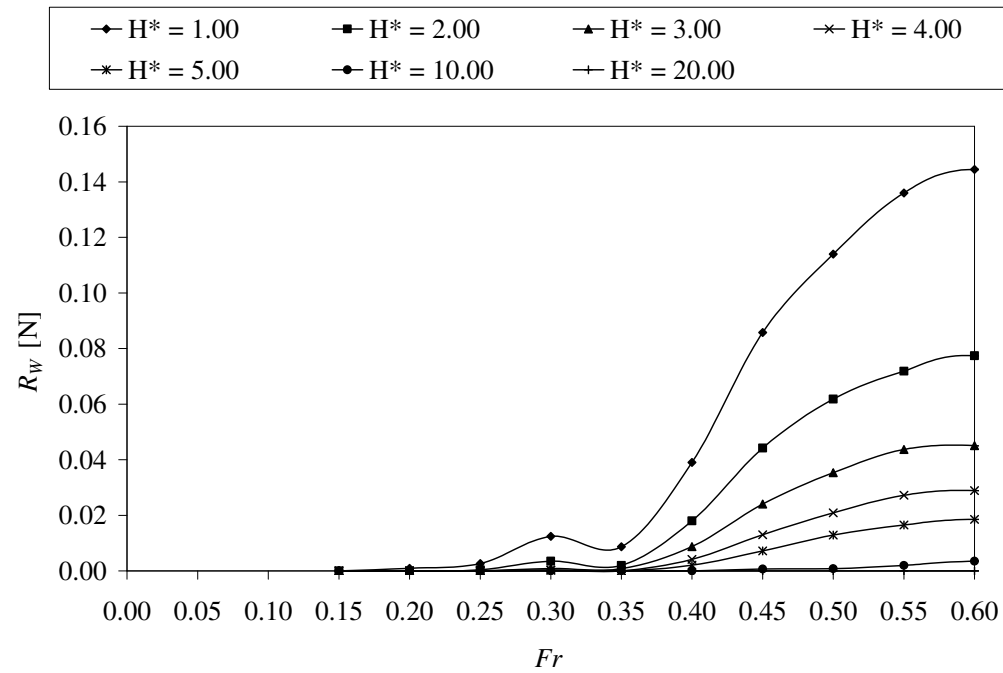


Figure 3-31 Wave making resistance for a spheroid calculated using a distributed source method $0.0 \leq Fn_L \leq 0.6$ (Wigley, 1953) Absolute values calculated using $\beta = 0.05$ with $L = 1.00$ m and $\Delta = \rho.V = 1.31$ kg where $\rho = 1000$ kg/m³ and $V = 1.31 \times 10^{-3}$ m³

Wigley's (1953) calculations of the lift force and trimming moment acting on the spheroid indicate several important features. The first of these is that at the slow speeds the lift force generated by the interaction of the body and the free-surface acts to push the body upwards and closer to the surface. The lift force increases to a maximum at around $Fr = 0.40$, after which it drops sharply and becomes negative at approximately $Fr = 0.60$. Beyond $Fr = 0.60$ the lift force acts to push the body away from the free-surface (Figure 3-32).

The trimming moment results indicate that there is no moment acting on the body from $Fr = 0.00$ until approximately $Fr = 0.15$. Beyond this speed the moment oscillates from positive to negative while remaining small in magnitude. This is most clearly observed for the shallowest submergence depth ($H^* = 1.00$) in Figure 3-33. For the remaining submergence depths, where the free-surface interaction effects are non-zero, the trimming moment becomes negative at $Fr = 0.35$ and increases to a peak value at approximately $Fr = 0.55$ (Figure 3-33). Beyond $Fr = 0.55$ the trimming moment gradually reduces and tends to zero as Froude number tends to infinity. In this instance a negative moment corresponds to a bow down (stern up) trimming moment (Wigley, 1953).

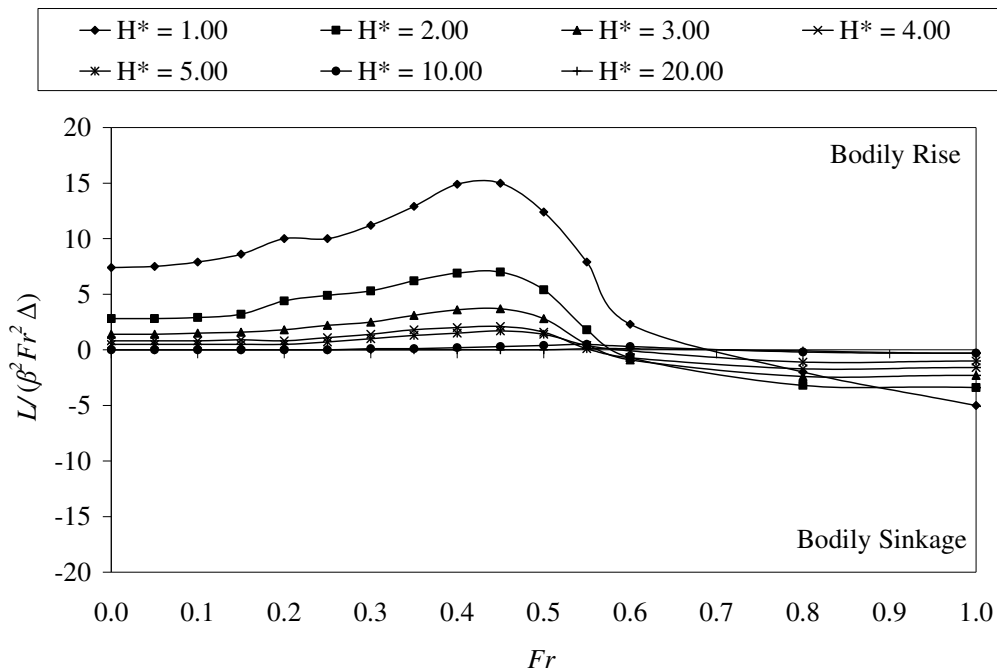


Figure 3-32 Lift coefficient acting on the spheroid due to the interaction between it and the free-surface (Wigley, 1953)

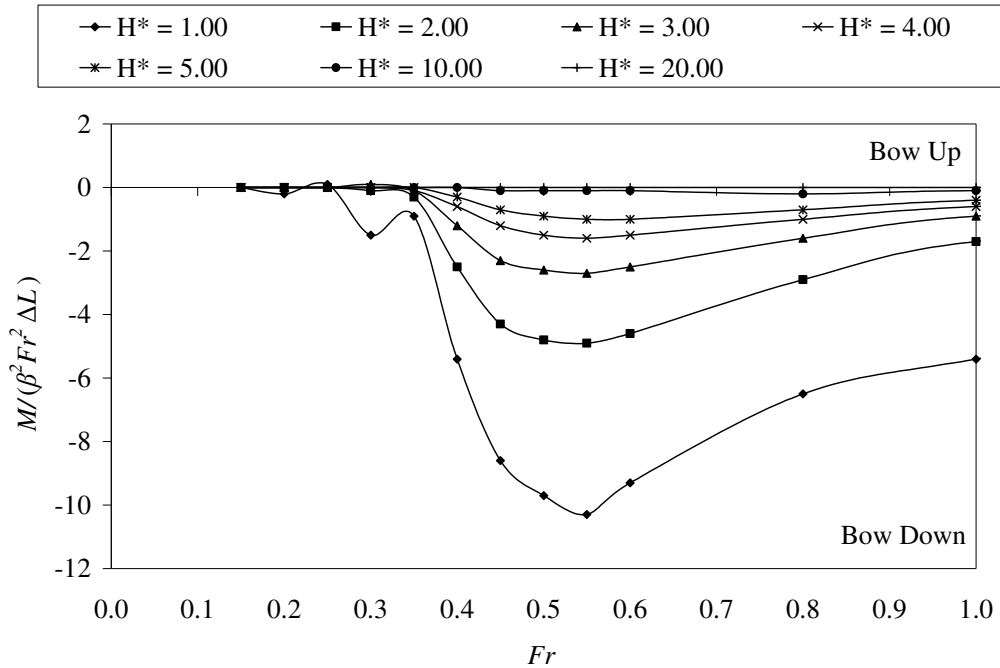


Figure 3-33 Trimming moment coefficient acting on the spheroid due to the interaction between it and the free-surface (Wigley, 1953)

Wigley (1953) provides a correction factor for the wave resistance, lift and moment results to account for less slender spheroid geometries. Although the correction value was found to vary slightly with velocity and submergence depth, Wigley (1953) provides a table of average values (Table 3-8) to be applied to the $L/D = 20.00$ data. The corrected force and moment data for a spheroid with $L/D = 5.00$ ($D/L = 0.20$) were calculated and made non-dimensional by dividing by the dynamic pressure and the wetted surface area and the dynamic pressure and the length squared multiplied by the diameter, respectively. The corrected data are presented in Figure 3-34, Figure 3-35 and Figure 3-36.

Table 3-8 Correction factor to apply to slender ($L/D = 20.00$) spheroid results to obtain results for spheroid geometries with smaller length-to-diameter ratios (Wigley, 1953)

D/L	L/D	Correction Factor
0.05	20	1.00
0.10	10	1.05
0.15	6.67	1.10
0.20	5	1.15

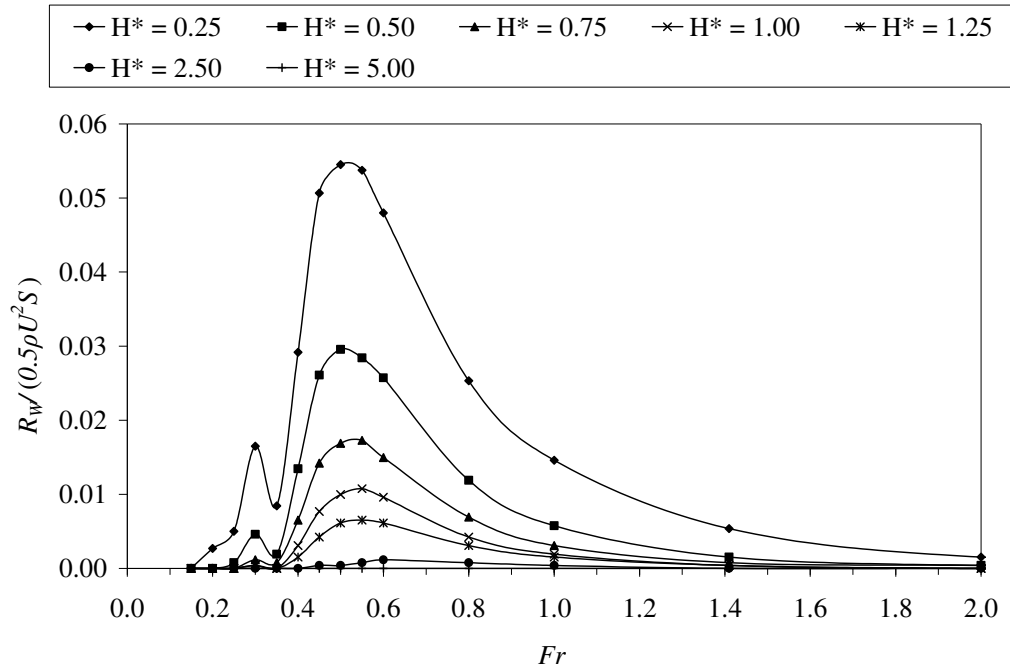


Figure 3-34 Wave resistance coefficient calculated for a spheroid with $L/D = 5.00$ ($D/L = 0.20$)

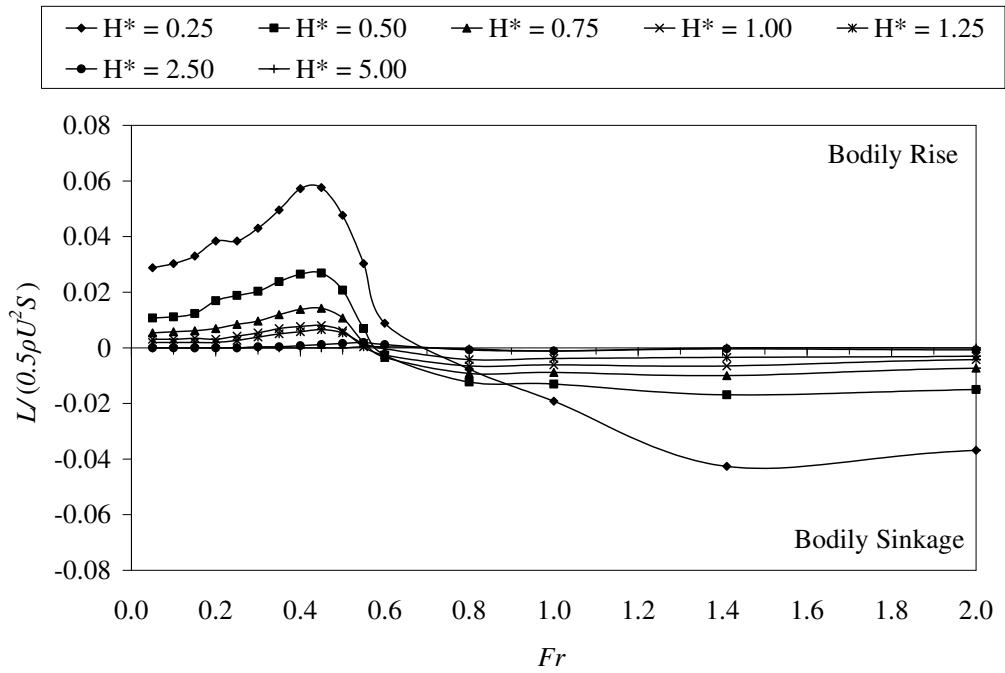


Figure 3-35 Lift coefficient calculated for a spheroid with $L/D = 5.00$ ($D/L = 0.20$)

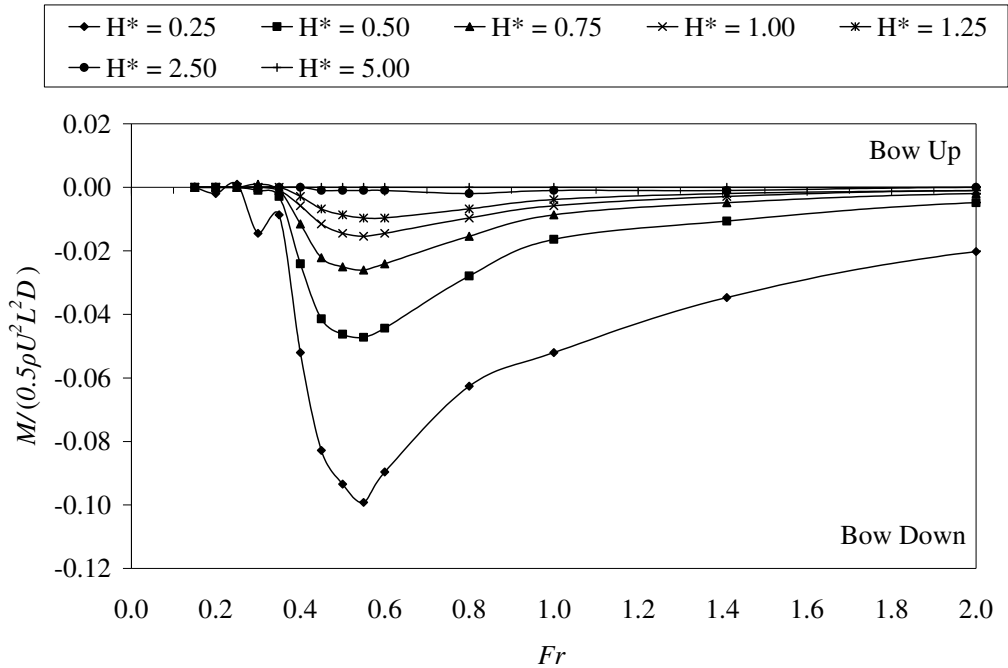


Figure 3-36 Trimming moment coefficient calculated for a spheroid with $L/D = 5.00$ ($D/L = 0.20$)

3.3.2 ON THE WAVE RESISTANCE OF A SUBMERGED SPHEROID (FARELL, 1973)

Farell (1973) presents the results of his numerical analysis of prolate spheroids of various length-to-diameter ratios using potential theory. In contrast to the method formulated by Havelock (1931a) and used by Wigley (1953), where the submerged spheroid geometry is described by a distribution of sources along its axis, Farell (1973) uses the Neumann-Kelvin method with a series representation of the surface source distribution to describe the surface of the geometry (Doctors and Beck, 1987). Nonetheless, Farell (1973) states that neither method actually describes a spheroid in the presence of a free-surface; rather, they are both first approximations and produce the same value for the first approximation of the wave resistance.

Farell (1973) presents the solution of wave resistance for spheroids with a length-to-diameter ratio of 4.5 to 10 inclusive. He uses the focus length of the ellipsoid (c) to non-dimensionalise the submergence depth, Froude number and wave resistance. The results presented by Farell (1973) have been reproduced by the author and include the appropriate modifications to relate them in terms of H^* , length Froude number and wave resistance with respect to wetted surface area. The results of Farell's (1973) computations of wave resistance for prolate spheroids with a length-to-diameter ratio of 5.00, 6.00 and 8.00 for a range of non-dimensional submergence depths are presented in Figure 3-37, Figure 3-38 and Figure 3-39 respectively. The prismatic coefficient of the prolate spheroids is $C_p = 0.67$.

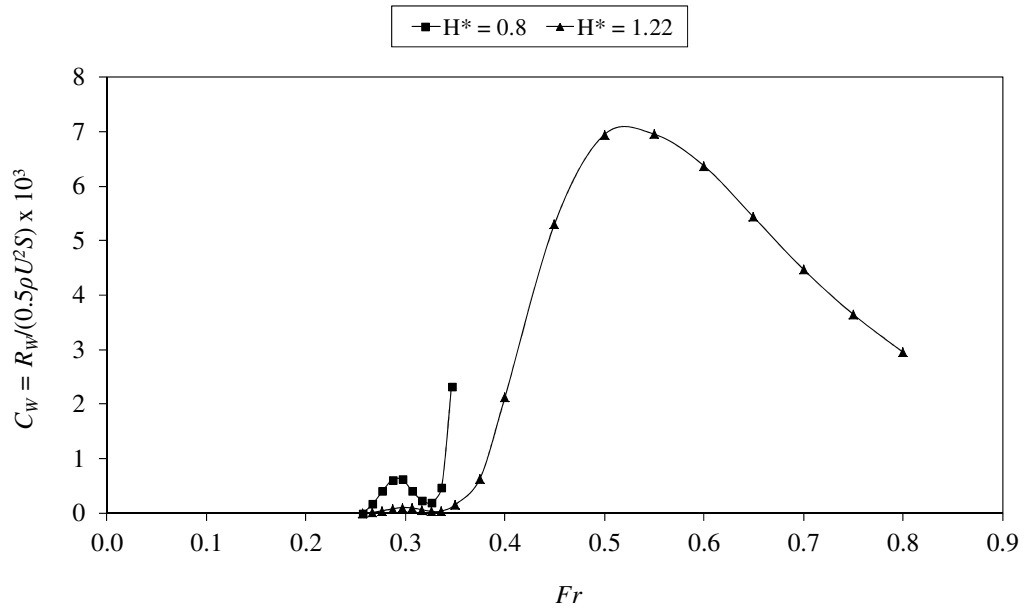


Figure 3-37 Wave resistance coefficient calculated for a spheroid with $L/D = 5.00$; $C_p = 0.67$ (Adapted from Farell (1973))

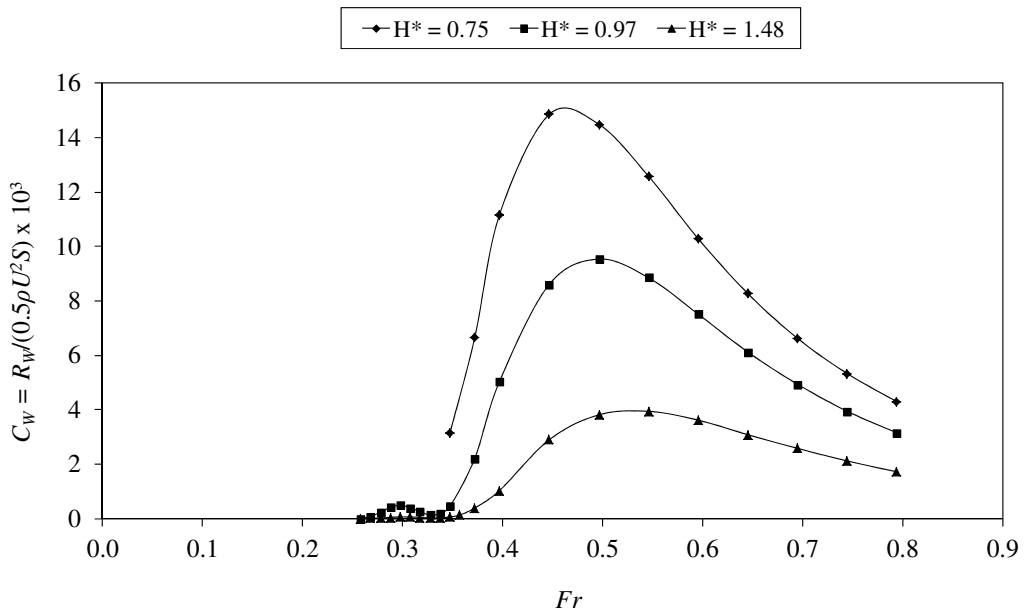


Figure 3-38 Wave resistance coefficient calculated for a spheroid with $L/D = 6.00$; $C_p = 0.67$ (Adapted from Farell (1973))

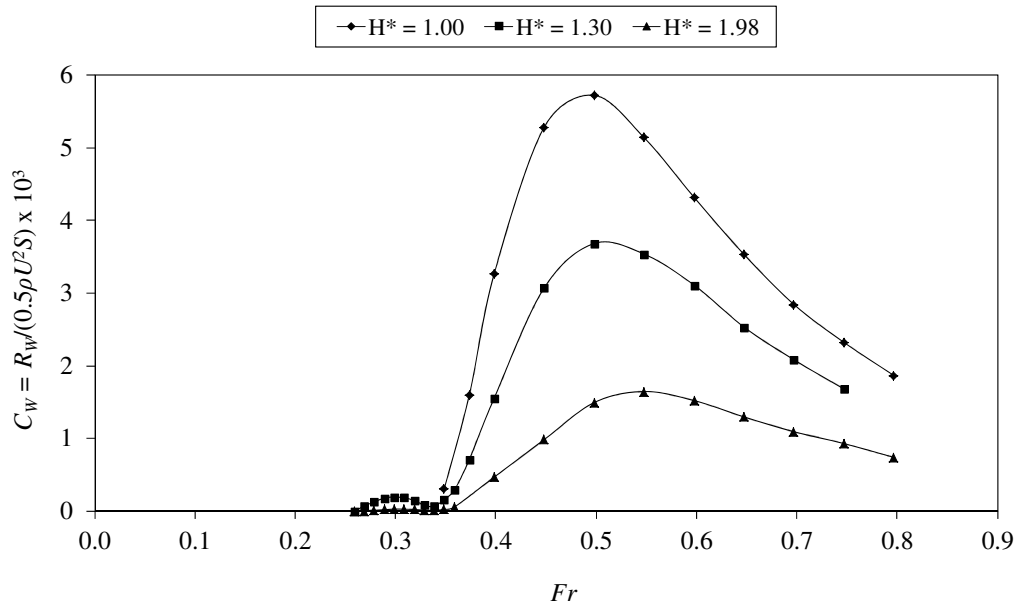


Figure 3-39 Wave resistance coefficient calculated for a spheroid with $L/D = 8.00$; $C_p = 0.67$ (Adapted from Farell (1973))

The wave resistance coefficient results presented here indicate similar characteristics to those observed experimentally by Weinblum et al. (1950) and Gertler (1950) and numerically by Wigley (1953). These characteristics are:

- a. a decrease in wave resistance with an increase in submergence depth;
- b. a periodically varying hump and hollow response in the wave resistance coefficient with a local maxima at $Fr = 0.30$ and $Fr = 0.50$ and a local minima at approximately $Fr = 0.34$;
- c. the maximum wave resistance coefficient occurs at approximately $Fr = 0.50$; and
- d. the local maxima at $Fr = 0.30$ diminishes to the extent that it becomes negligible as the submergence depth is increased.

Farell's (1973) results show that there is a consistent trend where an increase in length-to-diameter ratio leads to a reduction in wave resistance coefficient. However, it is important to consider that the non-dimensional submergence depth used by Farell (1973) is not equivalent to the H^* term used in the current work. The consequence of this is that the relative submergence depth to the top edge of the body varies substantially between the different length-to-diameter ratio spheroids. Nonetheless, a comparison of Farell's (1973) results corrected for H^* indicate that this trend still exists, at least for the $L/D = 6.00$ and $L/D = 8.00$ spheroids (Figure 3-40).

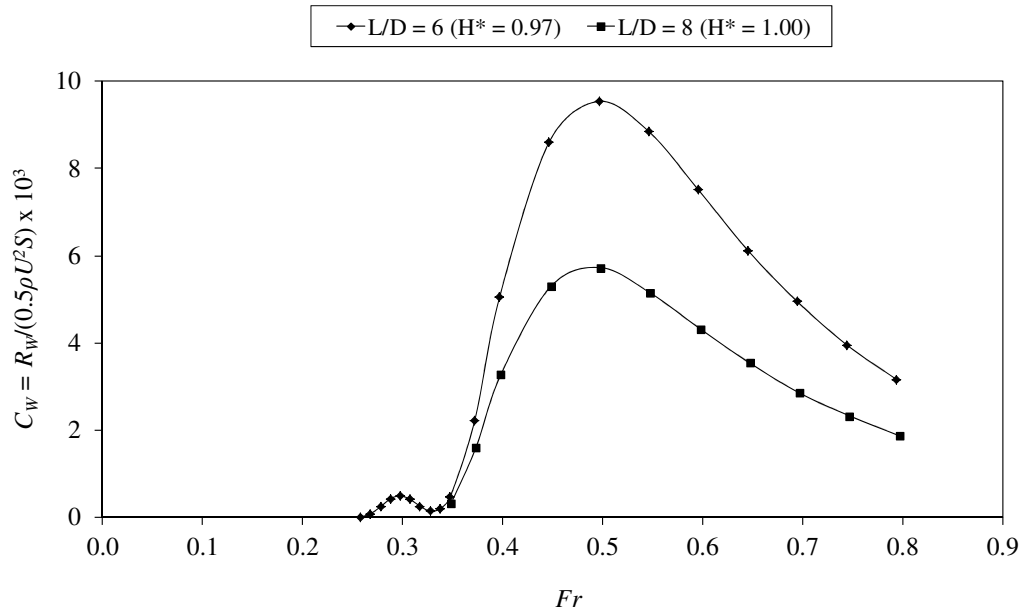


Figure 3-40 Relative effect of length-to-diameter ratio on the wave resistance coefficient for two spheroid at approximately the same depth-to-diameter ratio (H^*) $C_p = 0.67$ (Adapted from Farell (1973))

Farell (1973) also draws a direct comparison between his results and those published by Havelock (1931a) in addition to critically analysing the formulation presented by Havelock (1931a). Farell (1973) concludes that Havelock's results are erroneous and that this is due to the boundary condition of the spheroid not being satisfied exactly. In addition to this, Farell (1973) indicates that the wave resistance results presented in his work for Froude numbers between 0.35 and 0.40 are in good agreement with the experimental results published by Farell and Güven (1973).

3.3.3 CONVERGENCE PROPERTIES OF THE NEUMANN-KELVIN PROBLEM FOR A SUBMERGED BODY (DOCTORS AND BECK, 1987)

Further research into the wave making resistance, lift force and trimming moment experienced by a submerged spheroid using potential flow theory was conducted by Doctors and Beck (1987). In their study Doctors and Beck (1987) investigate the numerical performance of the Nuemann-Kelvin method to solve the flow past a spheroid moving with constant velocity and in proximity to the free-surface boundary. Unlike Farell (1973), Doctors and Beck (1987) use the panel method approach established by Hess and Smith (1964) to describe the surface of the spheroid geometry (Figure 3-41). Three different integration methods were evaluated; these were the monopole method, the panel method and the Galerkin method. The free-surface boundary is linearised and the boundary conditions are met by distributing Kelvin sources on the body of the spheroid.

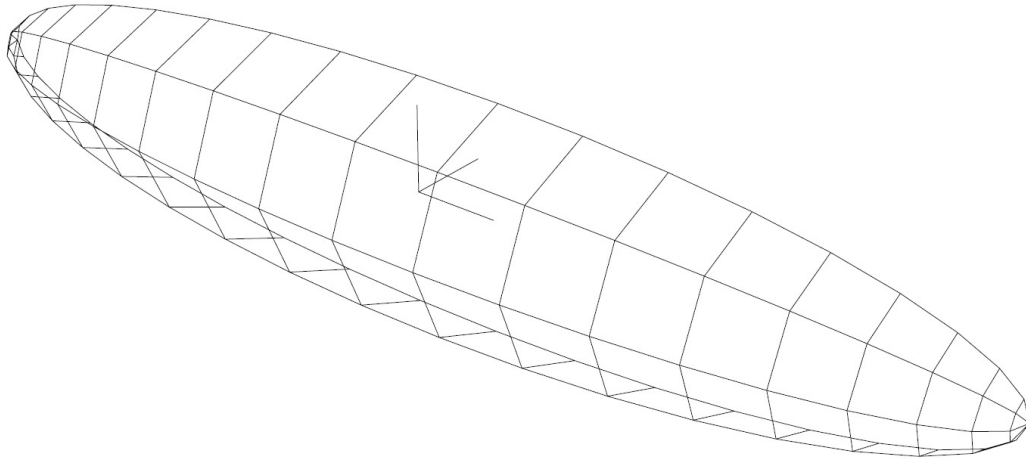


Figure 3-41 Panelised 5:1:1 spheroid geometry (half body shown) used by Doctors and Beck (1987). Panel spacing is uniform in the circumferential direction and cosine spacing in the longitudinal direction. Total panels for half body $N_p = 76$

Doctors and Beck (1987) present results of wave resistance coefficient, lift coefficient and trimming moment coefficient for the prolate spheroid for a Froude number range of $0.26 \leq Fr \leq 0.80$ and at non-dimensional depths of $H^* = 0.80$ and $H^* = 1.225$. The values of these parameters were selected to allow a direct comparison with the wave resistance results published by Farell (1973). These results were computed using the Galerkin Rankine term and Monopole Wave term method as this was found by Doctors and Beck (1987) to give the highest accuracy of the methods they had evaluated. They observed that their computed wave resistance results were in good agreement with Farell's (1973) results for $Fr > 0.34$ for the two submergence depths. The difference was found to be no more than two percent. However, a significantly greater difference was observed between the wave resistance results for $Fr < 0.34$, particularly at the shallowest submergence depth ($H^* = 0.80$). Doctors and Beck (1987) offer no explanation for the discrepancy despite their efforts to verify their results (Figure 3-42 and Figure 3-43). On reviewing the work of Hong (1983), Doctors and Beck (1987) note that Hong's (1983) computed wave resistance results showed a 93 percent difference to Farell's (1973) results at $Fr = 0.35$. In these instances, the magnitude of the wave resistance coefficient computed by Doctors and Beck (1987) and Hong (1983) is smaller than that published by Farell (1973).

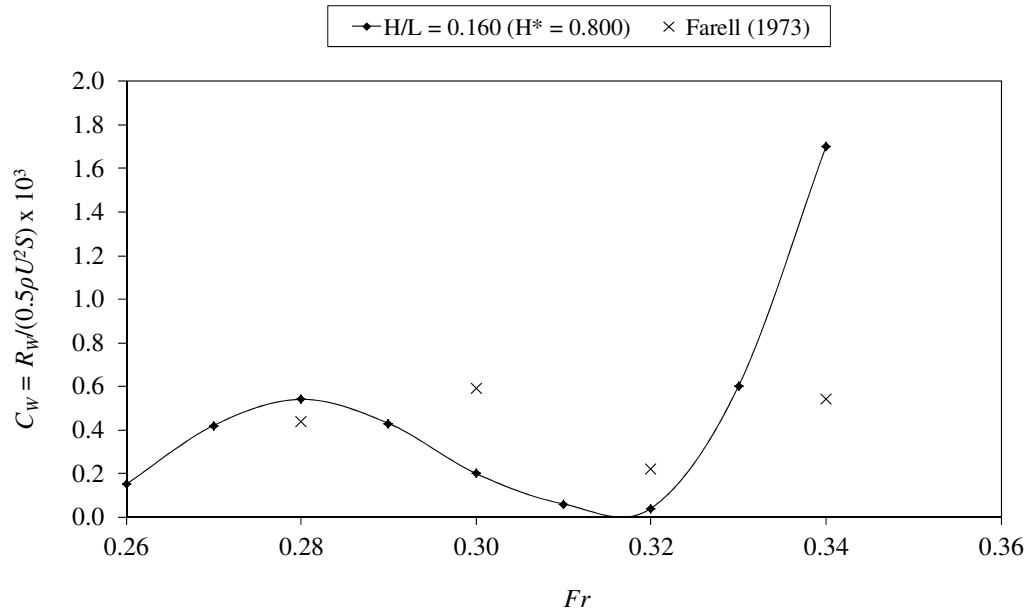


Figure 3-42 Wave resistance coefficient calculated for a spheroid with $L/D = 5.00$ by Doctors and Beck (1987) compared to the results of Farell (1973) (Adapted from Doctors and Beck (1987))

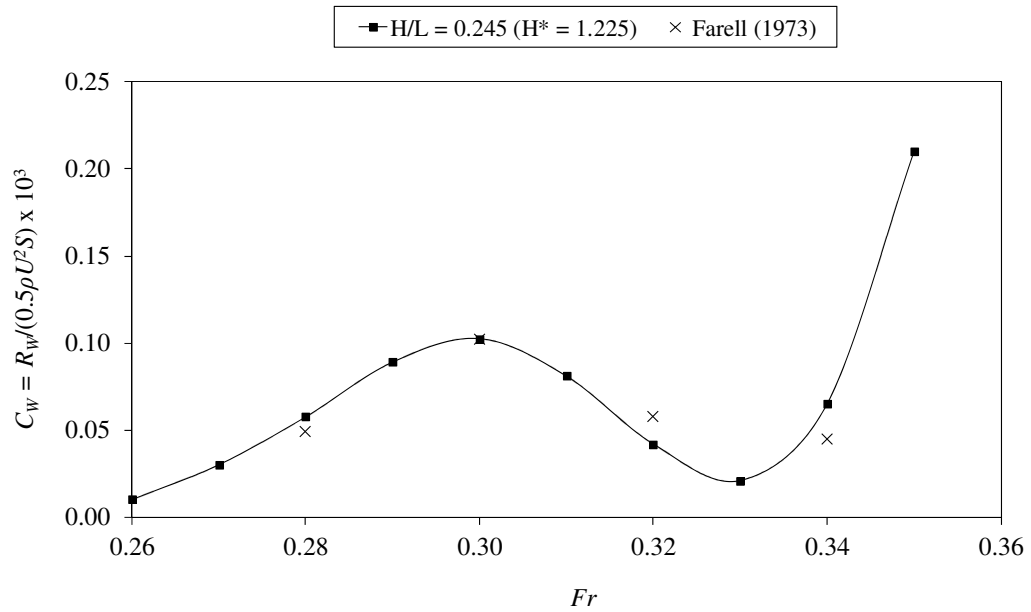


Figure 3-43 Wave resistance coefficient calculated for a spheroid with $L/D = 5.00$ by Doctors and Beck (1987) compared to the results of Farell (1973) (Adapted from Doctors and Beck (1987))

Despite the noted difference in wave resistance coefficient at low Froude numbers, the results presented by Doctors and Beck (1987) indicate similar trends to those produced by Wigley (1953) and Farrell (1973). These trends are:

- a. the periodic nature of the resistance coefficient with a peak values occurring in the region of $0.45 \leq Fr \leq 0.55$ and $Fr \approx 0.275$ (Figure 3-44);
- b. a lift force that causes a bodily rise at Froude numbers below $Fr \approx 0.60$ with a local maximum lift force at $Fr \approx 0.40$ (Figure 3-45);
- c. a pitching moment coefficient that indicates a small bow up pitching moment at $Fr \approx 0.30$ after which there is a significant bow down trimming moment that peaks in the region of $0.45 \leq Fr \leq 0.55$ and then decreases as speed increases (Figure 3-46);

In addition, there is a general trend that indicates that the magnitude of wave resistance, lift force and trimming moment reduces with an increase in submergence depth.

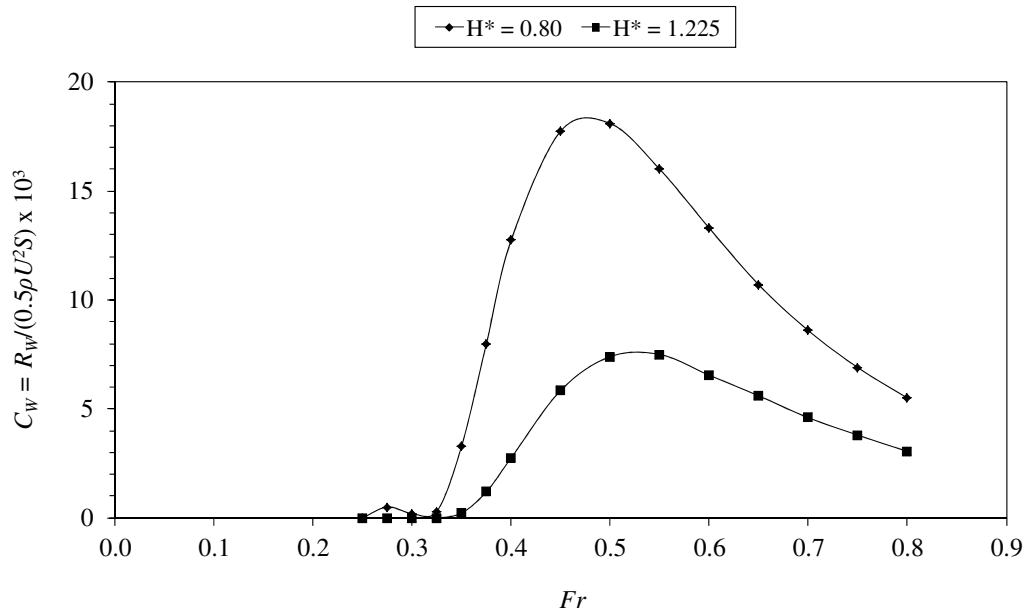


Figure 3-44 Wave resistance coefficient calculated for a spheroid with $L/D = 5.00$; $C_p = 0.67$ (Doctors and Beck (1987))

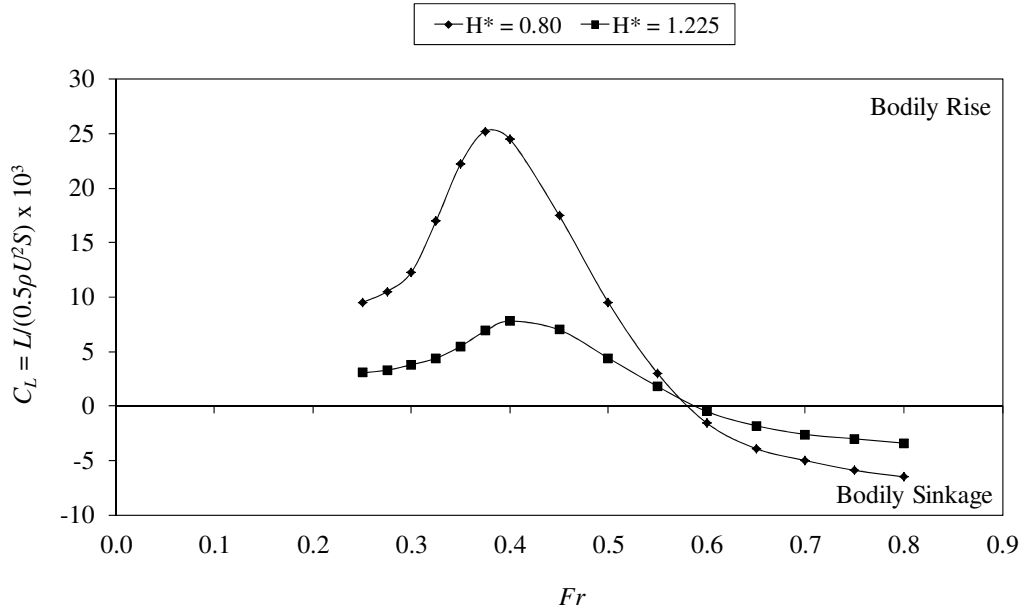


Figure 3-45 Lift force coefficient calculated for a spheroid with $L/D = 5.00$; $C_p = 0.67$ (Doctors and Beck (1987))

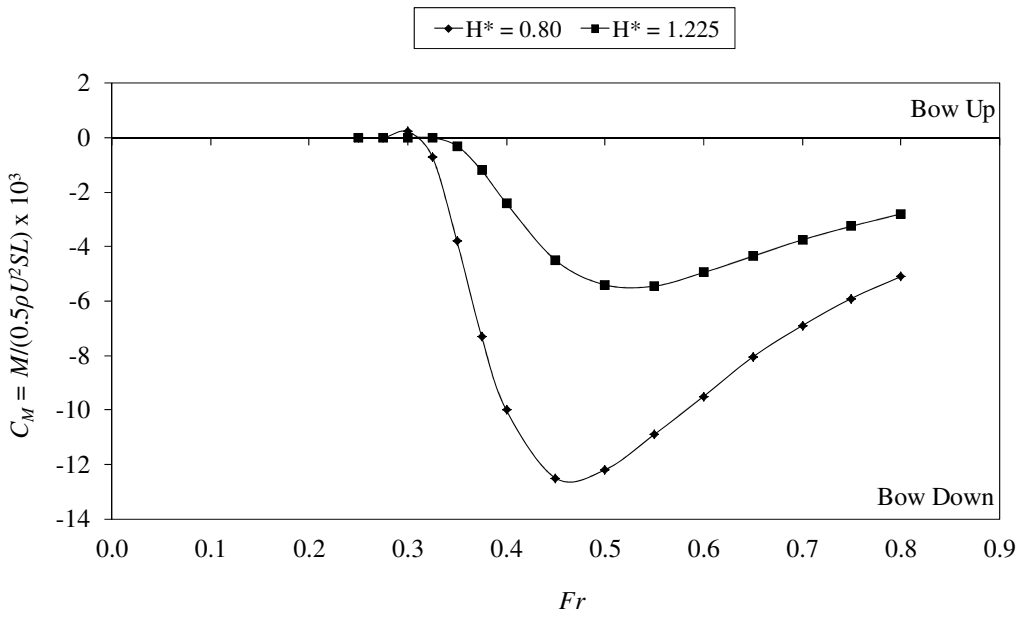


Figure 3-46 Trimming moment coefficient calculated for a spheroid with $L/D = 5.00$; $C_p = 0.67$ (Doctors and Beck (1987))

3.3.4 AN INITIAL ASSESSMENT OF FREE SURFACE EFFECTS ON SUBMERGED BODIES (CROOK, 1994)

Perhaps the most closely related work to the current research is that completed by Crook (1994). In his study of the effects of submergence depth and speed on the SUBOFF hull geometry, Crook (1994) uses the Neumann-Kelvin potential flow method with a linearised free-surface condition presented by Doctors and Beck (1987) to calculate the drag, lift and bow-up (trimming) moment coefficients due to the submerged body moving beneath the free-surface. Crook (1994) used the source panel method of Hess and Smith (1964) to define the submerged body's surface boundary.

Crook (1994) investigates the effects of calm and wave affected free-surface conditions on the force and moment coefficients generated by the interaction of the submerged body with the free-surface boundary. In addition, Crook (1994) presents the results of a submarine hull shape parametric study where the effects of constant diameter and variable length and displacement, and constant displacement and length and variable diameter are evaluated.

The two free-surface boundary conditions applied in Crook's investigation are that the pressure at the free-surface is constant (dynamic free-surface condition) and that there is no flow through the free-surface (kinematic free-surface condition). By equating these two conditions at $z = 0$ (calm water surface) and discounting the quadratic terms, Crook (1994) presents the linearised free-surface boundary condition (Equation 3-12). The body surface boundary condition is simply that there is no flow through the body, as is typical in most potential flow applications.

$$\Phi_{xx} + \frac{g}{U^2} \Phi_z = 0 \quad \text{Equation 3-12}$$

Only the bare hull configuration of the SUBOFF geometry was investigated by Crook (1994). The trimming moment coefficient calculated using the potential flow method employed by Crook is centred about the longitudinal amidships ($L/2$) position. The length-to-diameter ratio of the SUBOFF hull is $L/D = 8.57$. Simulations were completed for length Froude numbers from 0.18 to 0.75 inclusive and at the non-dimensional submergence depths listed in Table 3-9.

Table 3-9 Non-dimensionalised submergence depths (H/L) simulated by Crook (1994) and equivalent $H^* = H/D$ depths

H/L	H^*
0.100	0.857
0.110	0.943
0.120	1.029
0.125	1.072
0.135	1.158
0.150	1.286
0.175	1.501
0.200	1.715
0.225	1.929
0.250	2.144
0.300	2.572
0.400	3.430
0.500	4.287

The results of Crook's convergence study indicated that solution convergence was achieved with the model discretized into 25 longitudinal stations and 8 vertical points resulting in 168 quadrilateral panels for the half-body geometry. Vertical plane symmetry was assumed for all simulations (Crook, 1994).

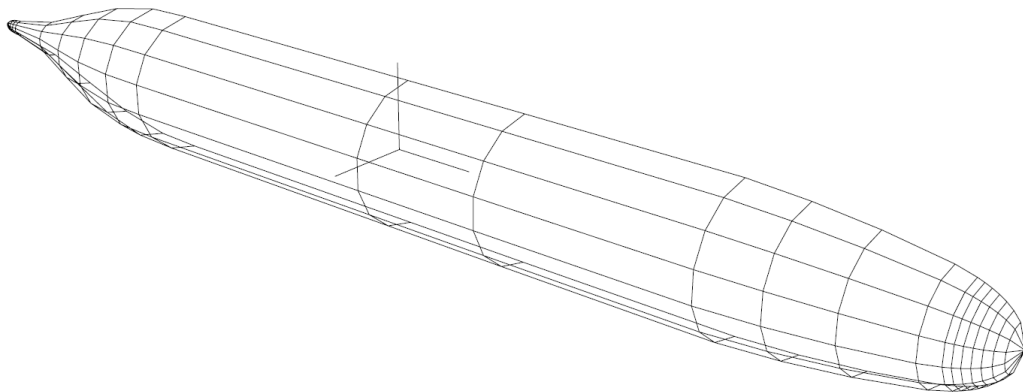


Figure 3-47 Panelised SUBOFF geometry used by Crook (1994)

The results of Crook's (1994) simulations for wave making resistance (drag) coefficient, lift coefficient and trimming moment coefficient are presented here in Figure 3-48, Figure 3-49 and Figure 3-50 respectively. Crook (1994) observed that the wave making resistance coefficient is highly periodic within the range of Froude numbers that he simulated and that the magnitude of wave resistance decreases with an

increase in submergence depth (Figure 3-48). Two local maxima are apparent at $Fr = 0.30$ and $Fr = 0.50$ with a local minima at $Fr \approx 0.20$ and $Fr \approx 0.35$. In general terms this behaviour is comparable to the results obtained by Farell (1973) and Doctors and Beck (1987) for the prolate spheroid. However, for the shallower submergence depth conditions, the magnitude of the peak wave resistance coefficient at $Fr = 0.30$ is very large compared to the second peak at $Fr = 0.50$. In addition, the wave resistance does not appear to converge on a zero value at the lower Froude numbers nor at the deepest submergence depths. This behaviour does not correlate with any of the experimental or numerical results presented so far.

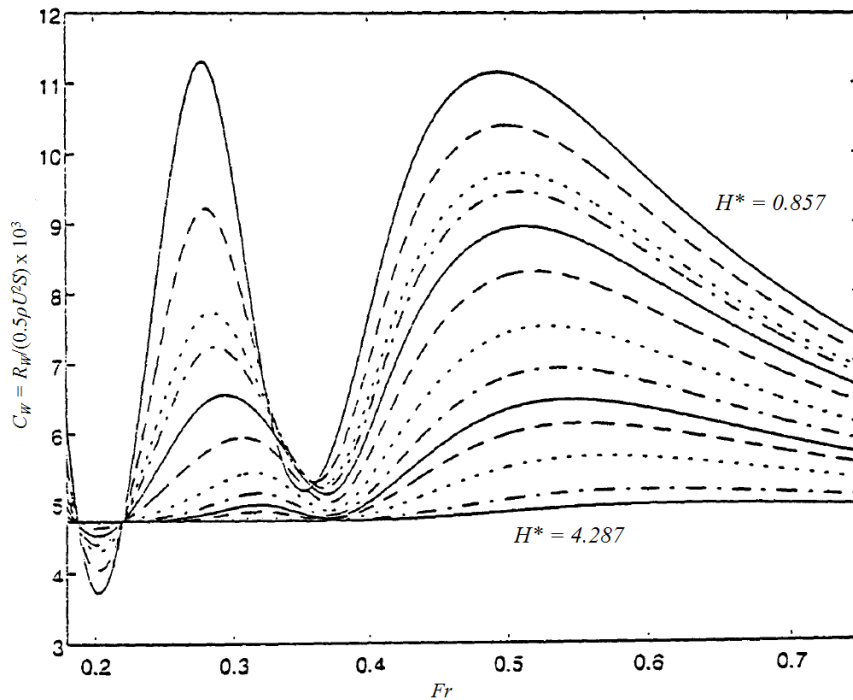


Figure 3-48 Effect of submergence depth (H^*) and Froude number on drag coefficient for SUBOFF geometry Crook (1994)

The trend of the lift coefficient curves presented in Figure 3-49 are again comparable with the results of Wigley (1953) and Doctors and Beck (1987) in regards to the periodicity and Froude number at which the peak values and the transition from a force causing a bodily rise to a bodily sinkage occur. However, the magnitude of the peak lift coefficient that occurs at $Fr \approx 0.225$ at the shallowest submergence depths is large in comparison to the peak at $Fr \approx 0.40$. Nonetheless, as the submergence depth is increased the effect of the free-surface diminishes and the lift force coefficient tends to a zero value for the range of simulated speeds.

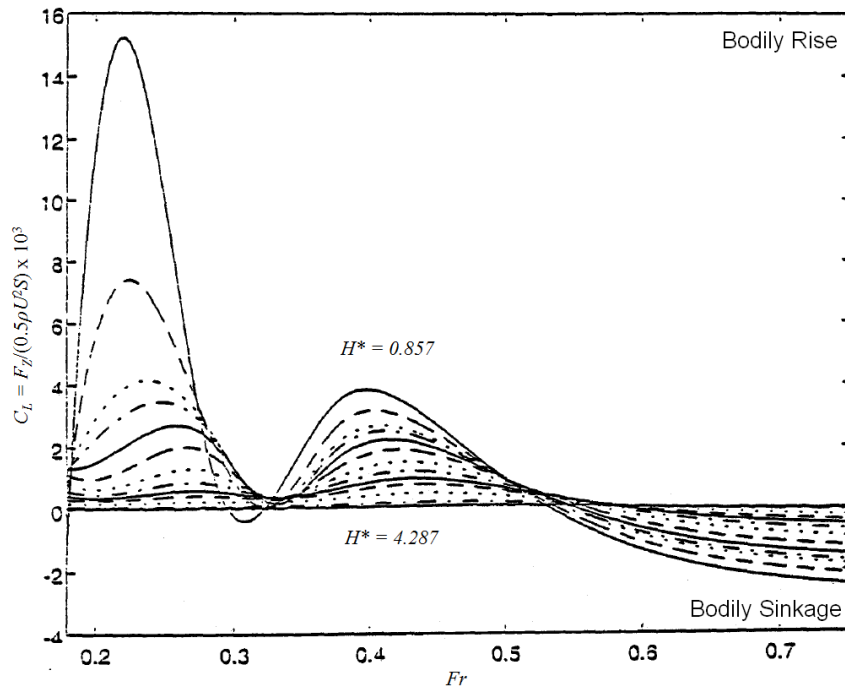


Figure 3-49 Effect of submergence depth (H^*) and Froude number on lift coefficient for SUBOFF geometry Crook (1994)

Similar to the wave resistance coefficient data, the trimming moment results presented in Figure 3-50 show a periodically varying moment which tends to a non-zero value as submergence depth increases and Froude number decreases. Again, this behaviour does not correlate with the results presented by Wigley (1953) and Doctors and Beck (1987). Crook's (1994) results indicate that the submarine body experiences a bow down trimming moment for the entire range of Froude numbers that he investigated. The Froude numbers at which the peak trimming moments occur are coincident with the peaks observed in the wave making resistance coefficient data (Figure 3-48).

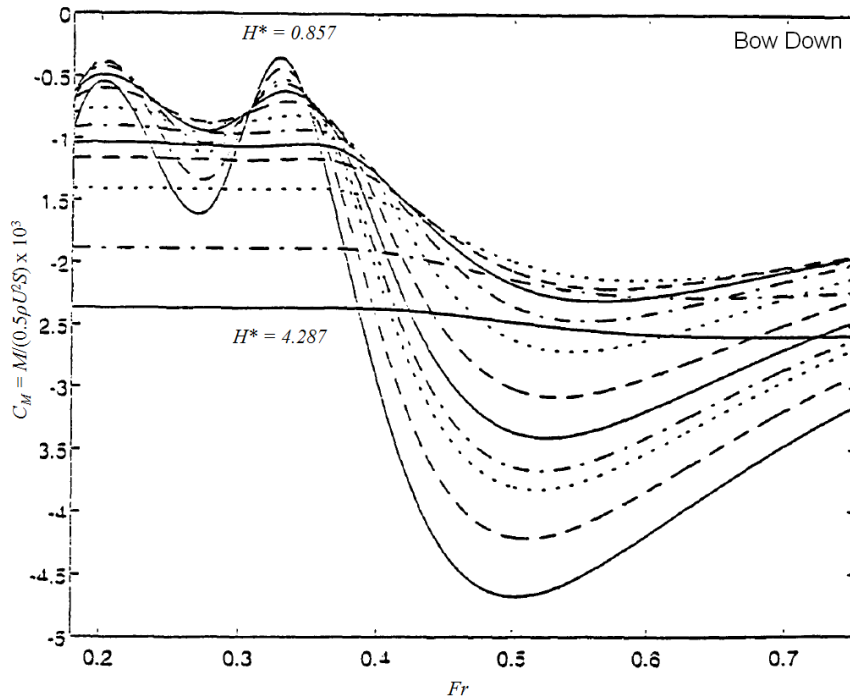


Figure 3-50 Effect of submergence depth (H^*) and Froude number on trimming moment coefficient for SUBOFF geometry Crook (1994)

A comparison between the wave resistance, lift and trimming moment coefficient data presented by Crook (1994) and the simulation data presented by Wigley (1953), Farell (1973) and Doctors and Beck (1987) suggests Crook's results are questionable. Neglecting any potential effects associated with the difference between the SUBOFF and 5:1 spheroid geometries, it is unlikely that at Froude numbers less than 0.20 the submerged body would experience a wave resistance force or trimming moment as significant as that presented by Crook (1994). In addition to this, the magnitude of the wave resistance coefficient value at $Fr = 0.30$ for the shallowest submergence depths is not considered feasible. Given the discussion presented by Doctors and Beck (1987) regarding the accuracy of their numerical predictions at low Froude numbers and the fact that Crook (1994) used their Neumann-Kelvin method, it is questionable whether the results presented by Crook (1994) for Froude numbers less than $Fr = 0.35$ are correct. Nonetheless, Crook (1994) contests that the results that he has produced are in agreement with the anecdotal evidence that was offered by submarine operators of the day.

Crook (1994) also provides the results of a parametric study into the effects of size and shape on the performance of a submerged body of revolution moving near the free-surface. The geometry of the body of revolution comprises three sections: the entrance, parallel mid-body section and the run. The size relation and geometric development of the shape is discussed in detail in Crook (1994). The geometry and parametric descriptors are illustrated in Figure 3-51.

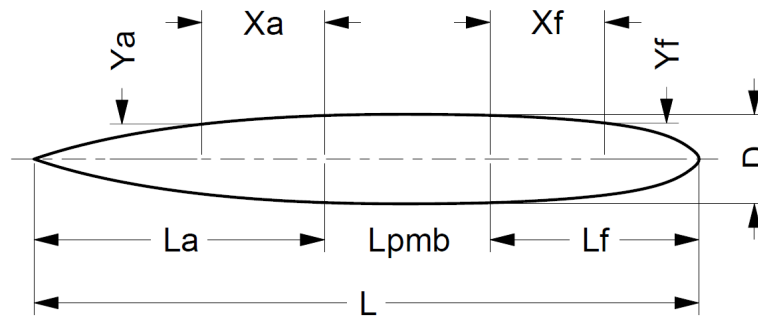


Figure 3-51 Variable geometry streamlined body of revolution used by Crook (1994) to investigate the effects of geometry on wave making resistance, lift and trimming moment during near-surface operation (Adapted from Crook (1994))

Crook (1994) presents the results of an investigation into the effects of length and diameter on a constant volume submerged body of revolution using the Nuemann-Kelvin method used by Doctors and Beck (1987). In the first instance, the volume and diameter were kept constant and the length was varied. In the second instance, the volume and length were kept constant and the diameter and parameters controlling the shape of the entrance and run were varied.

The approach used by Crook (1994) to vary the length of the body resulted in a variation of the prismatic coefficient of the entrance and run sections and subsequently the overall body. Secondly, rather than simulate each of the bodies at a common submergence depth, Crook (1994) opted to test at a submergence depth of one tenth of the length of the individual body. The geometric particulars for the bodies and the equivalent non-dimensional submergence depth (H^*) are listed in Table 3-10.

Table 3-10 Constant volume and diameter variable length body geometric parameters and non-dimensional submergence depth (adapted from Crook (1994))

Model	$n_a = n_f$	C_p	L/D	H^*
L-1	2.0	0.733	9.30	0.93
L-2	2.5	0.767	8.82	0.88
L-3	3.0	0.794	8.52	0.85
L-4	3.5	0.818	8.34	0.83
L-5	4.0	0.835	8.16	0.82
L-6	4.5	0.849	7.98	0.80

The wave resistance coefficient results presented by Crook (1994) for the six geometries are shown in Figure 3-52. The results show an almost monotonic increase in the resistance coefficient with a reduction in length. However, it is important to consider that the submergence depth decreases as the length decreases. As a consequence these results are not entirely indicative of the effects of length-to-diameter for a body submerged at a constant depth. In addition, the observable change in the ratio of the peak amplitude values at $Fr = 0.275$ and $Fr = 0.475$ with a change in

depth is not greatly dissimilar to the results Crook (1994) presents for the SUBOFF simulations (Figure 3-48). It is therefore difficult to attribute this solely to the change in length-to-diameter ratio. Crook (1994), however, asserts that a reduction in length-to-diameter ratio results in an increase in the magnitude of the wave making resistance.

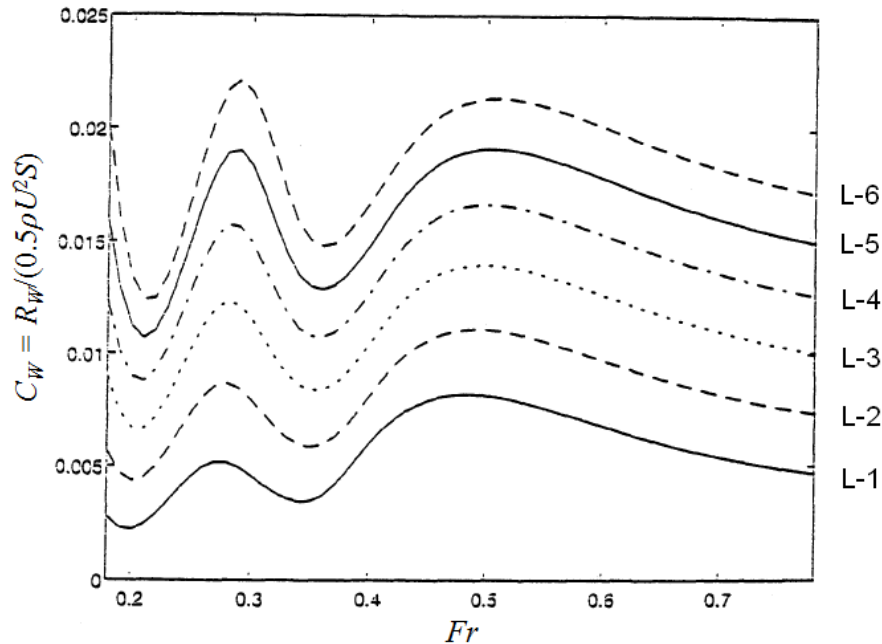


Figure 3-52 Effect of length and Froude number on wave resistance coefficient for a parametrically varied body of revolution (adapted from Crook (1994))

The effect of length-to-diameter ratio on the lift force coefficient shows similar trends to that of the wave resistance coefficient where the smallest L/D corresponds to the greatest lift coefficient. It is also observable from Crook's (1994) results that the lift force does not tend towards zero at the lower Froude numbers. As mentioned previously, this may be an error in the application of the Nuemann-Kelvin method. Similarly, Crook (1994) observed that the effect of length-to-diameter ratio on the trimming moment is such that the geometry with the lowest L/D corresponds to the greatest bow down trimming moment coefficient.

The second variation investigated by Crook (1994) involved changing the diameter for a constant length and volume. The geometric particulars of the six geometries that Crook (1994) simulated are listed in Table 3-11.

Table 3-11 Constant volume and length variable diameter body geometric parameters and non-dimensional submergence depth (adapted from Crook (1994))

Model	$n_a = n_f$	C_p	L/D	H^*
D-1	2.0	0.694	8.30	0.80
D-2	2.5	0.752	8.36	0.84
D-3	3.0	0.798	8.61	0.86
D-4	3.5	0.827	8.77	0.88
D-5	4.0	0.848	8.88	0.89
D-6	4.5	0.870	8.99	0.90

The wave resistance (drag) coefficient results presented by Crook (1994) show variability in the magnitude and location of the local maximum and minimum resistance coefficient between the smaller and larger diameter models (D-1 to D-6). The results indicate that as the geometric indices (n_a and n_f) are increased, the Froude number at which the local minimum and maximum resistance coefficient values occur increases (Figure 3-53). This behaviour is more apparent for $Fr > 0.30$. It can be inferred that the effect of prismatic coefficient has a more significant effect on the shape of the resistance coefficient curve than the length-to-diameter. Nonetheless, similar issues exist with the variable diameter results as were identified with the variable length results. These are: the relatively large value of the peak resistance coefficient value at $Fr \approx 0.275$; the indication that the resistance does not tend towards zero at a zero Froude number; and the inability to make an exact comparison with respect to a common non-dimensional submergence depth. Crook (1994) states that the rounder the ends and shorter along the mid-body (higher prismatic coefficient and lower length-to-diameter ratio) the greater the wave resistance coefficient.

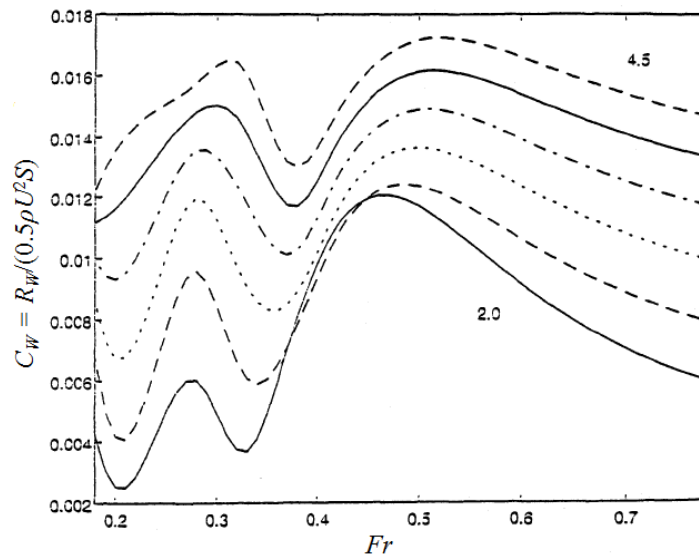


Figure 3-53 Effect of diameter and Froude number on wave resistance coefficient for a parametrically varied body of revolution (adapted from Crook (1994))

Crook (1994) observed a greater variability in the lift force coefficient curves for the variable diameter test case in comparison to the variable length test case, in particular for Froude numbers less than $Fr = 0.35$. Nonetheless, the general form of the lift force coefficient is similar to that observed for the variable length simulation results: a peak lift force pulling the body towards the free-surface is experienced at the lower Froude numbers while the lift force becomes negative at Froude numbers greater than approximately 0.55. Crook (1994) concludes that a streamlined body geometry with a high prismatic coefficient and length-to-diameter ratio is preferable as it induces a smaller lift force. The trimming moment coefficient results are again similar to the variable length test case with a periodically varying bow down moment with a peak value occurring at approximately $Fr = 0.475$. Crook's (1994) data show that the D-1 geometry (lowest prismatic coefficient and length-to-diameter ratio) has a very flat trimming moment response at lower Froude numbers ($Fr < 0.30$). This geometry also has the smallest trimming moment coefficient of all of the geometries in this speed range.

Overall, the results presented by Crook (1994) possess form that agrees with the results produced by Wigley (1953) and Doctors and Beck (1987); however, there are notable discrepancies. The most significant of these is the relative magnitude of the peak wave resistance coefficient that occurs at approximately $0.30 \leq Fr \leq 0.35$. Therefore, only tentative conclusions can be drawn as to the effect of length-to-diameter on the interaction effects of a submerged body travelling beneath the free surface. Despite this shortcoming, from Crook's (1994) results it would appear that an axisymmetric body with a low prismatic coefficient and high length-to-diameter ratio possesses minimum wave resistance, lift force and trimming moment.

3.3.5 SUMMARY

The use of potential flow formulations and panel methods to calculate the wave making resistance, lift and trimming moment acting on a shallowly submerged streamlined body has been investigated by numerous authors over the past century. The results of early formulations to the linearised free-surface problem have been shown to be inaccurate yet indicative of the forces acting on the submerged body. The more recent work of Doctors and Beck (1987) has been partially validated against experimental data and their results are shown to correlate well. In general, the form and behaviour of the calculated wave resistance results compare well against the experimental results of Weinblum et al. (1950), Gertler (1950) and Farell and Güven (1973). No comparisons were able to be made for the lift and moment data; however, there is general agreement among the potential flow results produced by independent authors including Wigley (1953), Farell (1973) and Doctors and Beck (1987).

The behaviour of the lift force and trimming moment and the influences of forward speed and submergence depth can be seen in the results of Wigley (1953) and Doctors and Beck (1987) for a spheroid with $L/D = 5.00$. The general behaviour indicates that for Froude numbers of up to approximately $Fr = 0.55$ the lift force acts to pull the body towards the free surface. The peak force occurs at approximately $Fr = 0.40$. At speeds greater than $Fr = 0.55$ the force acts to push the body away from the free-surface. While the form remains the same, the magnitude of the lift force decreases with an increase in submergence depth. The trimming moment experienced by the body indicates that there is negligible moment acting at low speed (Froude numbers

less than approximately $Fr = 0.20$). As the speed increases the trimming moment behaves in an oscillatory manner and may alternate between a small bow-up and bow-down trimming moment. As the speed increases above a Froude number of approximately $Fr = 0.35$ the trimming moment acts exclusively to trim the body by the bow (stern-up). This trimming moment increases to a local maximum at approximately $Fr = 0.50$. Beyond this speed the trimming moment slowly decreases and asymptotes at zero. Like the wave resistance and lift force, the magnitude of the trimming moment decreases with an increase in submergence depth.

While the results presented by Crook (1994) are questionable, the outcomes of his parametric investigations into the effects of length and diameter on a submerged body's wave resistance, lift force and trimming moment indicate that the preferable streamlined body form would possess a low prismatic coefficient and a high length-to-diameter ratio. This observation agrees with the outcomes of the experimental investigations conducted by Weinblum et al. (1950), Gertler (1950) and Alvarez et al. (2009).

Finally, drawing on Farrell and Güven's (1973) experimental research (Section 3.2.3), it is apparent that it is not an insignificant matter to determine the components that comprise the total resistance acting on a submarine. Despite this, the results of Doctors and Beck (1987), in particular, indicate that potential flow panel methods can be used to determine wave resistance with adequate accuracy. Application of these numerically determined results; however, appears to be an altogether different issue to be resolved.

4 IMPLICATIONS OF SMALL SCALE SUBMARINE MODEL TESTING

The implications of cost and practicality and the inability to maintain controlled environmental conditions makes detailed, full scale studies of external flows around a submarine an insurmountable task. Consequently, scale model testing techniques, equipment and facilities have been developed to address these prohibitive issues. Despite the successes of scale model testing methods there are still limitations that must be considered when designing an experiment such as that conducted in this research. It is important to produce model results that are representative of the full-scale condition or otherwise can be scaled to adequately represent a full-scale result. The fundamental issues that have been identified and addressed in the design of the constrained, small scale model experiments conducted in this research are:

- a. the extrapolation of model test results to full scale results;
- b. establishing and maintaining a turbulent boundary layer around the model; and
- c. the sting and post interference effects on the model's dynamic pressure field and the rigid body forces and moments and surface wave profile.

These issues and the strategies employed to resolve them are discussed in the following sections.

4.1 SCALE EFFECTS ON SUBMERGED BODY RESISTANCE TESTS

Extrapolation of resistance test data from model scale to full scale is not unique to submerged body experiments. However, the approach that has been established for surface or surfaced platforms has been found by Farell and Güven (1973) and Jolliff (1966) to be inappropriate for application to the submerged body problem. In his investigation into the critical scale effects acting on a specific submerged body of revolution being tested in a towing tank, Jolliff (1966) addressed the following objectives:

- a. Investigate whether the two-dimensional ITTC and Schoenherr friction expansion lines are appropriate for application to submerged bodies of revolution;
- b. Identify an effective boundary layer stimulation device that promotes a sustained turbulent boundary layer over the submerged body while contributing minimal parasitic drag; and
- c. Identify an appropriate form factor to account for the viscous pressure drag acting on the body.

Jolliff (1966) conducted his investigation using two geometrically similar bodies of revolution that are representative of a submarine hull. The smaller scale model measured 1.22 metres in length, while the larger scale model measured 4.57 metres in length. The models were tested in the Webb Institute towing tank and David Taylor Model Basin (DTMB) towing tank respectively. The length-to-diameter ratio of the geometry is $L/D = 7.30$. Jolliff's (1966) intention was to conduct measurements for a deeply submerged condition only. As a result, he conducted tests at the mid-depth of the tank. This resulted in a depth to diameter ratio of $H^* = 3.00$ in the Webb Institute tank and possibly $H^* = 5.30$ in the DTMB tank.

Based on the outcomes of his investigation, Jolliff (1966) formed the following conclusions:

- a. The two-dimensional friction expansion lines proposed by the ITTC and Schoenherr do not represent the friction resistance coefficient of the three-dimensional body of revolution such as those tested in his study.
- b. It is important to conduct a series of tests using candidate transition devices to identify which device will provide a sustained turbulent boundary layer with minimum contribution to drag for the range of velocities (Reynolds numbers) tested. Jolliff (1966) noted that three-dimensional transition devices are superior to two-dimensional devices and should be used exclusively. In his study of five transition devices, Jolliff (1966) varied the size, geometry and circumferential distribution of the device to identify the relative optimum configuration.
- c. In order to extrapolate the measured resistance of a scale model to full scale, it is necessary to apply a body specific form factor to the two-dimensional expansion line to obtain the correct shape of the viscous resistance curve. Through his investigation, Jolliff (1966) observed that the form factor is not constant and varies with speed, even when wave making is absent.

Although Jolliff's (1966) experimental methods were not as sophisticated or direct as those used by Farell and Güven (1973), their observations and conclusions are in agreement. Based on these observations it was considered prudent to similarly identify an effective transition device and extrapolation method for the models tested in this investigation.

4.2 TURBULENCE STIMULATION

The scale effects incurred by small scale experimental testing need to be minimised in order to obtain accurate and meaningful data. Where extrapolation to a full (large) scale system is required, the effects of boundary layer turbulence and separation need to be comprehensively accounted for when conducting scale model experiments.

Due to the small size of model and the subsequent low test velocities encountered throughout this research, a laminar boundary layer can extend aft from the leading edge of the three-dimensional body, far further than would be experienced at full scale. The principal effect of the laminar boundary layer is to provide an appreciably lower drag force when compared to an equivalent test condition with a turbulent boundary layer. Allan and Conn (1950) note that both the tangential stresses and normal pressures are affected by the condition of the boundary layer. Other implications such as laminar induced flow separation can also lead to misleading results.

The resistance of the submerged body can be divided into two parts: the viscous resistance and the residual resistance. While the viscous resistance is calculated using standardised formulae, the residual resistance is determined directly from experimental or numerical simulation data. The residual resistance is modelled based on the gravitational similarity law, while the frictional resistance assumes a turbulent boundary layer condition. Significant errors in predicting resistance from towing tank

tests have been found to be caused by the occurrence of large regions of laminar boundary layer flow (Kozlov, 1969).

The objective of a turbulence stimulation device is to effectively and efficiently transition the boundary layer flow from a laminar state to a sustained fully turbulent state at a specific location and in a coherent manner. When testing with small models (in the order of 1.2 to 2.4 m) it has been shown that consistent or reproducible test results are not achievable without stimulating turbulence and transitioning the boundary layer flow (Davidson, 1948).

Investigations conducted by Kozlov (1969) show that for a Reynolds number greater than 4×10^6 the effect of the boundary layer on the resistance of ship models can be considered to be negligible and in the order of 1-1.5% of the measured resistance. However, the foundation of this statement is strongly biased by the hull geometry and form factor. The relative flow velocity, and consequently Reynolds number, has a fundamental impact on the condition of the boundary layer. In instances where experiments are being conducted on small models and/or at low speeds, achieving a trans-critical Reynolds number can be difficult if not impossible. It is therefore crucial that every effort is made to transition the boundary layer with minimal impact on the drag quota of the body with a turbulent boundary layer. Further discussion of the characteristics of boundary layer transition over a three-dimensional body of revolution is presented by the author in Appendix A.

The efficiency and effectiveness of a transition device can be directly evaluated by determining its critical Reynolds number and contribution of parasitic drag. An ideal device would promote sustained boundary layer transition with a low critical Reynolds number (low velocity and or profile height) while contributing minimal or no additional drag. For a surface mounted device, the objective is to use a geometry which can generate a continuous three-dimensional flow disturbance with minimal parasitic drag. It has been found that for small models the parasitic drag incurred by the use of surface mounted boundary layer transition devices can be substantial (ITTC, 1990).

Of the available devices for artificial turbulence stimulation, in particular those recommended by the ITTC, Hama strips have been selected for use in the current experiments due to their reported high level of efficiency and the promise of easy application (ITTC, 1990). Experiments conducted by Hama (1957) and Lewandowski (1994) have shown that Hama strips provide a suitable level of sustained turbulent flow for a minimal increase in drag when compared to equivalent trip wire and sand roughness techniques. However, depending on the range of test velocities of interest, the Reynolds number and boundary layer thickness can vary significantly. As a consequence, the critical height will change and require a different device with an appropriate profile height to be used accordingly. An experimental study was conducted by the author to investigate the effect of forward velocity on the performance of the Hama strip used in this research and to identify an effective profile height for application to the models being tested. The results of this study are presented in the following section.

4.2.1 HAMA TURBULENCE STIMULATION STRIPS AND THEIR APPLICATION

The Hama strip geometry is comprised of a span-wise array of triangular plan form protuberances arranged in a repeating pattern. The apex of each triangle points towards the direction of the oncoming fluid flow (Figure 4-1). The appropriate profile height (k) of the strip is dependent on the incident boundary layer thickness and roughness Reynolds number (Re_k). As the free stream flow encounters the span-wise strip the incident streamlines on the surface of the body converge towards the internal apex. This acceleration and convergence causes a spiralling fluid motion to occur and a vortex loop to form (Figure 4-1). The vortices are found to deteriorate into turbulent flow in a span-wise front around the body (Hama, 1957).

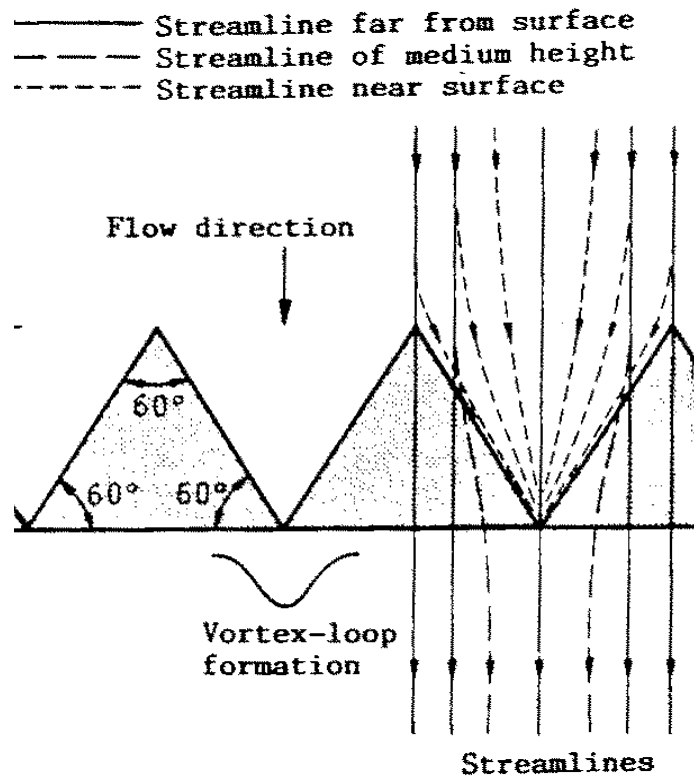


Figure 4-1 Hama turbulence strip plan form geometry and incident fluid streamlines (ITTC, 1990)

The method presented by Braslow & Knox (1958) was used to determine the critical height of the Hama strip based on the local flow velocity at the point of application. In the case of the SUBOFF and Joubert geometries, the Hama strip was affixed with its trailing edge at 5 percent of the overall hull length aft of the nose (Figure 4-2). The results of the critical height calculations are presented in Figure 4-3, where profile height (k) is plotted against test velocity (U).

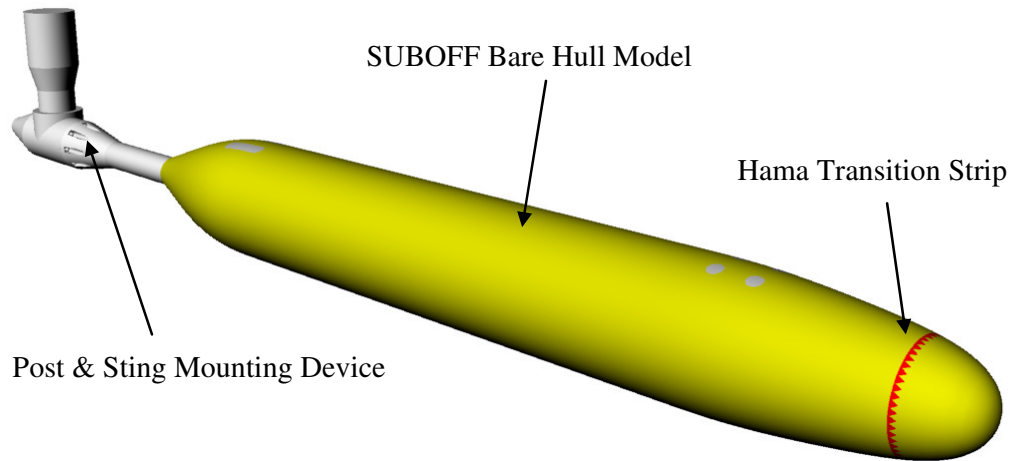


Figure 4-2 SUBOFF model with Hama boundary layer transition strip device affixed at 5% of the overall hull length aft of the leading edge

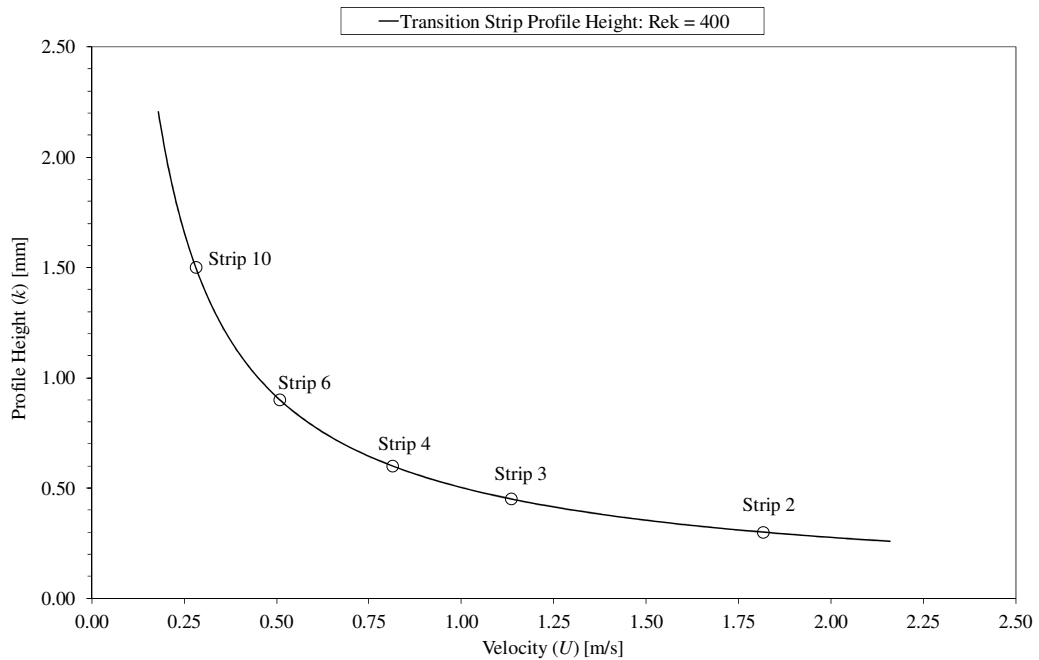


Figure 4-3 Transition strip profile height (also critical height) calculated for Hama strip turbulence stimulator study

Each Hama strip was fabricated by hand. The strips comprised multiple layers of self-adhesive polyester tape that were cut to match the Hama pattern illustrated in Figure 4-1. The dimensions of the strip geometry are illustrated in Figure 4-4. The tape's adhesive backing was found to be adequately water resistant and ensured that the strip remained firmly attached in place for the duration of the experiment. The Hama strip is considered to be superior to the more conventional stud arrangement as it can be easily affixed to the model and is superior to carborundum strips as it comprises a

uniform geometric distribution as opposed to a random distribution of roughness particles. Nonetheless, studs and carborundum strips are still effective means of stimulating a turbulent boundary layer.

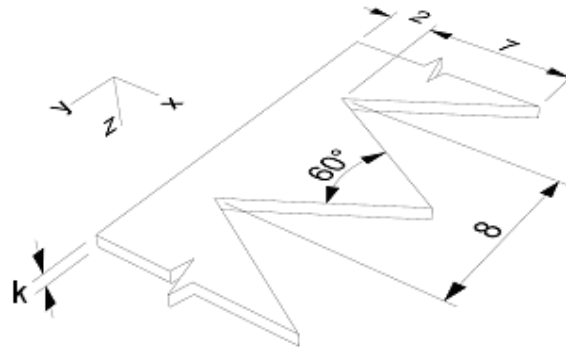


Figure 4-4 Hama turbulence strip used in the 2011 SUBOFF turbulence stimulator study (dimensions in millimetres)

Resistance tests were conducted for the SUBOFF model at a non-dimensional depth of $H^* = 3.30$ where the effect of free-surface interaction was considered to be negligible at low speeds in the AMC towing tank (Dawson et al., 2010). The test set-up and procedure used in the Hama strip study was the same as that used for the resistance and vertical force measurement tests that form the focus of this research. The details of the test procedure and setup are presented in Section 5.

The transition strip study comprised resistance tests across a range of forward velocities for each model and transition strip configuration. A range of Hama strips with different profile thicknesses were tested in addition to the no-transition device condition (bare hull only). The actual profile thicknesses tested were a direct function of the material thickness. The nominal thickness of the polyester tape was 0.15 millimetres. Consequently, Hama strips were fabricated based on multiples of this thickness. The profile heights of the tested strips are listed in Table 4-1.

Table 4-1 Hama transition strip profile heights used in the transition device study on the SUBOFF bare hull geometry

Strip (No. of Layers)	Profile Height (k) [mm]
2	0.30
3	0.45
4	0.60
6	0.90
10	1.50

The results of the study are presented in Figure 4-5, where the total measured resistance force has been non-dimensionalised by the dynamic pressure and the body wetted surface area to give the total resistance coefficient (C_T). The results clearly indicate the ability of the Hama strip to stimulate a turbulent boundary layer. At

Froude numbers above $Fr = 0.30$ Strips 2, 3, 4 and 6 can be observed to provide consistently similar resistance coefficient values. At Froude numbers below $Fr = 0.30$ it is evident that Strip 2 and Strip 3, those with the lowest profile height, start to become ineffective and the resistance coefficient diverges towards the no-transition strip result. This indicates that the boundary layer is tending towards one with a largely laminar condition. Conversely, the results of Strip 10 indicate that although the boundary layer is transitioned, there is an appreciable increase in the resistance that can be attributed to the parasitic drag contributed by the strip itself. Based on these results, Strip 4 is considered to possess the ideal profile height as it sustains a transitioned boundary layer at Froude numbers of at least 0.10 while contributing a minimal amount of additional drag.

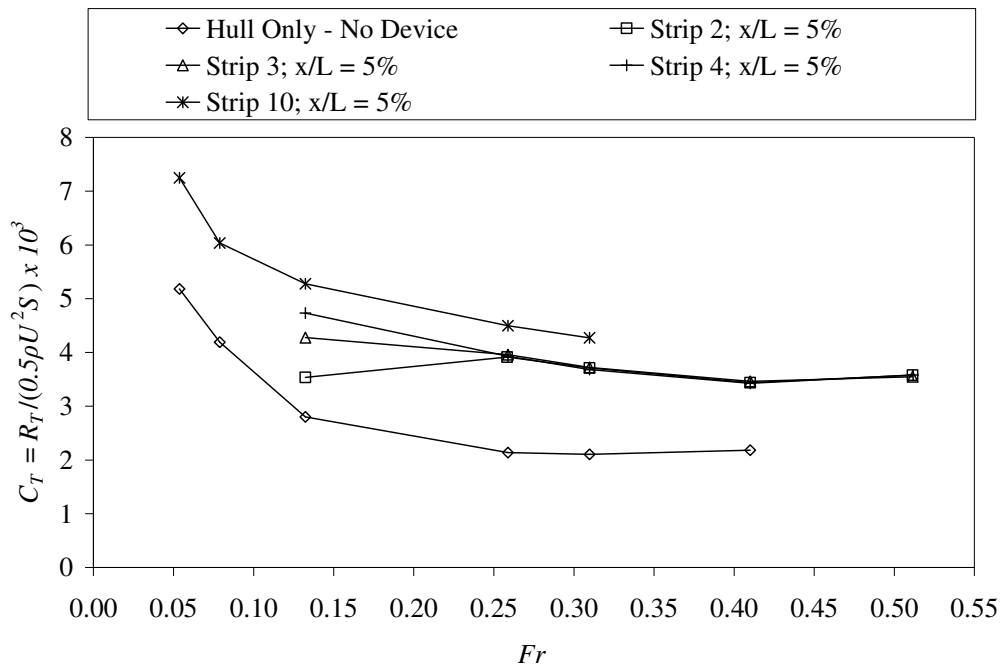


Figure 4-5 Hama turbulence strip study results of total resistance coefficient versus Froude number for the SUBOFF model $D = 0.181$ m; $H^* = 3.30$

Based on the results of the study and the experience gained with respect to the fabrication and application of the strips, the Hama transition device developed for the Joubert models has a profile height of 0.55 millimetres (Figure 4-6). Straight line resistance tests were conducted for the bare hull and hull with transition device to provide an indication of the strip's performance. Tests were conducted at a mid-tank submergence depth ($H^* = 3.46$ where $D = 0.23$ m). The results of these tests are presented in Figure 4-7. A trend in the total resistance coefficient, similar to that observed in the 2011 SUBOFF study, can be identified. In this case the transition strip was found to perform at Froude numbers as low as 0.118 ($Re_L = 734100$). At speeds below this, the measured resistance force fluctuated between the transitioned and laminar conditions, suggesting that the boundary layer was highly sensitive to the gross effects of the fluid environment and that the Hama strip was not able to provide a sustained transitioned boundary layer. The apparent rise in the total resistance coefficient values, for the model with the Hama strip, and for speeds greater than

$Fr = 0.425$ ($Re_L = 2630524$) is a result of the interaction between the model and the free-surface. It is not a boundary layer effect. The same set of data is plotted and overlaid on the laminar and turbulent flat plate friction coefficient data presented by Van Manen and Van Oossanen (1988) (Figure 4-8). It can be clearly seen that the resistance coefficient data produced by the model with the transition device aligns closely to the turbulent friction coefficient data and the fitted line. This implies that, despite any form effects, the body's boundary layer is in a transitioned condition. In addition to this, the resistance coefficient data produced by the model without any transition device aligns with the trends shown for a transitional friction coefficient.

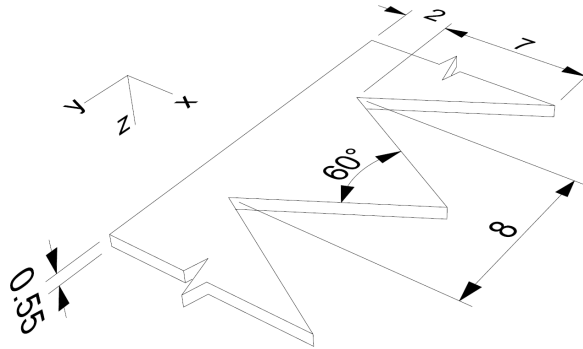


Figure 4-6 Hama turbulence strip used in the 2012 Joubert experiment (dimensions in millimetres)

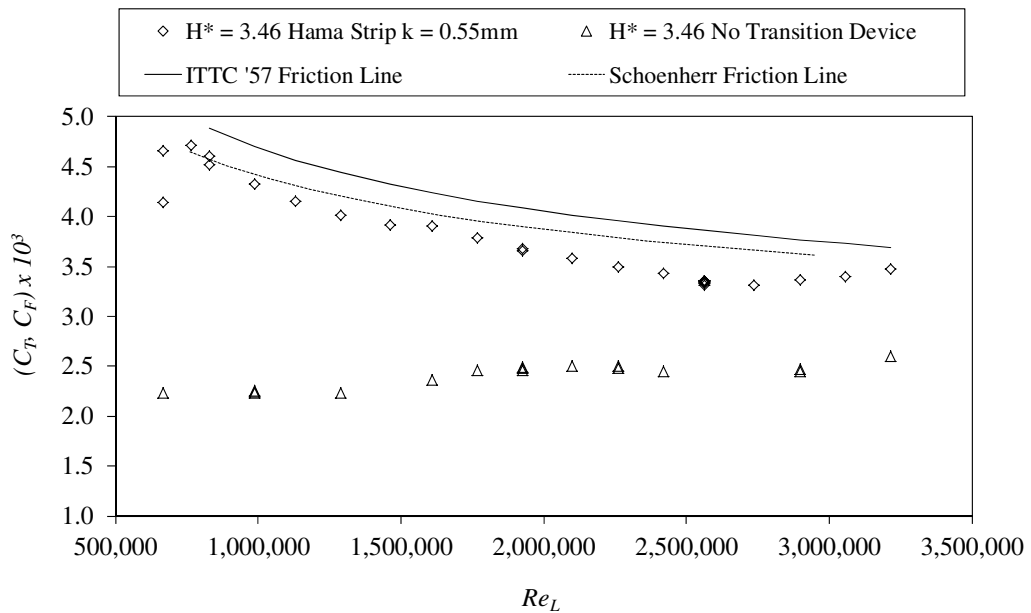


Figure 4-7 Comparison of Joubert $L/D = 7.30$ total resistance coefficient against established turbulent friction coefficient lines. Model test data corresponds to $H^* = 3.46$ depth and with and without the Hama transition device (at $0.05 x/L$)

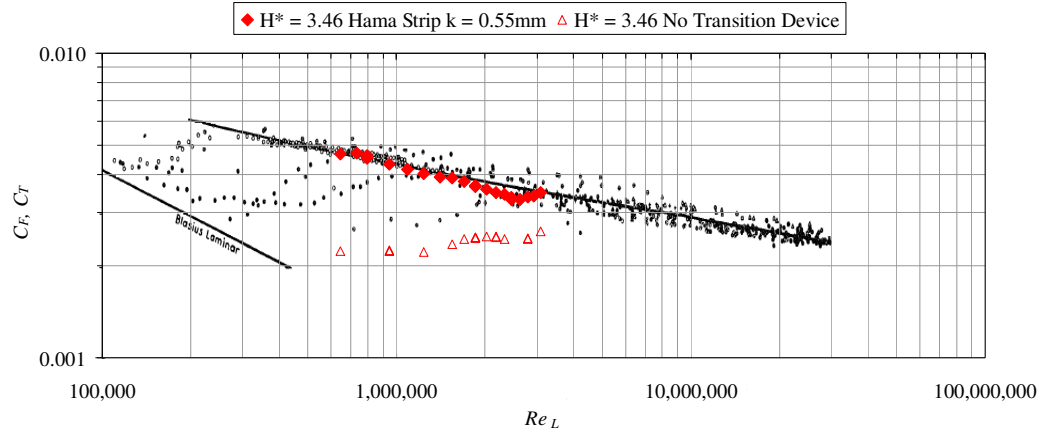


Figure 4-8 Joubert $L/D = 7.30$ total resistance coefficient for the model with and without the transition strip at $H^* = 3.46$ overlaid on the turbulent and laminar flat plate friction coefficient data presented by Van Manen and Van Oossanen (1988). Joubert C_T data shown is for $H^* = 3.46$ and $0.10 \leq Fr \leq 0.50$

4.3 FORM FACTOR AND FRICTION COEFFICIENT EXPANSION LINE

Jolliff (1966) makes the assertion that there is no single friction coefficient expansion curve that is applicable to a specific streamlined body whether it is a surface ship or a submerged body. Rather, Jolliff (1966) surmises that a family of curves would be more appropriate to account for the amount of the body's three-dimensionality. Nonetheless, any idealised two-dimensional friction curve like the Schoenherr turbulent friction line or the ITTC 1957 expansion line requires the use of a form factor to account for the three-dimensional form of the body. As has been discussed, the forms of the streamlined bodies of revolution studied in this research are three-dimensional. It can be inferred from the conclusions drawn by Farrell and Güven (1973) that the issues of the form factor and the friction expansion curve are further exacerbated when the body is only shallowly submerged and is interacting with the free-surface. Despite a rigorous literature review, no applicable form factor solutions were identified for the near-surface submerged body of revolution.

Nonetheless, a number of empirical and applied formulations of form factor have been investigated to evaluate their ability to be used in the extrapolation (expansion) of the model scale resistance coefficient results to full scale results. The following methods have been considered:

- a. the empirical formulation of Hendrix et al. (2001) used by Alvarez et al. (2009);
- b. the empirical formulation presented by Hoerner (1965) for subsonic three dimensional streamlined bodies;
- c. the method presented by Hughes (1954), which uses the measured total resistance coefficient and a theoretical friction coefficient for a turbulent flat plate flow; and

d. Prohaska's (1966) method, which is an extension of Hughes' (1954) method.

Despite Jolliff's (1966) assertion that the ITTC 1957 friction coefficient expansion line (Equation 4-1) is inappropriate for use with submerged bodies of revolution, the general shape of this equation correlates with the shape of the measured total resistance coefficient data of the Joubert models at a mid-tank submergence depth ($H^* = 3.46$) and for the Froude number regions where free-surface interaction is negligible (Figure 4-9). It was therefore decided to use the ITTC 1957 friction coefficient expansion line as the basis for any extrapolation from model to full scale resistance data.

$$C_{F_{ITTC'57}} = \frac{0.075}{(\log_{10} Re_L - 2)^2} \quad \text{Equation 4-1}$$

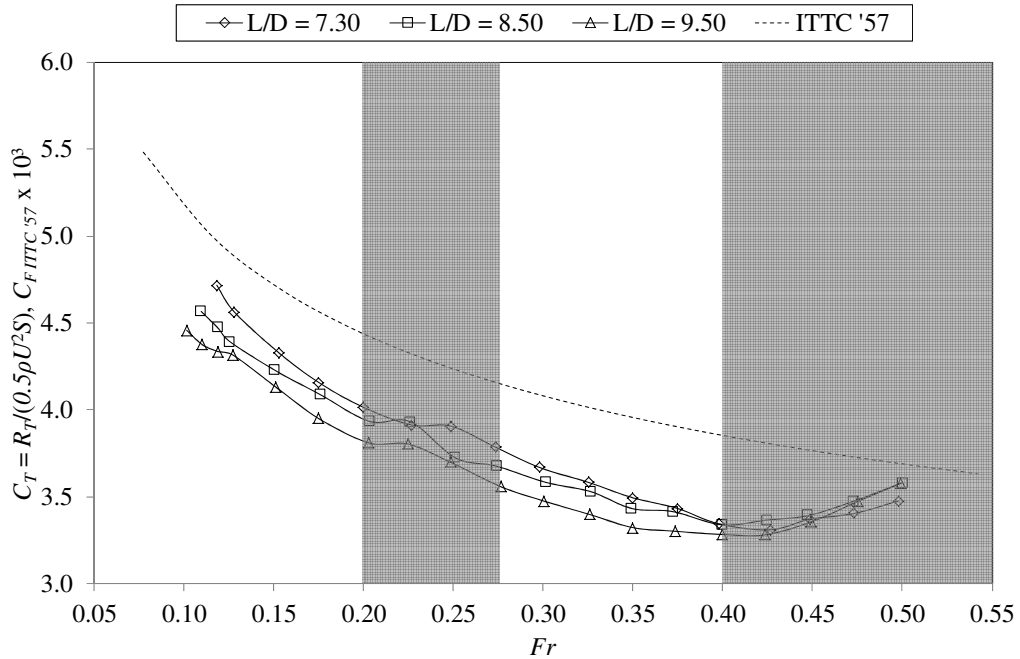


Figure 4-9 ITTC 1957 friction coefficient expansion line plotted with the total resistance coefficient for the Joubert models at $H^* = 3.46$: non-shaded regions indicate where wave making is considered to be negligible

The empirical formulations of Hendrix et al. (2001) and Hoerner (1965) are presented in Equation 4-2 and Equation 4-3 respectively and the formulations of form factor $(1+k)$ established by Hughes (1954) and Prohaska (1966) are presented in Equation 4-4 and Equation 4-5 respectively.

$$k = 0.6 \sqrt{\frac{D}{L^3}} + \frac{9D}{L^3} \quad \text{Equation 4-2}$$

$$k = 1.5\left(\frac{D}{L}\right)^{1.5} + 7\left(\frac{D}{L}\right)^3 \quad \text{Equation 4-3}$$

$$1 + k = \frac{C_T}{C_F} \quad \text{Equation 4-4}$$

$$\frac{C_T}{C_F} = (1 + k) + c \frac{Fr^4}{C_F} \quad \text{Equation 4-5}$$

A series of discrete data sets was used to calculate the form factor using Hughes' (1954) method. Sets of total resistance coefficient data of the three Joubert models were taken for the mid-tank submergence depth ($H^* = 3.46$) and for the speed ranges where wave making was considered to be negligible ($0.10 \leq Fr \leq 0.18$ and $0.30 \leq Fr \leq 0.40$). The resulting form factor for this data using Hughes' (1954) method is presented in Figure 4-10. It can be observed that there is a reduction in the form factor with an increase in Froude number. Nonetheless, this method indicates that the value of k is negative for the range of data analysed.

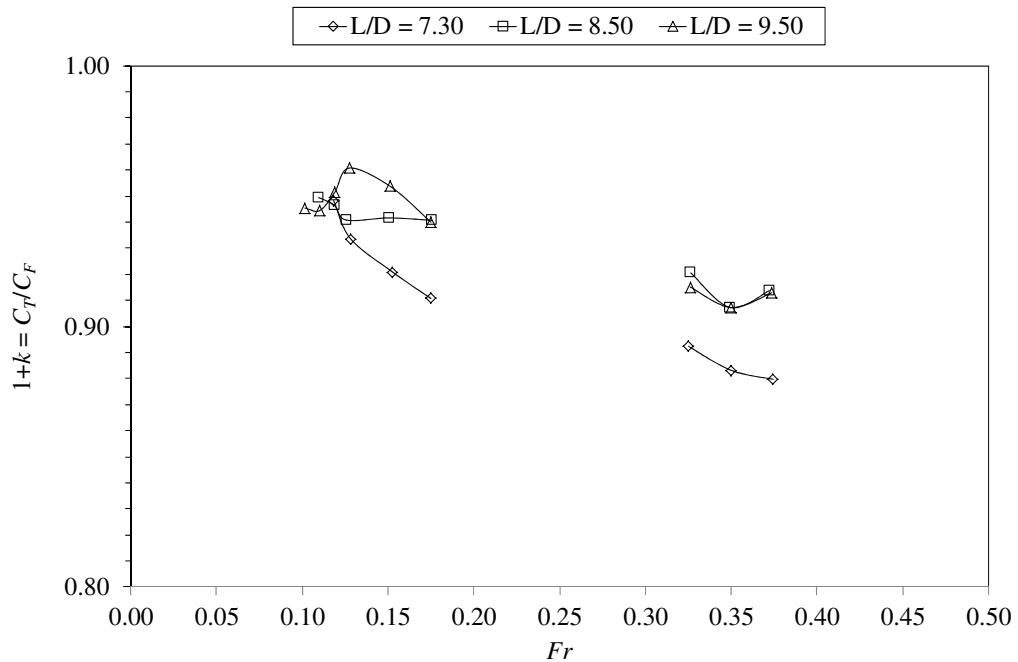


Figure 4-10 Hughes' (1954) method to determine the $(1+k)$ form factor for the three Joubert models at $H^* = 3.46$ and in the regions where wave making is considered to be negligible

The calculated form factors for the three Joubert models using these four methods are presented in Table 4-2. It can be seen that the empirical methods of Hendrix et al. (2001) and Hoerner (1965) both result in a positive k value and a form factor greater than 1. In comparison, the averaged values using Hughes' (1954) method for the two Froude speed ranges and the form factor determined using Prohaska's (1966) method result in a form factor less than 1. It can be inferred that this result affords a certain level of agreement with Jolliff's (1966) assertion that the use of an idealised two-dimensional friction line is invalid for the current application. Furthermore, without a body-specific friction expansion line the application of a generalised form factor is redundant. Subsequently, it is proposed that for a set of resistance measurements, such as those conducted in this research, it is more appropriate to establish a baseline resistance curve for each model where free-surface interaction is negligible or non-existent. This data set (curve) can then be used as the reference to determine the residuary resistance (surface interaction resistance effects) that is present in a shallowly submerged condition. While this approach is considered to provide a direct result at model scale, it does not resolve the issue of how to extrapolate the model scale results to a full scale condition using the form factor method. Resolving this issue is not addressed for the purpose of this research. Rather, only a comparison between the numerical simulation wave resistance coefficient data and the model scale residuary resistance coefficient data are attempted.

Table 4-2 Form factor ($1+k$) for streamlined body of revolution in subsonic flow for Joubert models using the methods of Hoerner (1965), Hendrix et al. (2001), Hughes (1954) and Prohaska (1966)

	<i>L/D</i> = 7.30	<i>L/D</i> = 8.50	<i>L/D</i> = 9.50
($1+k$) Hoerner (1965)	1.094	1.072	1.059
($1+k$) Hendrix et al. (2001)	1.570	1.382	1.288
($1+k$) _{μ} Hughes (1954) for $0.10 \leq Fr \leq 0.18$	0.928	0.944	0.949
($1+k$) _{μ} Hughes (1954) for $0.30 \leq Fr \leq 0.40$	0.885	0.914	0.912
($1+k$) Prohaska (1966)	0.942	0.947	0.953

4.4 STING MOUNT INTERFERENCE EFFECTS

By conducting constrained model tests it is impossible to avoid experiencing interference effects from the mounting system and the influence they have on the model's behaviour and consequently the measured data. As discussed in Chapter 5, the experiments conducted in this investigation utilised a horizontal sting and vertical post mounting arrangement to constrain the submarine model. The mounting arrangement required the truncation of the model's after-body in order to accommodate the sting diameter and with a margin of clearance (Figure 4-11).

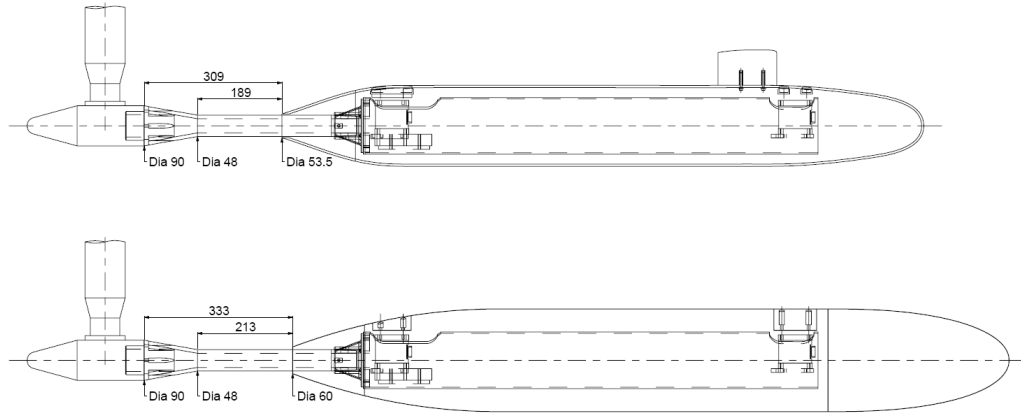


Figure 4-11 (Top) SUBOFF submarine model sting mounting arrangement: Full length geometry is 1.556 m; truncated model length is 1.440 m. (Bottom) Joubert submarine model sting mounting arrangement: Full length of $L/D = 7.30$ geometry is 1.679 m; truncated model length is 1.607 m. Dimensions in millimetres

The modification to the submarine model is relatively simple. For both the SUBOFF and Joubert models it is a case of truncating the length to accommodate the insertion of the sting support. Such a modification will result in a change in the drag and the longitudinal moments acting on the model due to the reduction in the hull area and the changed pressure field acting on the remaining after-body (Mackay, 1993).

In his study of the effects of sting interference on constrained submarine tests Mackay (1993) identified that there are several contributing mechanisms that lead to interference. The most prominent of these are related to the sting and the means by which it interfaces with the model. While the post is also considered to have an effect, its influence is typically much less significant. Mackay (1993) defines three forms of sting-borne interference:

- a. Overall disturbance: A disturbance to the bulk flow field caused by the presence of the sting directly downstream of the model and the pressure field that it generates;
- b. Local disturbance: Disturbances caused by localised flow effects that occur due to the interaction between the sting and the model's surfaces;
- c. Geometrical distortion: caused by the need to modify the model's geometry to accommodate the integration of the sting support.

In practice, these sources of interference will not act in isolation but influence each other. Mackay (1993) presents the formulations of several authors for quantifying the effects of overall interference.

Mackay (1993) presents a simplified criteria established by Cyran (1981) to determine the critical sting length and diameter. Through his work, Cyran observed that a sting diameter (d_s) of 0.40 to 0.73 times the base diameter (D_B) led to minimal interference effects. Cyran (1981) also concludes that the model's base pressure and consequently total drag is affected in configurations where the ratio of sting length to base diameter

(l_s/D_B) is less than 4 (Mackay, 1993). Using this approach, it is apparent that both the SUBOFF and Joubert models will experience some amount of interference as they exceed the criteria proposed by Cyran. The ratios of sting diameter to base diameter and sting length to base diameter for the SUBOFF and Joubert model to sting configurations are $d_s/D_B = 0.90$ and $l_s/D_B = 3.54$ and $d_s/D_B = 0.80$ and $l_s/D_B = 3.55$ respectively.

The more detailed formulation presented by Mackay (1993) is that of Tunnell, who uses a potential flow method to determine the pressure change at the trailing edge of the model due to the geometric characteristics of the sting. The pressure coefficient correction due to the longitudinal pressure gradient effects of the sting can be calculated for the model tests conducted in this investigation using Tunnell's formulation (Equation 4-6).

$$\Delta C_p = \left(\frac{D_s - d_s}{2L_s} \right) \left[\frac{1}{\sqrt{\left(\frac{2l_s}{d_s} \right)^2 + 1}} - \frac{\left(\frac{D_s}{d_s} \right)}{\sqrt{4 \left(\frac{L_s - l_s}{d_s} \right)^2 + 1}} \right] + \left(\frac{D_s - d_s}{2L_s} \right)^2 \left[\sinh^{-1} \left(\frac{2(L_s - l_s)}{d_s} \right) - \sinh^{-1} \left(\frac{-2l_s}{d_s} \right) \right] \quad \text{Equation 4-6}$$

Using Tunnell's formulation, the pressure coefficient correction (ΔC_p) for the SUBOFF and Joubert model geometries is 11.61×10^{-3} and 9.63×10^{-3} respectively. The geometric parameters used in Tunnell's formulation are listed in Table 4-3. The flare diameter and length dimensions pertain to the flared sting shaft as it transitions to interconnect with the vertical post (Figure 4-11).

Table 4-3 Geometric parameters used in Tunnell's formulation to determine the pressure coefficient correction due to sting interference

Parameter	SUBOFF Model	Joubert Models
Sting Diameter (d_s) [m]	0.048	0.048
Sting Length (l_s) [m]	0.189	0.213
Flare Diameter (D_s) [m]	0.090	0.090
Flare Length (L_s) [m]	0.120	0.120

Despite the efforts of several researchers who have investigated the sting interference phenomenon, it is still difficult to account for the combined effects described above. However, with the advancements made in computational fluid dynamics (CFD) methods it is now possible to complete comparative analyses to determine the effects of the presence of a sting on the hydrodynamic forces acting on a model. The results of such an approach have been used in this investigation to characterise and quantify the influence of the sting on the resistance force experienced by the model. The computations were conducted at the Australian Maritime College using the ANSYS CFX Reynolds Averaged Navier Stokes Equations (RANSE) CFD code (Cr  t  , 2013). The total drag force (resistance) was predicted using CFX for the bare hull

configuration for the three Joubert length-to-diameter models at submergence depths equivalent to $H^* = 1.02$ and 2.16. CFD computations of the truncated Joubert model with the sting were also completed for the $L/D = 7.30$ model at $H^* = 1.02$. The CFD simulations of the truncated model drag force show good correlation with the experimentally measured data (Figure 4-12).

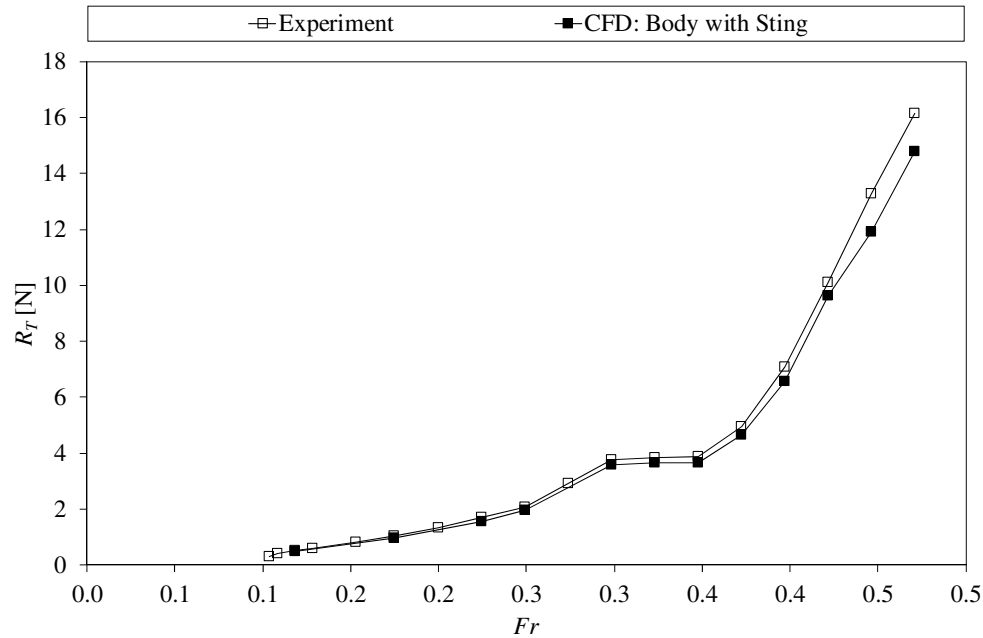


Figure 4-12 Comparison between the CFD simulation and experimentally measured total resistance force of the Joubert $L/D = 7.30$ bare hull body with the sting at $H^* = 1.02$

The influence of the sting on the total resistance coefficient was evaluated by calculating the relative difference between the CFD Joubert bare hull body data and the corresponding experimental (bare hull with sting) data. An example of the evaluation approach is shown in Figure 4-13. For each of the cases evaluated the relative difference was observed to fluctuate slightly across the Froude speed range; however, there were no clearly identifiable trends at this level. The mean of the relative differences was calculated for each of the model and submergence depth conditions simulated (Table 4-4). The results indicate that there is moderate variability in the influence of the sting due to the model length, submergence depth and forward speed. Based on these results it is asserted that the effect of the sting interacting with the truncated model reduces the total resistance of the bare hull-only geometry by between 10 and 20 percent and on average by 15 percent.

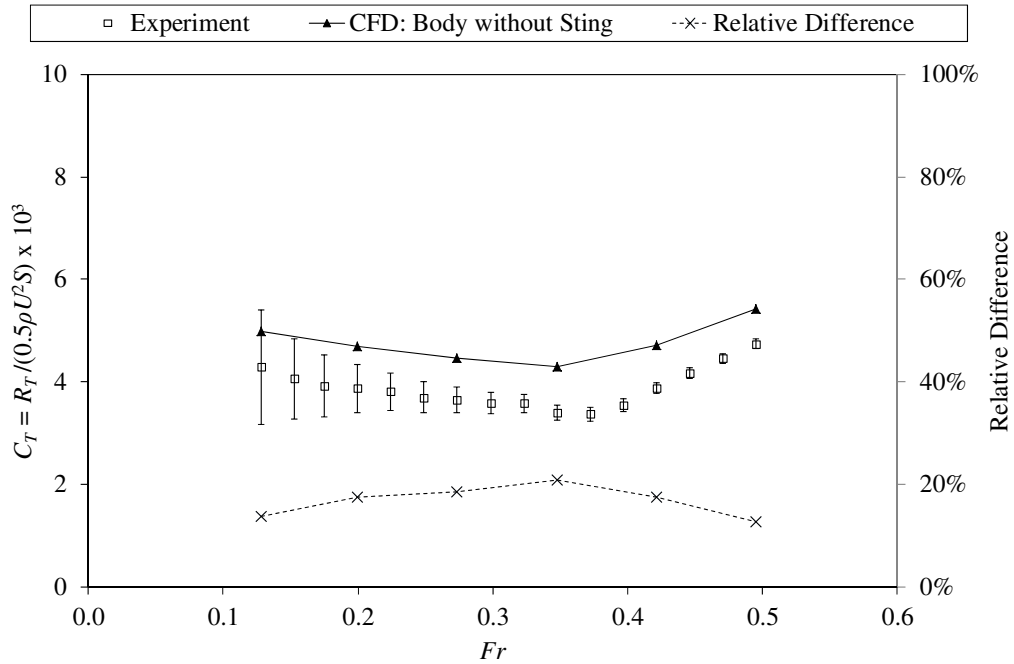


Figure 4-13 CFD simulated results of the total resistance coefficient of Joubert $L/D = 7.30$ bare hull geometry without the sting at $H^* = 2.16$ compared to the experimentally measured data of the bare hull model with the sting

Table 4-4 Quantified sting interference effects on total resistance coefficient (mean)

Length to Diameter (L/D)	Submergence Depth (H^*)	Mean Relative Difference ($\mu \pm \sigma$) [%]
7.30	1.02	19.71 ± 4.06
7.30	2.16	16.84 ± 3.03
8.50	1.02	11.10 ± 1.57
9.50	1.02	13.38 ± 3.11
9.50	2.16	13.23 ± 2.18

4.5 BLOCKAGE AND BOUNDARY INTERACTION

An evaluation of model blockage effects was completed using the findings of Achenbach (1974). Achenbach's investigation into the blockage effects on a sphere in a channel indicate that blockage effects become non-negligible when the ratio of the sphere's diameter to the channel width (D/W) exceeds 0.30. In the case of the SUBOFF and Joubert models used in this research the ratio of model diameter to towing tank width is significantly less than the $D/W = 0.30$ threshold (Table 4-5).

Table 4-5 Ratio of model diameter to towing tank width

Parameter	SUBOFF Model	Joubert Models
Maximum diameter (D) [m]	0.181	0.230
Width of AMC towing tank (W) [m]	3.55	3.55
Ratio of model diameter to tank width (D/W)	0.05	0.06

The same approach was used to evaluate the range of submergence depths tested in this research. For the deepest submergence depths tested using the SUBOFF and Joubert models the ratio of half model diameter (model radius) to centreline stand-off distance from the tank base was found to be well below the threshold limit of 0.30 (Table 4-6).

Table 4-6 Ratio of model radius to centreline stand-off distance from the towing tank base

Parameter	SUBOFF Model	Joubert Models
Model radius ($D/2$) [m]	0.091	0.115
Model centreline stand-off distance (z) [m]	0.504 ($H^* = 5.50$)	0.903 ($H^* = 3.46$)
Ratio of model radius to stand-off distance ($D/2z$)	0.18	0.13

Based on these results, it was concluded that there are no appreciable towing tank blockage effects influencing the model test results.

5 EXPERIMENTAL INVESTIGATION

5.1 EXPERIMENTS AND OBJECTIVES

A series of experiments was conducted to investigate the effects of submergence depth, velocity and length-to-diameter ratio on the hydrodynamic forces and moments acting on a submerged axisymmetric body and the surface wave profile it generates. Axial, lateral and vertical forces were directly measured using two 6 component strain gauge load cells to quantify the resistance and lift forces, while the trimming moment was calculated using the two vertical force measurements. Wave profile measurements were made using an array of four resistance type static wave probes arranged in a span-wise direction across one half of the towing tank. All tests were conducted in the Australian Maritime College's towing tank facility.

Only the experimental setup and procedure used in the Joubert length-to-diameter experiment are discussed in detail here as these tests were designed, planned and conducted exclusively by the author with assistance from an AMC undergraduate student. The SUBOFF experiment results presented in this thesis are the result of a collaboration between the author and several AMC undergraduate students. The author designed and directed the experiments in partnership with the students and their academic supervisors, although the actual tests were conducted by the students. For further information on the SUBOFF experiments and their results refer to the following publications:

- a. SUBOFF bare hull configuration tests (Wilson-Haffenden, 2009)
- b. SUBOFF hull and sail configuration tests (Neulist, 2011)

5.2 PHYSICAL MODELS: SUBOFF AND JOUBERT GEOMETRIES

Five unique model configurations were tested as part of this research. The models are the DARPA SUBOFF submarine geometry (SUBOFF) and three length-to-diameter configurations of the Joubert submarine geometry. The SUBOFF was tested in the bare hull and hull with sail configurations (Figure 5-1). A detailed description of the geometry is presented by Groves et al. (1989). The length-to-diameter of the SUBOFF geometry is 8.60.

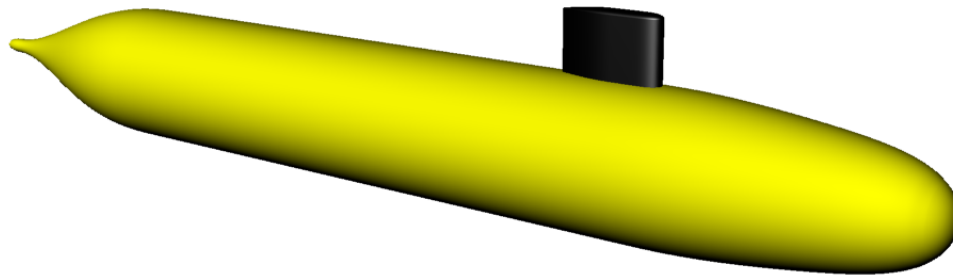


Figure 5-1 SUBOFF submarine geometry (hull with sail configuration)

The Joubert geometry is a generic conventional submarine configuration that has been developed by the Australian Department of Defence's Defence Science and Technology Organisation (DSTO) in collaboration with Emeritus Professor Peter Joubert (Anderson et al., 2012). The baseline submarine geometry comprises an axisymmetric body of revolution as the hull, a blended casing, a sail and X-plane aft control surfaces (Figure 5-2). The baseline geometry has a length-to-diameter ratio of 7.30. In this configuration the hull possesses a parallel mid-body section that is approximately 45% of the overall length and commences at $x/L = 0.23$ aft of the leading edge of the hull (Figure 5-3). The bow and tail shapes are of elliptical and parabolic form, respectively. The lines plan of the Joubert hull geometry is shown in Figure 5-4.

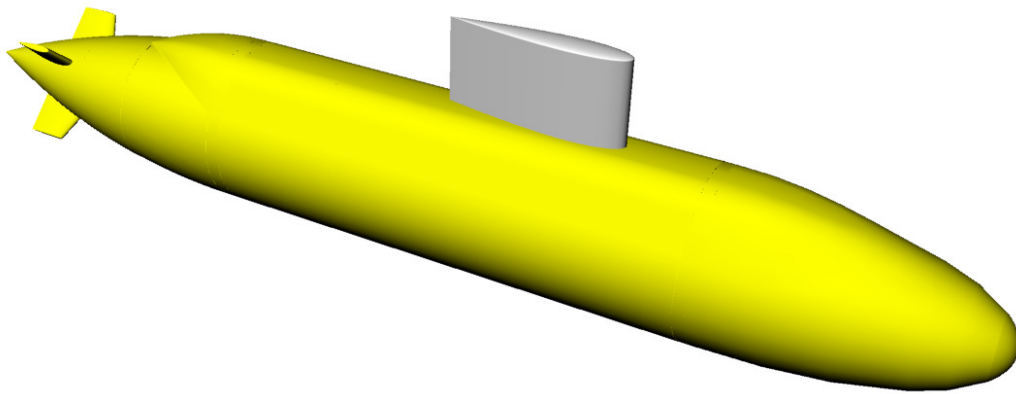


Figure 5-2 Complete Joubert submarine geometry (not tested in this experimental research)

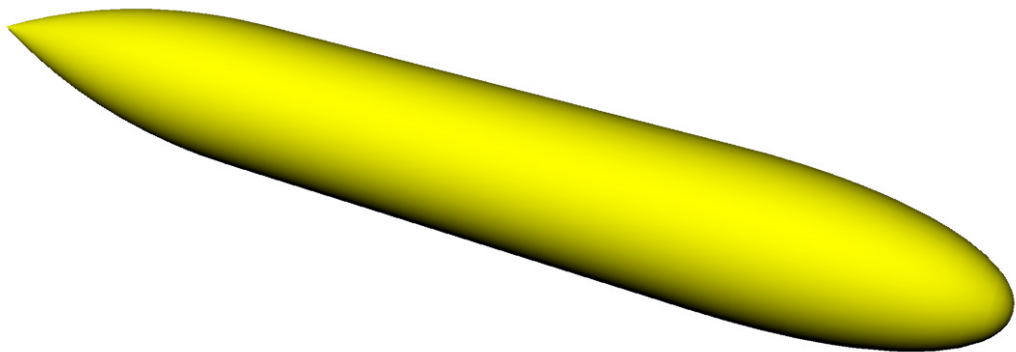


Figure 5-3 Baseline Joubert axisymmetric hull geometry $L/D = 7.30$

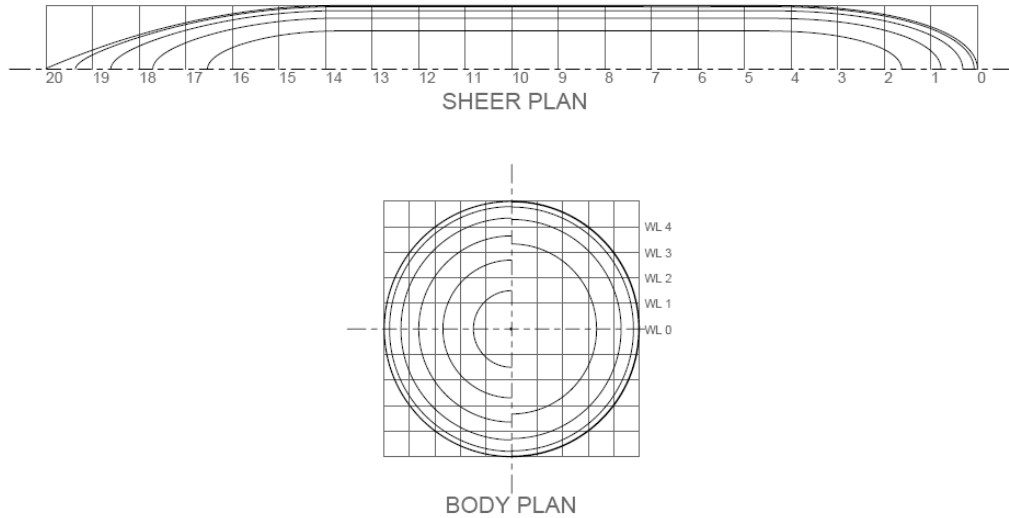


Figure 5-4 Baseline Joubert axisymmetric hull geometry $L/D = 7.30$ lines plan

The experimental model of the Joubert geometry used in this research has a maximum hull diameter of 0.23 metres. The $L/D = 8.50$ and $L/D = 9.50$ configurations were developed by inserting a section of parallel midbody aft of the termination of the bow entrance. In effect, the baseline hull ($L/D = 7.30$) and its two length-to-diameter derivatives possess the same maximum hull diameter, bow shape and tail shape. The Joubert and SUBOFF model principal dimensions are presented in Table 5-1.

Table 5-1 Model principal dimensions (*SUBOFF hull and sail)

Parameter	SUBOFF <i>L/D = 8.60</i>	Joubert <i>L/D = 7.30</i>	Joubert <i>L/D = 8.50</i>	Joubert <i>L/D = 9.50</i>
Overall Length (<i>L</i>) [m]	1.556	1.679	1.955	2.185
Diameter (<i>D</i>) [m]	0.181	0.230	0.230	0.230
Truncated Model Length (<i>L_M</i>) [m]	1.440	1.607	1.883	2.113
Start of parallel midbody aft of leading edge [m]	0.324	0.383	0.383	0.383
End of parallel midbody aft of leading edge [m]	1.185	1.149	1.425	1.655
Wetted Surface Area (<i>S</i>) [m ²]	0.763 0.777*	1.041	1.238	1.405
Hull Prismatic Coefficient (<i>C_p</i>)	0.796	0.785	0.815	0.835

The SUBOFF and Joubert models used in the experiments are manufactured from glass fibre reinforced polymer (GRP) with an enamel paint surface finish. The nominal wall thickness of the hull model is 5 millimetres. The dimensional tolerance of the models is ± 0.001 metres.

5.3 TEST FACILITY AND EQUIPMENT

5.3.1 AUSTRALIAN MARITIME COLLEGE TOWING TANK

All tests were conducted in the AMC towing tank facility. The submarine model was sting mounted to the towing tank carriage using the horizontal planar motion mechanism (HPMM) and a vertical post arrangement (Figure 5-5). It is important to note that the HPMM was used only as a mounting interface. The vertical post is constructed such that it can be extended or shortened to accommodate the different test submergence depths while remaining structurally rigid. The test runs were conducted along the lateral centreline of the tank. The general specifications of the towing tank are presented in Table 5-2.

Table 5-2 AMC Towing Tank general specifications

Length	100 m
Width	3.55 m
Water Depth	0 to 1.60 m (Standard = 1.50 m)
Model Towing Carriage Speed	0 to 4.60 m/s
Typical Model Lengths	1.00 to 2.50 m

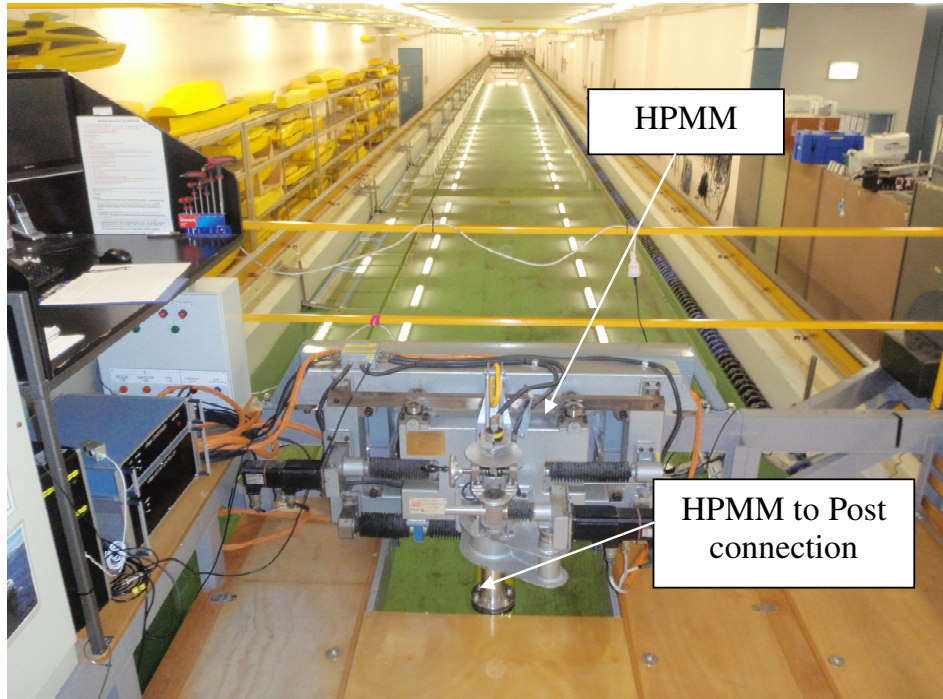


Figure 5-5 AMC Towing tank and carriage with the HPMM, model (post-sting) mount and SUBOFF model attached (obscured from view by post connection)

5.3.2 FORCE BALANCE AND MOUNTING CONFIGURATION

Each of the models was mounted to an internal force balance (dynamometer) that was connected using a sting and post arrangement. The force balance (Figure 5-6) comprised a cylindrical strong-back and two six component load cells. The load cells were affixed to the strong-back and model to provide an interface that allowed the three axial forces (F_x , F_y , F_z) experienced by the model to be measured and recorded. The SUBOFF and Joubert models were manufactured in sections so as to allow the force balance to be inserted into the main section of the model. The model to force balance connection arrangement is illustrated in Figure 5-7 and Figure 5-8.

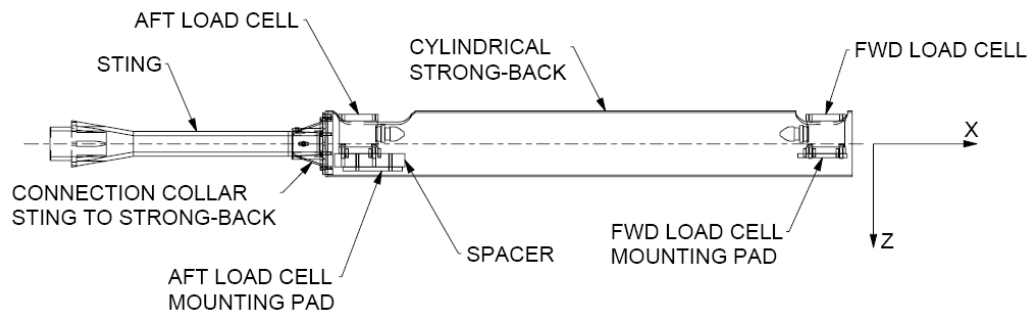


Figure 5-6 Force balance with sting attachment

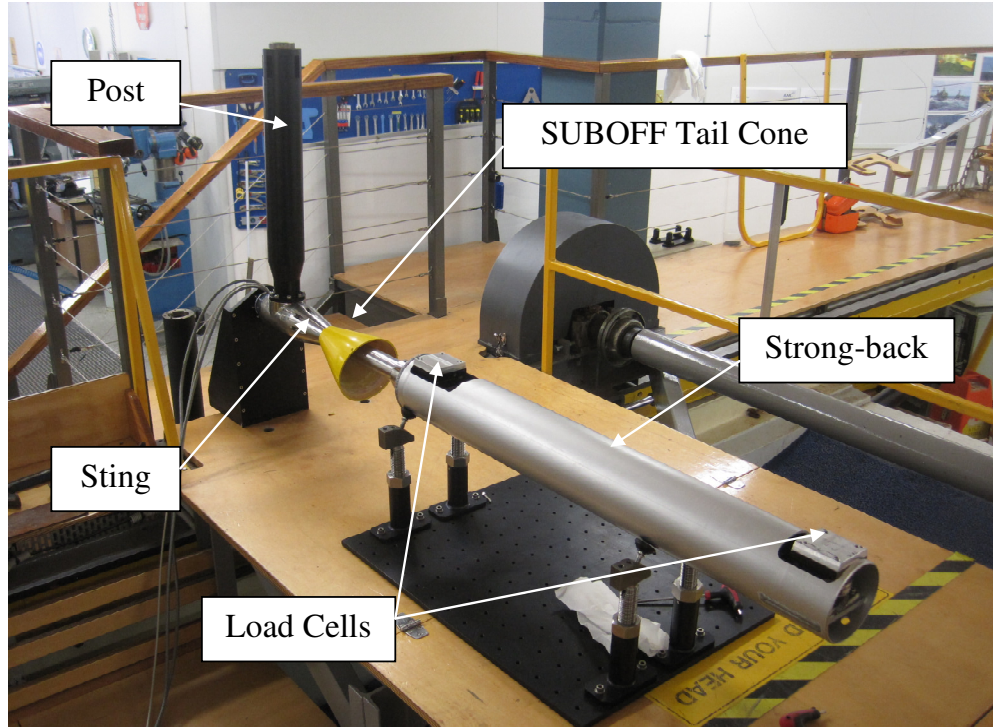


Figure 5-7 Force balance with sting and post attachment and SUBOFF tail cone section prior to connecting the SUBOFF model's forward (main) section

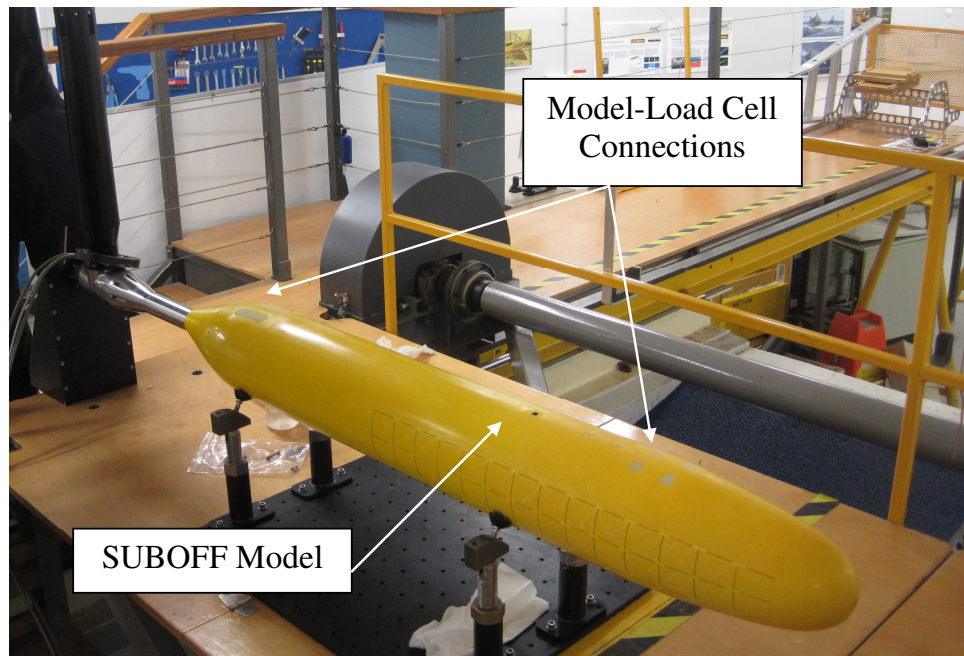


Figure 5-8 SUBOFF hull-only test model connected to the force balance and sting and post system. This represents the test configuration prior to connecting the post to the towing tank carriage using the HPMM

5.3.3 POST ATTACHMENT

The submergence depth of the model's centreline axis was set using a series of post inserts (Figure 5-9). The same set of inserts were used in the SUBOFF and Joubert test programs. Subsequently, the non-dimensional submergence depth (H^*) was not common to the SUBOFF and Joubert model geometries due to their differing maximum hull diameters and the fixed lengths of the post inserts.



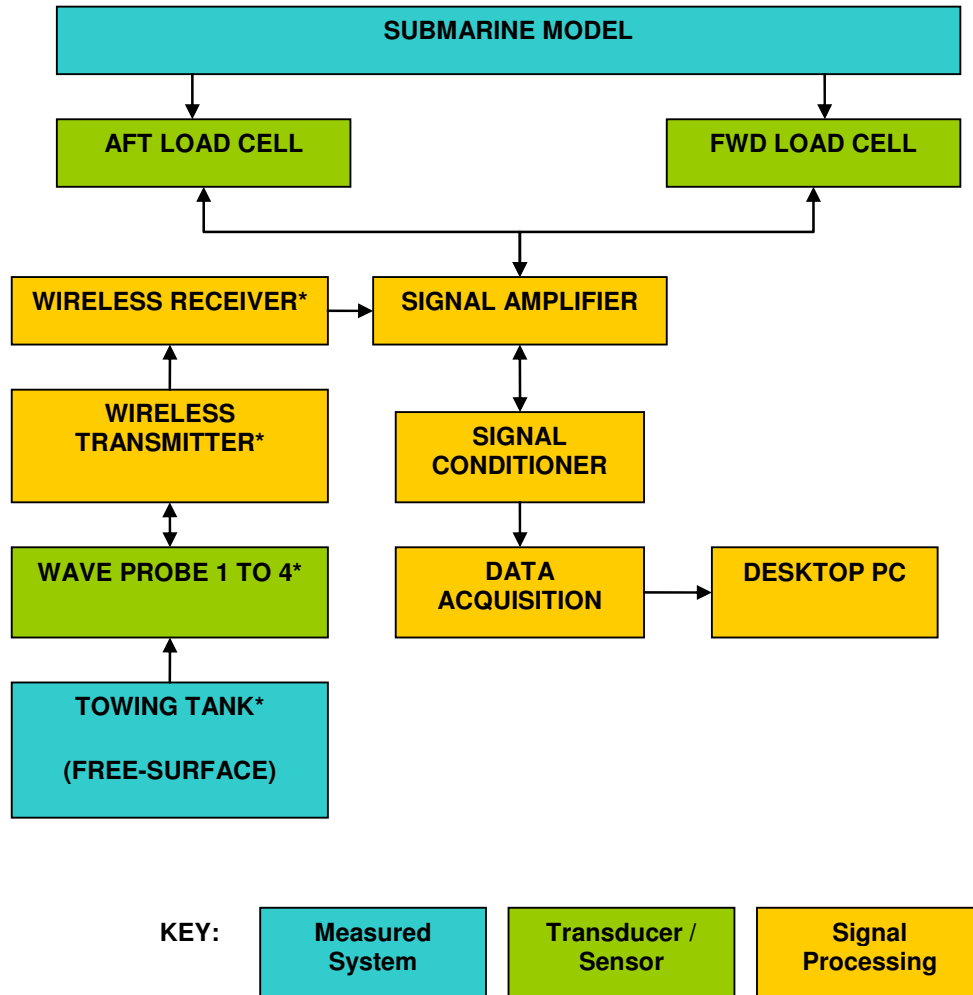
Figure 5-9 Post attachment insert: From left to right: $H^* = 1.10, 1.65, 2.20, 2.75$ and 3.30 for the SUBOFF model and $H^* = 1.02, 1.30, 2.16, 2.60$ and 3.46 for the Joubert models

5.3.4 MEASUREMENT SYSTEM

An integrated measurement system was used to measure and record the body forces and free-surface wave heights during the experiments (Figure 5-10). No wave height measurements were conducted for the SUBOFF model tests. While the force measurement system used in the SUBOFF tests resembles that shown in Figure 5-10, the type and model of the load cells used varied. For specific information on the test equipment used in the SUBOFF experiments refer to Wilson-Haffenden (2009) and Neulist (2011).

The Joubert experiment measurement system comprised two AMTI six component strain gauge load cells: one of model AMTI-M3631 mounted at the forward end of the force balance and one of model AMTI-M3633 mounted at the aft end of the force balance. The range of the load cells are 222 Newtons in the x and y axes (longitudinal and lateral) and 444 Newtons in the z axis (vertical). The load cells were connected to a Matronix signal amplifier and filter unit and then to a Measurements Group Model 2150 strain gauge signal conditioner unit. The values of the amplifier and signal conditioner gains and the filter settings for each test configuration are presented in Appendix B. It was noted that the forces that would be measured by the load cells were small relative to their range. An investigation was conducted to identify a commercial off-the-shelf load cell with a measurement range more appropriate for the proposed application. Despite the efforts of the author and the AMC, no solution was able to be identified, irrespective of cost.

Four resistance type fluid level sensors (static wave probes) were arranged in a span-wise array across the half-width of the towing tank to measure the change in free-surface elevation of the propagated waves (Figure 5-11). The array was positioned at approximately two thirds of the tank length from the carriage starting point. The four wave probe signals were sent via a wireless (transmitter/receiver) network to the towing tank carriage data acquisition system. The wave probe signals were processed using the Matronix amplifier and filter unit. The load cell and wave probe signals were recorded using a National Instruments PC acquisition board and an AMC developed Labview acquisition software program.



* Joubert tests only

Figure 5-10 Body force and free-surface wave height measurement system block diagram.

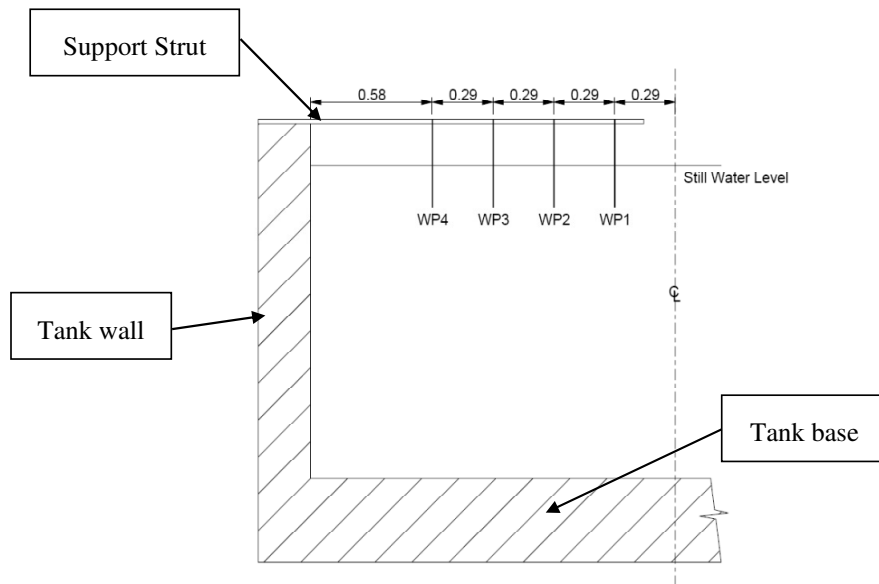


Figure 5-11 Wave probe setup across half-width of towing tank (centreline section) dimensions in metres

5.3.5 EQUIPMENT CALIBRATION

The two strain gauge load cells were calibrated on the bench prior to the commencement of testing and at each instance when the model was removed entirely from the towing tank. The load cells were calibrated in the direction of the three principal translational axes and in both the positive and negative directions using a series of standard test weights. The load cell calibration and correlation coefficient data is presented in Appendix B. The response of the two load cells was observed to be linear through the calibration range.

The wave probes were calibrated at the start of each day of testing. The probes were calibrated by raising and lowering them into the tank water at specific positions relative to the still water level and recording the voltage output signal. The wave probe responses were also observed to be linear through the calibration and measurement range. The wave probe calibration data is presented in Appendix B.

5.3.6 TRANSITION DEVICE

A Hama type transition strip was affixed to the nose section of the Joubert model at 0.084 metres aft of the leading edge (Figure 5-12). This distance corresponds to $x/L = 0.05$ of the overall length of the baseline ($L/D = 7.30$) model. This location was used for the longer $L/D = 8.50$ and $L/D = 9.50$ model configurations. A detailed discussion of the transition strip geometry is presented in Section 4.2.

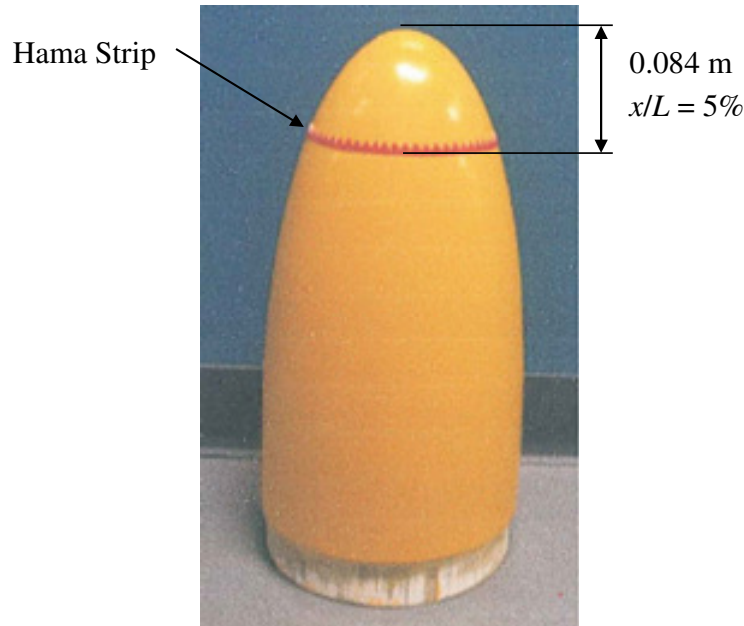


Figure 5-12 Joubert model nose section with Hama strip $k = 0.55\text{mm}$ affixed 0.084m aft of the leading edge.

5.4 TESTING PROGRAM

The body of research conducted by the author comprised four discrete experiments, each of which was conducted in collaboration with undergraduate engineering students at the Australian Maritime College. A brief overview of the four experiments that were conducted is presented in the following paragraphs:

- a. In 2009 an initial set of tests was completed using the bare hull SUBOFF model geometry to observe and measure the wave resistance of a submerged axisymmetric body (see Wilson-Haffenden (2009)). In these tests the SUBOFF model was fitted to the strong-back with one six component load cell mounted at the forward mounting location and a low friction slider fitted at the aft mounting location. The objective of this research was to investigate the effects of submergence depth and forward velocity on the wave making resistance of a streamlined body of revolution moving in close proximity to the free-surface. Wilson-Haffenden (2009) completed tests at non-dimensional depths of $H^* = 1.10, 1.30, 2.20, 3.30, 4.40$ and 5.50 and across a Froude speed range of $0.13 \leq Fr \leq 0.67$.
- b. In 2010 the SUBOFF hull and sail configuration was tested by Van-Steel (2010) using the same methodology and setup as Wilson-Haffenden (2009). The objective of this research was to investigate the influence of the sail on the wave making resistance of the submerged body.
- c. In 2011 Neulist (2011) extended the work of Van-Steel (2010) and tested the SUBOFF hull and sail configuration in the shallow submergence depth region ($H^* = 1.10, 1.65, 2.20, 2.75,$ and 3.30) and across a lower range of Froude numbers ($0.05 \leq Fr \leq 0.51$). The depth and speed range tested was focussed on the typical range of operating conditions experienced by conventional

submarines when operating in a littoral region or conducting operations that require near-surface navigation. Neulist (2011) in collaboration with the author also investigated the performance of Hama strip transition devices and their application to small scale submerged streamlined body resistance testing.

- d. In 2012 the author completed a comprehensive test program using the Joubert bare hull submarine geometry. The objective of the experiment was to investigate the effects of submergence depth, forward speed and body length-to-diameter ratio on the wave making resistance, lift force and trimming moment acting on the shallowly submerged body. This experiment forms the principal focus of the research presented in this thesis.

5.4.1 TEST MATRIX: SUBMERGENCE DEPTH, FORWARD VELOCITY AND TRANSITION DEVICE

Axial and vertical force and free-surface wave profile measurements were conducted at a series of submergence depths and forward velocities for the three Joubert model configurations. The depths tested spanned from 0.20 metres to 1.00 metre, where the depth is measured from the free-surface to the centreline of the submarine hull as illustrated in Figure 3-12. The submergence depth is non-dimensionalised using Equation 3-8 and the hull diameter (0.23 m). The test matrix executed in the Joubert length-to-diameter model experiments is presented in Table 5-3.

Table 5-3 Joubert length-to-diameter experiment test matrix: submergence depth, forward velocity and transition device

Model Configuration (L/D)	Non-dimensional Depth (H^*)	Froude Number (Fr)	Boundary Layer Transition Device
7.30	1.02	0.100	No Device ($H^* = 3.46$ only) Hama Strip: $x = 0.084\text{m}$; $k = 0.55\text{mm}$
	1.30	0.108	
	2.16	0.117	
	2.60	0.125	
	3.46	0.150	
8.50	1.02 1.30 2.16 3.46	0.175	Hama Strip: $x = 0.084\text{m}$; $k = 0.55\text{mm}$
		0.200	
		0.225	
		0.250	
		0.275	
9.50	1.02 1.30 2.16 3.46	0.300	Hama Strip: $x = 0.084\text{m}$; $k = 0.55\text{mm}$
		0.325	
		0.350	
		0.375	
		0.400	
		0.425	
		0.450	
		0.475	
		0.500	

5.5 TEST PROCEDURE

Once the model and sensor system had been connected to the towing tank carriage the following activities were completed to conduct the tests:

The transverse alignment (drift angle) of the model was determined by reviewing the steady state side force measured during a test run. Any misalignment was corrected for by rotating the post/model. This process was repeated to converge on a minimal side force and correct model alignment. The threshold for model alignment was that the measured side force was no greater than $\pm 5\%$ or the total resistance force. The average misalignment of all of the qualified test runs conducted is $\pm 0.61\%$ with a standard deviation of 0.62% . The alignment was monitored during the subsequent test runs. The alignment process was repeated whenever there was a change in the submergence depth or model configuration (L/D).

Once the model was aligned, the resistance test runs were conducted. The standard AMC resistance test run process was followed. In summary, a test run was started after 15 minutes of the carriage returning the start position. This was done to allow the the tank free-surface to settle and the turbulence and flow within the fluid to dissipate and decay. At the start of each test run the carriage on-board power distribution system was activated and a zero sensor reading was recorded for each of the sensors. After recording the zero, the carriage drive system was activated. Moving data acquisition was activated once the carriage had reached a steady state velocity.

On completion of the test run, and prior to the following run, the recorded sensor signal data was visually inspected to identify any abnormalities such as a sensor failure, a measurement signal exceeding the voltage range or excessive non-linearity in the data. No data acquisition system abnormalities were observed during the experiment. In the case of the load cell force measurements, a window of the recorded data was selected to determine the average (steady state) measurement value.

At least two test runs were repeated for each depth and model configuration combination to evaluate the precision of the sensor and the repeatability of the test set-up. The repeat test runs were not conducted sequentially. A series of ten repeat test runs was completed for the $L/D = 7.30$ model at $H^* = 3.46$ and $Fr = 0.40$ to determine the statistical variance in the test measurement. This data is discussed in further detail in Section 5.7.2.

5.6 DATA PROCESSING

The measured sensor signal data were processed to determine the steady state values of the force measurements. All of the load cell force measurements (voltage signal multiplied by the calibration factor minus the zero value) are determined in grams.

5.6.1 RESISTANCE AND LIFT FORCE MEASUREMENTS

The total resistance (drag) force was determined by the summation of the two axial force measurements (Equation 5-1) measured on the forward and aft load cells. Similarly, the total vertical (lift) force is determined by the summation of the two vertical force measurements (Equation 5-2). The trimming moment is calculated by taking moments about the longitudinal midships location (x_{MS}). The forward and aft load cell vertical force measurements are multiplied by their respective levers and summed to give the total trimming moment (Equation 5-3). The relative distances between the vertical axis of the load cells and the midship location (levers) for the three Joubert model configurations are presented in Table 5-4. An illustration of the lever convention is presented in Figure 5-13.

$$R_T = F_{X_F} + F_{X_A} \quad \text{Equation 5-1}$$

$$F_Z = F_{Z_F} + F_{Z_A} \quad \text{Equation 5-2}$$

$$M_Z = F_{Z_F} \cdot x_{F-MS} + F_{Z_A} \cdot x_{A-MS} \quad \text{Equation 5-3}$$

Table 5-4 Trimming moment levers relative to midships for the Joubert model configurations

Model Configuration (L/D)	7.30	8.50	9.50
Forward lever (x_{F-MS}) [m]	0.360	0.202	0.107
Aft lever (x_{A-MS}) [m]	0.545	0.703	0.798

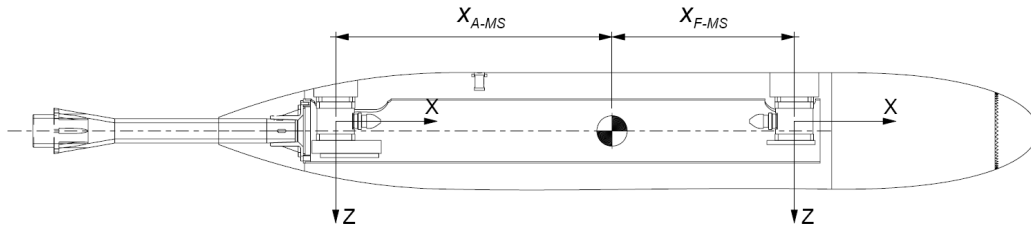


Figure 5-13 Definition of trimming moment levers relative to midships (MS)

5.6.2 DATA REDUCTION

Unless otherwise stated, the data reduction equations of the total resistance coefficient, lift force coefficient and trimming moment coefficient, used to non-dimensionalise the test measurement data, are defined by Equation 5-4, Equation 5-5 and Equation 5-6 respectively.

$$C_T = \frac{R_T}{0.5\rho \cdot U^2 \cdot S} \quad \text{Equation 5-4}$$

$$C_L = \frac{F_Z}{0.5\rho \cdot U^2 \cdot S} \quad \text{Equation 5-5}$$

$$C_M = \frac{M}{0.5\rho \cdot U^2 \cdot S \cdot L} \quad \text{Equation 5-6}$$

Despite the observations made by Farell and Güven (1973) pertaining to the influence of the free-surface on a shallowly submerged body's viscous resistance (its variation with velocity and relatively large contribution), it was decided to use an idealised, model-specific, deeply submerged resistance coefficient curve to determine the residuary resistance of the experimental resistance data measured as part of this research. The idealised curve is based on the ITTC 1957 friction coefficient line and adjusted (shifted vertically) such that it is coincident with the low speed total resistance coefficient data. The residuary resistance coefficient was determined by subtracting the corresponding values of the idealised frictional resistance coefficient ($C_{F'}$) from the total resistance coefficient (C_T) as indicated in Equation 5-7. The adjustment coefficient (ΔC_F) is determined for each configuration of model length-to-diameter and submergence depth. The coefficient is constant for each configuration, but varies between the different configurations.

$$C_R = C_T - C_{F'} = C_T - \left(C_{F_{ITTC'57}} - \Delta C_F \right) \quad \text{Equation 5-7}$$

5.7 UNCERTAINTY ANALYSIS AND TEST REPEATABILITY

5.7.1 GENERAL UNCERTAINTY ANALYSIS

A general uncertainty analysis was conducted using the error propagation method presented by ITTC (1999 and 2002a). The uncertainty equations for the total resistance coefficient, lift force coefficient and trimming moment coefficient are presented in Equation 5-8, Equation 5-9 and Equation 5-10 respectively. Details of their derivation and tables of the measurement uncertainty are presented in Appendix C.

$$U_{C_T} = C_T \cdot \sqrt{\left(\frac{U_{R_T}}{R_T}\right)^2 + \left(-\frac{U_\rho}{\rho}\right)^2 + \left(-2\frac{U_U}{U}\right)^2 + \left(-\frac{U_S}{S}\right)^2} \quad \text{Equation 5-8}$$

$$U_{C_L} = C_L \cdot \sqrt{\left(\frac{U_{F_X}}{F_X}\right)^2 + \left(-\frac{U_\rho}{\rho}\right)^2 + \left(-2\frac{U_U}{U}\right)^2 + \left(-\frac{U_S}{S}\right)^2} \quad \text{Equation 5-9}$$

$$U_{C_M} = C_M \cdot \sqrt{\left(\frac{U_M}{M}\right)^2 + \left(-\frac{U_\rho}{\rho}\right)^2 + \left(-2\frac{U_U}{U}\right)^2 + \left(-\frac{U_S}{S}\right)^2 + \left(-\frac{U_L}{L}\right)^2} \quad \text{Equation 5-10}$$

5.7.2 TEST REPEATABILITY AND PRECISION

An evaluation of the precision and repeatability of the test procedure and measurement system was completed by conducting 10 repeat tests for a single forward speed, submergence depth and model configuration. The tests were conducted during the test runs for the $L/D = 7.30$ model configuration at $H^* = 3.46$ and at $Fr = 0.40$. The repeat test runs were interspersed among the other speed runs; therefore no two repeat runs were conducted in succession. The test data and the absolute force data for the ten repeat runs and their mean (μ) and standard deviation (σ) are presented in Table 5-5 and Table 5-6.

Table 5-5 Test precision and repeatability evaluation: test data

Run	U [m/s]	F_{XF} [N]	F_{YF} [N]	F_{ZF} [N]	F_{XA} [N]	F_{YA} [N]	F_{ZA} [N]
1	1.61	2.298	0.077	1.524	2.220	-0.090	0.781
2	1.61	2.313	0.097	1.516	2.194	-0.108	0.784
3	1.61	2.335	0.099	1.515	2.181	-0.102	0.823
4	1.61	2.350	0.099	1.48	2.175	-0.105	0.844
5	1.61	2.309	0.070	1.522	2.201	-0.080	0.772
6	1.61	2.324	0.098	1.496	2.195	-0.106	0.799
7	1.62	2.097	0.096	1.337	2.460	-0.104	0.862
8	1.62	2.217	0.115	1.447	2.359	-0.109	0.814
9	1.62	2.163	0.080	1.439	2.365	-0.099	0.816
10	1.62	2.227	0.079	1.533	2.316	-0.090	0.747
μ	1.614	2.263	0.091	1.481	2.267	-0.099	0.804
σ	0.005	0.084	0.014	0.060	0.100	0.010	0.035
σ/μ	0.32%	3.71%	14.92%	4.05%	4.42%	9.65%	4.32%

Table 5-6 Test precision and repeatability evaluation: total force data

Run	R_T [N]	F_Y [N]	F_Z [N]
1	4.518	-0.013	2.304
2	4.507	-0.011	2.300
3	4.517	-0.003	2.339
4	4.526	-0.006	2.324
5	4.510	-0.010	2.294
6	4.519	-0.008	2.295
7	4.557	-0.008	2.200
8	4.575	0.005	2.261
9	4.527	-0.019	2.255
10	4.543	-0.011	2.280
μ	4.530	-0.008	2.285
σ	0.022	0.006	0.039
σ/μ	0.48%	77.11%	1.72%

The test results and the statistical measures indicate that the experiment setup produces precise and repeatable data for the total resistance (R_T) and total vertical (lift) force (F_Z). Despite this, there is a greater level of variability observed in the individual load cell measurement data, indicating that there may be some hysteresis in the system that influences the load sharing between the forward and aft load cells. This is more easily observed in Figure 5-14, Figure 5-15 and Figure 5-16. There is a considerably greater amount of variability in the side force measurement data. Nonetheless, the level of precision in the total side force measurement is considered acceptable due to the absolute magnitude of the measured data, the measurement range of the load cells and the fact that the data is used to verify the model's alignment with the centreline axis of the towing tank.

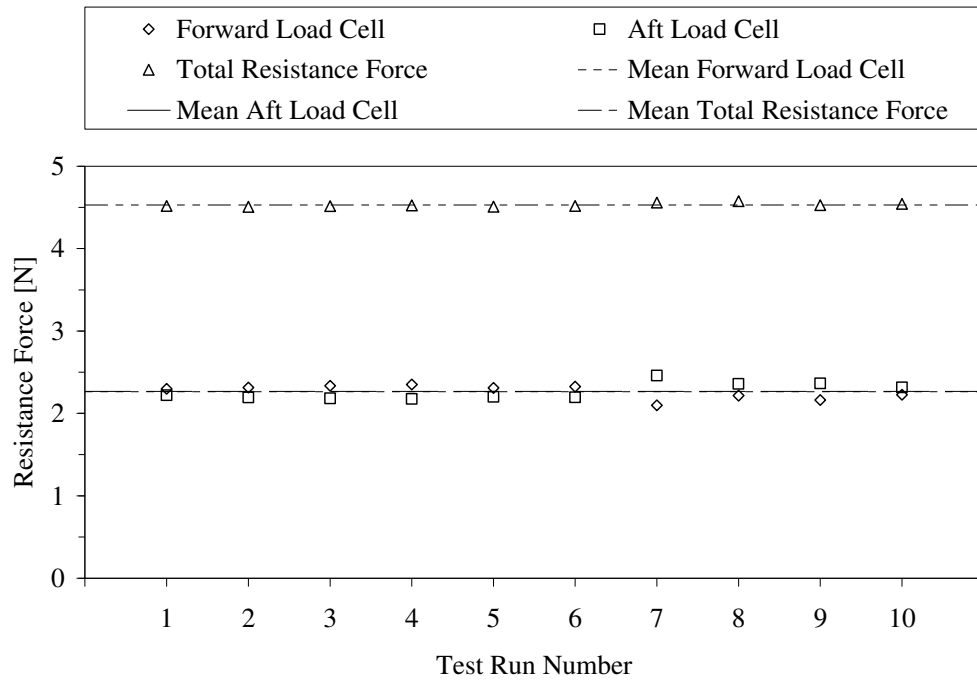


Figure 5-14 Repeatability and precision analysis: Individual load cell and combined total resistance (drag) force for the Joubert $L/D = 7.30$ model at $H^* = 3.46$ and $Fr = 0.40$

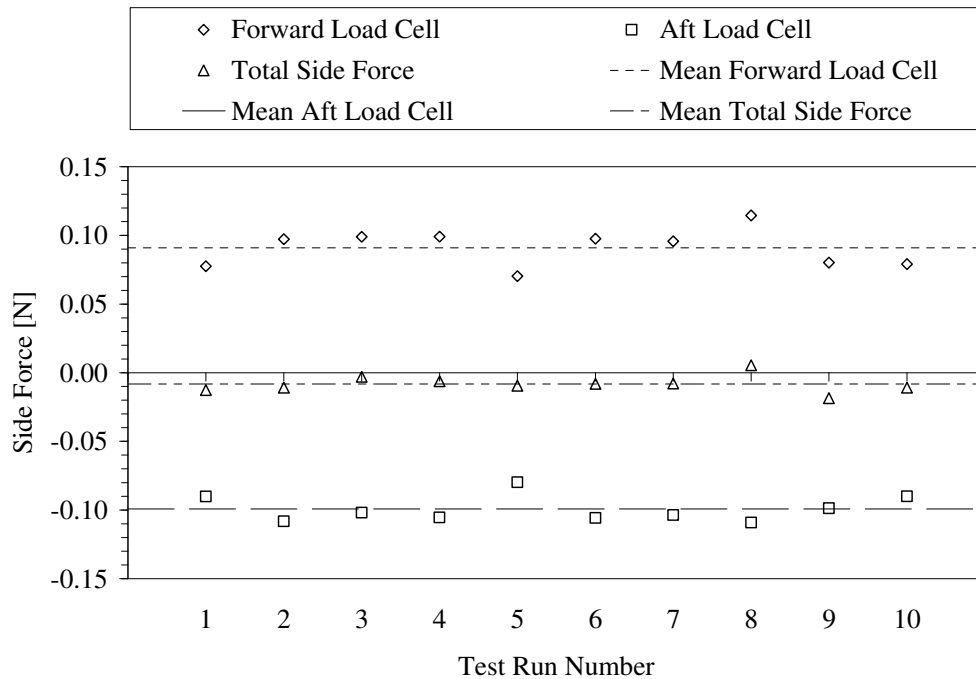


Figure 5-15 Repeatability and precision analysis: Individual load cell and combined total side (sway) force for the Joubert $L/D = 7.30$ model at $H^* = 3.46$ and $Fr = 0.40$

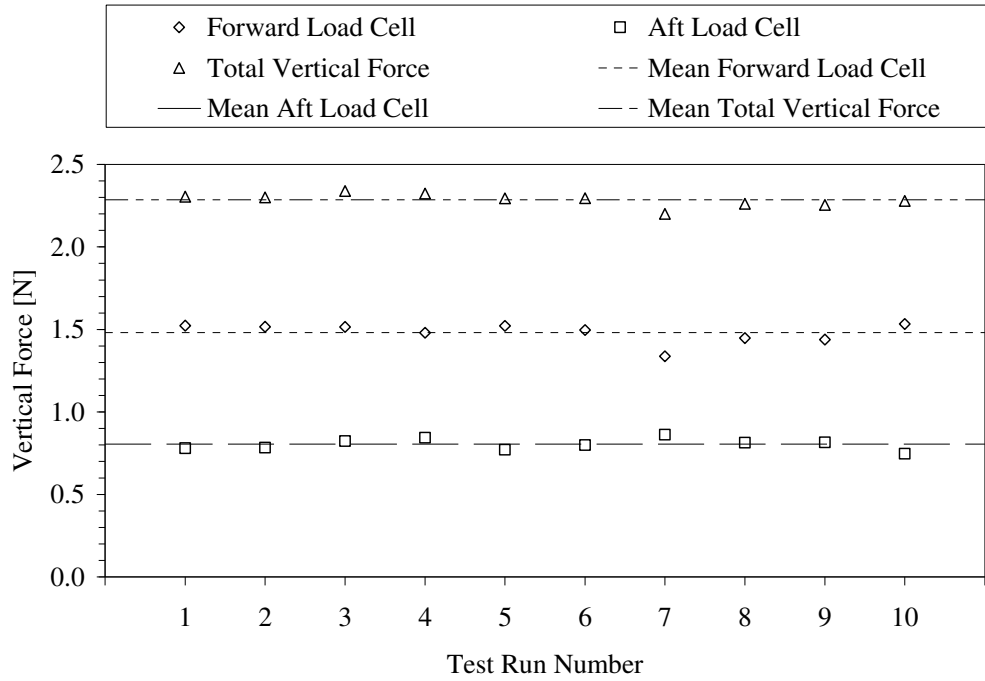


Figure 5-16 Repeatability and precision analysis: Individual load cell and combined total vertical (lift) force for the Joubert $L/D = 7.30$ model at $H^* = 3.46$ and $Fr = 0.40$

6 NUMERICAL INVESTIGATION: SHIPFLOW

As previously discussed in Section 3.3, the development of numerical methods to predict the flow around a streamlined body has resulted in a range of tools that can be used to calculate the drag, lift and moment acting on a body in relative motion with a fluid. The two common types of tool used to predict and analyse the fluid flow around a body are the potential flow (PF) method (also referred to as the boundary element method) and the volume of fluid (VoF) method. The latter is commonly referred to as the computational fluid dynamics (CFD) approach; however, both types use computational techniques to determine the pressure and velocity on the body's surface or in the surrounding flow field. The advantage of PF methods is that they are computationally efficient and can return a solution in a relatively short time (seconds, minutes or hours). In comparison, CFD methods require significantly more time and or computational resources to determine a stable solution. Depending on the type of CFD solver used, a solution may take from hours to weeks to converge. Of course, the complexity of the modelled domain and the physics of the problem being analysed will affect the performance and requirements of either of the two methods. A principal difference between the two is that PF methods neglect the effect of viscosity, while CFD solvers use a range of formulations and routines to account for the effects of viscosity and the different flow domains shown in Figure 3-1.

The benefit of using a numerical tool such as a PF code or a CFD code to analyse the behaviour of a marine craft is that it can generate indicative, if not entirely accurate, results that provide valuable insight into the performance characteristics of the craft. Computational methods offer significant cost savings in the design and analysis phases of the development of a new or existing ship or submarine as they can be used to generate data that would otherwise have to be measured experimentally. The ranges of predicted parameters, operational conditions and design configurations that can be analysed are virtually endless. When coupled with optimisation routines, such as the approach used by Alvarez et al. (2009) (Section 3.2.4), these computational analysis methods can be used to determine the best performer from a set of design options. At this point the designer can decide whether it is necessary to conduct an experiment to verify and validate the numerical solution and build a level of confidence in the performance predictions made using the numerical method. A more detailed discussion of the advantages, disadvantages and sources of errors of the computational methods is presented by Larsson and Raven (2010).

In this investigation it was decided to use a commercially available potential flow software program to complete simulations and predictions of the interaction effects that occur when a submerged streamlined body of revolution is travelling in proximity to the free-surface boundary. As previously discussed, the potential flow method lends itself well to modelling and simulation of the near-surface submerged body problem as the principal phenomenon of interest are the generated waves, a problem that can be treated with an inviscid flow domain. The SHIPFLOW Version 4.7.01 potential flow simulation and analysis software program was used exclusively in this research. The SHIPFLOW program is an established tool that is used widely in the global maritime design and shipbuilding industries. The program comprises a series of modules that are used to model and solve the flow field on and around surface ships, submarines and the free-surface. Extensions of the program also allow the prediction

and analysis of the flow field and surface pressure distribution on and around marine propulsors as well as a viscous solver that enables boundary layer flows to be modelled. In this investigation only the baseline SHIPFLOW simulation and analysis package was used to determine the wave resistance coefficient, lift force and trimming moment acting on a shallowly submerged streamlined body and the free-surface waves that are generated.

6.1 SHIPFLOW OVERVIEW AND STRUCTURE

The SHIPFLOW software used in this research comprises three modules: XFLOW, XMESH and XPAN. Together, these modules allow the user to model and mesh the physical problem of interest (body and free-surface boundaries), initialise the operational environment (flow speed and submergence depth) and manage the solution method and criteria used to generate a numerical solution. A brief description of the three modules is presented in Table 6-1.

Table 6-1 Description of SHIPFLOW modules (FLOWTECH, 2012)

Module	Description
XFLOW	XFLOW is effectively the wrapper that initialises the simulation and calls the XMESH and XPAN modules.
XMESH	XMESH is the panel generation routine used to provide the panellised model of the body and the free surface to XPAN.
XPAN	XPAN is the potential flow solver that calculates the flow field around the body and free-surface. XPAN uses a surface singularity panel method to solve for the singularity strengths and calculate the flow related characteristics. XPAN can be used to determine the: wave resistance from the pressure field integration or from transverse wave-cuts; free-surface wave pattern; pressure contours, velocity vectors; sinkage and trim of the body and the lift and induced drag.

Unlike the methods presented by the author in Section 3.3, SHIPFLOW uses Rankine source panels to describe the free-surface boundary. In the case of both body and free-surface, only quadrilateral panels are available for use to discretize the surface boundary. SHIPFLOW, however, does provide a number of panel distribution (stretch function) options for each individual surface domain. A detailed discussion of the methods and algorithms used by SHIPFLOW is beyond the scope of this investigation and the reader is directed to the SHIPFLOW V4.7 software user manuals and the thorough discussion presented by Larsson and Raven (2010) on the numerical prediction of resistance and the free-surface flow around the hull of a ship or submerged body. In general terms SHIPFLOW, like all potential flow methods, simplifies the fluid domain problem by treating the fluid as inviscid and irrotational. In addition to this the velocity potential must satisfy the Laplace (continuity) equation (Equation 6-1) and the pressure is determined from the Bernoulli equation (Equation 6-2). As reported by Larsson and Raven (2010), SHIPFLOW uses a complete non-linear free-surface condition for the three-dimensional fluid flow.

$$\nabla^2\Phi = 0 \qquad \text{Equation 6-1}$$

$$\frac{1}{2}(\nabla\Phi \cdot \nabla\Phi) + \frac{P}{\rho} + gz = \text{Constant} \quad \text{Equation 6-2}$$

6.2 PROBLEM DEFINITION

The simulations completed using SHIPFLOW primarily focussed on the relative motion of a streamlined body of revolution beneath the free-surface boundary. The inherent symmetry in the geometry (zero incidence angles) meant that only one half of the model and free-surface domain needed to be modelled. The following geometries and test conditions were simulated:

- a. The $L/D = 5.00$ spheroid geometry described by Doctors and Beck (1987) was simulated at $0.10 \leq Fr \leq 0.80$ and $H^* = 0.80$ and 1.225 to enable a comparison to be made between SHIPFLOW and the results presented by Doctors and Beck (1987).
- b. The Series 58 model 4166 presented by Gertler (1950) was simulated in an infinite water and for $0.10 \leq Fr \leq 1.50$ and $H^* = 1.413$.
- c. The three Joubert L/D geometries were simulated at $0.10 \leq Fr \leq 1.00$ and $H^* = 1.02, 2.16$ and 3.46 in a fluid domain of infinite depth to provide a comprehensive set of numerical results and enable a comparison between SHIPFLOW and the experimental data recorded in this research.

6.3 MODELLING AND PANELISATION

As discussed briefly above, the symmetry of the problem enabled only one half of the body and free-surface domain to be modelled, meshed and solved. The width and length of the free-surface domain was defined with respect to the body length. The overall free-surface length is six body lengths with one body length upstream of the leading edge of the body and four body lengths downstream of the trailing edge. These lengths were selected to adequately capture the bow wave system, which originates at leading edge but propagates just ahead of the leading edge, and the trailing wave system. Four body lengths were considered to be adequate to allow the wave field to establish itself within the panel domain. The width of the domain was two body lengths. This was selected to prevent the body's wave system from exiting the free-surface domain through the side boundary until as far downstream as possible, if at all. The free-surface boundary with the Joubert $L/D = 7.30$ model is illustrated in Figure 6-1.

Several best practice modelling and meshing techniques were used to achieve a balance between the model and mesh complexity (computational expense) and the introduction of modelling and discretization errors. As discussed by Larsson and Raven (2010) these techniques are:

- a. panels are sized so that the important properties of the body boundary and the flow field can be resolved;
- b. free-surface panels should be no greater than 5 percent of the transverse wavelength; and

- c. the aspect ratio of the quadrilateral panels should be close to a value of 1 as possible (the ideal).

In the case of the streamlined bodies of revolution examined in this investigation, the discretization of the body surface boundary was based on maintaining an ideal aspect ratio across the mid-body section and at the bow and stern where the acute curvature of the geometry can lead to highly skewed panels. To achieve this, the bodies were modelled using the hyperbolic stretch function at both the forward and aft ends of the body domain. This allowed the axial panel length to increase at a rate such that, together with the corresponding increase in circumference, the panel aspect ratio was kept as close to the ideal as practicable. The importance of this feature is that the axial body force calculations are predominantly dependent on the contributions made by these forward and aft facing panels. The Joubert and spheroid mesh geometries are presented in Figure 6-2 and Figure 6-3 respectively. The discretization metrics of the bodies simulated using SHIPFLOW are presented in Table 6-2. These values were determined based on the results of the mesh independence study presented in Section 6.5.

**Table 6-2 Discretization metrics of bodies simulated using SHIPFLOW
(per half body geometry)**

Body	Stations	Points	Panels	Hyperbolic Stretch Value
Joubert $L/D = 7.30$	100	13	1188	0.001
Spheroid	71	13	840	0.001
4166 Gertler (1950)	91	13	1080	0.001

Based on the $6L$ by $2L$ free-surface domain size, the free-surface panel length and width was $0.053L$ for all simulations, which met the minimum requirement of no greater than 5 percent for the shortest wavelength experienced at $Fr = 0.10$. In all, 4800 panels were used to define the free-surface. The SHIPFLOW input files used in the simulations are included in Appendix E.

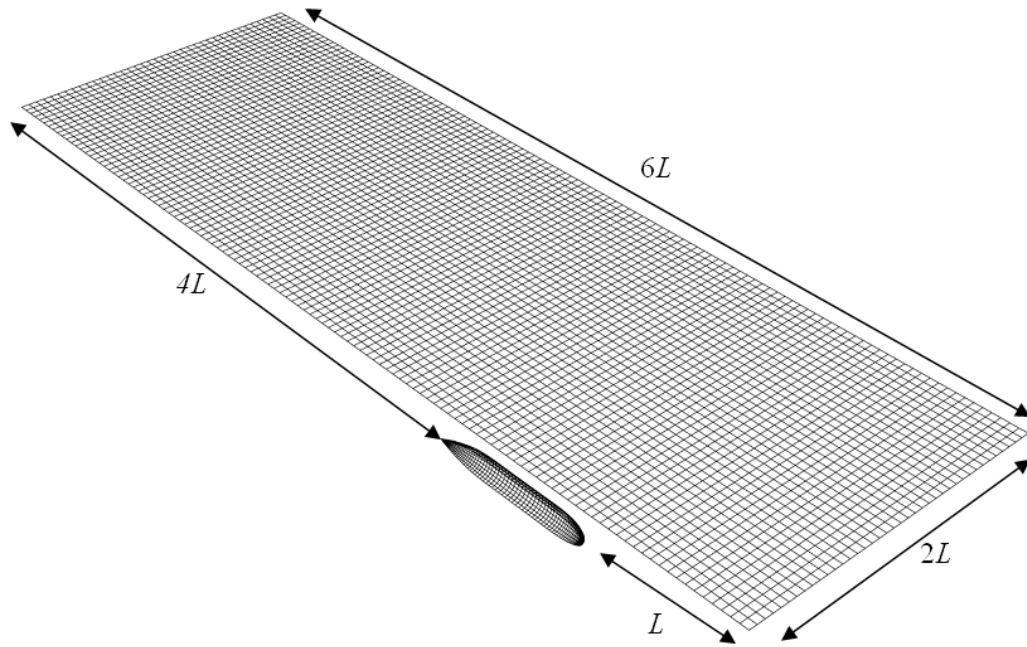


Figure 6-1 Mesh geometry (panels) of submerged body and free-surface boundary (port geometry shown)

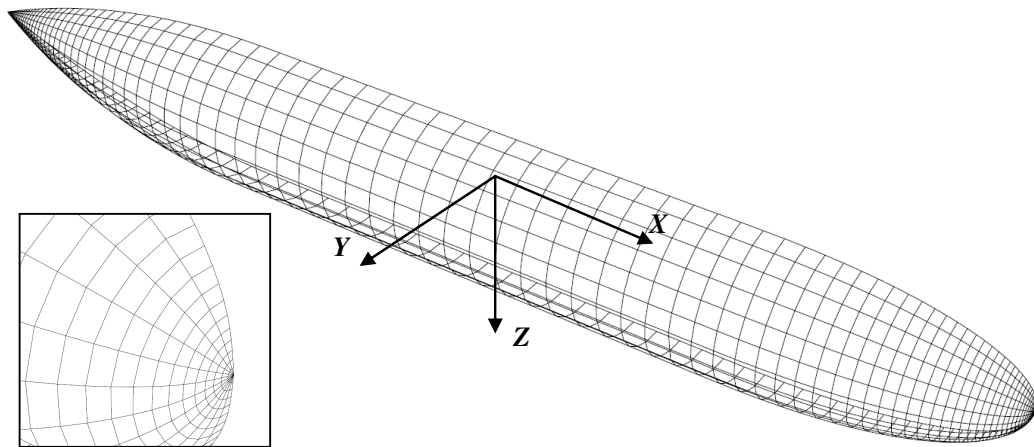


Figure 6-2 Joubert bare hull mesh geometry: 100 stations; 13 points; 1188 panels per half body (shown). Inset: bow panel geometry and aspect ratio.

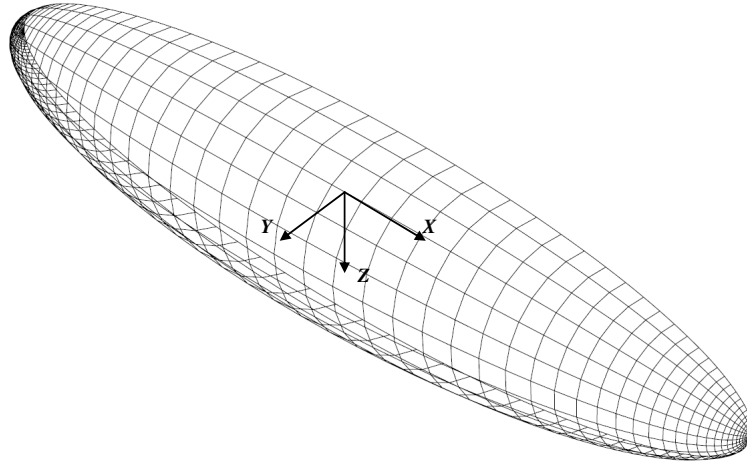


Figure 6-3 $L/D = 5.00$ Spheroid: 71 stations; 13 points; 840 panels per half body (shown)

6.4 CONVERGENCE CRITERIA

The XPAN module provides several options on which to base the simulation convergence criteria: change in trim angle, change in sinkage, change in wave height in non-linear simulations and the maximum allowable change in consecutive waveheights. The change in waveheight criterion was used to manage the convergence of the simulations. The convergence criterion value was set to 1.00×10^{-5} , where the change in wave height is non-dimensionalised by the body length (H_w/L). For the $L/D = 9.50$ Joubert model the solution was deemed to have converged when the change in waveheight between two successive solutions was less than 0.02 millimetres. While this is perhaps excessive for conditions where the body is generating moderate to large surface waves, it did allow a reliable solution to be converged on for the low Froude number and deeper submergence depths where the free-surface disturbance is itself small.

When evaluating the mesh independence of the Joubert and spheroid bodies, the solution convergence criteria was based on the integrated pressure coefficient (C_P). In this case convergence was deemed to have been achieved if $C_P < 1.00 \times 10^{-3}$.

6.5 MESH INDEPENDENCE

A global assessment of the body mesh topography was completed using the integrated pressure coefficient in the three principal axes: C_{PX} , C_{PY} and C_{PZ} . The integrated pressure coefficient solutions returned by SHIPFLOW were compared against the limiting criteria of $C_{P(X,Y,Z)} < 1.00 \times 10^{-3}$. A localised assessment of the body mesh was completed by comparing the longitudinal pressure coefficient distribution against measured or analytical data. A dedicated mesh independence study was completed to determine the free-surface discretisation (panellisation) required to achieve a mesh independent solution. An example of the approach used is presented in Figure 6-4 and Figure 6-5 for the $L/D = 5.00$ spheroid model. A mesh independent model was achieved once the difference between consecutive solutions was sustained below 5 percent.

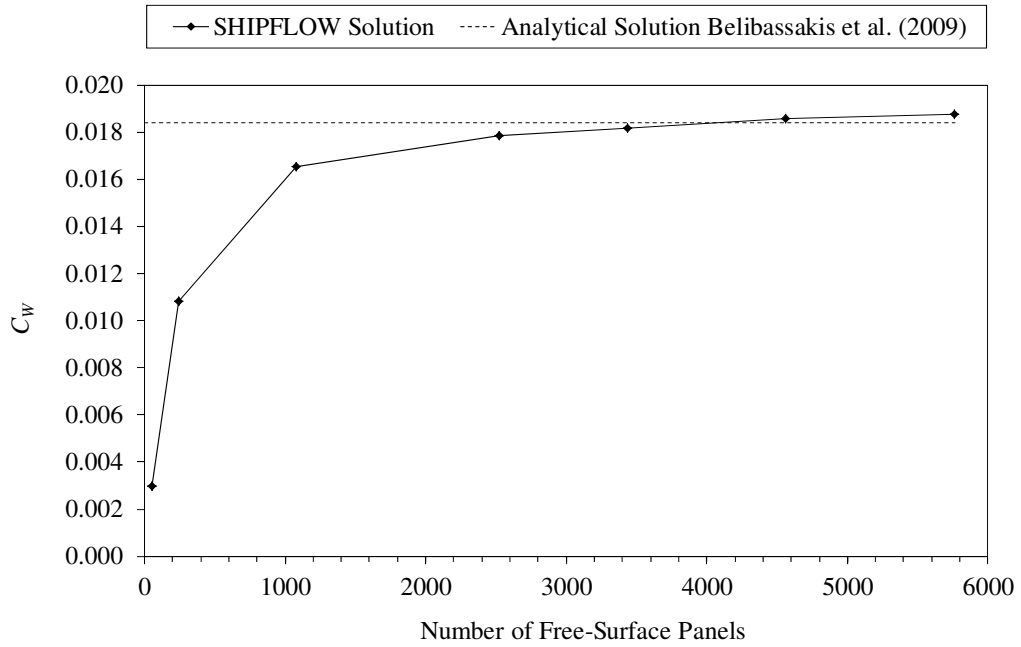


Figure 6-4 Example of free-surface mesh independence on wave resistance coefficient for an $L/D = 5.00$ spheroid at $H^* = 0.80$ and $Fr = 0.50$. SHIPFLOW solution compared to the analytic solution presented by Belibassakis et al. (2009)

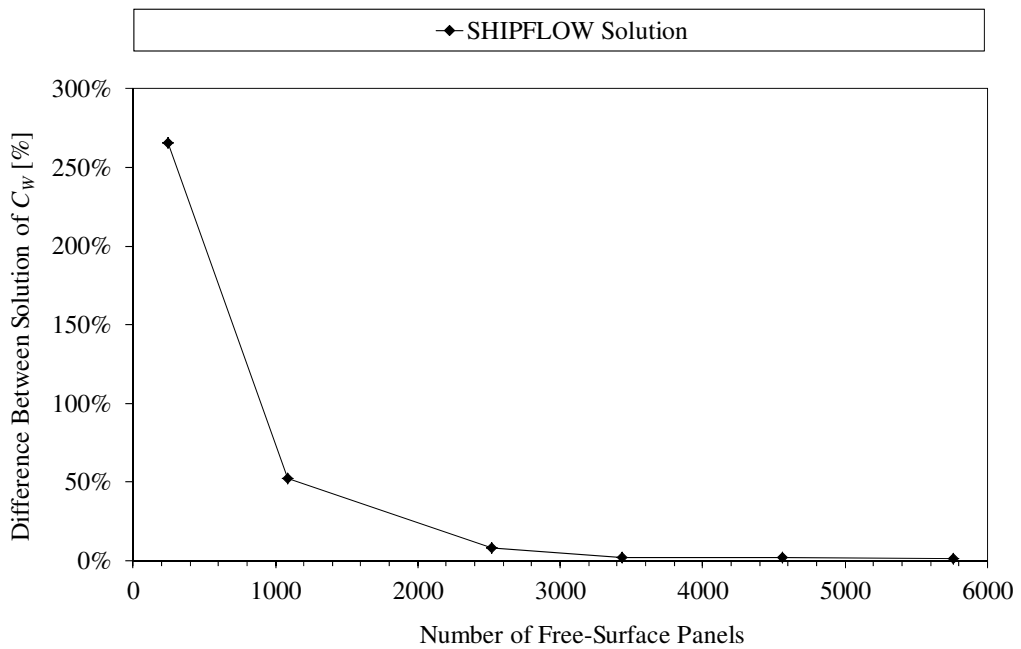


Figure 6-5 Convergence to a free-surface mesh independent solution for the wave resistance coefficient of an $L/D = 5.00$ spheroid at $H^* = 0.80$ and $Fr = 0.50$.

6.6 BOUNDARY AND INITIAL CONDITIONS

The boundary conditions satisfied in the SHIPFLOW simulation are that:

- a. flow is tangential to the free-surface at the free-surface boundary;
- b. the pressure is constant and equal to atmospheric pressure at the free-surface;
and
- c. there is no flow across the body or free-surface boundary.

In all simulation cases, except where the towing tank boundary was modelled, the water depth is assumed to be infinite. The submerged body is not free to trim or sink due to the free-surface interaction effects. In addition, the body travels at a constant relative velocity and submergence depth. The free-surface wave decay condition is such that the surface is not disturbed in front of or at great distance from the submerged body.

6.7 CALCULATION OF THE PARAMETER SOLUTIONS

6.7.1 WAVE RESISTANCE COEFFICIENT

The transverse wave-cut method was used to determine the wave resistance coefficient of the models in each of the simulations. Van Mierlo (2006) indicates that the wave-cut method is preferable to the body oriented integrated pressure method as it is not as dependent on the mesh topography of the body itself. In addition, the pressure integration method combines the hydrostatic and hydrodynamic pressure contributions. At low speeds and deep submergence depths, the hydrostatic pressure component dominates the total pressure coefficient and the resultant solution is more prone to sources of modelling and numerical integration errors. The SHIPFLOW transverse wave-cut method parameter settings used to generate a wave resistance coefficient solution are listed in Table 6-3.

Table 6-3 SHIPFLOW transverse wave-cut method solution parameter settings

Parameter	Parameter Value
Longitudinal position of first wave-cut (xstwc)	1 (x/L)
Longitudinal position of last wave-cut (xentwc)	5 (x/L)
Number of transverse wave-cuts (statwc)	500
Stretch function for wave-cut distribution (strtwc)	0 (uniform)
Number of data points generated on each wave-cut (nvaltw)	100
Number of wave number included in the computation (nwavnu)	20

6.7.2 LIFT FORCE AND TRIMMING MOMENT COEFFICIENT

The lift force and trimming moment were calculated based on the panel pressure coefficient and normal vector data generated by SHIPFLOW. The panel pressure coefficient was resolved into the principal axis of interest (vertical or longitudinal) based on the panel normal vector. The resolved pressure coefficient was then dimensionalised using the panel area to provide the force acting on the panel in the direction of interest. The total lift force acting on the body was calculated by summing the vertical force components of all of the body panels (n panels) as indicated in Equation 6-3.

$$F_z = \sum_{i=1}^{i=n} \left(C_{Pz_i} \cdot 0.5 \cdot \rho \cdot U^2 \cdot S_i \right) \quad \text{Equation 6-3}$$

The trimming moment was calculated by summing the moments of the panel vertical and axial force contributions relative to the origin located at the mid-length of the body (Equation 6-4).

$$M = \sum_{i=1}^{i=n} \left(F_{X_i} \cdot z_i + F_{Z_i} \cdot x_i \right) \quad \text{Equation 6-4}$$

The lift force and trimming moment coefficient values were calculated using Equation 5-5 and Equation 5-6 respectively.

7 EXPERIMENT RESULTS

The results of the Joubert L/D experiment are presented in this section. The results of the SUBOFF tests conducted by Wilson-Haffenden (2009) and Neulist (2011) are included in Appendix D.

7.1 EFFECTS OF SUBMERGENCE DEPTH AND SPEED ON TOTAL RESISTANCE COEFFICIENT

The total resistance coefficient data for the $L/D = 7.30$, $L/D = 8.50$ and $L/D = 9.50$ Joubert model configurations are presented in Figure 7-1, Figure 7-2 and Figure 7-3 respectively. The results indicate that there is significant free-surface interaction at submergence depths of $H^* = 1.02$ and $H^* = 1.30$ for $Fr > 0.20$ for all three of the model configurations. At $H^* > 2.16$ there is a discernible increase in the resistance coefficient for $Fr > 0.375 \sim 0.40$, indicating that interaction between the body and the free-surface is occurring and that the resistance coefficient is deviating from the deeply submerged condition. The resistance coefficient response is characteristic of the presence and influence of wave making. The significant observation to note is that there are clearly defined peaks in the total resistance coefficient curves for $H^* < 2.16$ that occur at $Fr = 0.30$ and at approximately $Fr = 0.50$ for all of the models. There is a third peak at $Fr \approx 0.23$ that appears to occur only for the $L/D = 8.50$ and $L/D = 9.50$ models (Figure 7-2 and Figure 7-3). Based on the models' prismatic coefficient and using the method developed by Baker and Kent (1919), as discussed in section 3.1.3, all three peaks coincide with the Froude numbers at which constructive wave interaction is predicted to occur. However, this does not preclude constructive interaction occurring for the $L/D = 7.30$ model at $Fr \approx 0.23$. Rather, it is likely that the amount of interaction experienced by the $L/D = 7.30$ model does not result in a significant increase in resistance at $Fr \approx 0.23$ or that this feature was not adequately captured in the experiment.

For each of the model configurations the results indicate that there is a reduction in the interaction effects as the submergence depth increases. The total resistance coefficient is observed to vary periodically with Froude number for the shallower submergence depths of $H^* = 1.02$ and $H^* = 1.30$. However, for the submergence depths greater than $H^* = 1.30$ the interaction effects are observed to decrease with a reduction in Froude number. For $Fr < 0.375 \sim 0.40$ and for $H^* > 2.16$ the resistance coefficient data indicates that the free-surface has negligible influence on the submerged bodies' total resistance. Excluding the regions in the speed profile where free-surface interaction results in destructive wave interaction ($Fr \leq 0.20$, $Fr \approx 0.25$ and $Fr \approx 0.35$), the free-surface interaction effect is observed to diminish rapidly with an increase in depth and varies as a negative-exponent power function. This behaviour is illustrated for the three L/D geometries at $Fr = 0.30$, 0.40 and 0.50 in Figure 7-4, Figure 7-5 and Figure 7-6 respectively.

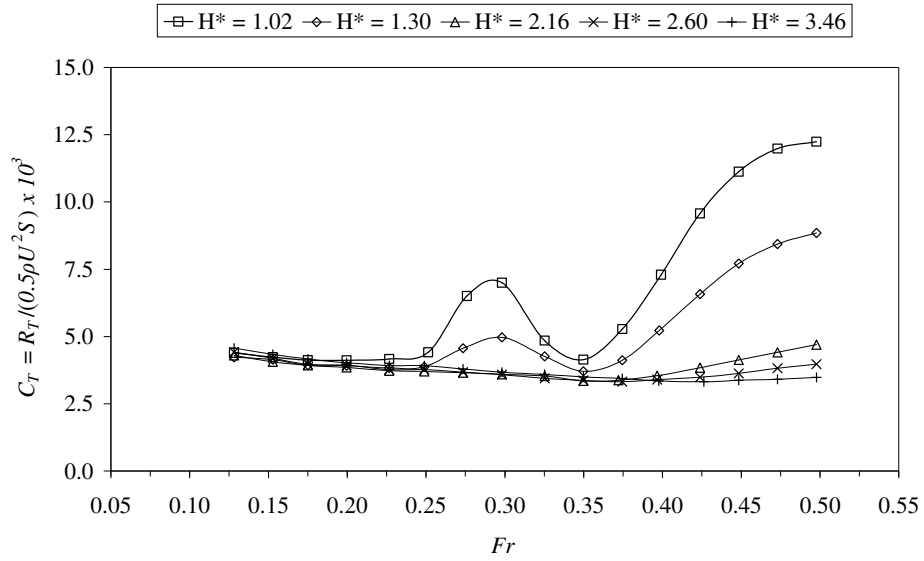


Figure 7-1 Total resistance coefficient (C_T) versus Froude number for Joubert $L/D = 7.30$ model

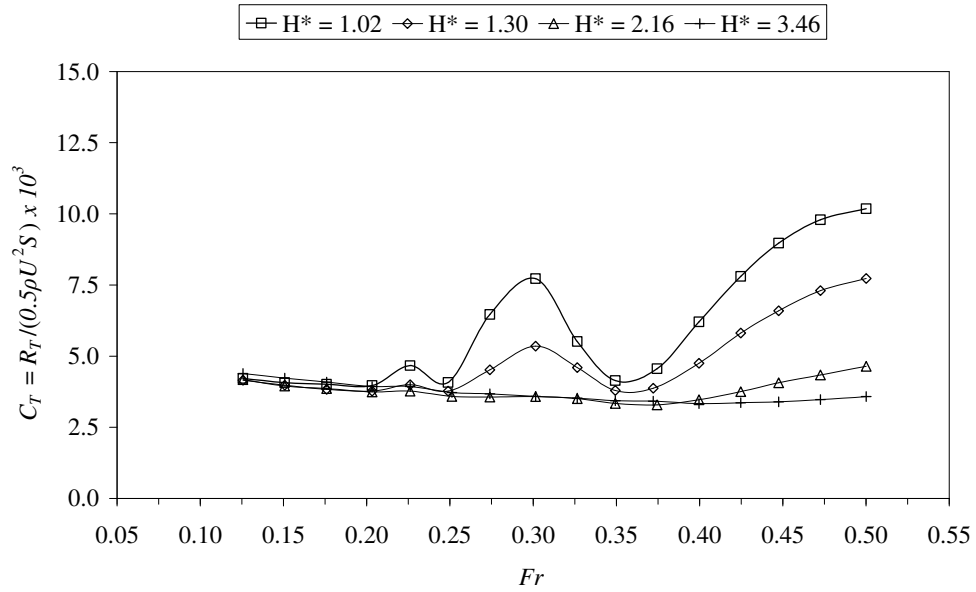


Figure 7-2 Total resistance coefficient (C_T) versus Froude number for Joubert $L/D = 8.50$ model

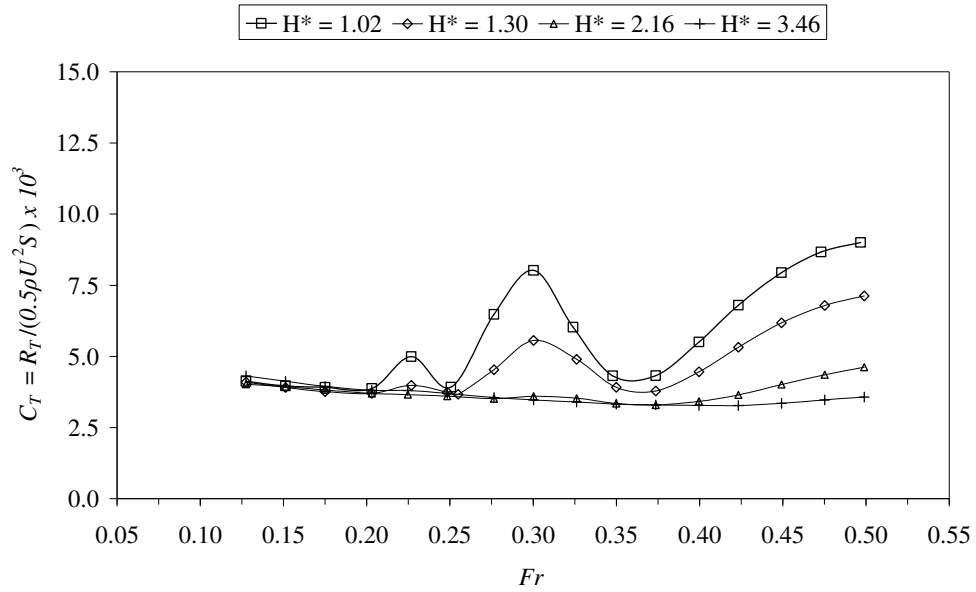


Figure 7-3 Total resistance coefficient (C_T) versus Froude number for Joubert $L/D = 9.50$ model

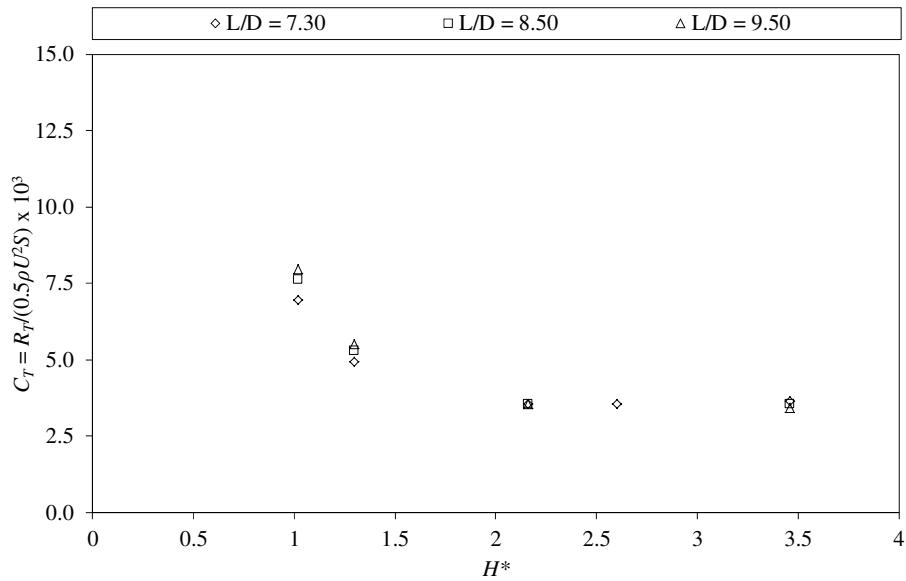


Figure 7-4 Total resistance coefficient (C_T) versus non-dimensional submergence depth (H^*) for $Fr = 0.30$

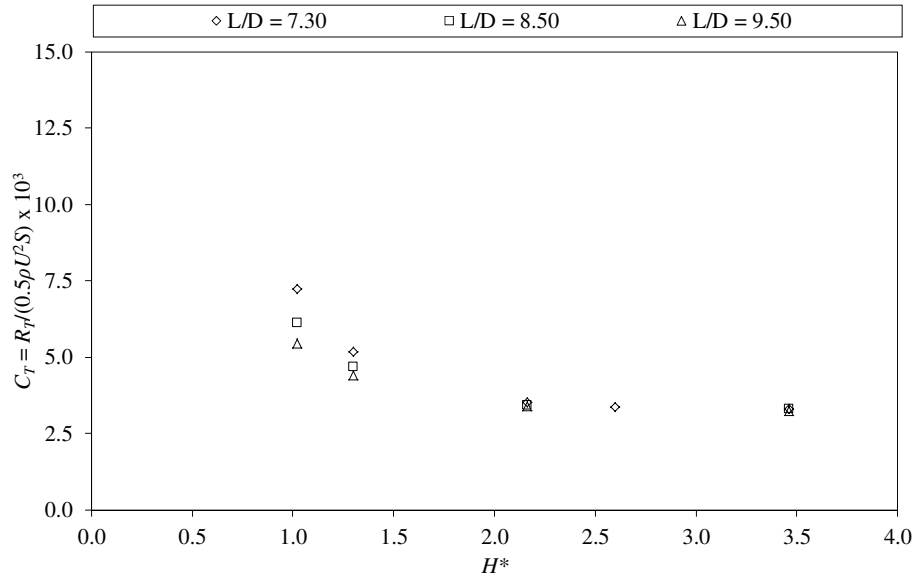


Figure 7-5 Total resistance coefficient (C_T) versus non-dimensional submergence depth (H^*) for $Fr = 0.40$

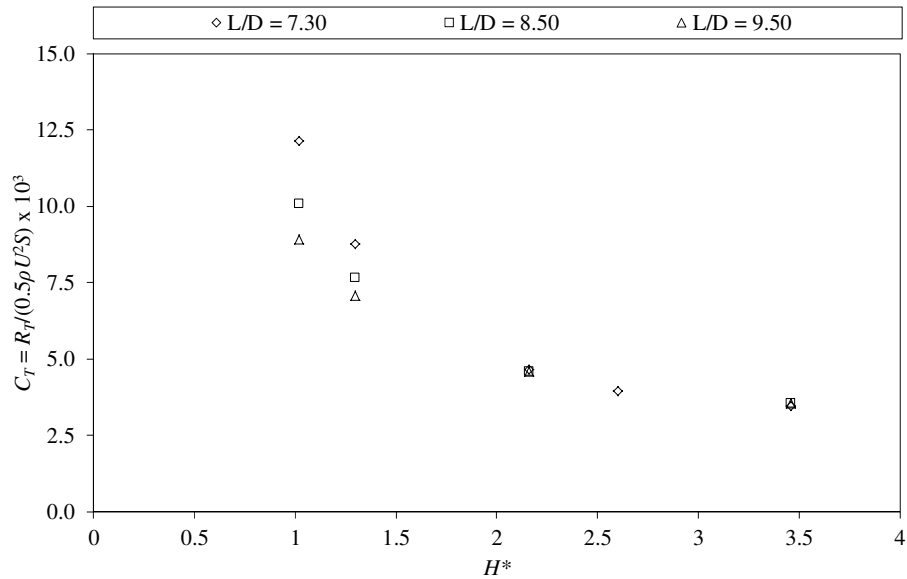


Figure 7-6 Total resistance coefficient (C_T) versus non-dimensional submergence depth (H^*) for $Fr = 0.50$

It is apparent from the total resistance coefficient data that wave making resistance becomes non-negligible only at the upper end of the near-surface operational speed range for centreline submergence depths of approximately two and a half hull diameters or less. At submergence depths less than $H^* = 2.50$ the free-surface interaction effects appear to have more influence on the lower length-to-diameter ratio

hull geometry ($L/D = 7.30$) when compared to the $L/D = 8.50$ and $L/D = 9.50$ models. As the Froude number increases above $Fr \approx 0.20$ the relative effect of the free-surface changes to one where the $L/D = 9.50$ geometry has the greater total resistance coefficient and the $L/D = 7.30$ geometry has the lesser. At speeds above $Fr \approx 0.35$ the order reverts to one where the $L/D = 7.30$ geometry possesses the greater total resistance coefficient and the $L/D = 9.50$ has the lesser. This indicates that, although constructive wave interaction does not have a significant influence within the operational speed range (up to 10 knots), the total resistance coefficient of the lower length-to-diameter Joubert geometry is consistently greater, albeit marginally, than the two larger L/D geometries.

The results of the SUBOFF experiments conducted by Wilson-Haffenden (2009) and Neulist (2011) are in agreement with the observations made based on the Joubert experiments: free-surface interaction varies periodically with speed, reduces as a negative-exponent power function with respect to non-dimensional submergence depth and is not a primary concern for submarine operational effectiveness during near-surface operations. Despite this, it is important to note the observations made by Farell and Güven (1973) that clearly indicate that there is an increase in the viscous resistance component that will affect the total resistance of a submarine when operating in proximity to the free-surface.

7.2 EFFECT OF LENGTH-TO-DIAMETER ON TOTAL RESISTANCE COEFFICIENT

The presence of the additional total resistance coefficient peak at $Fr \approx 0.23$ and the effect of length-to-diameter are more apparent when comparing the results of each of the three models at coincident submergence depths. Figure 7-7 clearly indicates the absence of the resistance peak at $Fr \approx 0.23$ for the $L/D = 7.30$ model. As previously discussed, it is apparent that the amount of interaction at this speed is not significant enough to result in a noticeable increase in the body's total resistance. Furthermore, the results indicate that the greater the length-to-diameter ratio the greater the relative value of the resistance coefficient peak at $Fr \approx 0.23$ and $Fr = 0.30$ and the lower the peak resistance coefficient value at $Fr = 0.50$. This behaviour is a feature of the method used to non-dimensionalise the total resistance coefficient (surface area) and the relative amount of energy expended by the body per unit surface area. The results also indicate that there is a horizontal (Froude based) offset in the $L/D = 7.30$ total resistance coefficient curve in comparison to the $L/D = 8.50$ and 9.50 data. The data shows that the local minimum and maximum resistance occurs at a marginally lower Froude number for the $L/D = 7.30$ model. This behaviour is likely to occur as a result of the difference in the bodies' prismatic coefficient and the effect that this parameter has on the Froude number at which peak wave interaction occurs. This characteristic is clearly observable at the shallower submergence depths ($H^* < 1.30$) in Figure 7-7 and Figure 7-8.

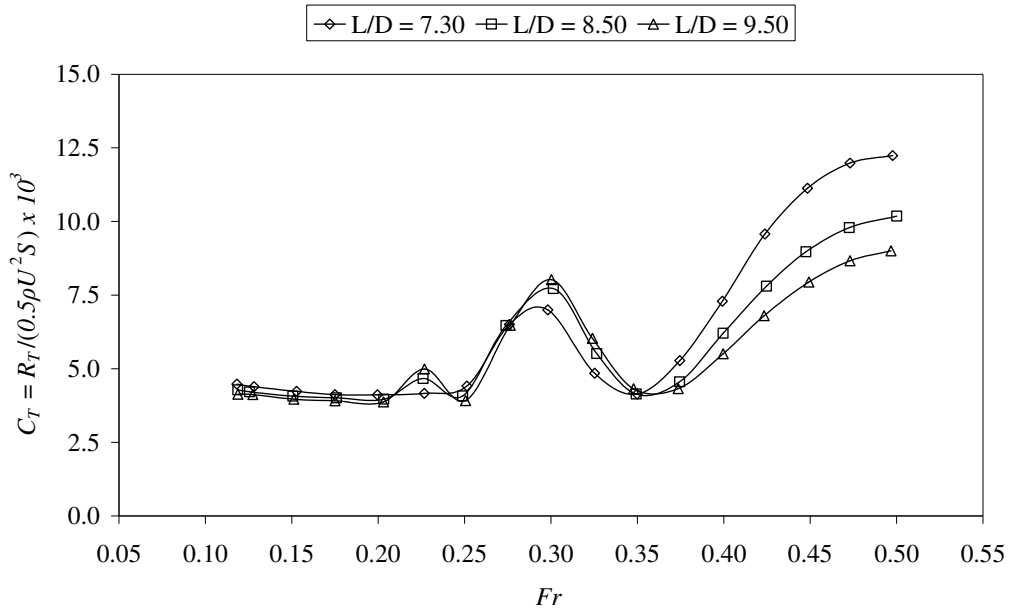


Figure 7-7 Effect of L/D on the total resistance coefficient (C_T) $H^* = 1.02$ (Joubert Models)

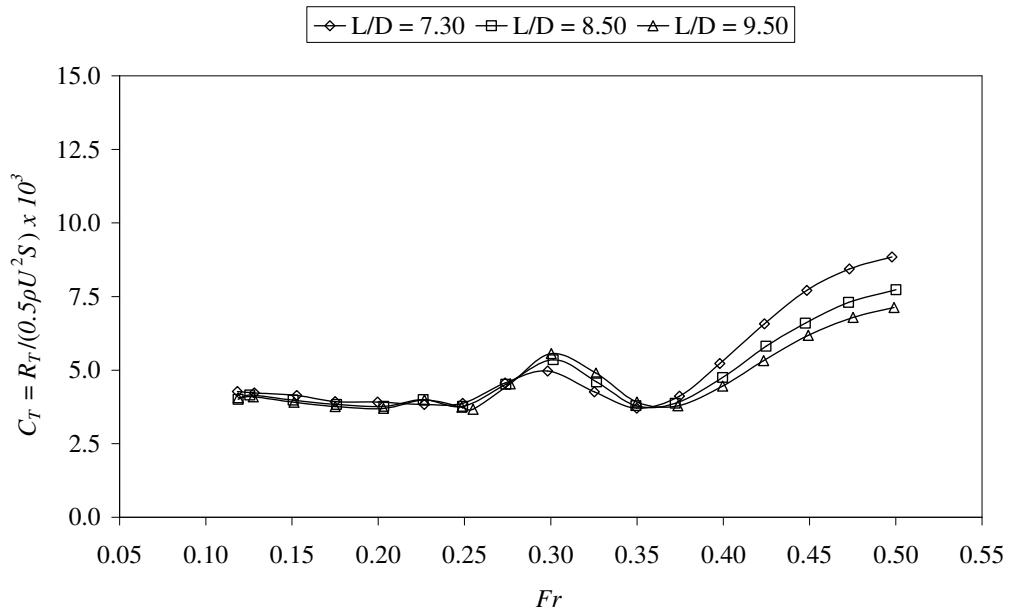


Figure 7-8 Effect of L/D on the total resistance coefficient (C_T) $H^* = 1.30$ (Joubert Models)

The effects of L/D for the deeper submergence depths ($H^* = 2.16$ and $H^* = 3.46$) are presented in Figure 7-9 and Figure 7-10. At these depths the influence of length-to-diameter appears to be negligible, despite the apparent free-surface interaction effects at $Fr > 0.375$. At these depths the resistance coefficient data for the three models is converged on a single curve.

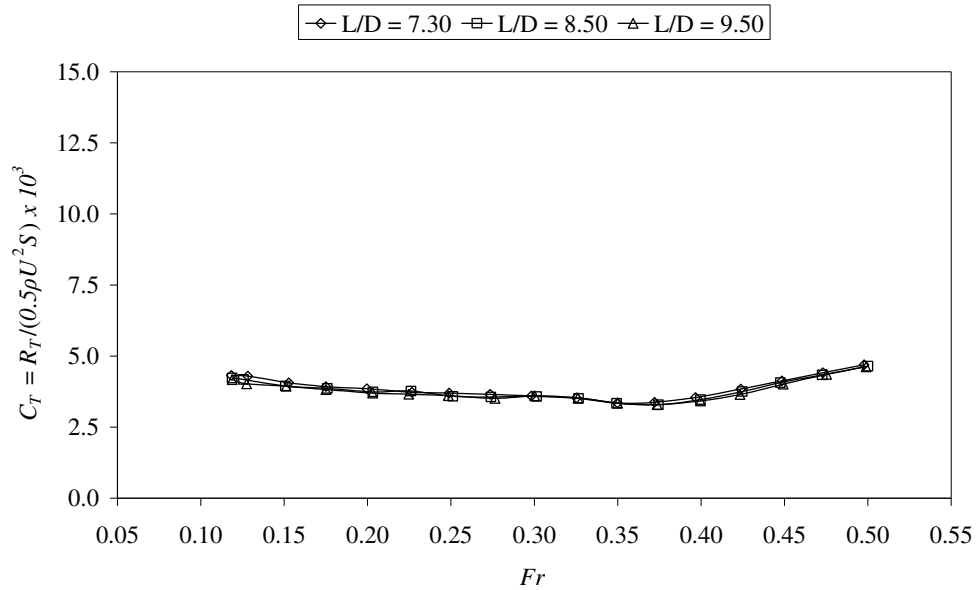


Figure 7-9 Effect of L/D on the total resistance coefficient (C_T) $H^* = 2.16$ (Joubert Models)

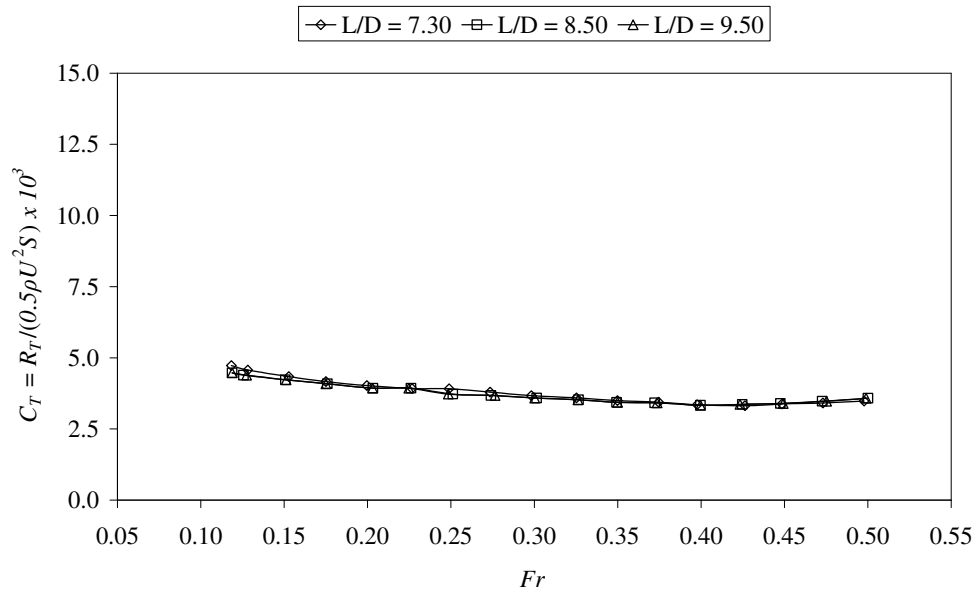


Figure 7-10 Effect of L/D on the total resistance coefficient (C_T) $H^* = 3.46$ (Joubert Models)

Although Gertler (1950) concluded that the optimum length-to-diameter for a deeply submerged streamlined body of revolution is $L/D \approx 6.00$ and for a practical submarine design it is $L/D \approx 7.00$, this characteristic is also dependent on the body's shape. As a result, Gertler's findings are inextricably linked to the Series 58 geometries that he tested. The optimum near surface resistance performance of the Joubert geometries investigated in this research is not so definitive. However, it is apparent that the lower L/D geometry ($L/D = 7.30$) has the greater resistance coefficient for the Froude number range corresponding to current submarine near surface operating speeds.

7.3 VERTICAL PLANE FORCE AND MOMENT

7.3.1 LIFT FORCE COEFFICIENT

The lift force coefficient data for the $L/D = 7.30$, $L/D = 8.50$ and $L/D = 9.50$ Joubert model configurations are presented in Figure 7-11, Figure 7-12 and Figure 7-13 respectively. The data presented has been adjusted to account for an angular misalignment of the post and sting setup in the vertical plane that was present during testing. The misalignment was found to induce a small downward lift force on the model in all test conditions. The correction applied to the lift force data was to shift the data set vertically downwards so that the low speed mid-tank submergence lift coefficient data corresponds to a nominally zero lift force.

The data indicates that there is significant free-surface interaction occurring for all models for submergence depths down to $H^* = 2.16$ and in the case of the $L/D = 7.30$ model, down to $H^* = 2.60$ for $Fr > 0.40$. The behaviour at the shallower submergence depths is characterised by the lift force coefficient varying periodically with Froude number. The local peak values occur at $Fr \approx 0.25$ and $Fr \approx 0.40$ with a local minimum value occurring at $Fr \approx 0.325$ and separating the two peaks. For $Fr > 0.4$ the lift coefficient decreases rapidly and it is surmised that it would transition to a positive value representing a change from a force acting to move the body towards the free-surface to a force acting to move the body away from the free-surface.

This behaviour can be attributed to the relative position and wavelength of the body-generated free-surface wave system and how it changes the pressure distribution acting on the body. The mechanism which causes the lift force is similar to that experienced by ships navigating in restricted water depths: the acceleration of the flow between the body and boundary results in a pressure decrease in that region and an attraction between the body and the boundary. Because the free-surface is a flexible boundary, its shape is dependent on the speed and submergence depth of the body travelling beneath it. The relative separation of the body from the free-surface boundary can be non-uniform along the body's length. Furthermore, the pressure distribution around the body is highly asymmetric across the depth of the body (from top to bottom or its deck to its keel). As a result, the relative lift force will vary depending on the position and amplitude of the wave system's crests and troughs and the steady-state pressure distribution acting on the body's surface.

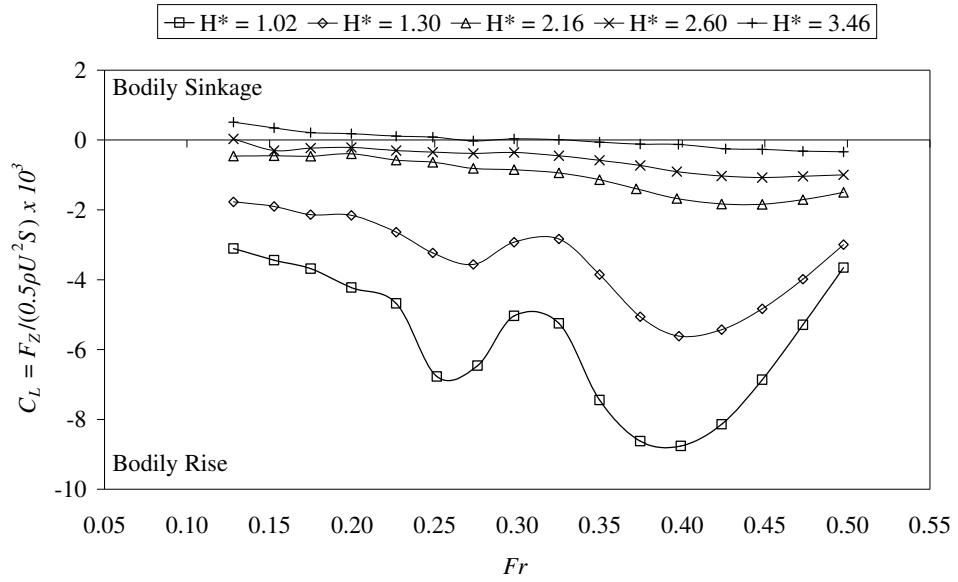


Figure 7-11 Lift force coefficient (C_L) Joubert $L/D = 7.30$

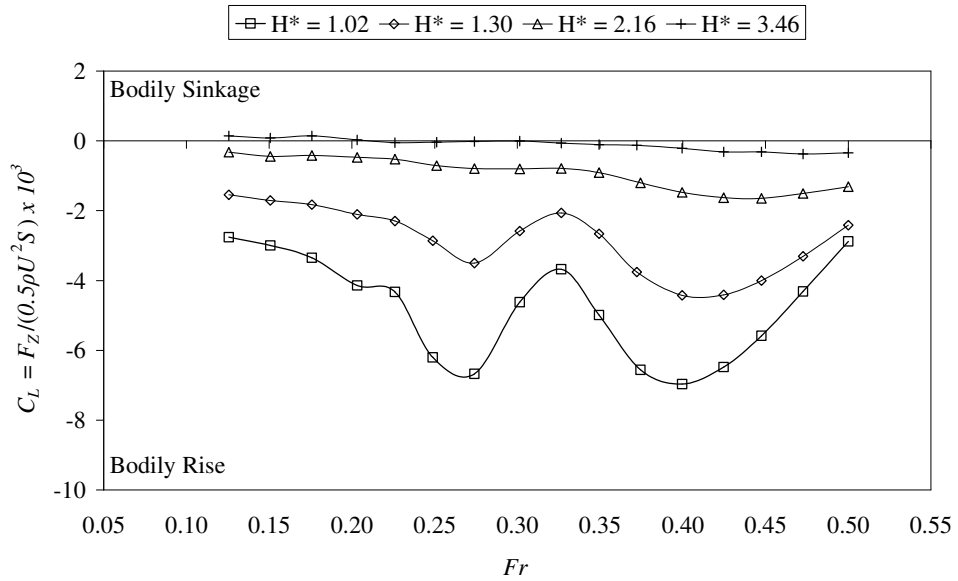


Figure 7-12 Lift force coefficient (C_L) Joubert $L/D = 8.50$

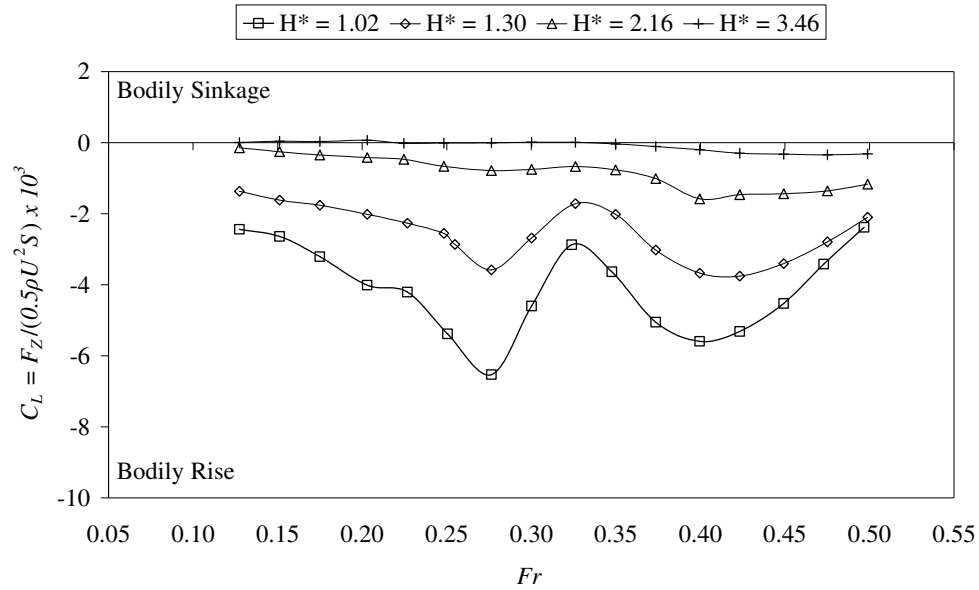


Figure 7-13 Lift force coefficient (C_L) Joubert $L/D = 9.50$

The length-wise normal pressure coefficient data calculated using the SHIPFLOW software provides a clear illustration of the effects of the free-surface wave on the non-zero lift force that acts on the submerged body. It is important to reiterate that the numerical results presented here are limited to an inviscid solution and are only suitable for making comparisons between body geometries. Figure 7-14 illustrates the effect of the free-surface wave on the vertical component of the pressure distribution acting along the top edge of the body for the Froude speeds at which the abovementioned local peaks occur. The Baseline data presented in Figure 7-14 represents the infinite fluid domain condition where there is no free-surface interaction. For the shallow submergence depths, the simulation results indicate that there is a significant change in the body's normal pressure distribution that corresponds with the steady-state wave system generated on the free-surface. The relative position of the wave system's crests and troughs result in localised regions of high and low pressure. The relative position of these peaks is observed to shift aft along the body as the wavelength increases with an increase in speed.

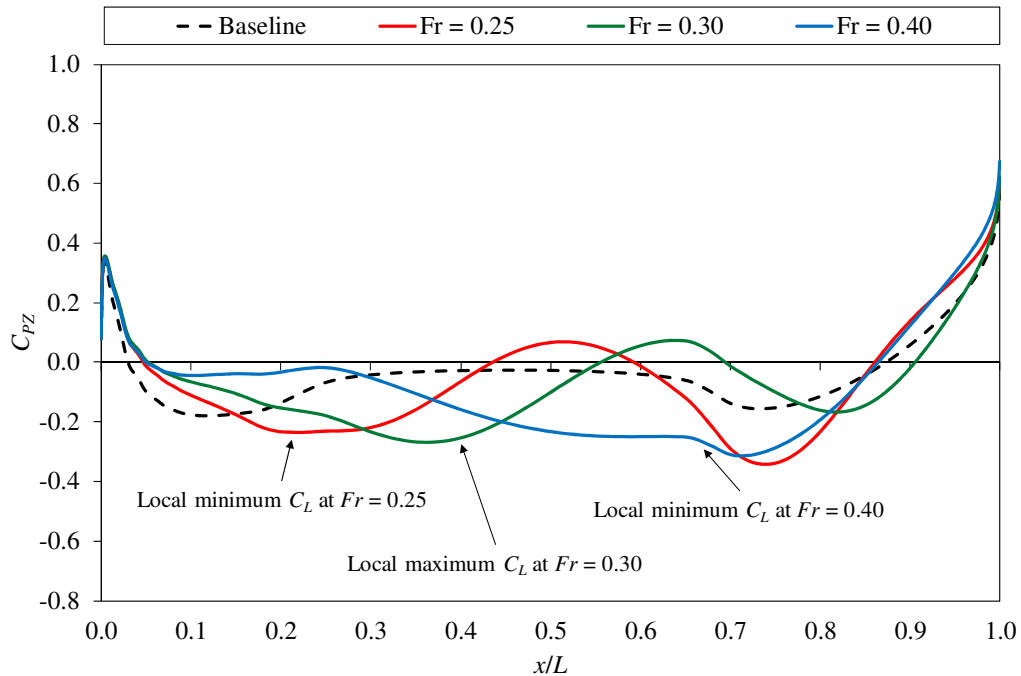


Figure 7-14 SHIPFLOW simulation results: effect of Froude number on the distribution of the vertical pressure coefficient component (C_{pz}) along the length of the Joubert $L/D = 7.30$ geometry at $H^* = 1.02$. The normal pressure coefficient is predicted along the panels with their centre at 7.50 degrees off the top dead-centre (TDC) meridian.

As previously discussed, the total lift force is determined by summing all of the vertical pressure components acting on the surface of the submerged body. Figure 7-15, Figure 7-16 and Figure 7-17 illustrate the distribution of the pressure coefficient along the length and from the bottom to the top of the body for the speeds at which the local maximum and minimum lift force occur. In Figure 7-15 and Figure 7-17 it can be observed that there is a region of higher relative pressure acting on the bottom of the body and regions of lower relative pressure acting on the top of the body. The three-dimensional pressure differential results in a negative vertical lift force which causes the body to rise towards the free-surface. At $Fr = 0.30$ (Figure 7-16) the pressure distribution is more uniform along the length of the body resulting in a lower pressure differential and lift force.

Of course, the effects of the non-uniform pressure distribution result in a lift force and trimming moment couple. The influence of the body's pressure distribution on its trimming moment is discussed in section 7.3.3.

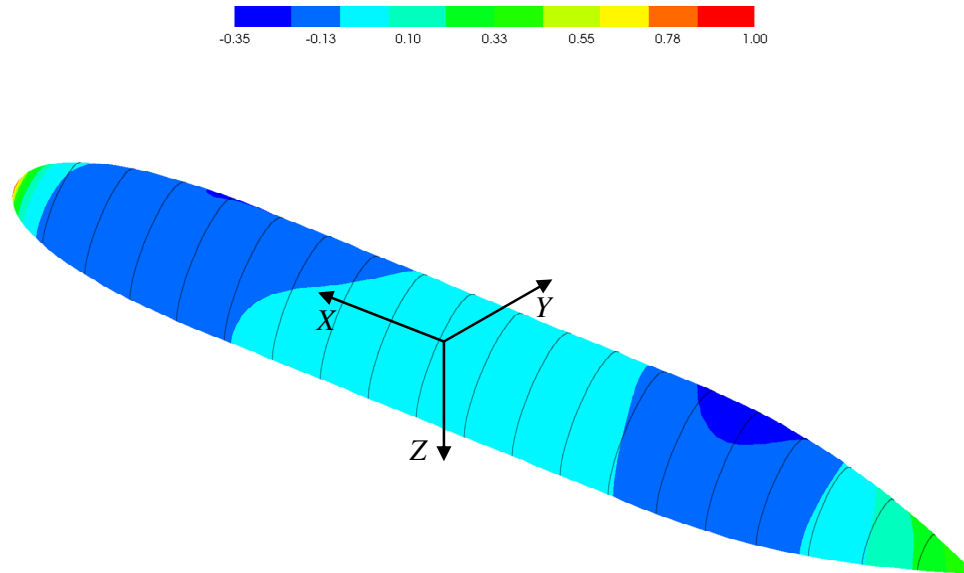


Figure 7-15 SHIPFLOW simulation results: Normal pressure coefficient (C_p) distribution along the length of the Joubert $L/D = 7.30$ geometry at $H^* = 1.02$ and $Fr = 0.25$. Pressure coefficient data is calculated at panel centres.

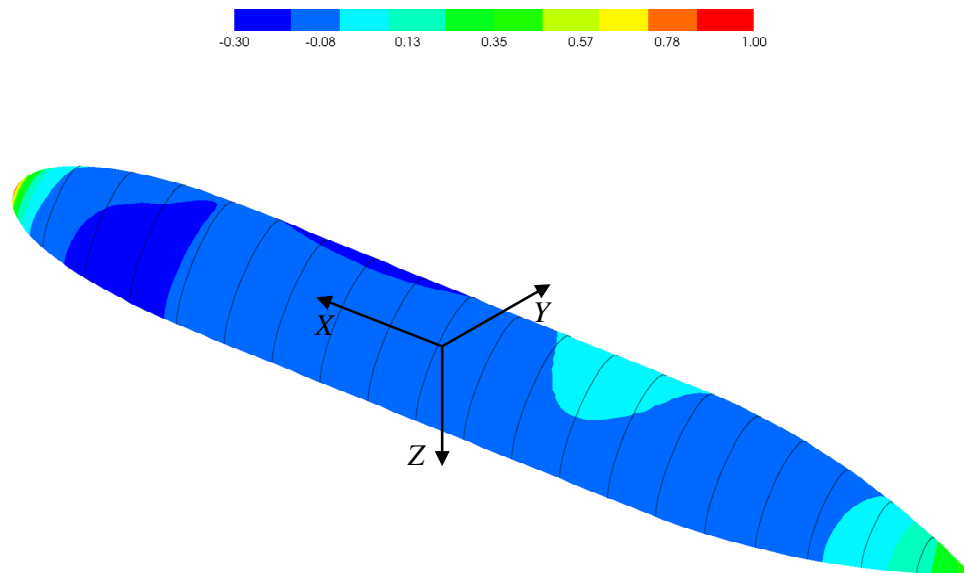


Figure 7-16 SHIPFLOW simulation results: Normal pressure coefficient (C_p) distribution along the length of the Joubert $L/D = 7.30$ geometry at $H^* = 1.02$ and $Fr = 0.30$. Pressure coefficient data is calculated at panel centres.

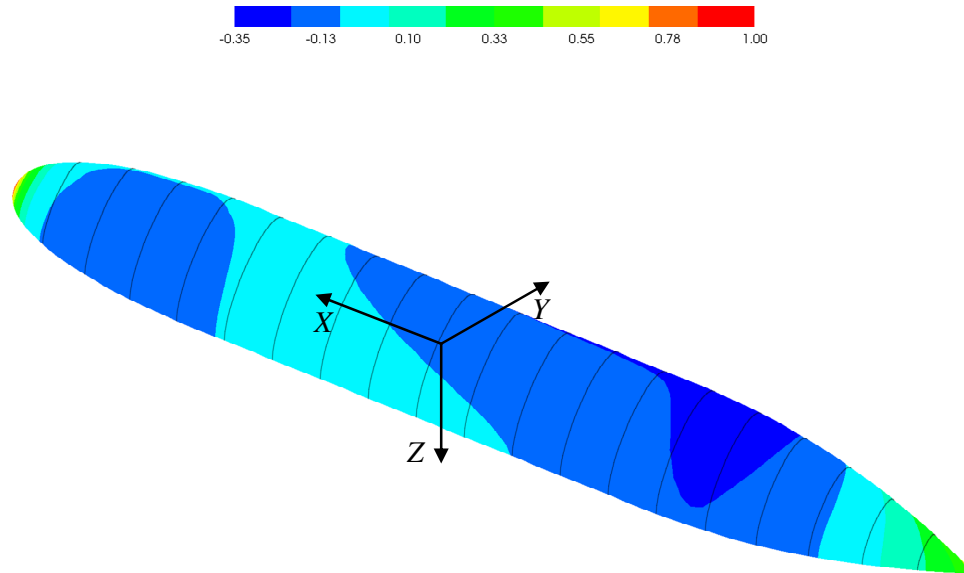


Figure 7-17 SHIPFLOW simulation results: Normal pressure coefficient (C_p) distribution along the length of the Joubert $L/D = 7.30$ geometry at $H^* = 1.02$ and $Fr = 0.40$. Pressure coefficient data is calculated at panel centres.

Compatible with the total resistance coefficient results, there is negligible interaction occurring at the $H^* = 3.46$ submergence depth for Froude number less than $Fr \approx 0.375$. By contrast the total resistance coefficient data, the submerged body experiences interaction effects and a resultant lift force for the shallower submergence depths ($H^* = 1.02$ and 1.30) for the entire speed range tested. Figure 7-18 illustrates the rapidity with which the pressure distribution changes with an increase in submergence depth. The lift coefficient is observed to decrease exponentially with an increase in submergence depth. Figure 7-19 through Figure 7-23 illustrates the rate of change of the lift force coefficient as a function of submergence depth and with respect to Froude number. At $Fr = 0.50$ the rate of decay is relatively low in comparison to the lower Froude numbers; however, this is the Froude region where the lift force coefficient becomes small as it transitions from an upwards force to a downwards force. The rate of decay is steepest in the region of the localised peak lift force ($Fr = 0.25$ and $Fr = 0.40$) as illustrated in Figure 7-20 and Figure 7-22. For the range of Froude numbers tested in this investigation, the lift force coefficient is observed to approach an asymptote at zero as the non-dimensional submergence depth increases beyond $H^* \approx 2.50$.

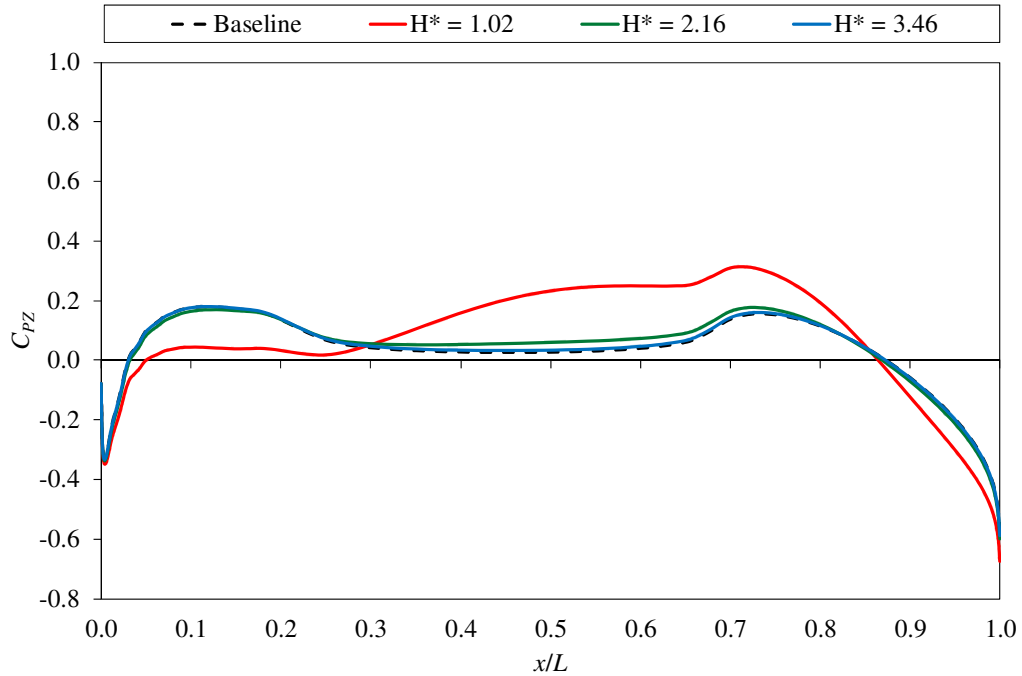


Figure 7-18 SHIPFLOW simulation results: effect of submergence depth on the distribution of the vertical pressure coefficient component (C_{pz}) along the length of the Joubert $L/D = 7.30$ geometry at $Fr = 0.40$. The normal pressure coefficient is predicted along the panels with their centre at 7.50 degrees off the top dead-centre (TDC) meridian.

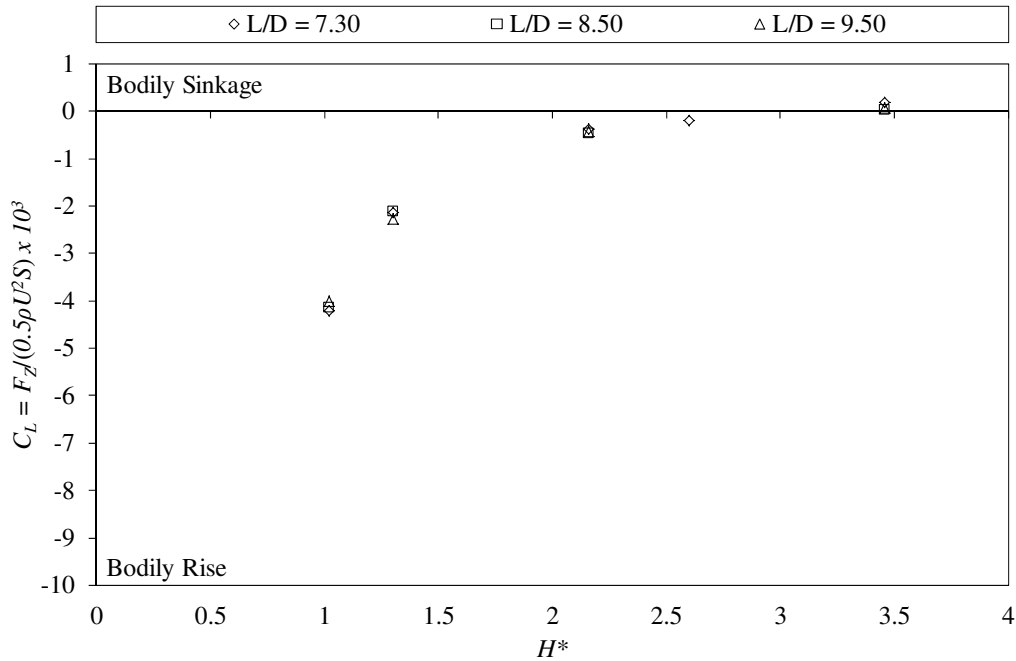


Figure 7-19 Effect of submergence depth (H^*) on lift force coefficient (C_L) at $Fr = 0.20$ (Joubert Models)

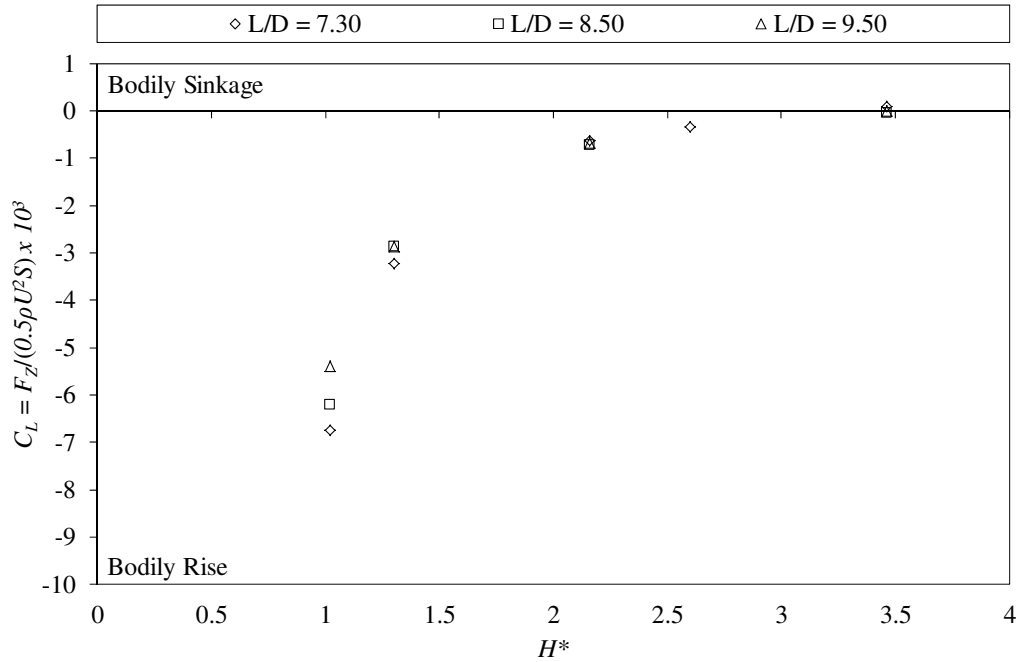


Figure 7-20 Effect of submergence depth (H^*) on lift force coefficient (C_L) at $Fr = 0.25$ (Joubert Models)

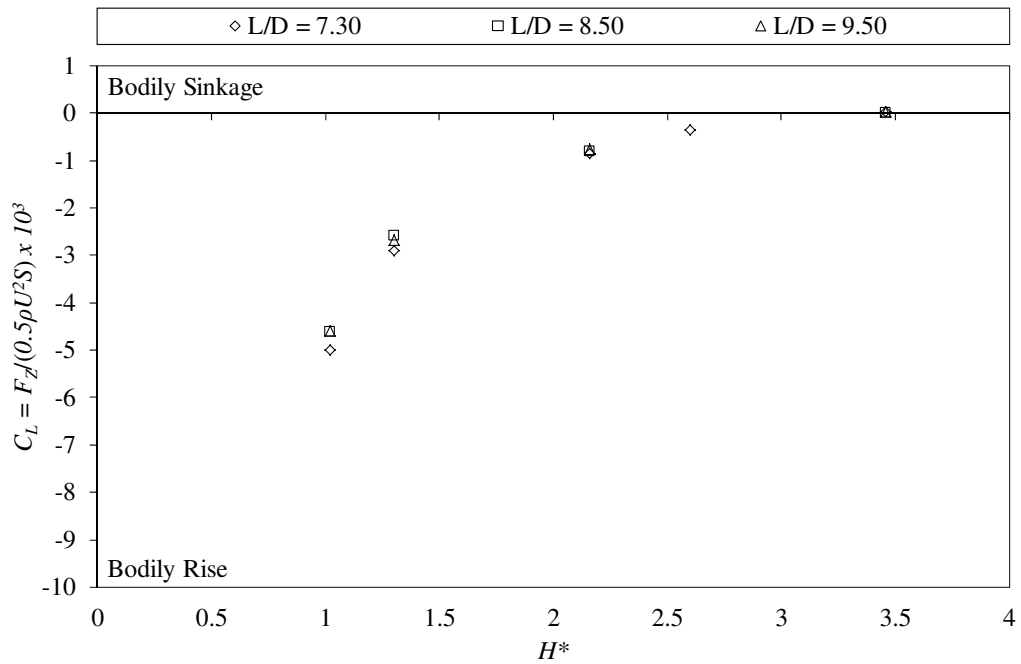


Figure 7-21 Effect of submergence depth (H^*) on lift force coefficient (C_L) at $Fr = 0.30$ (Joubert Models)

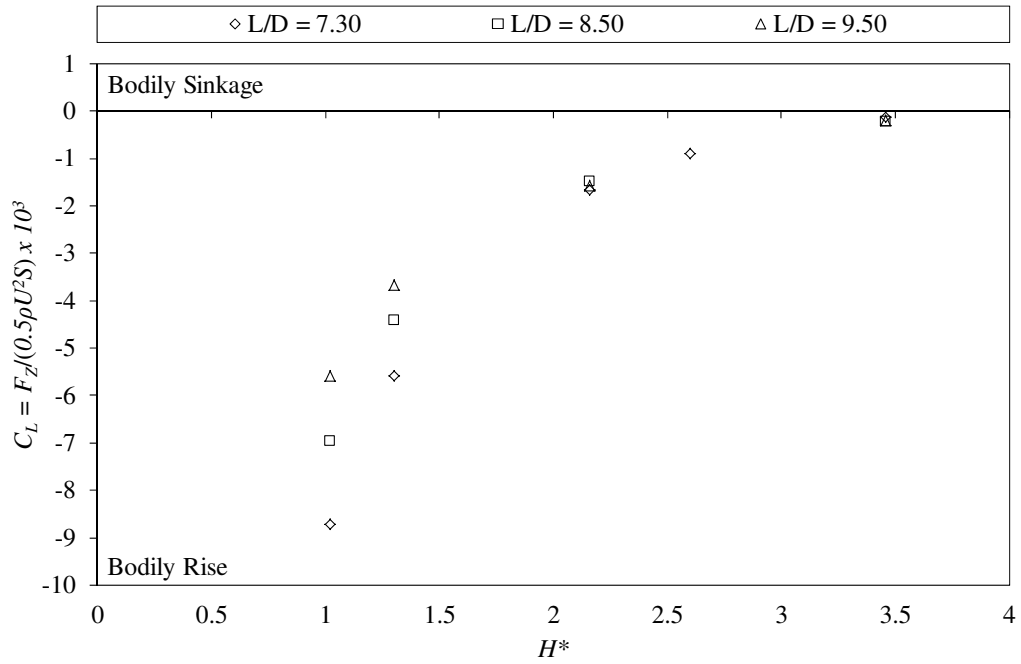


Figure 7-22 Effect of submergence depth (H^*) on lift force coefficient (C_L) at $Fr = 0.40$ (Joubert Models)

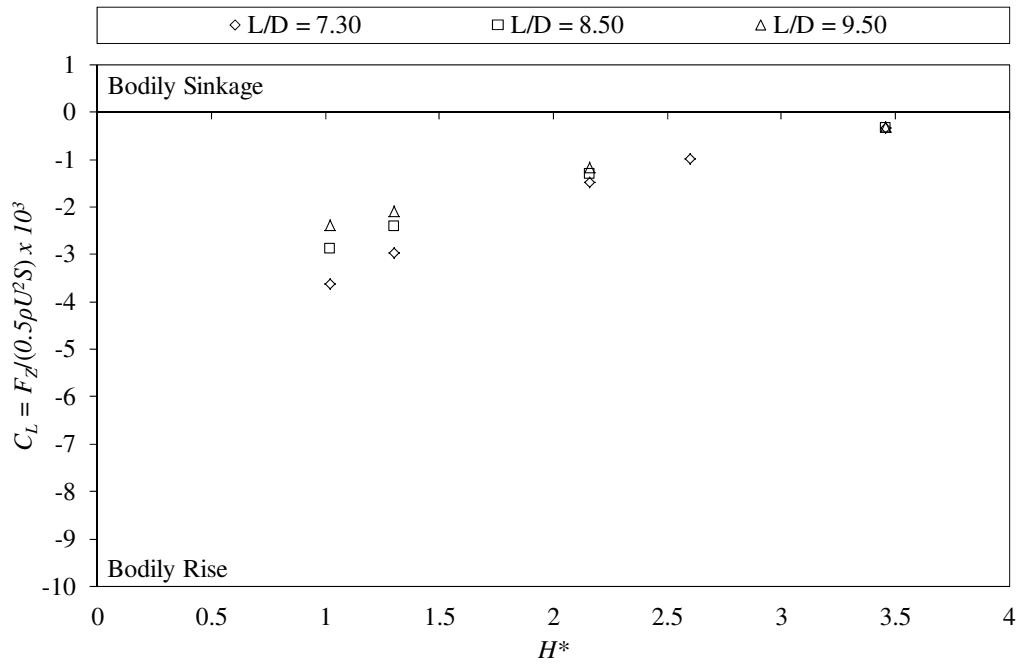


Figure 7-23 Effect of submergence depth (H^*) on lift force coefficient (C_L) at $Fr = 0.50$ (Joubert Models)

7.3.2 EFFECT OF LENGTH-TO-DIAMETER ON LIFT FORCE COEFFICIENT

The relative effects of the body's length-to-diameter on the lift force coefficient can be observed in Figure 7-24, Figure 7-25, Figure 7-26 and Figure 7-27 for $H^* = 1.02, 1.30, 2.16$ and 3.46 respectively. Figure 7-24 and Figure 7-25 show that the effects of length-to-diameter are most significant for $Fr > 0.30$ for the shallower submergence depths of $H^* = 1.02$ and 1.30 . The consistent trend indicates that the free-surface interaction effect diminishes with increasing length-to-diameter. For $Fr < 0.30$ the effects are not as significant and the lift force coefficient is similar for the three bodies. Similar to the results of the length-to-diameter comparison of total resistance coefficient (Figure 7-9 and Figure 7-10), the length-to-diameter of the body appears to have negligible influence on the lift force coefficient for the $H^* = 2.16$ and $H^* = 3.46$ submergence depths (Figure 7-26 and Figure 7-27). The lift force coefficient data presented in Figure 7-27 indicates that there is only a marginal influence of the free-surface acting on the model at $Fr > 0.375$. Below $Fr = 0.375$ there is negligible interaction for the models at the $H^* = 3.46$ depth.

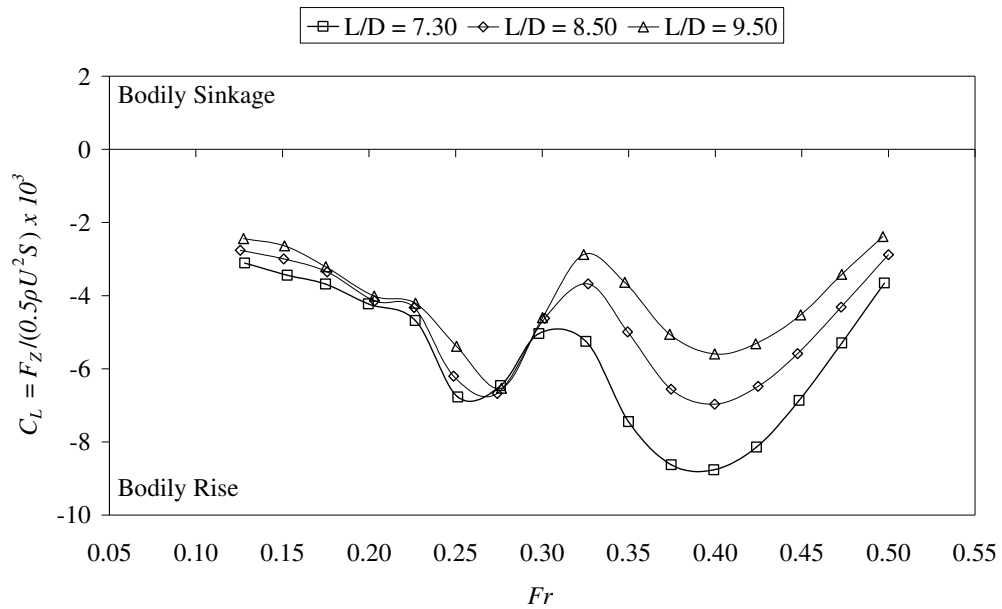


Figure 7-24 Lift force coefficient (C_L) $H^* = 1.02$ (Joubert Models)

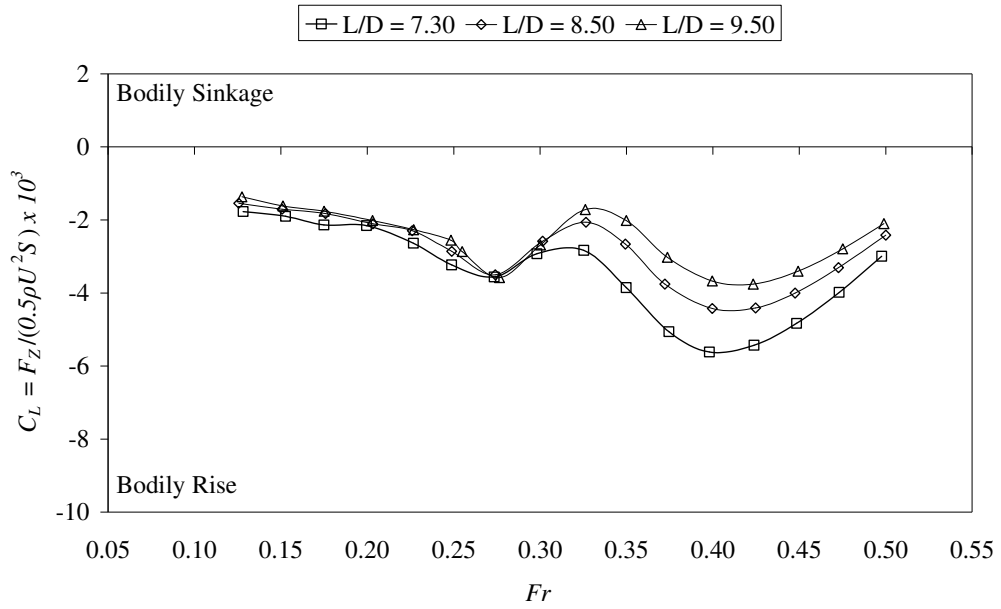


Figure 7-25 Lift force coefficient (C_L) $H^* = 1.30$ (Joubert Models)

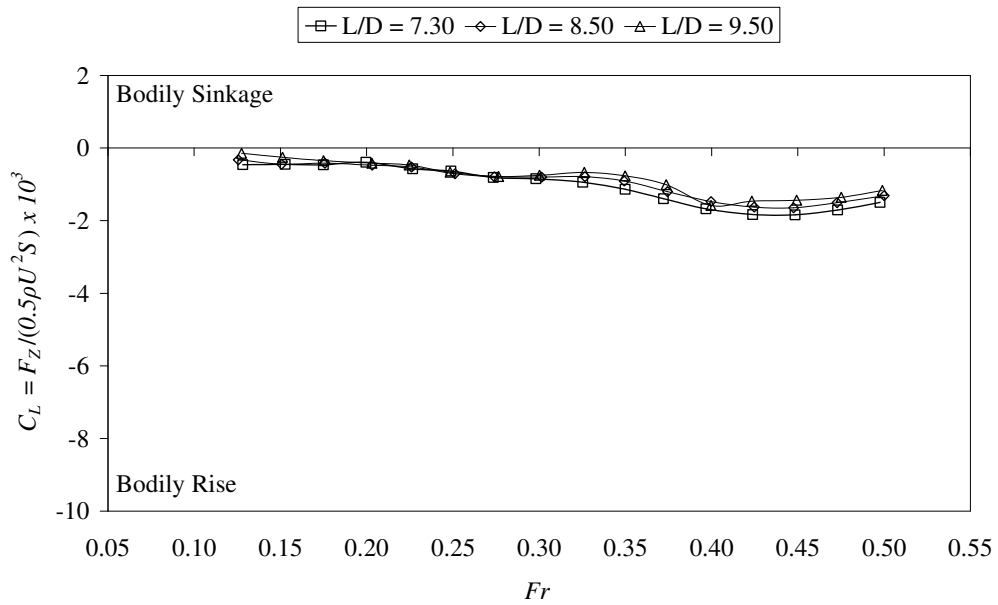


Figure 7-26 Lift force coefficient (C_L) $H^* = 2.16$ (Joubert Models)

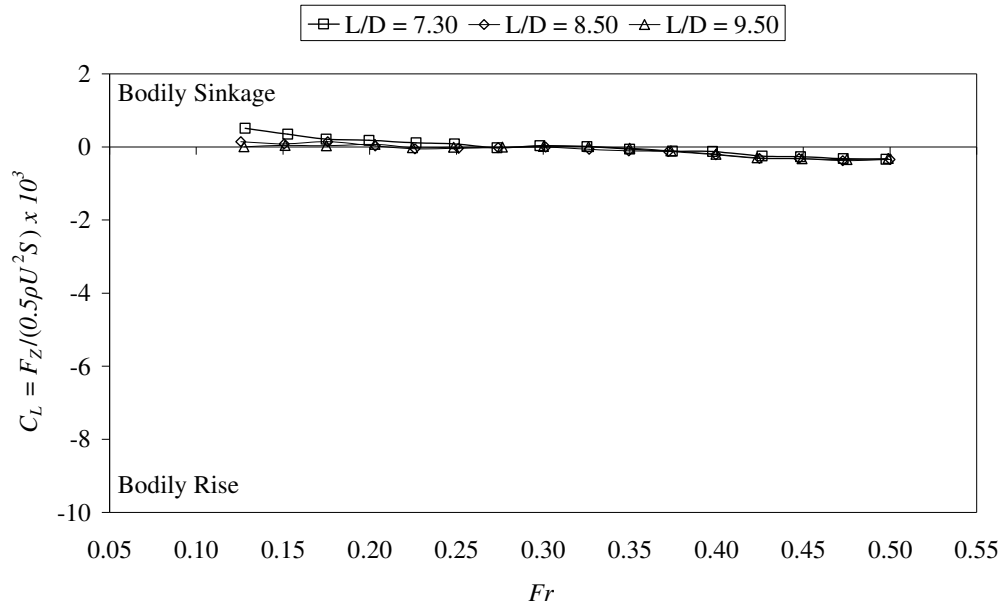


Figure 7-27 Lift force coefficient (C_L) $H^* = 3.46$ (Joubert Models)

The influence of the body's length-to-diameter ratio observed for $Fr > 0.30$ is due to the relative difference in the pressure distribution and resultant vertical force that acts on each of the three models. Figure 7-28 and Figure 7-29 provide a clear indication of the differences in the distribution of the vertical component of the normal pressure coefficient for the three different length-to-diameter geometries. Although not explicitly indicated in Figure 7-28 and Figure 7-29, the differences in the pressure distribution acting on the models results in the lower L/D geometry experiencing a greater total lift force per unit area. It is apparent that for this series of bodies, the lift force per unit area decreases with an increase in length-to-diameter ratio.

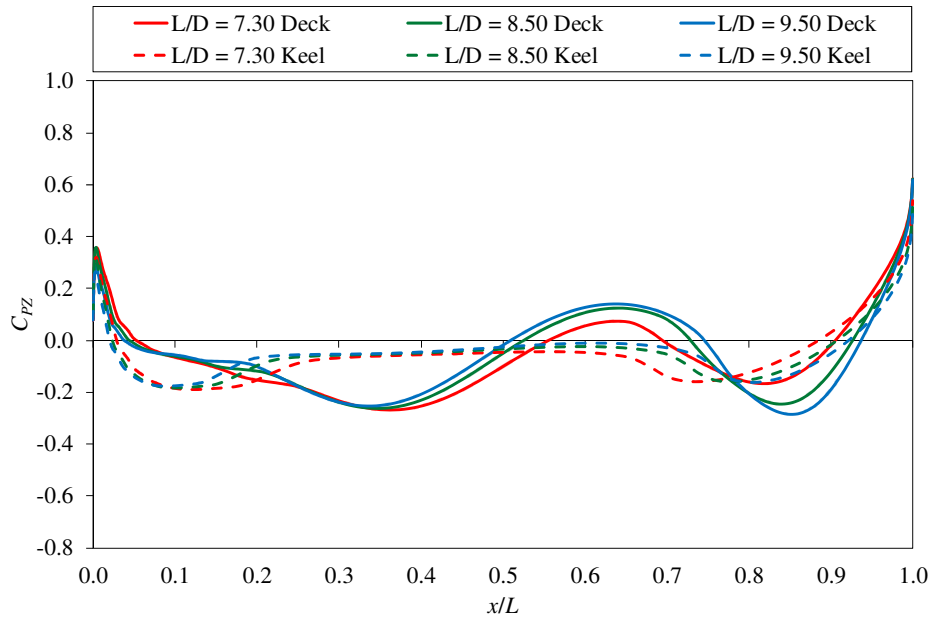


Figure 7-28 SHIPFLOW simulation results: effect of L/D on the distribution of the vertical pressure coefficient component (C_{pz}) along the length of the Joubert geometry at $H^* = 1.02$ and $Fr = 0.30$.

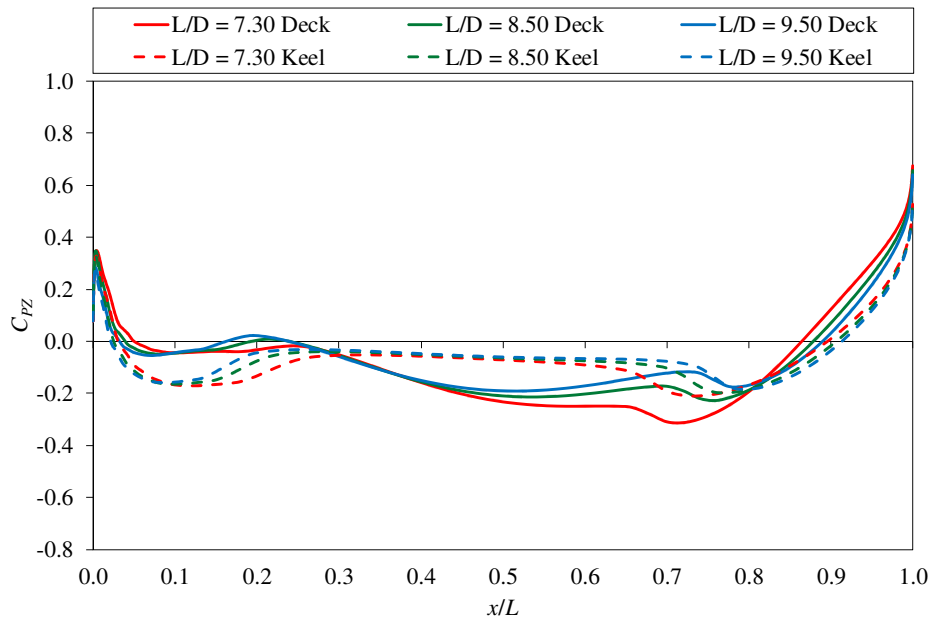


Figure 7-29 SHIPFLOW simulation results: effect of L/D on the distribution of the vertical pressure coefficient component (C_{pz}) along the length of the Joubert geometry at $H^* = 1.02$ and $Fr = 0.40$.

7.3.3 TRIMMING MOMENT COEFFICIENT

The trimming moment coefficient data for the $L/D = 7.30$, $L/D = 8.50$ and $L/D = 9.50$ Joubert model configurations are presented in Figure 7-30, Figure 7-31 and Figure 7-32 respectively. The data indicates that there are significant interaction effects occurring for the shallower submergence depths ($H^* = 1.02$ and 1.30); however, the influence of the free-surface diminishes rapidly between $H^* = 1.30$ and 2.16 . At $H^* = 1.02$ and 1.30 the trimming moment response of the models varies periodically with Froude number and oscillates between a slightly bow up and a slightly bow down trimming moment until approximately $Fr = 0.35$. Beyond $Fr = 0.35$ the models develop a substantial trim down by the bow. Like the total resistance response, the free-surface interaction effects diminish with a reduction in speed and an increase in submergence depth. The oscillation between the bow up and bow down trimming moments is attributed to the change in the wavelength of the body-generated free-surface wave system and the influence that it has on the pressure field surrounding the submerged body. As the wave system's wavelength and amplitude change with a change in speed, the net centre of pressure acting on the body is shifted about the trimming moment datum (the body's mid-length) resulting in a change in the direction and magnitude of the trimming moment. The effect of the body length-to-diameter is consistent with the lift force coefficient results, where an increase in L/D results in a reduction in the lift force per unit area and consequently, a reduction in the trimming moment for the speeds at which free-surface interaction occurs (Figure 7-33).

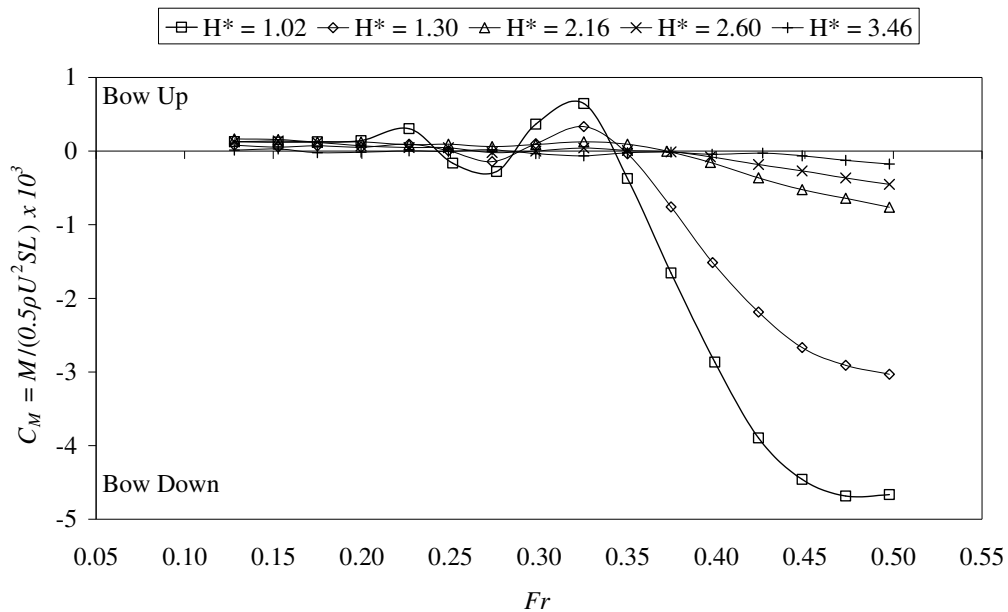


Figure 7-30 Trimming moment coefficient (C_M) Joubert $L/D = 7.30$

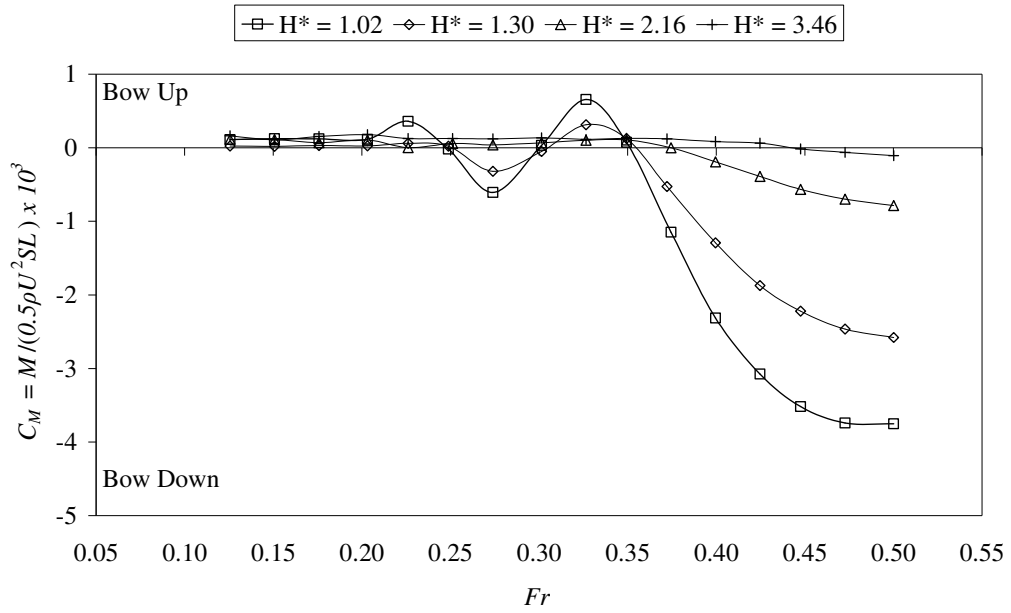


Figure 7-31 Trimming moment coefficient (C_M) Joubert $L/D = 8.50$

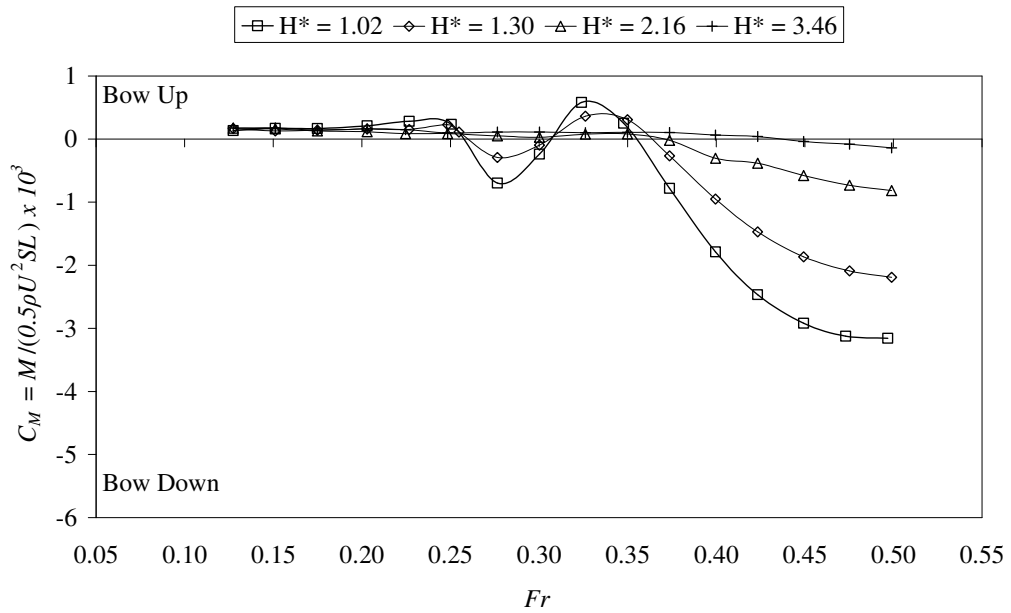


Figure 7-32 Trimming moment coefficient (C_M) Joubert $L/D = 9.50$

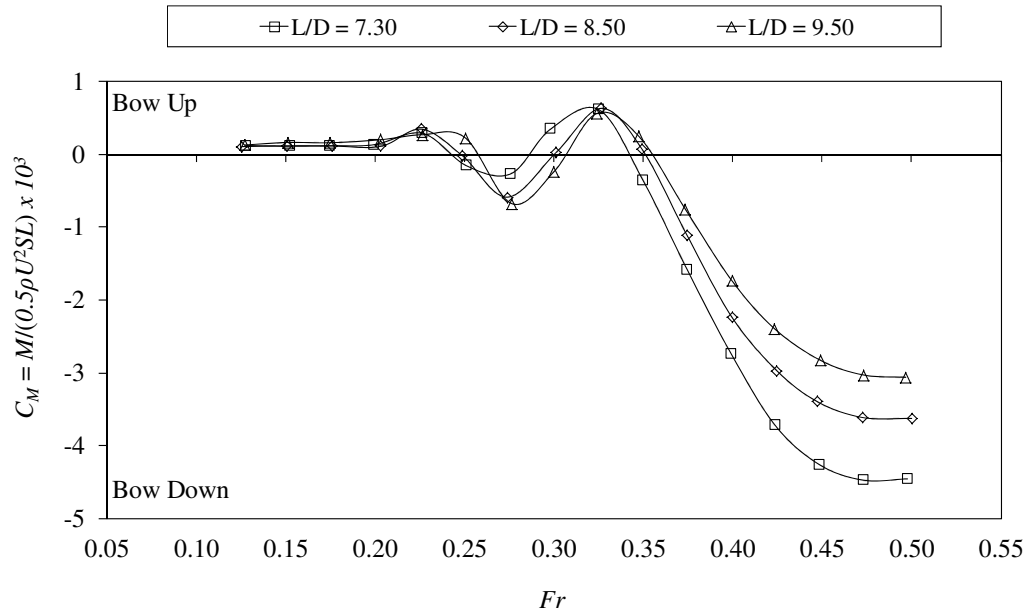


Figure 7-33 Trimming moment coefficient (C_M) $H^* = 1.02$ (Joubert Models)

Experimentally measured data for the three Joubert geometries indicate that the trimming moment acting on the submerged bodies due to their self-induced free-surface wave system is near-negligible for centreline submergence depths of approximately two hull diameters or more for the range of near-surface operational speeds. At the Froude numbers where the local peak trimming moment occurs and for $Fr > 0.35$ the trimming moment decays exponentially with an increase in submergence depth (Figure 7-34 to Figure 7-38). For the range of speeds and depths tested in this investigation, the observed rate of decay of the trimming moment coefficient is not as large as the lift force coefficient. This indicates that there is a greater reduction in the lift force than the trimming moment for an equal increase in submergence depth.

At the shallower submergence depths the trimming moment oscillates between a bow up and a bow down trimming moment as speed increases above $Fr \approx 0.20$ (around 10 knots). Below $Fr \approx 0.20$ the trimming moment appears to be negligible. The effect of the body length-to-diameter ratio indicates that the shorter ($L/D = 7.30$) geometry is more strongly influenced by the free-surface interaction and experiences the greater trimming moment coefficient for the range of speeds and submergence depths investigated. Similar to the lift force coefficient results, the trimming moment behaviour of the three Joubert models is in agreement with the anecdotal evidence provided by Crook (1994) and the numerical results published by Doctors and Beck (1987).

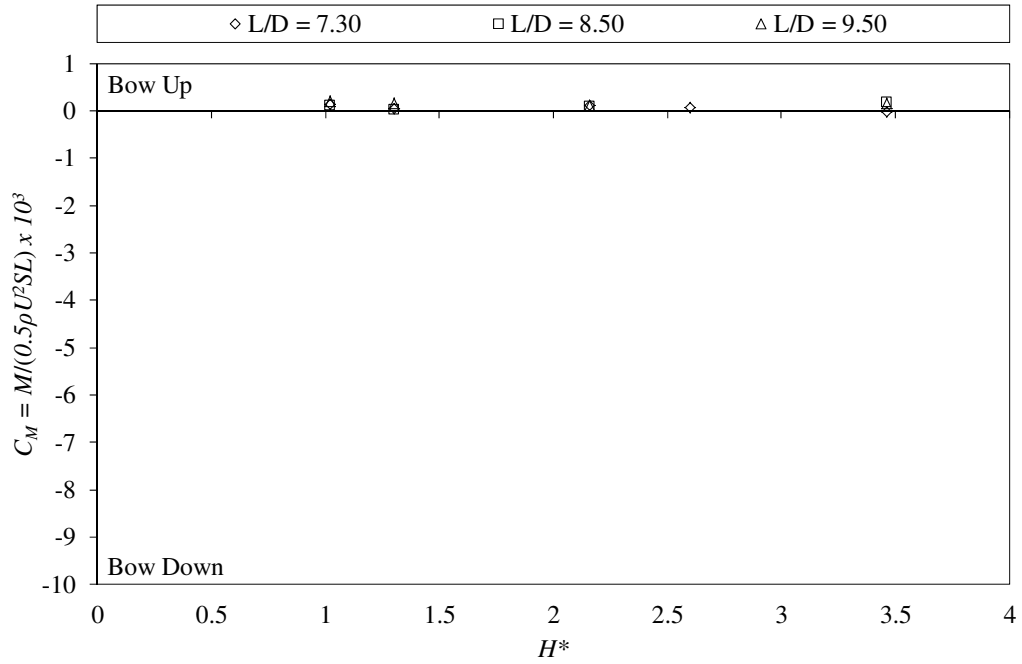


Figure 7-34 Effect of submergence depth (H^*) on trimming moment coefficient (C_M) at $Fr = 0.20$ (Joubert Models)

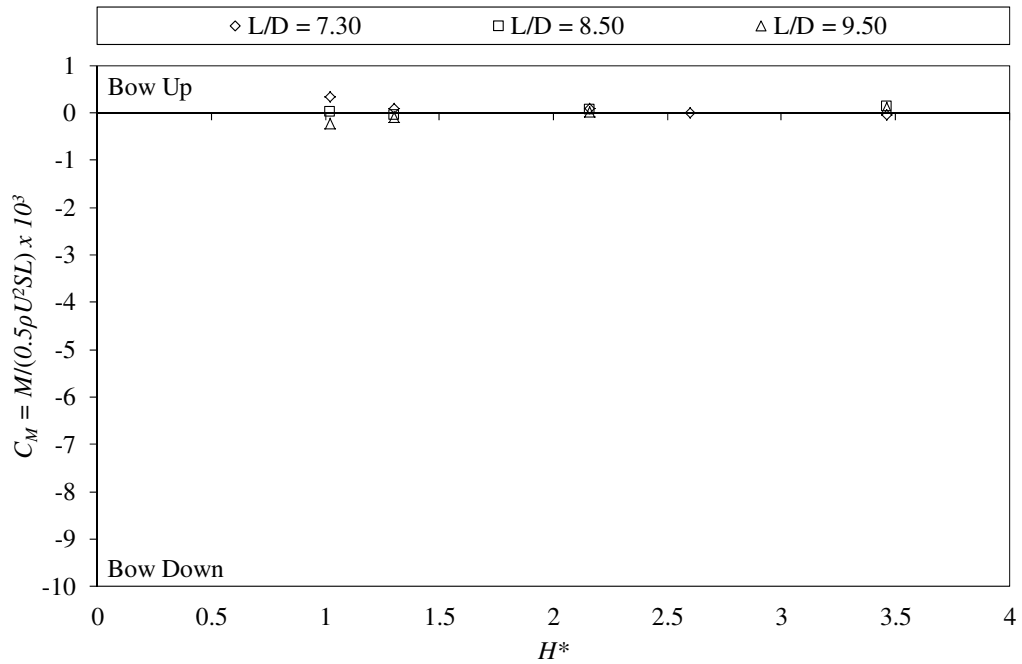


Figure 7-35 Effect of submergence depth (H^*) on trimming moment coefficient (C_M) at $Fr = 0.30$ (Joubert Models)

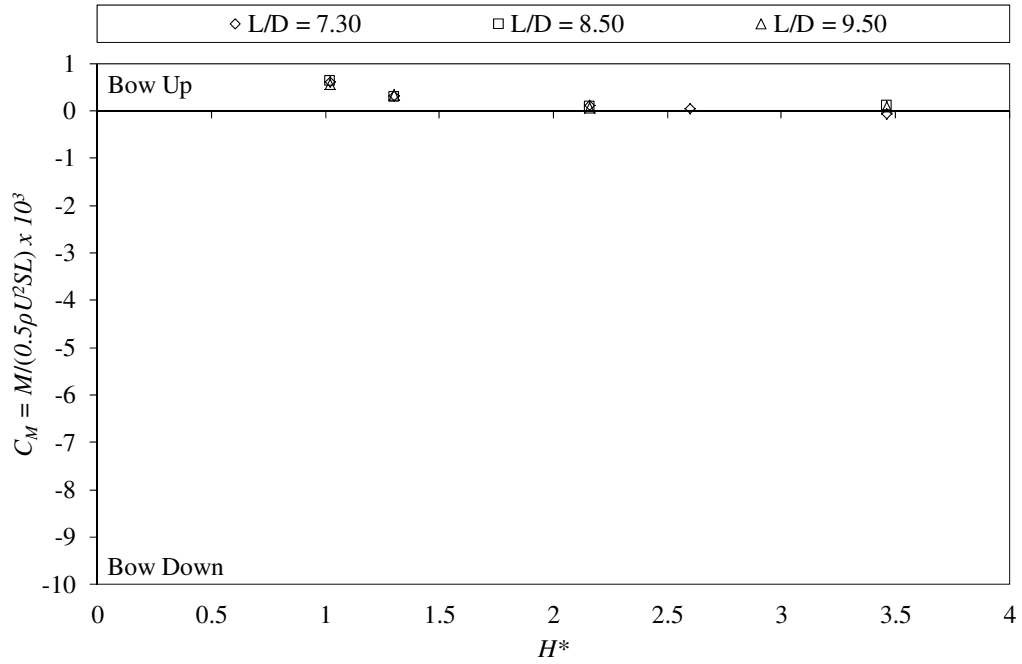


Figure 7-36 Effect of submergence depth (H^*) on trimming moment coefficient (C_M) at $Fr = 0.325$ (Joubert Models)

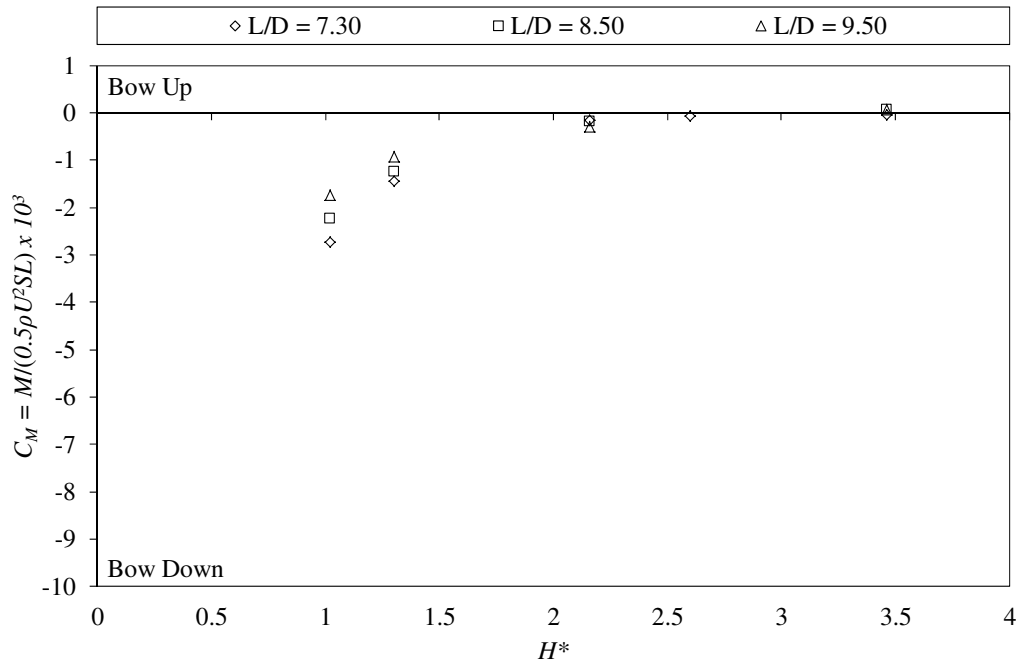


Figure 7-37 Effect of submergence depth (H^*) on trimming moment coefficient (C_M) at $Fr = 0.40$ (Joubert Models)

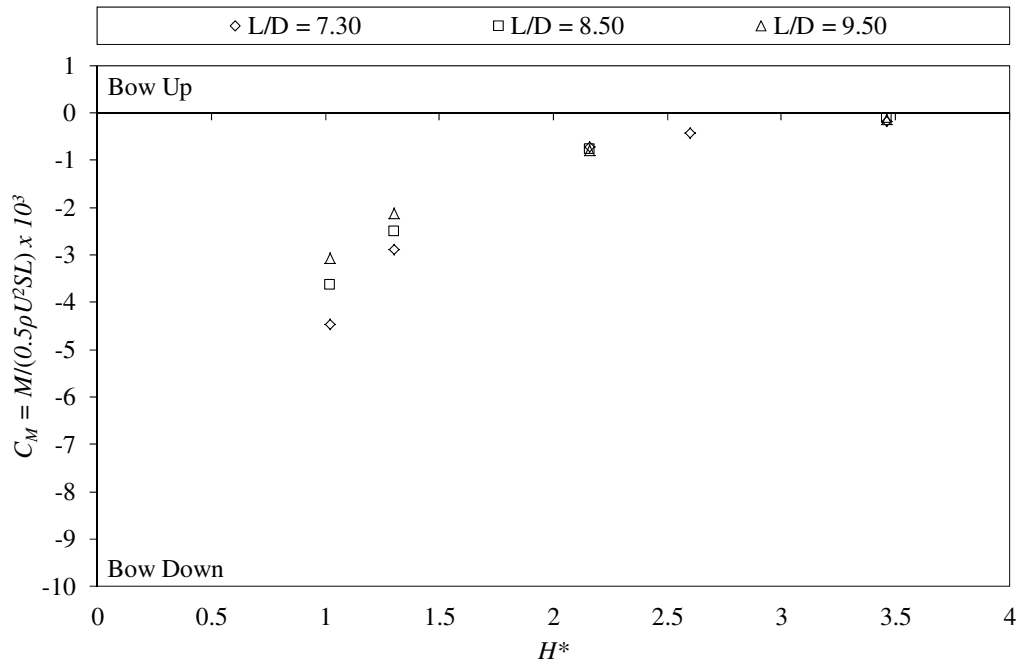


Figure 7-38 Effect of submergence depth (H^*) on trimming moment coefficient (C_M) at $Fr = 0.50$ (Joubert Models)

7.3.4 FREE-SURFACE WAVE PROFILE

The free-surface wave profiles measured for the three Joubert models displayed the following behaviours:

- The length and height of the waves generated by the models increased with an increase in forward speed.
- Wave height decreased with an increase in submergence depth for a constant speed.
- The free-surface wavelength is equal to the body length at approximately $Fr = 0.40$.
- The free-surface wave generated by the submerged body is initiated forward of the leading edge of the body.

The influence of Froude number on wavelength and wave height described above can be observed in Figure 7-39. This behaviour was found to be consistent for each of the three Joubert models across the range of Froude numbers tested.

Where wavelength and wave height are non-dimensionalised by the body length, the free-surface wave profiles are generally consistent between the three models. There is significant wave interaction generated by the mounting post as its wave field passes the wave probe array. As a consequence, the length of the body-only wave field data record is limited and is dependent on the test velocity: the slower the test velocity the longer the undisturbed wave field measurement record (Figure 7-40 and Figure 7-41).

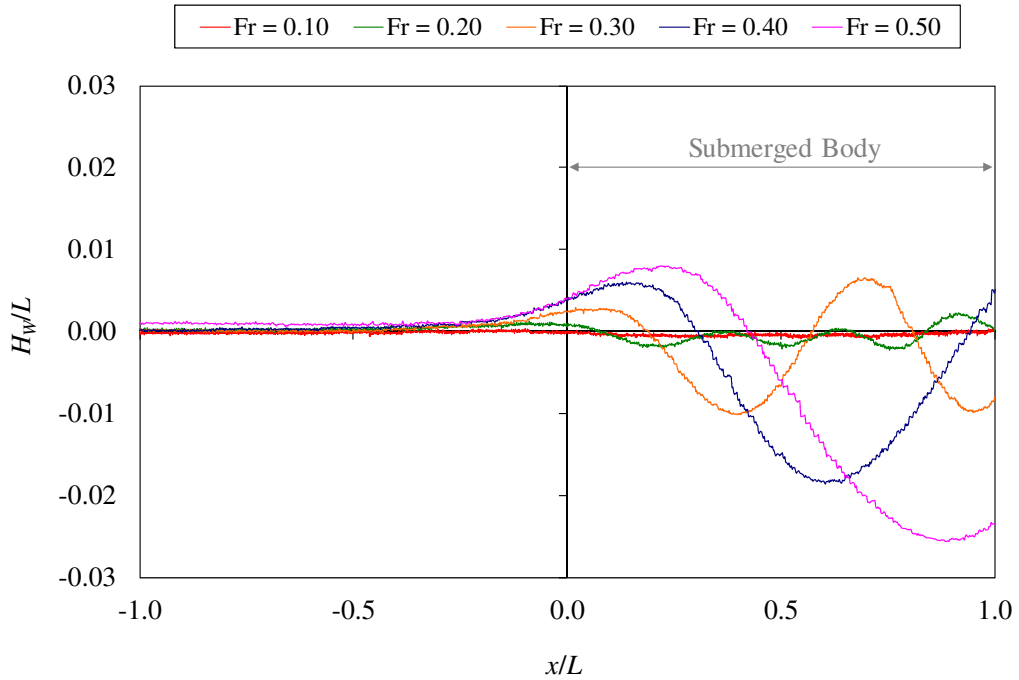


Figure 7-39 Effect of Froude number on wavelength and wave height: $H^* = 1.02$; Joubert $L/D = 7.30$; Wave Probe 1 ($y/D = 1.26$ off centreline) Note abscissa and ordinate scales

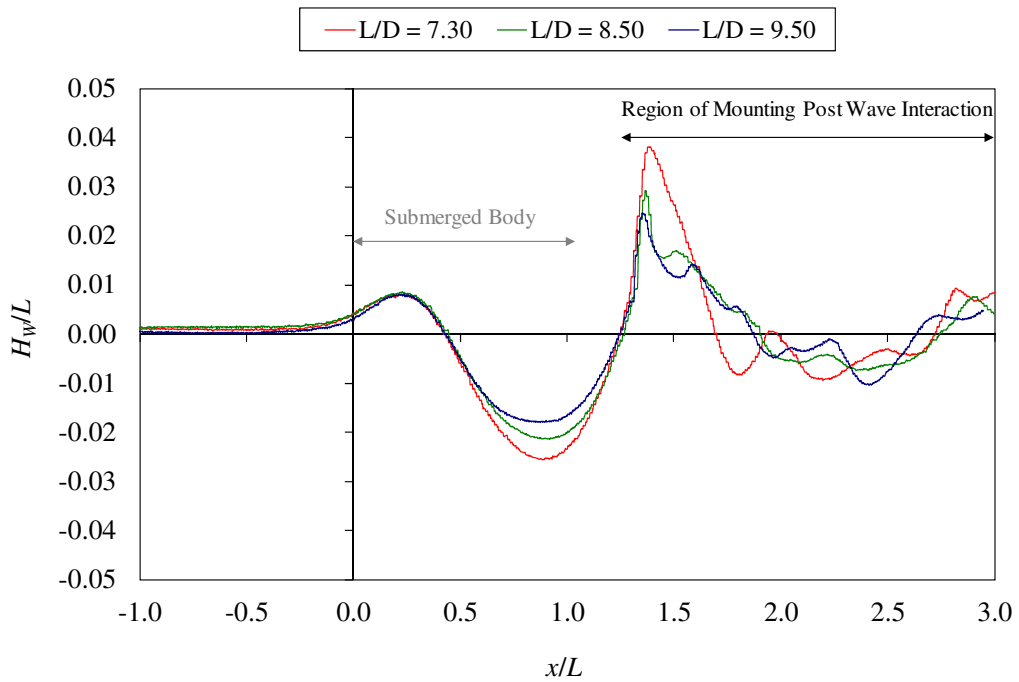


Figure 7-40 Effect of length-to-diameter ratio on wavelength and wave height: $H^* = 1.02$; $Fr = 0.50$; Wave Probe 1 ($y/D = 1.26$ off centreline) (Joubert Models) Note abscissa and ordinate scales

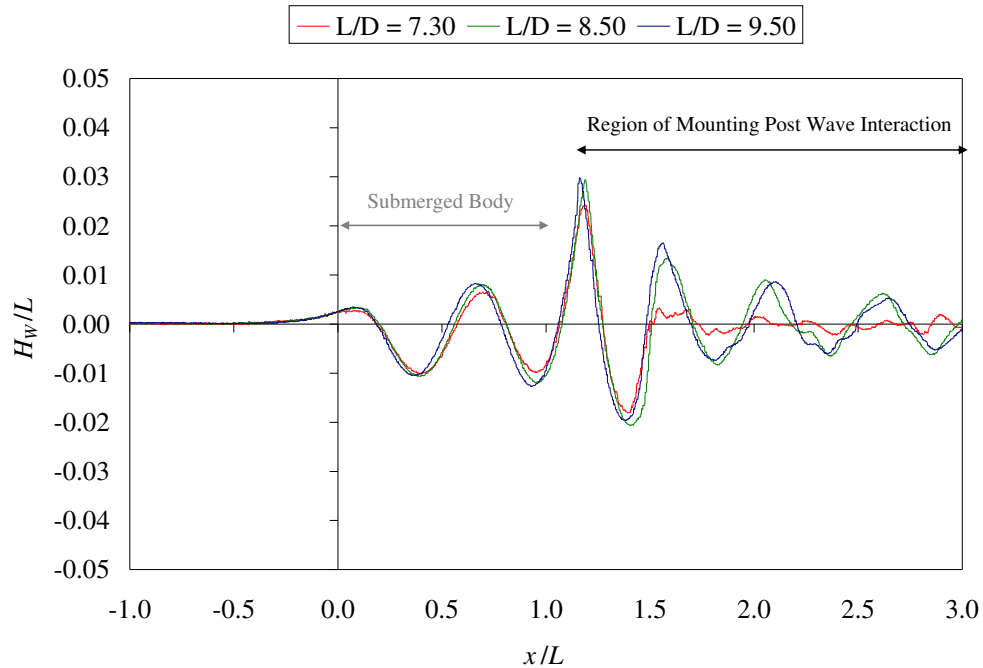


Figure 7-41 Effect of length-to-diameter ratio on wavelength and wave height:
 $H^* = 1.02$; $Fr = 0.30$; Wave Probe 1 ($y/D = 1.26$ off centreline) (Joubert Models)
Note abscissa and ordinate scales

As described in section 3.1.3, the geometric attributes of the body-generated steady-state wave system are directly related to the hydrodynamic pressure field surrounding the body. Figure 7-42 and Figure 7-43 illustrate the relationship between the pressure distribution on the body (the regions of relative high and low pressure) and the wave profile (the wave crests and troughs). Although this comparison is made using the inviscid solution generated using SHIPFLOW which, as previously discussed, differs from the viscous solution in the region of the body's trailing edge, it is evident there is good correlation between the locations of high and low pressure and the wave's crests and troughs.

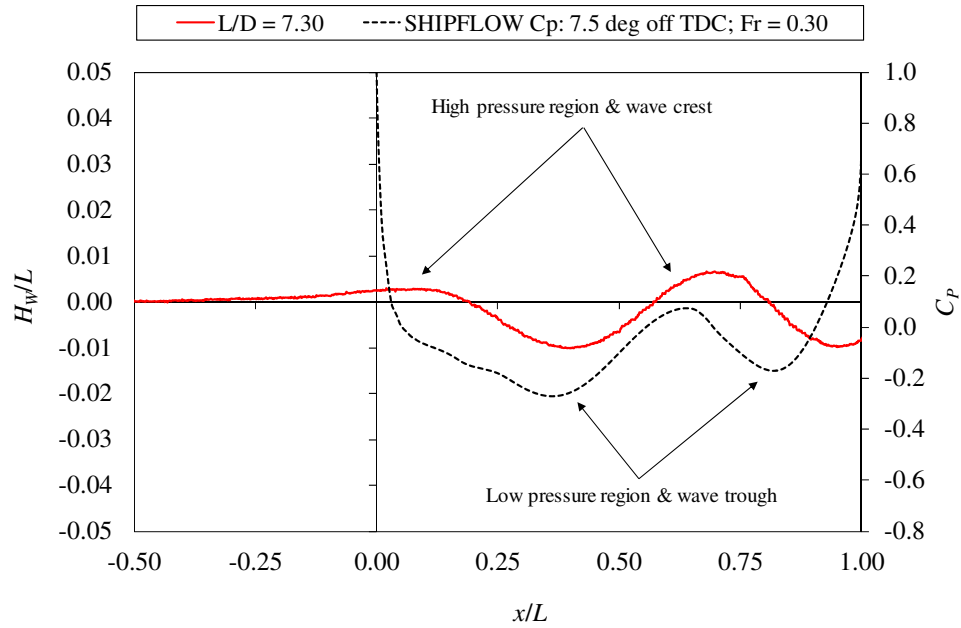


Figure 7-42 Comparison between SHIPFLOW predicted (inviscid) pressure coefficient distribution along the top of the Joubert $L/D = 7.30$ geometry at $H^* = 1.02$ and $Fr = 0.30$ and the experimentally measured wave profile at Wave Probe 1 ($y/D = 1.26$ off centreline)

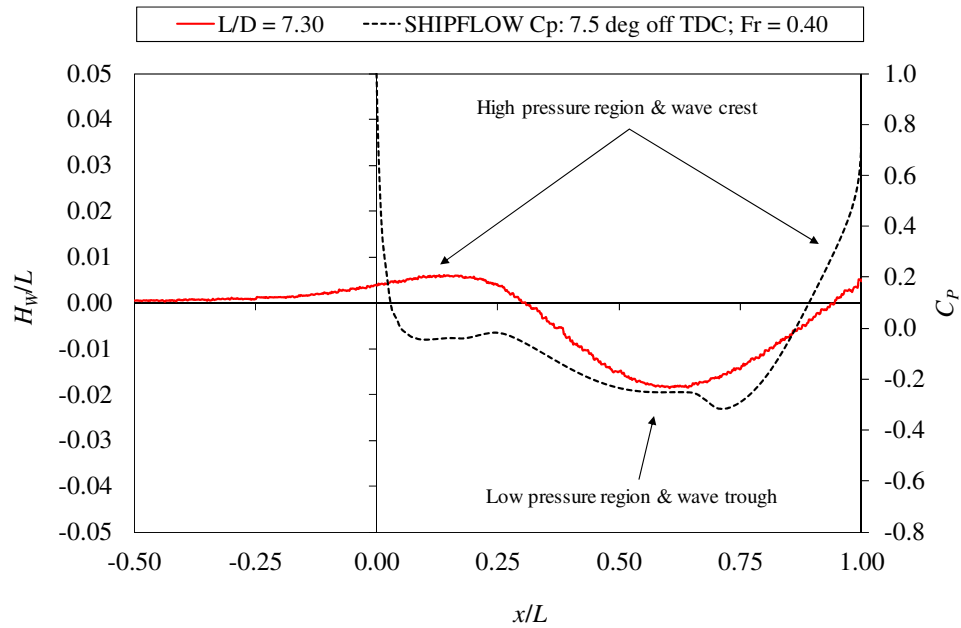


Figure 7-43 Comparison between SHIPFLOW predicted (inviscid) pressure coefficient distribution along the top of the Joubert $L/D = 7.30$ geometry at $H^* = 1.02$ and $Fr = 0.40$ and the experimentally measured wave profile at Wave Probe 1 ($y/D = 1.26$ off centreline)

The quasi-three dimensional measurement of the wave field provides an insight into the nature of the steady-state physical disturbance created by the submerged body as it moves beneath the free surface. The wave probe array measurements are presented with respect to the submerged body for $Fr = 0.20, 0.30, 0.40$ and 0.50 in Figure 7-44, Figure 7-45, Figure 7-46 and Figure 7-47 respectively. The wave-cut data illustrates the influence of forward velocity on the generation and propagation of the wave field on the free-surface. The data presented in these figures includes the wave fields generated by the body and the mounting system; however, the full hull geometry is presented instead of the actual test geometry for illustrative purposes. The geometric properties presented in these figures are to scale with regard to one another.

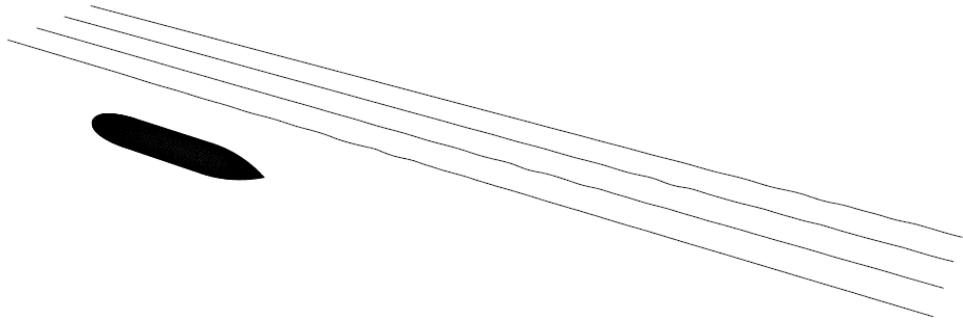


Figure 7-44 Longitudinal wave-cut Joubert $L/D = 7.30$; $H^* = 1.02$; $Fr = 0.20$

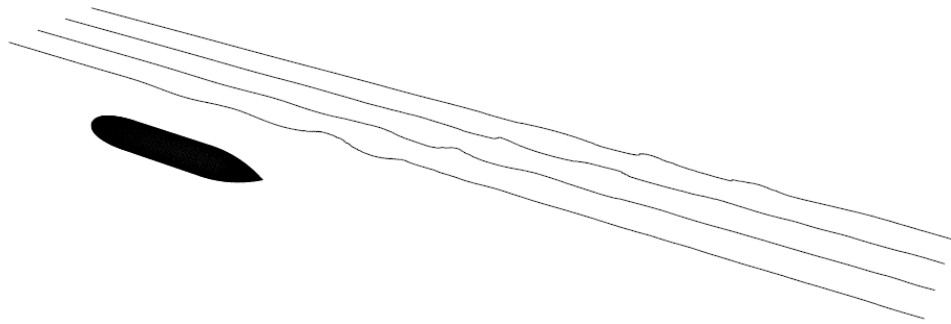


Figure 7-45 Longitudinal wave-cut Joubert $L/D = 7.30$; $H^* = 1.02$; $Fr = 0.30$

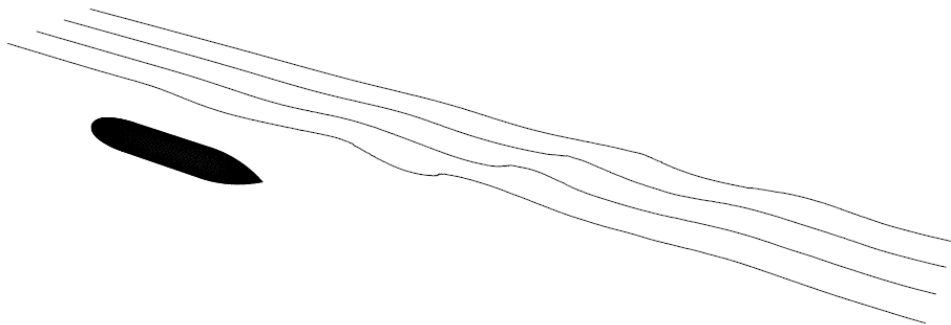


Figure 7-46 Longitudinal wave-cut Joubert $L/D = 7.30$; $H^* = 1.02$; $Fr = 0.40$

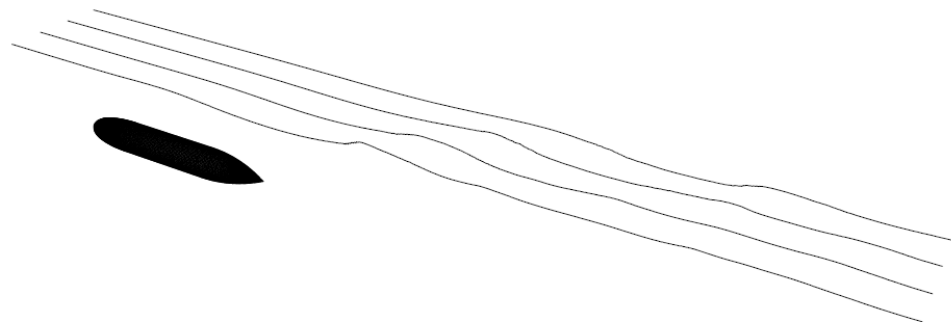


Figure 7-47 Longitudinal wave-cut Joubert $L/D = 7.30$; $H^* = 1.02$; $Fr = 0.50$

The wavelengths generated by the models were calculated based on the measured wave-cut data for $Fr = 0.20, 0.30, 0.40$ and 0.50 . Calculations were attempted at $Fr = 0.10$; however, the generated waves were indistinguishable from the measurement record at this speed. Comparisons were made against the theoretical wavelength formulation (previously presented by Weinblum et al. (1950)). The calculated data for the three Joubert models at $H^* = 1.02$ and 1.30 are presented in Table 7-1 and Table 7-2 respectively. It was observed that there is good agreement between the measured and theoretical ratio of wavelength to body length for the three Joubert models at $Fr = 0.20$ and 0.30 . At $Fr = 0.40$ the correlation is less accurate than at the lower speeds; however, it is still favourable. At $Fr = 0.50$ the calculated results based on the test data are consistently below the theoretical value. This behaviour can be readily observed in Figure 7-48 and Figure 7-49. It is surmised that the observed discrepancy is an artefact of the experiment and is related to the viscosity and surface tension of the fluid. As discussed in Section 8.3.2, the inviscid numerical solutions show a strong correlation across the Froude range tested.

Table 7-1 Wavelength to body length ratio for $H^* = 1.02$

	7.30	8.50	9.50	Theoretical
Fr	λ/L	λ/L	λ/L	$\lambda/L = 2\pi Fr^2$
0.10	-	-	-	0.06
0.20	0.24	0.31	0.29	0.25
0.30	0.55	0.55	0.55	0.57
0.40	0.96	0.87	0.86	1.01
0.50	1.33	1.38	1.27	1.57

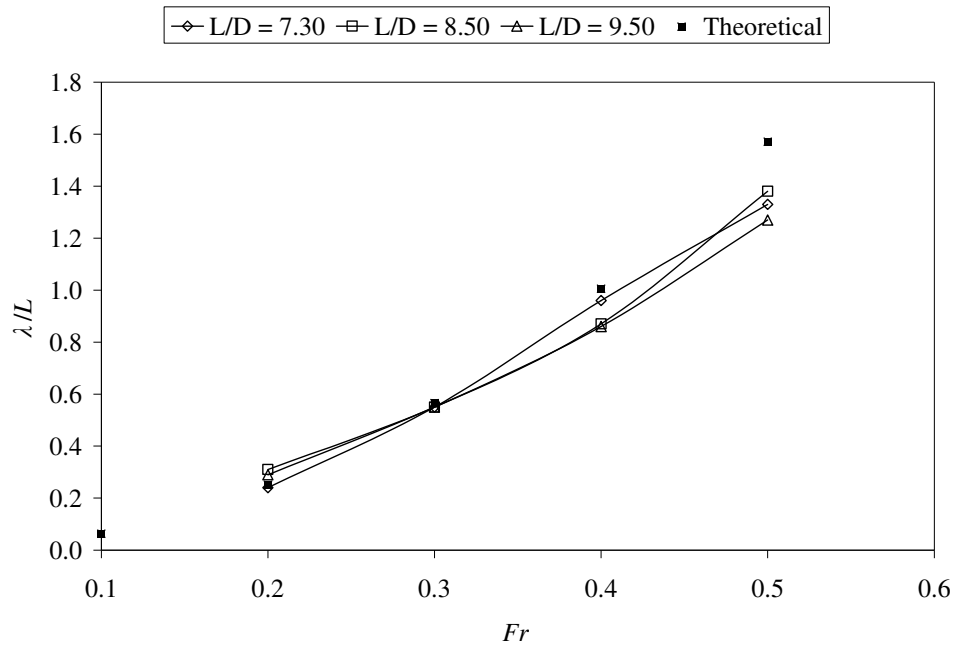


Figure 7-48 Effect of Froude number on non-dimensional wavelength (λ/L) for all Joubert models at $H^* = 1.02$

Table 7-2 Wavelength to body length ratio for $H^* = 1.30$

	7.30	8.50	9.50	Theoretical
Fr	λ/L	λ/L	λ/L	$\lambda/L = 2\pi \cdot Fr^2$
0.10	-	-	-	0.06
0.20	0.24	0.30	0.27	0.25
0.30	0.54	0.55	0.55	0.57
0.40	0.99	0.89	0.86	1.01
0.50	1.38	1.40	1.41	1.57

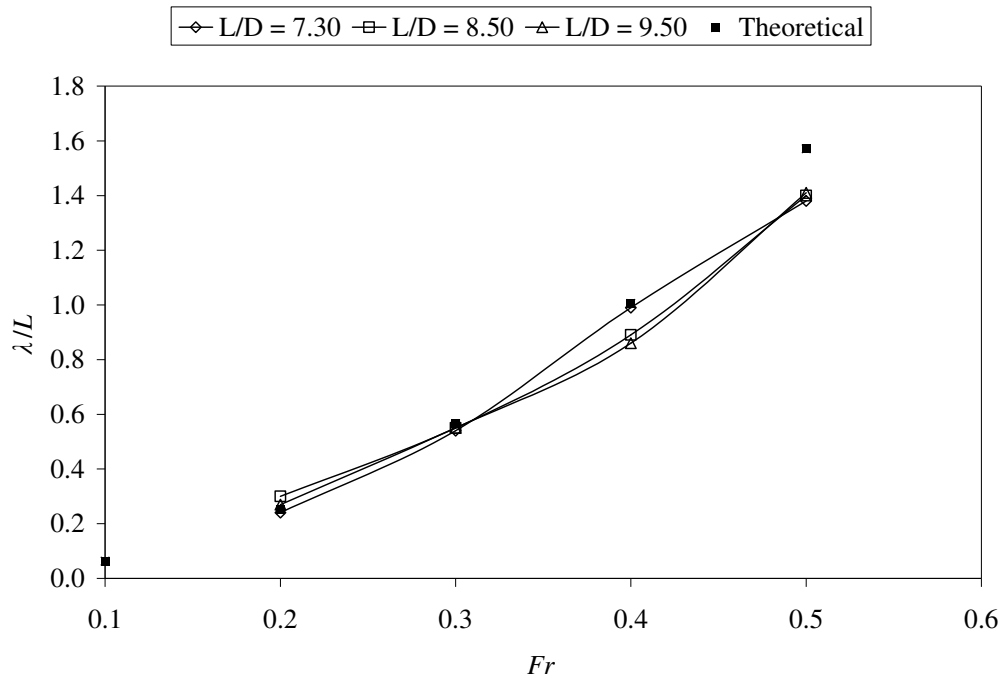


Figure 7-49 Effect of Froude number on non-dimensional wavelength (λ/L) for all Joubert models at $H^* = 1.30$

8 NUMERICAL RESULTS

The results of the SHIPFLOW simulations conducted as part of this research are presented in this section. In most cases the results are compared directly to the experimental and numerical results of other authors as well as against the experimental results generated as part of the current research. Where necessary, the results of other authors have been digitised from copies of the original data. In these instances every effort has been made to ensure that the digitised results are an accurate reproduction of the originating material.

8.1 BASELINE STUDY OF A $L/D = 5.00$ PROLATE SPHEROID

The results of the SHIPFLOW simulation of the $L/D = 5.00$ spheroid for $H^* = 0.80$ and 1.225 are presented in this section. The simulation scenarios completed using SHIPFLOW represent those presented by Doctors and Beck (1987). The SHIPFLOW simulation model characteristics are described in Section 6. The spheroid's normal pressure coefficient distribution was computed using SHIPFLOW. The velocity ratio (u/U) was calculated based on the pressure coefficient using Equation 8-1. A comparison was made between the longitudinal velocity ratio distribution derived from the SHIPFLOW data and the analytical solution published by Belibassakis et al. (2009). The SHIPFLOW solution data was observed to be in good agreement with the analytical solution (Figure 8-1).

$$\frac{u}{U} = \sqrt{1 - C_P} \quad \text{Equation 8-1}$$

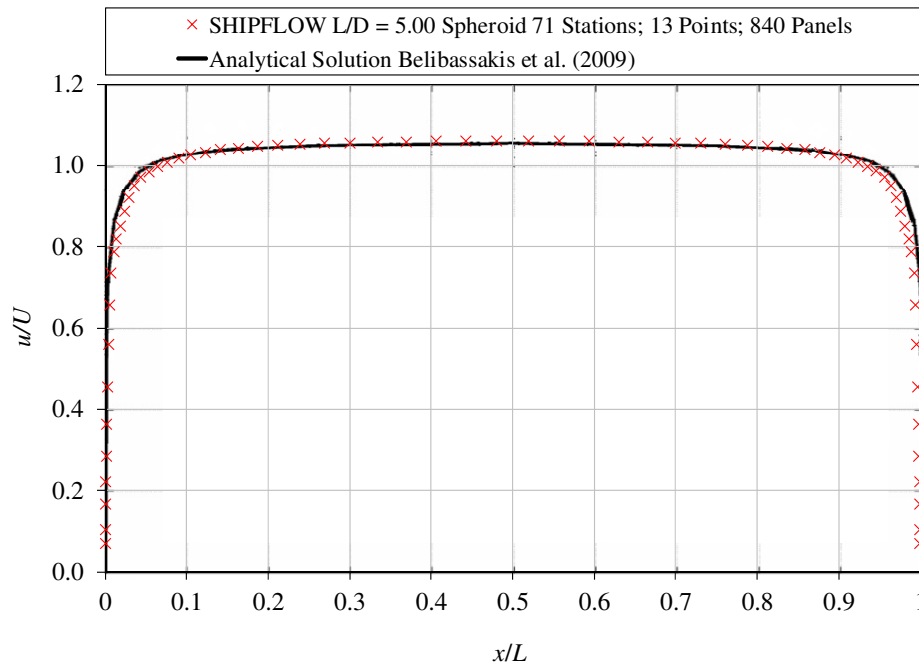


Figure 8-1 Velocity distribution along the longitudinal axis of the spheroid: Comparison between SHIPFLOW result and the analytic solution presented by Belibassakis et al. (2009)

A comparison between the SHIPFLOW simulated wave resistance coefficient and the results published by Doctors and Beck (1987) is presented in Figure 8-2. It can be seen that there is excellent agreement between the two sets of results at both submergence depths, in particular for Froude numbers greater than $Fr = 0.45$. At Froude numbers less than $Fr = 0.45$ the SHIPFLOW results are consistently higher than those generated by Doctors and Beck (1987) using the Galerkin method; however, the trend is consistent between the two sets of data.

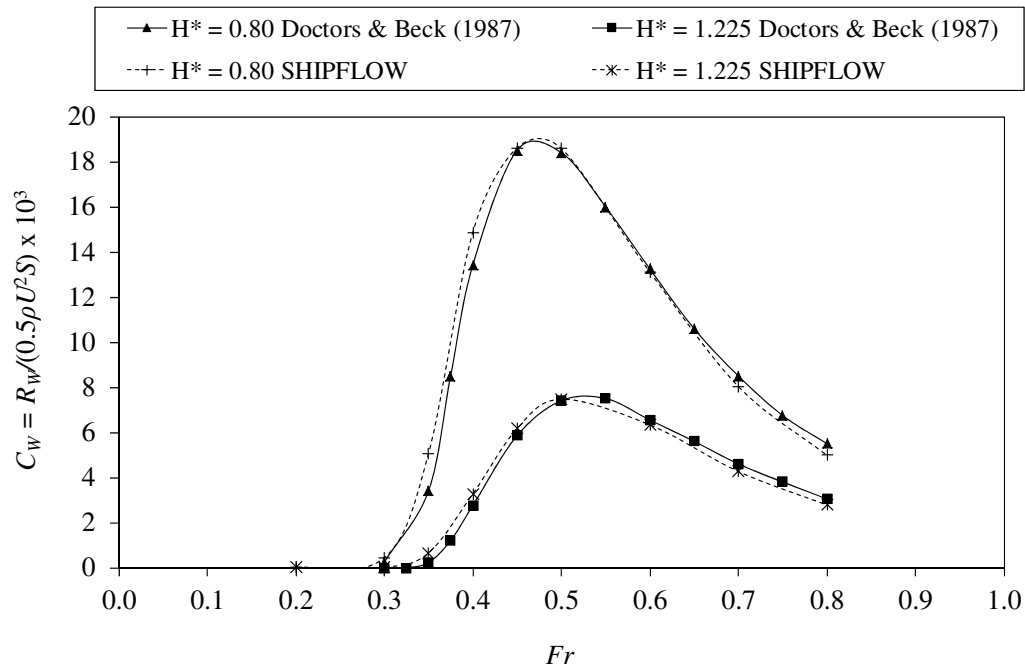


Figure 8-2 Wave resistance coefficient of 5:1 spheroid: comparison between SHIPFLOW solution and results presented by Doctors & Beck (1987).

The comparison between the SHIPFLOW lift coefficient data and the results generated by Doctors and Beck (1987) are presented in Figure 8-3. It can be seen that there is excellent agreement at the deeper submergence depth ($H^* = 1.225$); however, at $H^* = 0.80$ the comparison shows that the lift force coefficient predicted using SHIPFLOW is typically lower than that calculated by Doctors and Beck (1987).

A direct comparison between the SHIPFLOW trimming moment coefficient data (Figure 8-4) and the results presented by Doctors and Beck (1987) has not been made, because Doctors and Beck (1987) use a different reference system to the midship location used in this research. It is understood that Doctors and Beck (1987) calculated their trimming moment coefficient based on an origin located on the free-surface and not on the spheroid body itself. The exact location of the origin used by Doctors and Beck (1987) is not known and therefore no correction could be made to enable a comparison of equivalent data. Nonetheless, the form of the SHIPFLOW trimming moment coefficient results is consistent with those observed in the results of Doctors and Beck (1987).

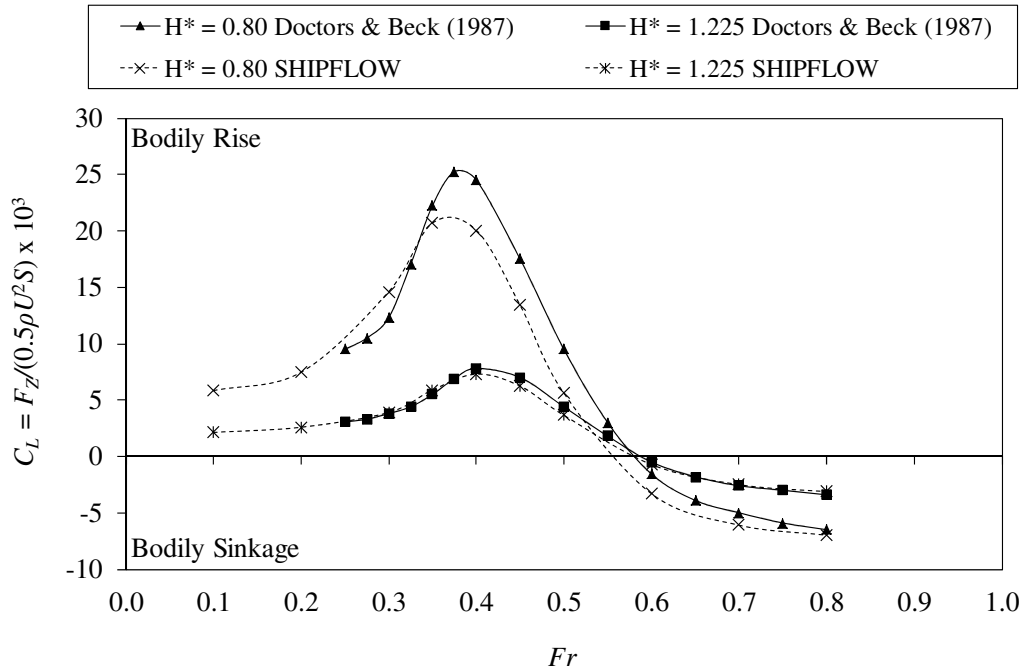


Figure 8-3 Lift coefficient of 5:1 spheroid: comparison between SHIPFLOW solution and results presented by Doctors & Beck (1987)

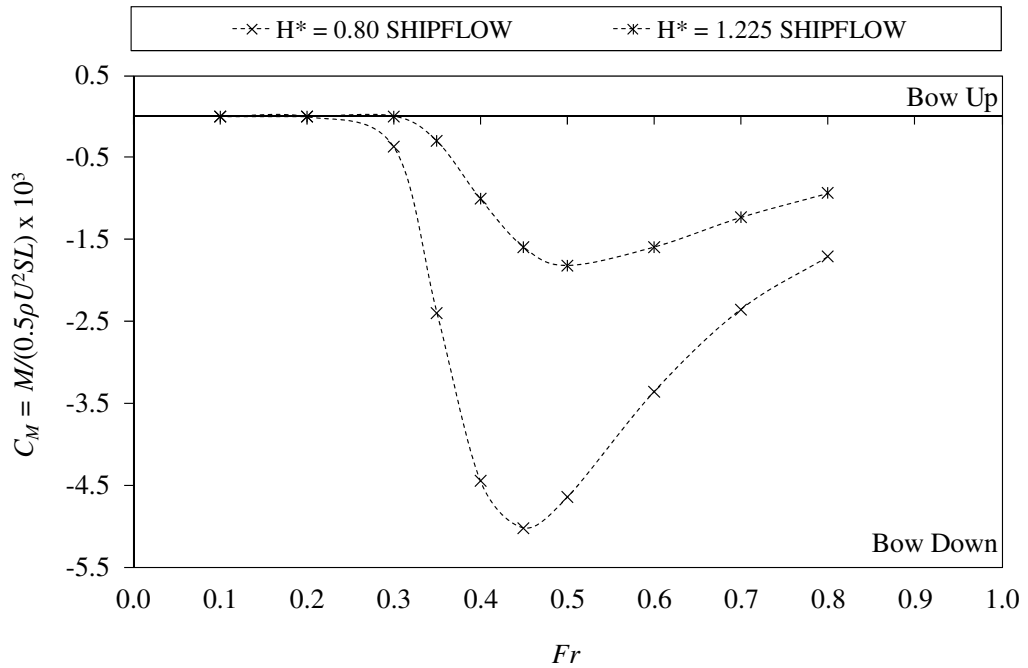


Figure 8-4 SHIPFLOW trimming moment coefficient of 5:1 spheroid

8.2 SHIPFLOW WAVE RESISTANCE FOR SERIES 58 MODEL 4166

The wave resistance coefficient of the Series 58 model 4166 was calculated using SHIPFLOW at the $H^* = 1.413$ submergence depth. This simulation scenario is equivalent to the residuary resistance coefficient test data presented by Gertler (1950) for the same model. A comparison between the residuary resistance coefficient published by Gertler (1950) and the wave resistance coefficient calculated using SHIPFLOW is presented in Figure 8-5. It is important to consider that the residuary resistance coefficient determined by Gertler (1950) is equal to the difference between the measured total resistance coefficient and the Schoenherr friction coefficient line (Equation 8-2).

$$C_R = C_T - C_{F_{Schoenherr}} \quad \text{Equation 8-2}$$

The comparison indicates that there is good agreement in the features displayed by the two sets of results: a well defined peak resistance coefficient value at $Fr = 0.50$ and a less clearly defined localised peak at $Fr = 0.30$. However, the relative magnitude of the two resistance coefficient curves is not consistent. Moreover, when the vertical offset is removed from the residuary resistance coefficient data the relative difference between the two data sets is non-uniform and varies with Froude number (Figure 8-6). This discrepancy is potentially due to the form effects of the three-dimensional body and the interaction effects observed by Farell and Güven (1973), where the interaction between the free-surface and the body results in a speed dependent increase in the viscous resistance component due to the deceleration of the flow surrounding the aft region of the body.

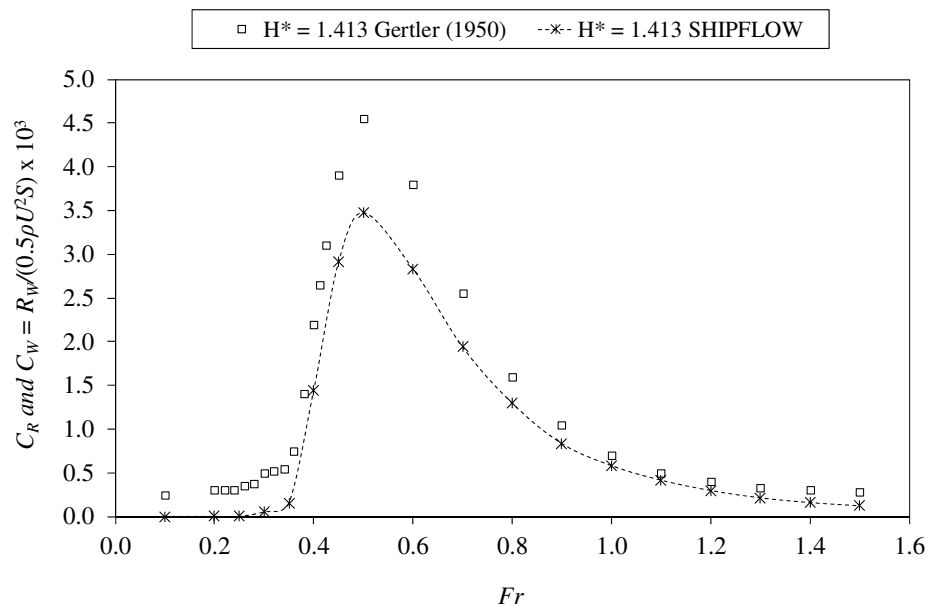


Figure 8-5 Residual resistance coefficient (C_R) of model 4166 measured by Gertler (1950) compared against wave resistance coefficient (C_W) calculated using SHIPFLOW $H^* = 1.413$

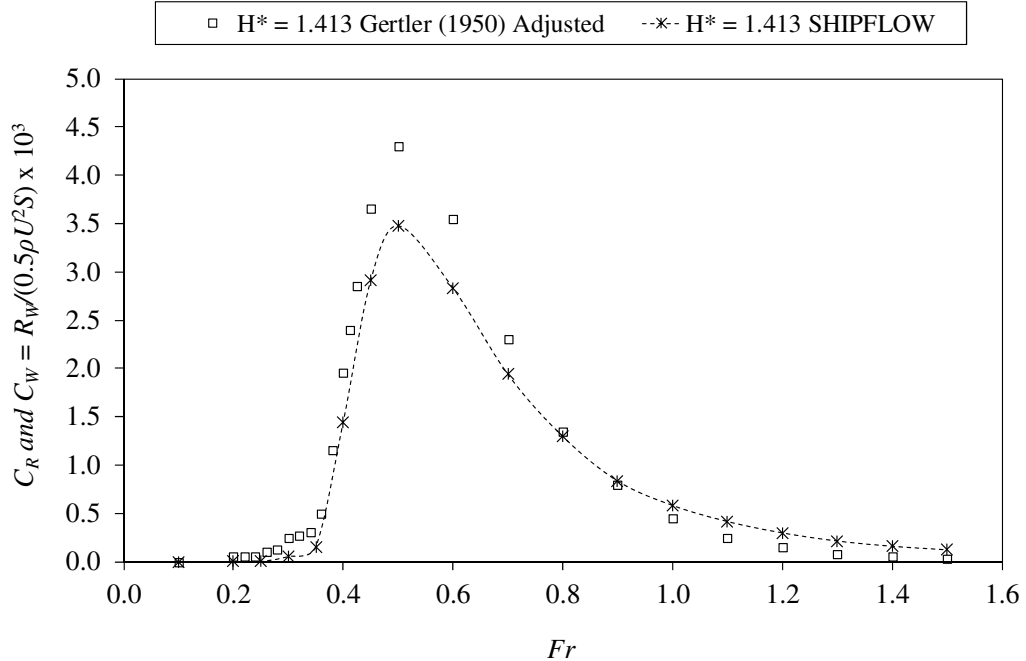


Figure 8-6 Adjusted residual resistance coefficient (C_R) of model 4166 measured by Gertler (1950) compared against wave resistance coefficient (C_W) calculated using SHIPFLOW $H^* = 1.413$

Since Gertler (1950) did not make measurements of the lift force and trimming moment acting on the Series 58 models, no direct comparisons can be made. Nonetheless, this data was calculated using SHIPFLOW. The lift force and trimming moment coefficients are presented in Figure 8-7 and Figure 8-8 respectively. The behaviour illustrated in these two data sets correlates with the observations made based on the numerical investigations reviewed in Section 3.3.

- a. There is a peak upwards lift force coefficient at approximately $Fr = 0.40$ and a transition from an upwards to a downwards lift force at approximately $Fr = 0.60$ (Figure 8-7).
- b. There is an oscillating trimming moment coefficient at low Froude numbers with a peak bow down trimming moment at approximately $Fr = 0.50$ and a trend indicating the trimming moment coefficient tending towards zero as the speed increases above $Fr = 0.50$ (Figure 8-8).

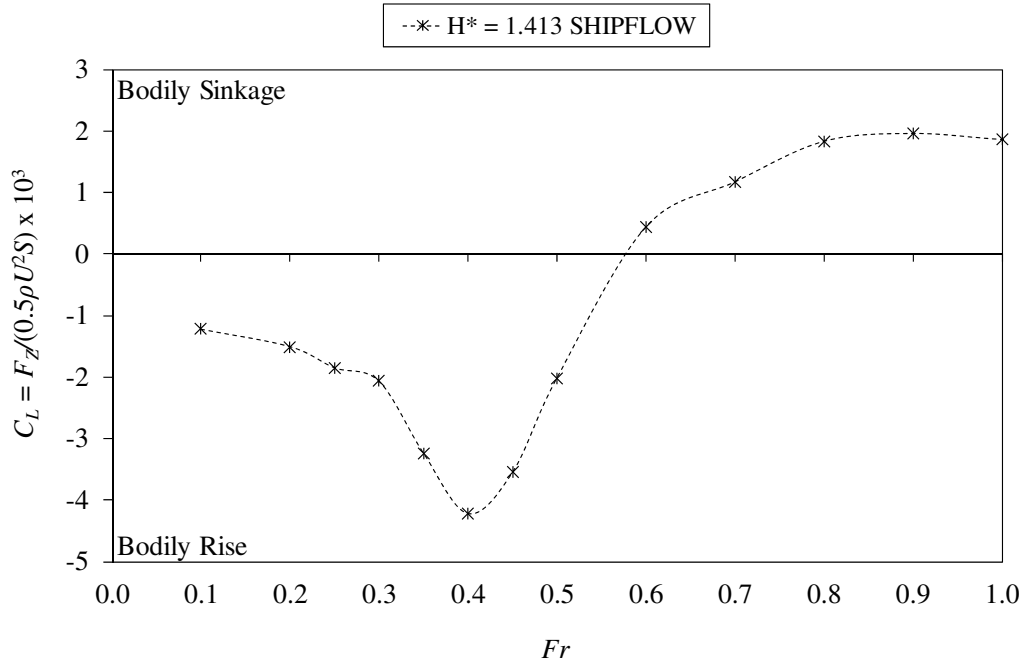


Figure 8-7 Lift coefficient (C_L) of model 4166 calculated using SHIPFLOW $H^* = 1.413$

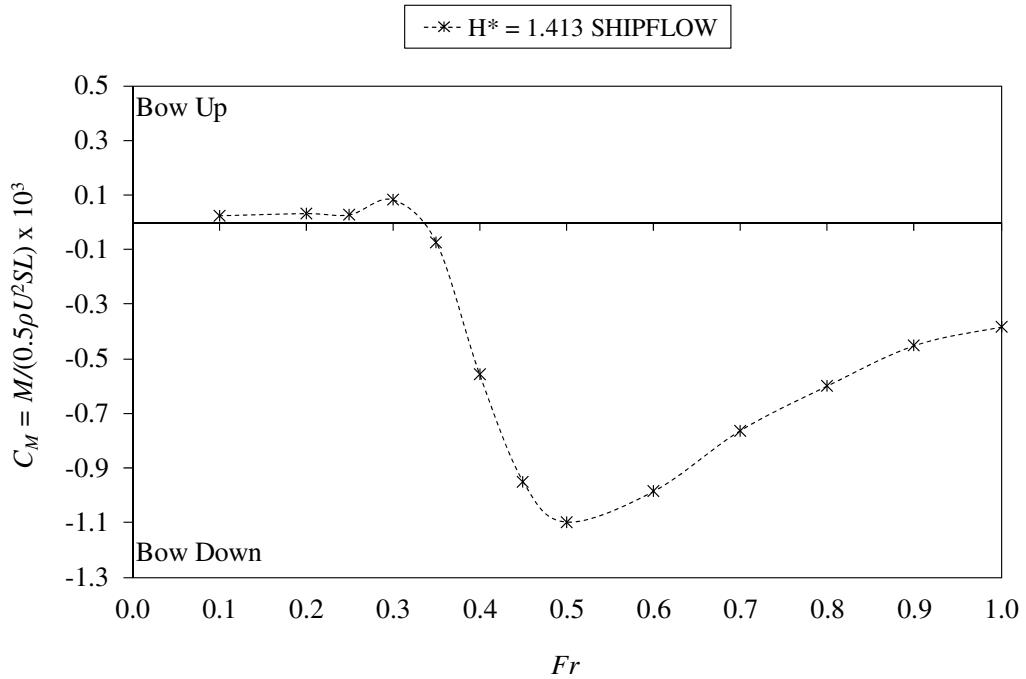


Figure 8-8 Trimming moment coefficient (C_M) of model 4166 calculated using SHIPFLOW $H^* = 1.413$

8.3 SHIPFLOW JOUBERT LENGTH-TO-DIAMETER SIMULATIONS

Numerical simulations of the Joubert bare hull geometry were completed using SHIPFLOW. The calmwater resistance coefficient, lift force coefficient and trimming moment coefficient data are compared with the corresponding experimental data for the three model configurations at submergence depths of $H^* = 1.02, 2.16$ and 3.46 . As described in Section 6.3, the simulated model comprised the submerged bare hull geometry and the free-surface only. However, the experimental data represents the forces and moments acting on the sting mounted truncated model.

8.3.1 PRESSURE COEFFICIENT

The pressure coefficient distribution of the $L/D = 7.30$ Joubert bare hull geometry was computed in an infinite fluid domain condition using SHIPFLOW. The numerical results are compared against the wind tunnel measurements of the same model geometry completed by Anderson et al. (2012). As can be seen in Figure 8-9, there is very good correlation between the calculated and measured pressure coefficient for the length of the body, up until approximately $x/L = 0.90$. Beyond this point and for the remainder of the length of the body the computed pressure coefficient diverges from the measured data. This is simply a result of the ideal fluid assumption on which the SHIPFLOW method is based: that the fluid is inviscid and therefore total pressure recovery is achieved.

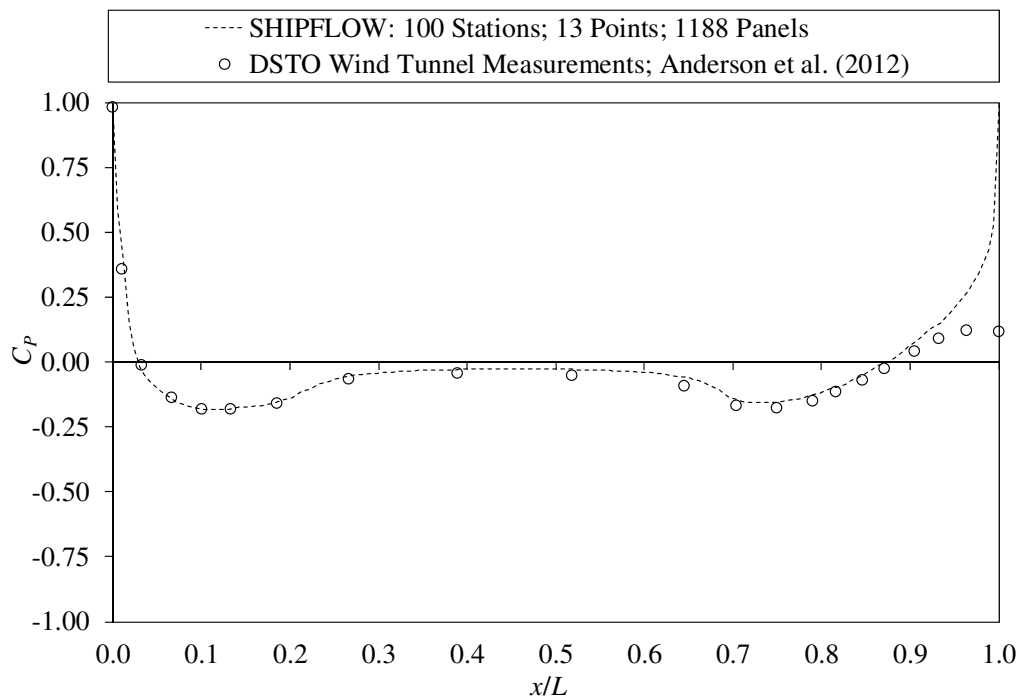


Figure 8-9 Joubert model: SHIPFLOW model: Longitudinal distribution of static pressure coefficient (C_p) Wind tunnel measurements taken at $U = 40$ m/s ($Re_L \approx 3,600,000$)

8.3.2 WAVE RESISTANCE COEFFICIENT

The wave resistance coefficient was calculated for the three Joubert length-to-diameter models at submergence depths equivalent to $H^* = 1.02$, 2.16 and 3.46 using SHIPFLOW and the transverse wave-cut method described in section 6.7.1. The results are compared with the residual resistance coefficient determined from the experimentally measured total resistance coefficient. The data is presented for the $L/D = 7.30$, 8.50 and 9.50 models in Figure 8-10, Figure 8-11 and Figure 8-12 respectively. The comparisons indicate that there is favourable correlation between the numerical and experimental data at $H^* = 3.46$ for $0.10 \leq Fr \leq 0.50$. For the $H^* = 1.02$ and 2.16 submergence depths the correlation is relatively poor for all of the models. There are significant discrepancies between the numerical and experimental resistance coefficient values in the regions of the localised peaks ($Fr \approx 0.30$ and $Fr \approx 0.50$). This discrepancy is further exacerbated when accounting for the approximately 15 percent increase in the total resistance due to the removal of the sting mounting system. Despite this, the wave-cut method was able to model these peaks. Due to the limited number of numerical simulations that were completed it cannot be determined whether the wave-cut method would adequately model the localised peak coefficient value that was observed at $Fr \approx 0.225$ for the $L/D = 8.50$ and 9.50 models (Figure 8-11 and Figure 8-12).

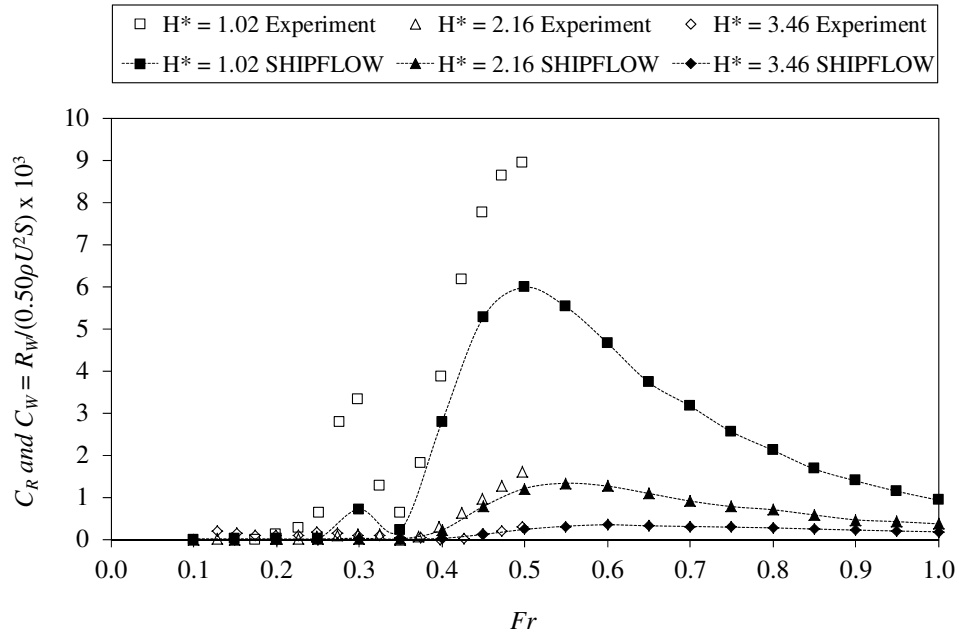


Figure 8-10 SHIPFLOW computations of $L/D = 7.30$ Joubert bare hull wave resistance coefficient (transverse wave-cut method) compared with residual resistance coefficient determined from experimental measurements

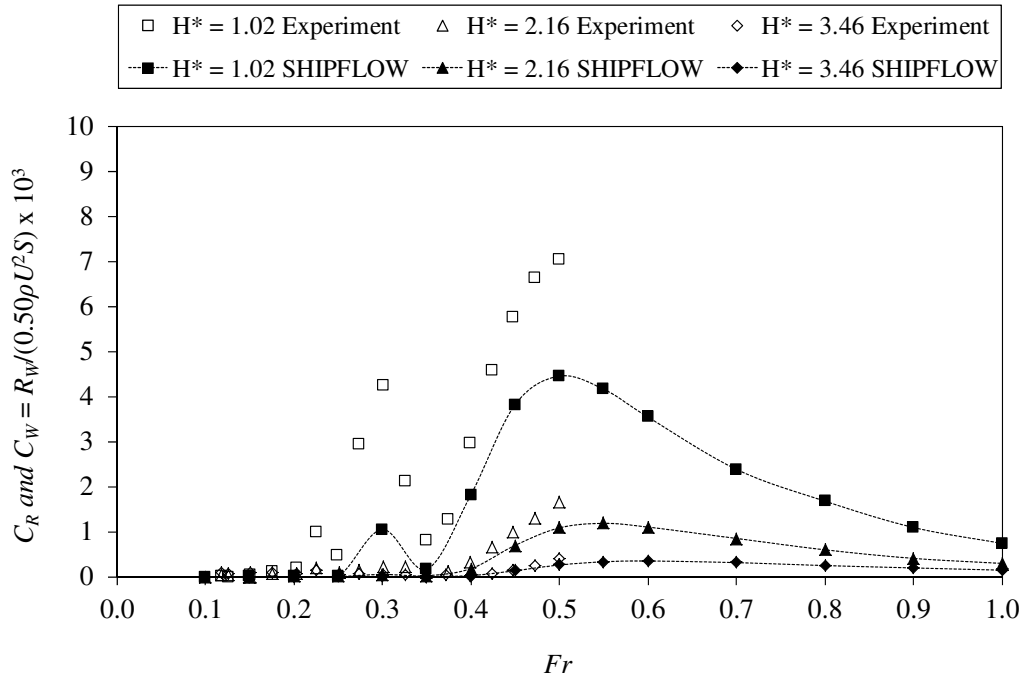


Figure 8-11 SHIPFLOW computations of $L/D = 8.50$ Joubert bare hull wave resistance coefficient (transverse wave-cut method) compared with residual resistance coefficient determined from experimental measurements

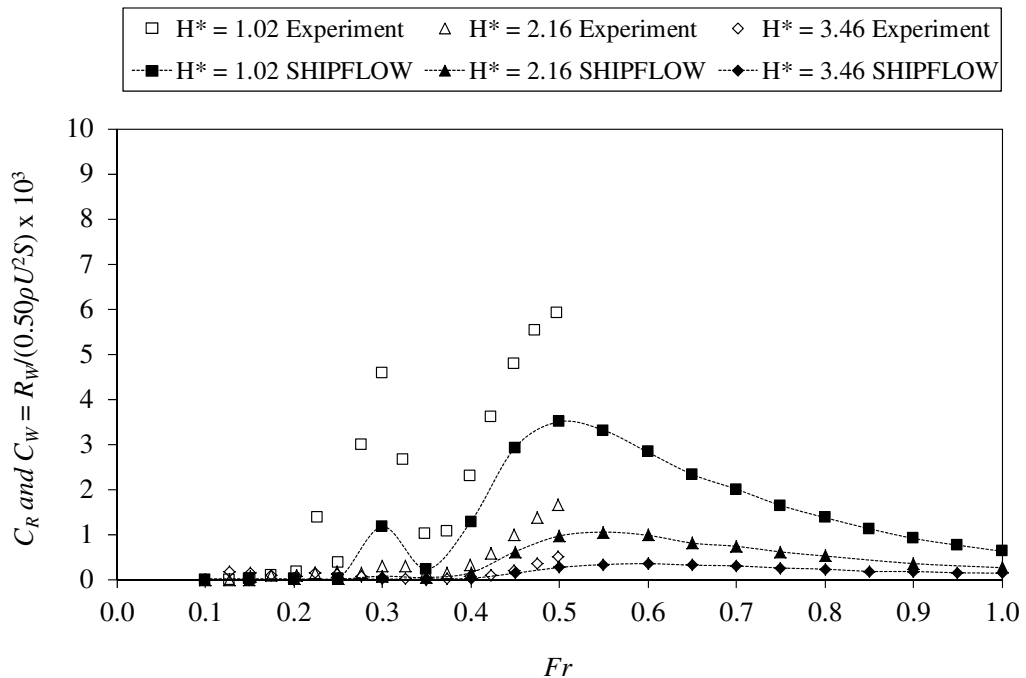


Figure 8-12 SHIPFLOW computations of $L/D = 9.50$ Joubert bare hull wave resistance coefficient (transverse wave-cut method) compared with residual resistance coefficient determined from experimental measurements

After a review of the wave-cut method results data, further analysis was completed to simulate and calculate the wave resistance coefficient of the three Joubert models using the integrated panel pressure method. The method is a standard approach to determining the force acting on the body by summing the force components which act on the body panels in the direction parallel to its longitudinal axis. The individual forces are determined by applying the panel pressure across the panel area and resolving it into its principal components. The results of the panel pressure method are compared with the transverse wave-cut method and the corresponding experimental data (presented in Figure 8-13, Figure 8-14 and Figure 8-15). The integrated panel pressure results show a more favourable agreement with the experimental data than the wave-cut method, in particular at $Fr = 0.30$. However, the integrated panel pressure method can be observed to under-predict the resistance coefficient for the majority of the Froude numbers tested.

It is surmised that the observed discrepancy is due to the following factors:

- a. The inviscid solver used in this investigation does not model the effect that viscosity has on the body's pressure distribution and the pressure recovery at its trailing edge. As discussed in section 3.1.1, this approach results in a zero drag force despite the relative velocity of the body through the fluid (D'Alembert's Paradox). Also, the method used to determine the experimental residual resistance coefficient does not separate the non-zero pressure drag force from the total resistance coefficient. As a result the residuary resistance coefficient will be greater than the inviscid wave resistance coefficient.
- b. The inviscid solver is unable to model the viscous boundary layer and wake field. As discussed earlier, the free-surface has been found to have a significant influence on the body's wake field and pressure distribution around the after-body which causes a considerable increase in the viscous drag component. This near-surface phenomenon is not accounted for in the method used to determine the residual resistance coefficient. Furthermore, as Farell and Güven (1973) state, it is necessary to complete wake field measurements to accurately determine the magnitude of this velocity dependent effect.
- c. The sting mounting arrangement was not included in the numerical model. The effect of the sting is related not so much to the reduced surface area upon which the pressure can act as to the reduction in the base pressure at the trailing edge of the experimental model. The presence of the sting results in a reduction in the normal pressure acting on the aft region of the experimental model and a net increase in the total pressure drag force.
- d. Due to the observed differences between the transverse wave-cut and panel pressure integration methods, it is possible that the numerical modelling and solution methods used also contribute to the difference between the residuary and wave resistance coefficients.

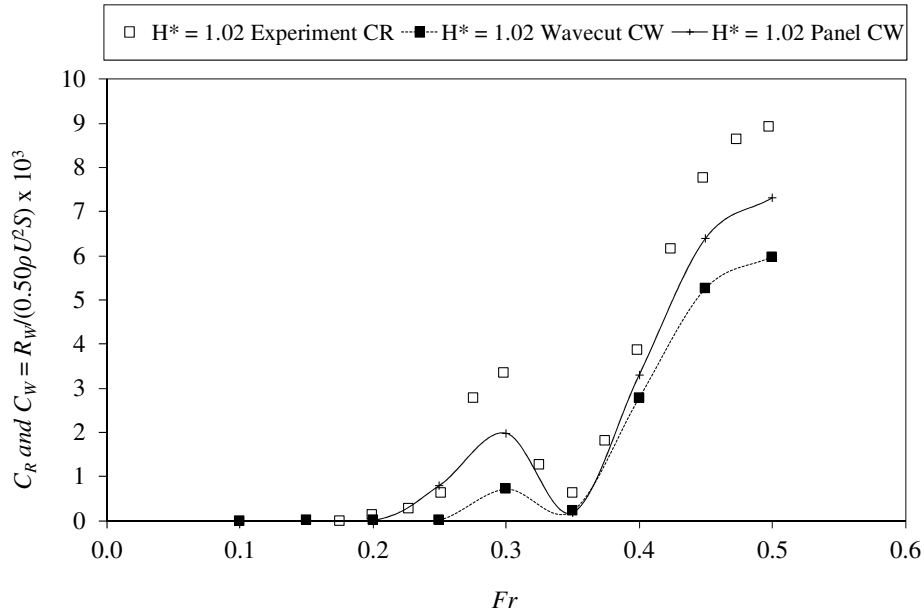


Figure 8-13 SHIPFLOW computations of $L/D = 7.30$ Joubert bare hull wave resistance coefficient (transverse wave-cut and integrated panel pressure method) compared with residual resistance coefficient determined from experimental measurements

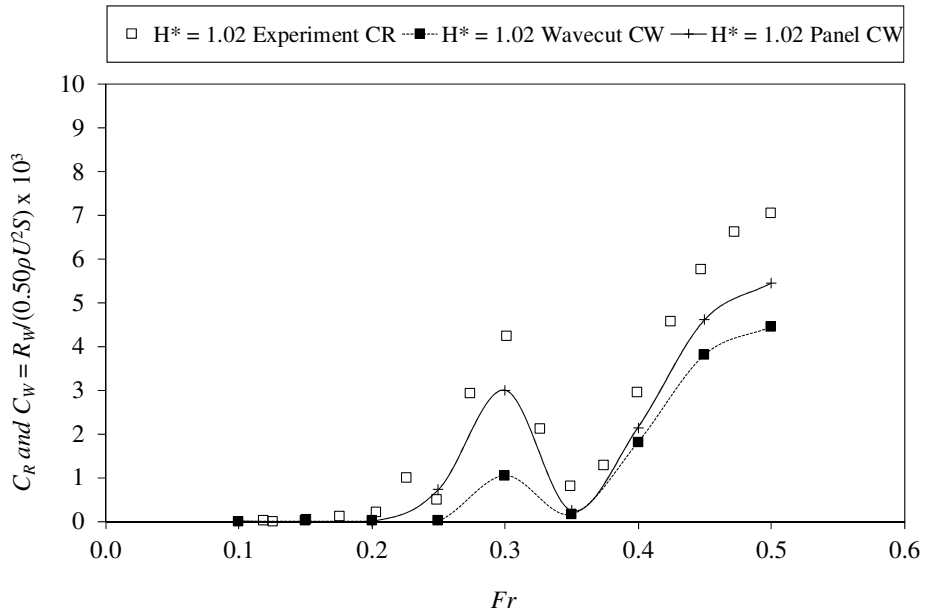


Figure 8-14 SHIPFLOW computations of $L/D = 8.50$ Joubert bare hull wave resistance coefficient (transverse wave-cut and integrated panel pressure method) compared with residual resistance coefficient determined from experimental measurements

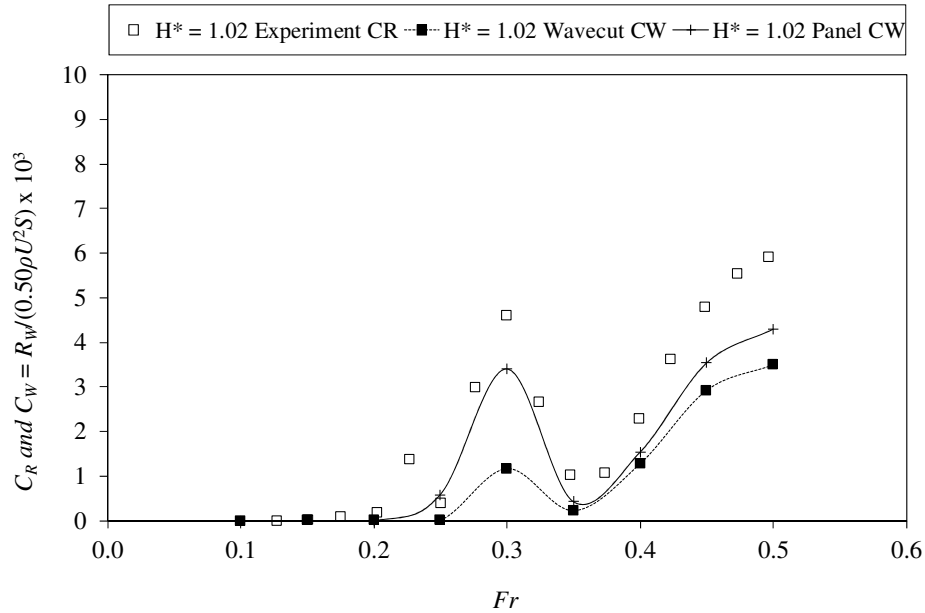


Figure 8-15 SHIPFLOW computations of $L/D = 9.50$ Joubert bare hull wave resistance coefficient (transverse wave-cut and integrated panel pressure method) compared with residual resistance coefficient determined from experimental measurements

Notwithstanding the influence of the free-surface it is apparent that, contrary to Van Mierlo's (2006) assertion, the transverse wave-cut method did not perform as well as the standard integrated panel pressure method. It is expected that if an extension of this research were undertaken to investigate the sensitivity of the wave-cut method dependent parameters, then more favourable results might be realised. However, completing such a study was in conflict with the schedule of the research program and was not completed.

Despite the discrepancy in magnitude, the SHIPFLOW wave resistance coefficient data is coherent and in agreement with the form observed by Weinblum et al. (1950) and Gertler (1950): the wave resistance coefficient varies periodically with Froude number, has a peak value that occurs at $Fr \approx 0.5$ and then diminishes towards zero as the speed increases. In addition, the numerical results show the distinct reduction in free-surface interaction as submergence depth is increased.

8.3.3 LIFT FORCE COEFFICIENT

The lift force coefficient data of the three Joubert models were determined using the body panel pressure integration method described in Section 6.7.2 and the simulation results data generated using SHIPFLOW. The comparison between the experimental and numerical results for the $L/D = 7.30$, 8.50 and 9.50 models are presented in Figure 8-16, Figure 8-17 and Figure 8-18 respectively. The comparison indicates that there is very good correlation between the numerical and experimental data, most notably for the $H^* = 2.16$ and 3.46 submergence depths.

At $H^* = 1.02$ the form of the numerical results shows good agreement with the experiment: the relative magnitude of the localised peak transitions from the larger

magnitude occurring at $Fr \approx 0.40$ at $L/D = 7.30$ to the larger magnitude occurring at $Fr \approx 0.275$ at $L/D = 9.50$. Although there is a visible difference between the apparent locations of the localised features, this is potentially a result of the limited number of points in the numerical data set. Unfortunately, limitations in the research schedule precluded additional simulations being completed.

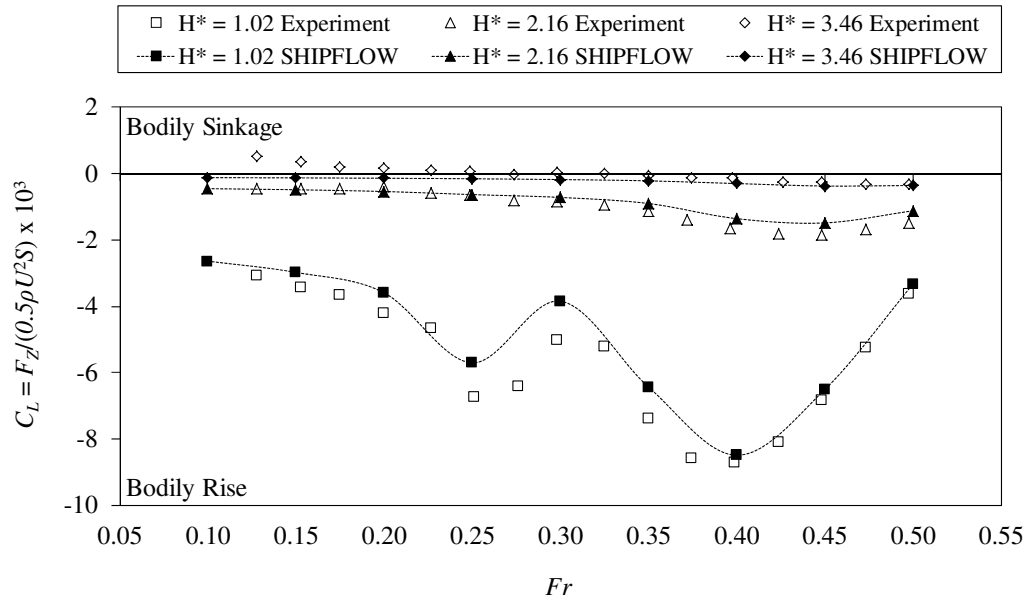


Figure 8-16 Comparison of SHIPFLOW computations of $L/D = 7.30$ Joubert model lift force coefficient (integrated pressure on body panels) compared with the lift force coefficient determined from experimental measurements

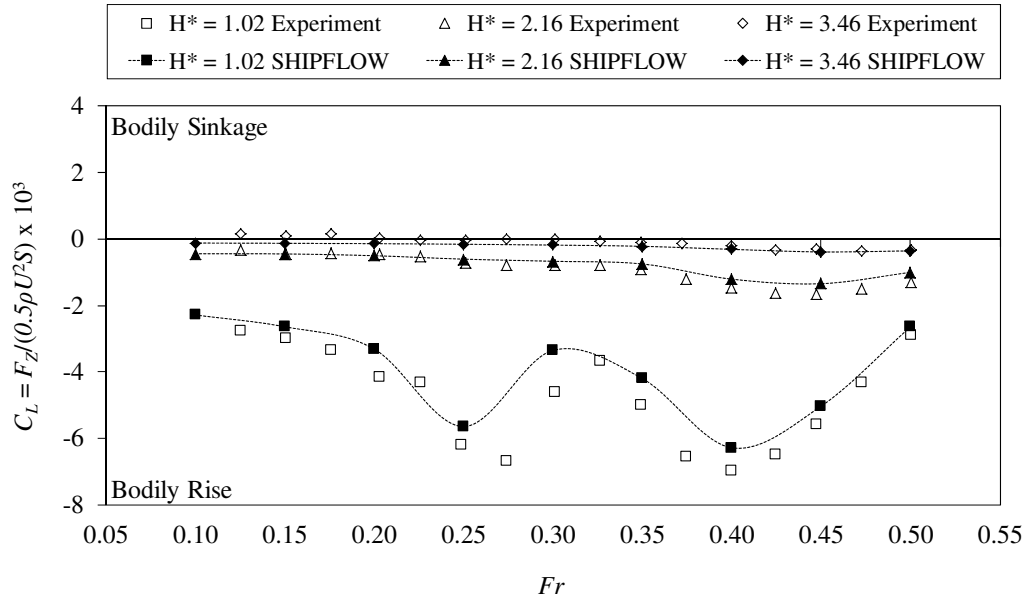


Figure 8-17 Comparison of SHIPFLOW computations of $L/D = 8.50$ Joubert model lift force coefficient (integrated pressure on body panels) compared with the lift force coefficient determined from experimental measurements

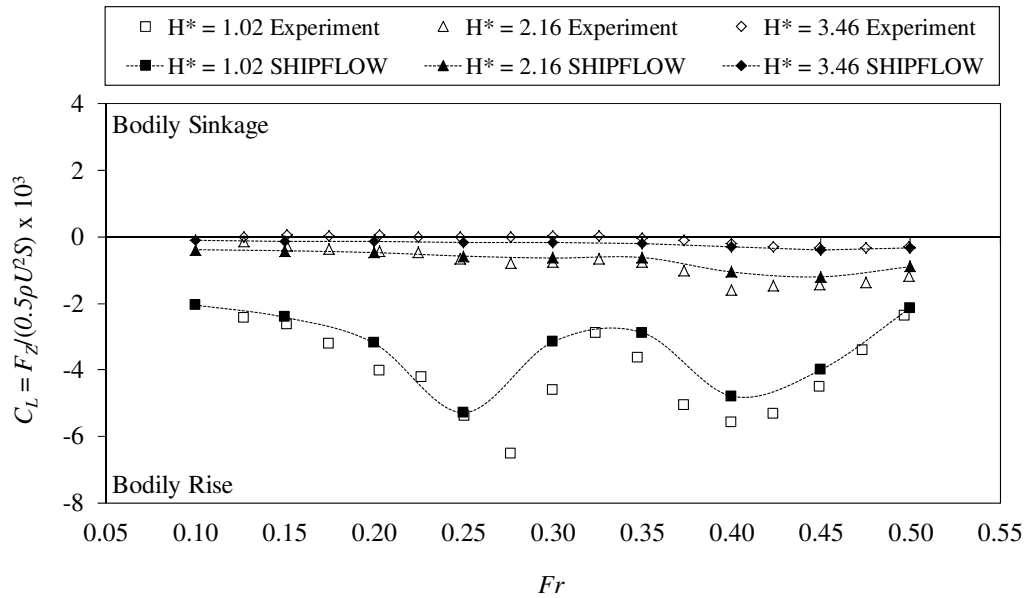


Figure 8-18 Comparison of SHIPFLOW computations of $L/D = 9.50$ Joubert model pitching moment coefficient (calculated from body panels) compared with the lift force coefficient determined from experimental measurements

8.3.1 TRIMMING MOMENT COEFFICIENT

The trimming moment coefficient data of the three Joubert models were determined using the body panel pressure integration method described in Section 6.7.2 and the simulation results data generated using SHIPFLOW. The comparison between the experimental and numerical results for the $L/D = 7.30$, 8.50 and 9.50 models are presented in Figure 8-19, Figure 8-20 and Figure 8-21 respectively. Similar to the lift coefficient results, the comparison indicates that there is very good correlation between the numerical and experimental data, most notably for the $H^* = 2.16$ and 3.46 submergence depths. Once again, the limited number of simulation data points precludes a comprehensive comparison of the localised trimming moment response.

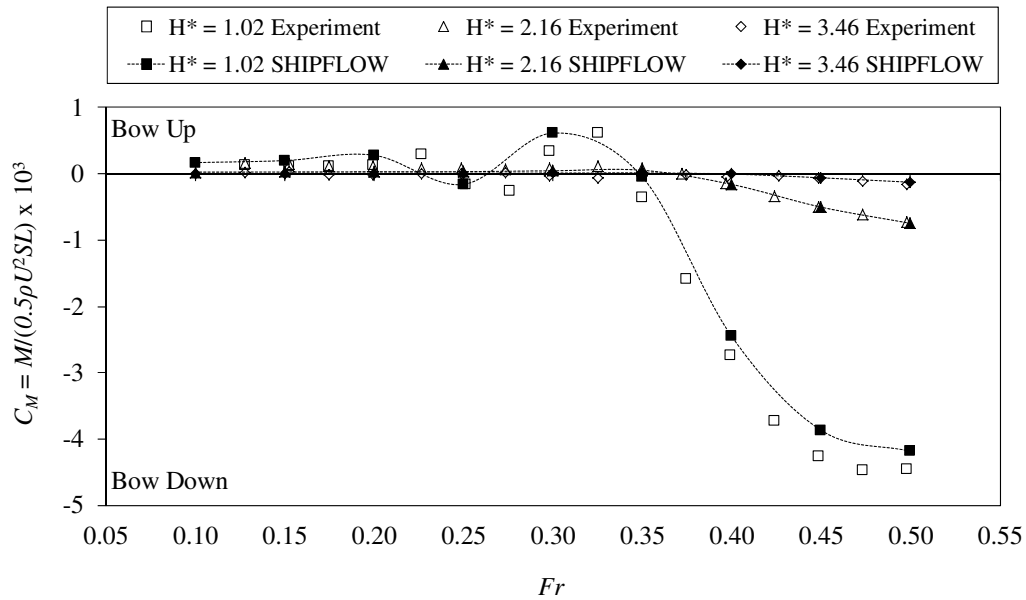


Figure 8-19 Comparison of SHIPFLOW computations of $L/D = 7.30$ Joubert model trimming moment coefficient (integrated pressure on body panels) compared with the trimming moment coefficient determined from experimental measurements

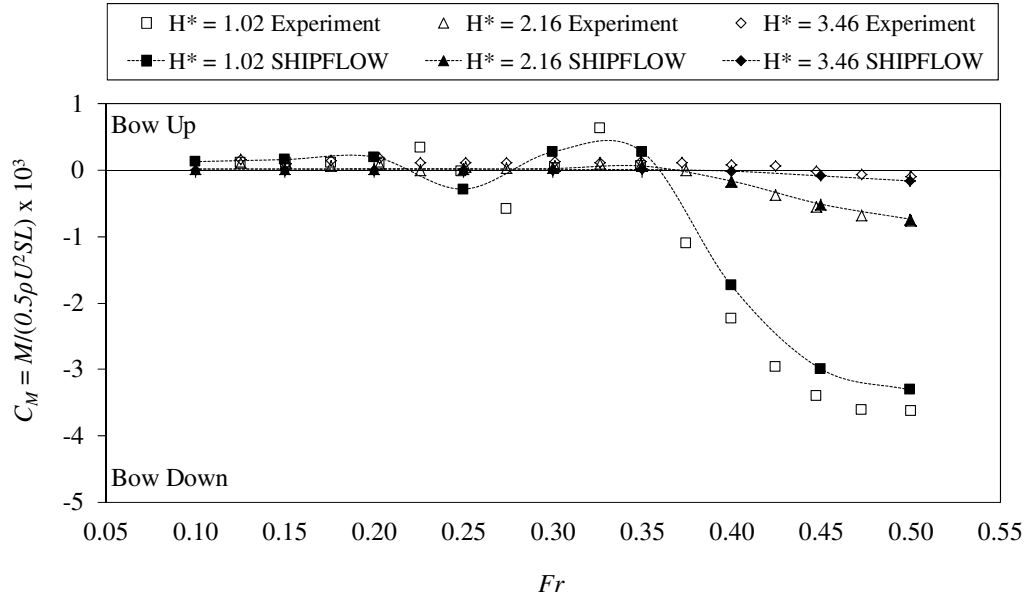


Figure 8-20 Comparison of SHIPFLOW computations of $L/D = 8.50$ Joubert model trimming moment coefficient (integrated pressure on body panels) compared with the trimming moment coefficient determined from experimental measurements

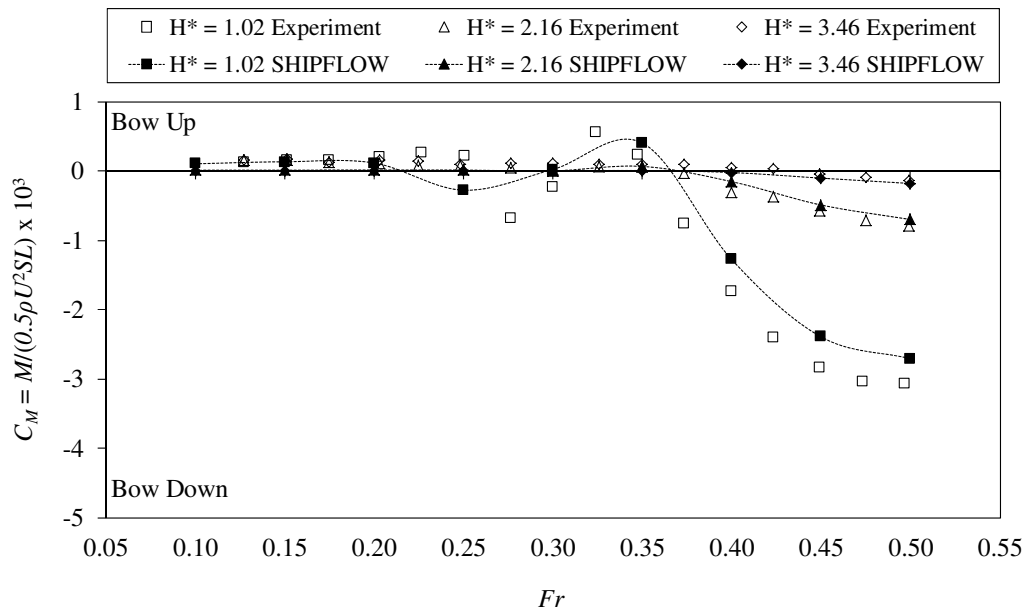


Figure 8-21 Comparison of SHIPFLOW computations of $L/D = 9.50$ Joubert model trimming moment coefficient (integrated pressure on body panels) compared with the trimming moment coefficient determined from experimental measurements

8.3.2 COMPARISON OF WAVE PROFILE DATA

The steady-state free-surface wave field was computed for each of the simulated models, speed and depth configurations using SHIPFLOW. Longitudinal wave-cut data was computed at transverse locations coincident with those used in the Joubert model experiments. A comparison between the experimentally measured and numerically predicted wave-cut profiles showed very good agreement for the region spanning upstream of the submerged body to just downstream of the body's trailing edge: the region free from interference from the mounting post wave system. This level of agreement was observed for each of the wave-cuts and for all of the simulated speeds and submergence depths. Figure 8-22 illustrates the correlation between the numerical and experimental wave-cut profile for the $L/D = 8.50$ geometry at $H^* = 1.02$ and $Fr = 0.30$.

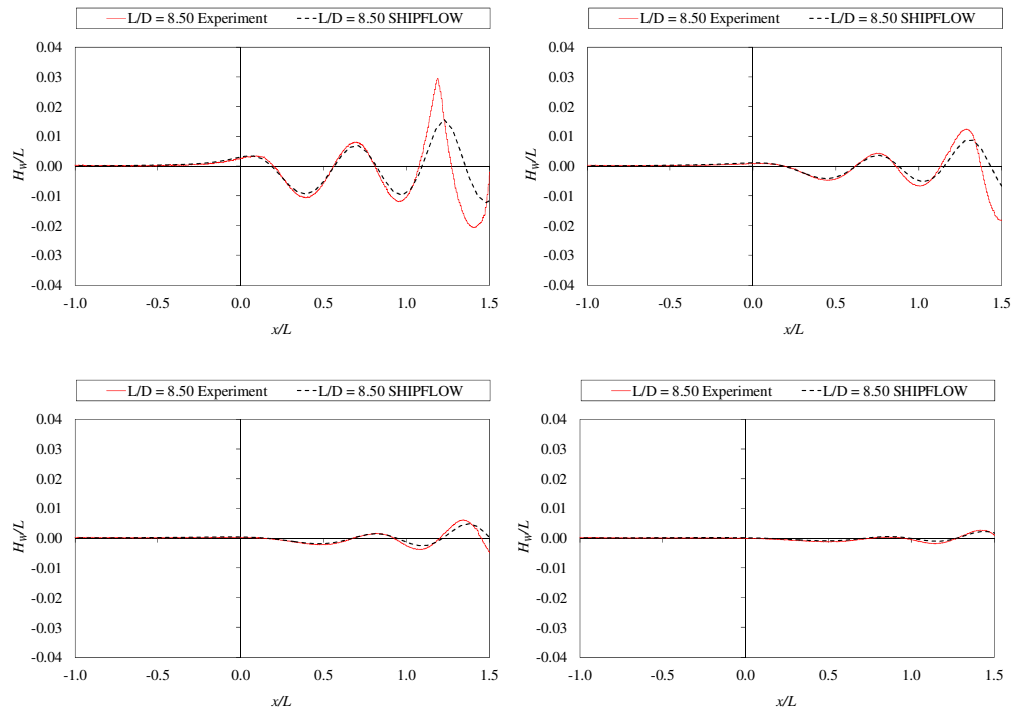


Figure 8-22 Comparison of SHIPFLOW computed wave-cut profiles and the experimentally measured wave-cuts for the Joubert $L/D = 8.50$ model at $H^* = 1.02$ and $Fr = 0.30$. Top left: $y/D = 1.26$, Top right: $y/D = 2.52$, Bottom left: $y/D = 3.78$, Bottom right: $y/D = 5.04$

As a result of the correlation between the experimental and numerical wave-cut data, the SHIPFLOW free-surface wave-cuts exhibit the same characteristics as the experimental data with respect to the effects of speed (Froude number) and submergence depth on the body-generated free-surface wave height and wavelength. As can be observed in Figure 8-23, an increase in Froude number at a constant submergence depth results in an increase in wavelength and wave height. The non-dimensional wavelength was calculated from the numerical wave-cut data for a discrete set of speeds and compared with the theoretical relationship derived from Equation 3-10 (Table 8-1). As was observed with the experimental wave-cut data, the

wavelength was indistinguishable at $Fr = 0.10$. However, for the remaining Froude numbers analysed the SHIPFLOW wave-cut non-dimensionalised wavelengths were found to be in agreement with the theoretical formulation, in particular for $0.30 \leq Fr \leq 0.50$. In addition to this, the simulated non-dimensional wavelengths are more consistent when compared to the experimental data (Figure 8-24).

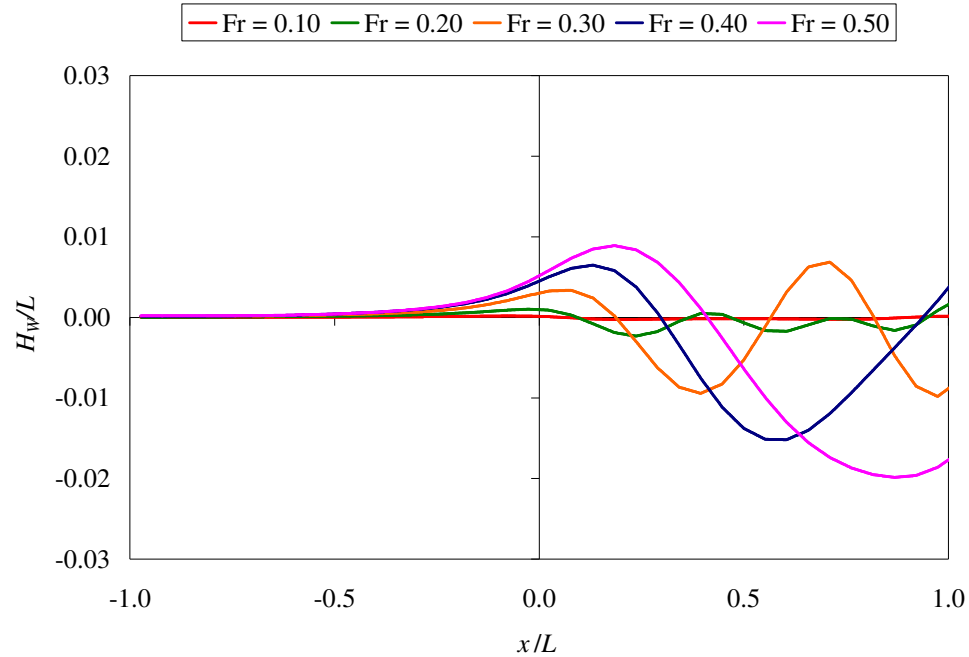


Figure 8-23 SHIPFLOW Effect of Froude number on wavelength and wave height: $H^* = 1.02$; $L/D = 8.50$; Wave Probe 1 ($y/D = 1.26$ off centreline) Note abscissa and ordinate scales

Table 8-1 SHIPFLOW: Wavelength to body length ratio for $H^* = 1.02$

	7.30	8.50	9.50	Theoretical
Fr	λ/L	λ/L	λ/L	$\lambda/L = 2\pi Fr^2$
0.10	-	-	-	0.06
0.20	0.31	0.32	0.31	0.25
0.30	0.60	0.61	0.58	0.57
0.40	1.01	1.03	0.99	1.01
0.50	1.58	1.60	1.59	1.57

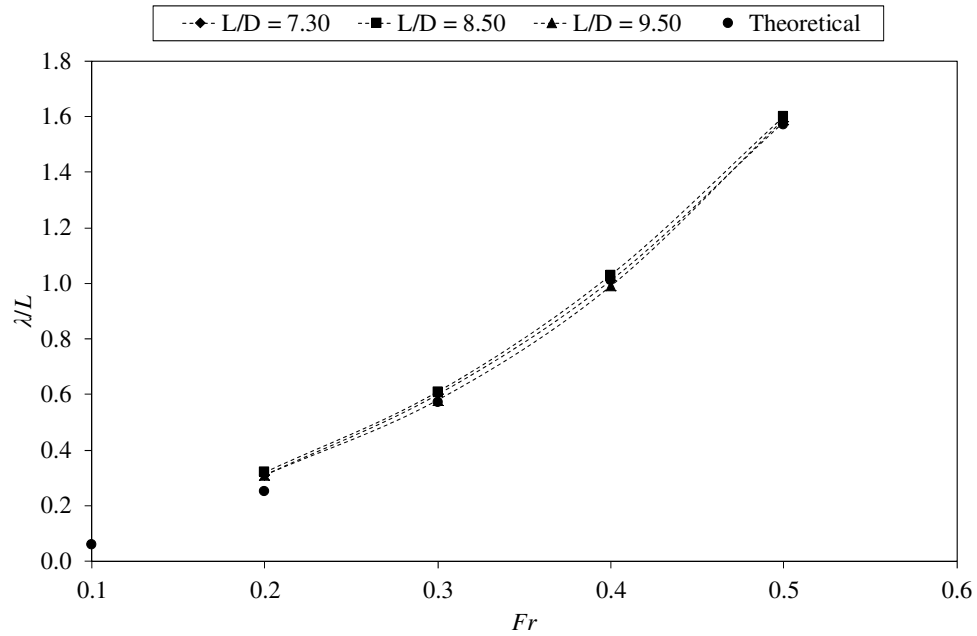


Figure 8-24 SHIPFLOW Effect of Froude number on non-dimensional wavelength (λ/L) for all Joubert models at $H^* = 1.02$ based on SHIPFLOW longitudinal wave-cut data

Figure 8-25 shows a comparison and the strong correlation between the experimentally measured and numerically predicted wave-cut profile for the $L/D = 8.50$ Joubert geometry at $H^* = 1.02$.

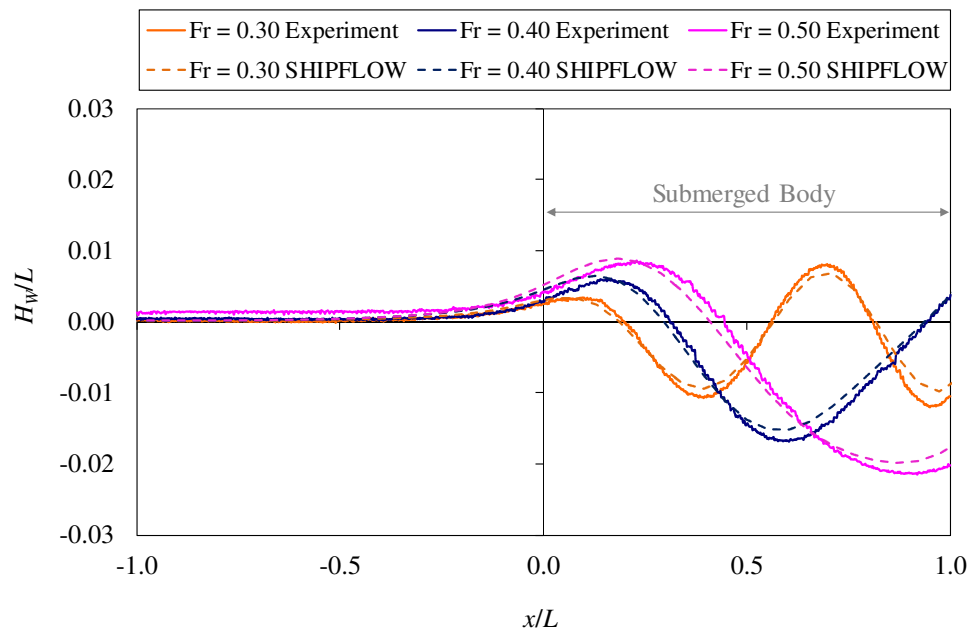
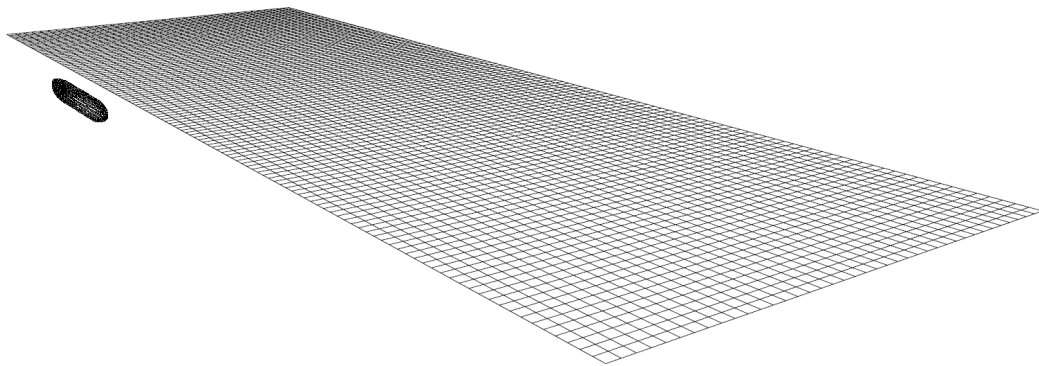
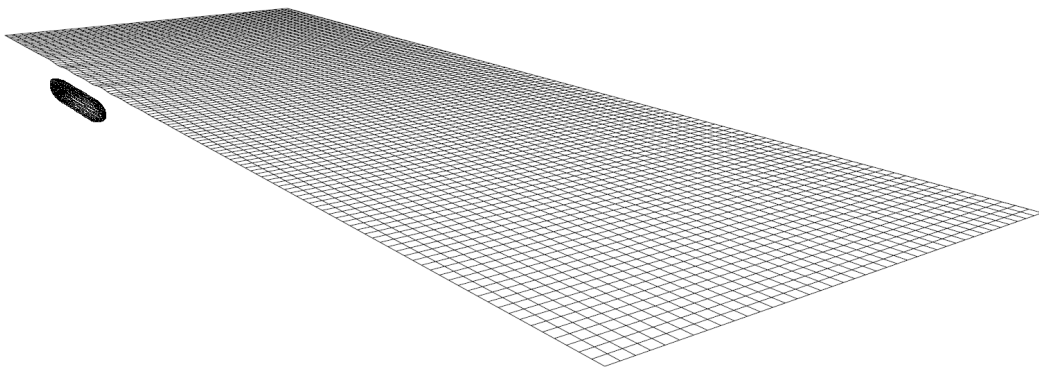


Figure 8-25 Comparison of SHIPFLOW and experimental wave-cuts for the Joubert $L/D = 8.50$ geometry at $H^* = 1.02$. Wave Probe 1 ($y/D = 1.26$ off centreline) Note abscissa and ordinate scales

The SHIPFLOW three-dimensional panelised free-surface solutions for the Joubert $L/D = 7.30$ geometry $H^* = 1.02$ simulation scenarios are presented in Figure 8-26, Figure 8-27, Figure 8-28, Figure 8-29 and Figure 8-30 as they provide an insightful representation of the free-surface disturbance generated by the submerged body. The free-surface solutions show the near-field and far-field disturbance generated by the submerged body's pressure distribution. The wave pattern consists of the transverse and divergent wave systems that are typical of a ship or a point disturbance moving with a constant velocity through calm water. The solution also confirms that, for the range of speeds simulated, the wave field exits the free-surface domain at the downstream boundary and not through the side boundary (a modelling criterion discussed in section 6.3).



**Figure 8-26 SHIPFLOW free-surface solution: Joubert $L/D = 7.30$; $H^* = 1.02$;
 $Fr = 0.10$**



**Figure 8-27 SHIPFLOW free-surface solution: Joubert $L/D = 7.30$; $H^* = 1.02$;
 $Fr = 0.20$**

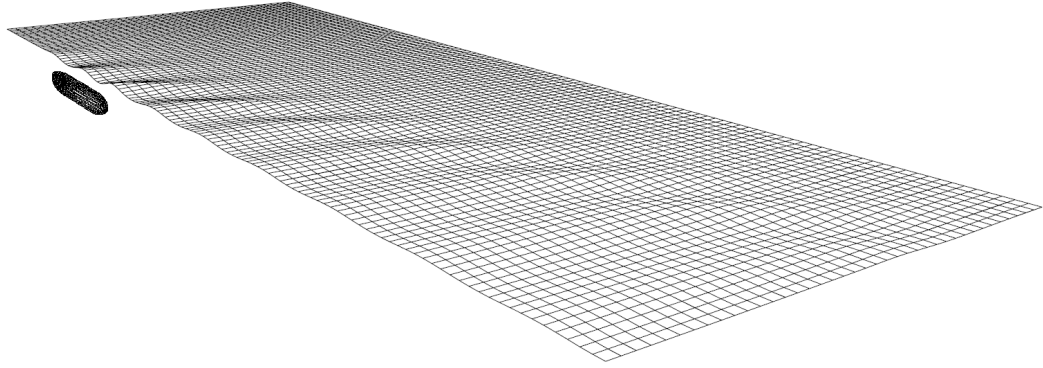


**Figure 8-28 SHIPFLOW free-surface solution: Joubert $L/D = 7.30$; $H^* = 1.02$;
 $Fr = 0.30$**

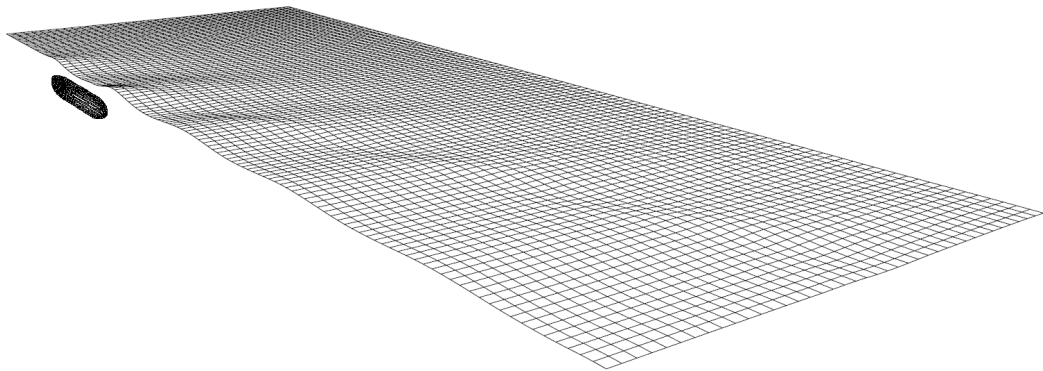


**Figure 8-29 SHIPFLOW free-surface solution: Joubert $L/D = 7.30$; $H^* = 1.02$;
 $Fr = 0.40$**

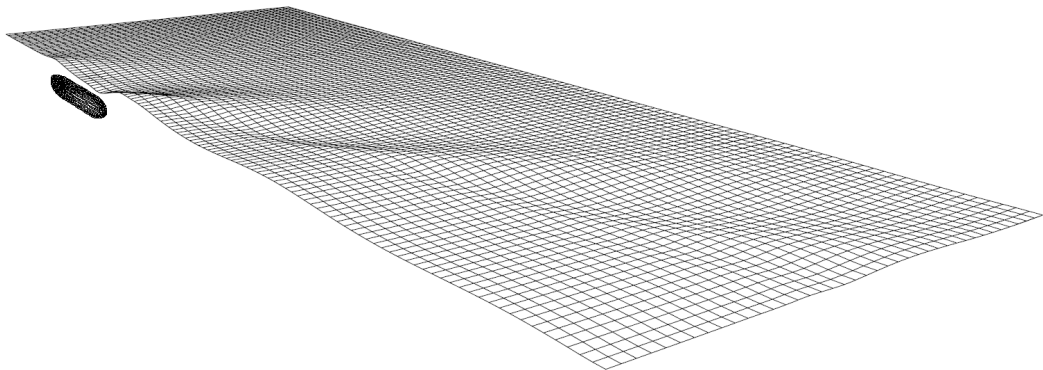


**Figure 8-30 SHIPFLOW free-surface solution: Joubert $L/D = 7.30$; $H^* = 1.02$;
 $Fr = 0.50$**

9 CONCLUDING REMARKS AND RECOMMENDATIONS

9.1 CONCLUDING REMARKS

The frequency of near-surface submarine operations continues to increase in response to the strategic and tactical operational requirements of the world's navies. It is now common for both conventional and nuclear type submarines to operate in littoral regions and at shallow submergence depths to achieve their mission objectives. Maintaining control of the submarine when travelling beneath the free-surface at shallow depths and low speeds is a critical and complex task. Managing the submergence depth and attitude of the submarine requires the helmsman to exert significant effort. Understanding and predicting the forces and moments that influence the submarine's vertical motions and attitude during near-surface operations is very important as it informs the design, mission planning and operational decision making process with the aim of minimising risk and achieving operational success.

An experimental investigation has been undertaken to investigate the effects of submergence depth, speed and length-to-diameter ratio on the forces and moments acting on a streamlined body travelling beneath a calm free-surface. Numerical simulations of the experimental test configurations have been completed to evaluate the ability of a commercial potential flow software program to predict the forces and moment acting on a shallowly submerged body.

The results of the investigation have provided valuable insight into the performance characteristics of a series of streamlined bodies of revolution travelling beneath a free-surface. If the results are considered in the context of contemporary near-surface naval submarine operation, it is apparent that the effects of wave making resistance do not significantly impinge on the propulsive performance of the submarine for the operational speed range (up to 10 knots). For this speed range it was observed that the interaction of the body generated free-surface wave system components has a negligible effect. Despite this, there will be a general increase in the total resistance over the deeply submerged condition due to an increase in the viscous wake as a result of the body's interaction with the free-surface. There is also a non-negligible vertical lift force that acts on the submarine to pull it towards the free-surface. In combination with these forces, there is a trimming moment that acts to trim the submarine initially down by the stern and then down by the bow as the speed reaches the upper end of the near-surface speed range (10 knots).

The lift force and trimming moment occur due to the interaction of the submerged body with the free-surface and the steady-state wave system that it generates. The periodicity of the wave resistance, lift force and trimming moment are principally dependent on the combination of the body length and the speed at which the body is travelling, as these two parameters directly influence the free-surface wave field (wavelength, wave height and the relative location and interaction of hull-borne wave components). The experimental results indicate that, for near-surface operations, the interaction between the submerged body and the free-surface diminishes exponentially with an increase in centreline submergence depth and becomes all but negligible at depths beyond two and a half hull diameters.

Due to the interaction of the submerged body with its self-generated free-surface wave system there is a localised peak lift force that occurs at approximately $Fr = 0.275$. The peak corresponds to the upper end of the near-surface operational speed range for naval submarines. This behaviour is in agreement with the anecdotal evidence provided by Crook (1994) and the numerical results published by Doctors and Beck (1987). Although it has been shown numerically that with an increase in speed the lift force transitions from a force pulling the body towards the free-surface to a force pushing the body away from the free-surface, the speed at which this occurs is well above the speed range maintained by naval submarines when operating near the free-surface. Similarly, the localised minimum lift force coefficient that occurs at $Fr \approx 0.375$ corresponds with an operational speed of approximately 18-22 knots and therefore provides little benefit when low speed near-surface operations are being conducted.

The effect of submergence depth is such that the lift force coefficient diminishes exponentially with an increase in depth and more rapidly than the trimming moment coefficient for an equivalent increase in submergence depth. There is little discernable difference between the $L/D = 7.30$, $L/D = 8.50$ and $L/D = 9.50$ geometries with regard to the lift force coefficient for the range of near-surface operating speeds. Nonetheless, the results suggest that the shortest ($L/D = 7.30$) body experiences the greatest lift force per unit surface area of the three geometries for the range of submergence depths and speeds tested.

The wave profile measurements made during the experiments indicate that the amplitude and wavelength of the free-surface wave system generated by the submerged body are very small for the range of operational depths and speeds experienced by naval submarines during near-surface operations. It is beyond the scope of this research to evaluate whether the body-generated wave field would be detectable by modern sensors. However, it is surmised that localised visual signatures such as the wake from a submarine's snort or antenna masts would be more readily detectable than the hull-borne wave system. Nonetheless, the results of the wave profile measurements indicate that the wavelength of the free-surface wave field can be reliably determined using the theoretical relationship of wavelength and speed for deep water. The effect of the hull-borne wave system is to generate an asymmetric pressure distribution that acts on the submerged body and can induce a combined lift force and trimming moment. The magnitude and direction of the force and moment is dependent on the wavelength of the steady-state free-surface wave field and is therefore a function of body length and speed.

Although wave resistance has been found not to be the principal issue at near-surface operational speeds, the influence of the free-surface results in the lower length-to-diameter geometry generating the greater total resistance through this speed range. In addition, the geometry with a high length-to-diameter ratio performs more favourably with respect to lift force and trimming moment. Of course, achieving a balanced design is a not a trivial task and the overall dimensions of naval submarines are driven as much if not more by internal payload and manufacturing infrastructure than by hydrodynamic performance. Despite the non-negligible difference in the volumetric displacement of the three Joubert model geometries, the difference in prismatic coefficient is not significant. In the context of submarine design and fabrication, the

three models represent a viable family of hull forms as it is more realistic to incorporate and increase mission capability by extending the length of a submarine rather than its diameter, or both concurrently.

The use of a potential flow numerical software tool (SHIPFLOW 4.7) has been shown to adequately predict the lift force and trimming moment of a streamlined body of revolution travelling beneath a free-surface. Mixed results were obtained in this research when evaluating the software's ability to predict submerged body wave resistance. For the simulation parameters used in this research, the integrated panel pressure method was observed to perform significantly better than the transverse wave-cut method. Notwithstanding this difference, it was found that the total resistance quota of a submerged body travelling beneath the free-surface comprises resistance components that are not readily predictable using traditional analytical methods and impossible to predict using inviscid prediction tools. Of these, the most significant is the increase in the body's viscous resistance due to the divergence of the wake field around the after-body region. This phenomenon is reported to be highly dependent on the speed of the body and its proximity to the free-surface boundary. As a result, the contribution to the total resistance can be significant and vary across the body's range of forward speeds. Therefore, determining the wave resistance component of the experimentally measured total resistance is not an uncomplicated process. Futhermore, making a direct comparison between a potential flow wave resistance prediction and an experimental result is not readily achievable without a significant investment in the experimental process.

Despite this, the research results provide adequate evidence to conclude that potential flow methods are suitable for predicting the vertical forces and moments acting on a submarine hull travelling beneath the free-surface. Futhermore, it is apparent that the physical problem and phenomena that are inherent to the near-surface operational condition can be treated using an inviscid analysis technique.

9.2 RECOMMENDATIONS FOR EXTENDING THIS RESEARCH

During the course of this research there have been several points of significance that have been identified that relate to the behaviour and evaluation of submerged bodies travelling beneath the free surface. A comprehensive investigation into these points of significance was not undertaken in order to achieve the research objectives specific to this investigation and deliver the associated outcomes within the research schedule. However, it is recommended that future research efforts are focussed on the following areas:

- a. The effect of prismatic coefficient on the wave resistance, lift force and trimming moment should be investigated. While length-to-diameter has been identified as a design attribute that influences the near-surface performance of a submerged body, observations made based on the work of Weinblum et al. (1950) and Gertler (1950) suggest that the body's prismatic coefficient may have an equal level of influence.
- b. The effect of appendages, in particular the submarine sail, on the wave resistance, lift force and trimming moment should be investigated. The relative size of the sail and its proximity to the free-surface introduces a secondary wave system that acts in combination with the hull's wave system. Measuring the influence of an appendage using small scale model tests is considered to be unsuitable due to the relatively small forces that are contributed by the sail to the total system. Rather, a numerical approach using either potential flow or viscous CFD methods is suggested.
- c. The effect of a non-zero relative flow angle (trim angle and/or yaw angle) should be addressed to identify its effect on the interaction between the body and the free-surface. Due to the complex flow structures that occur on the submarine body when moving relative to the surrounding fluid with a non-zero flow angle, it is likely that the use of a potential flow method to generate absolute force and moment data would be limited. It is more likely that a viscous CFD method would enable an accurate evaluation of the effects of a trimmed or yawed body.
- d. The influence of the submerged body's trim angle on the body's equilibrium condition should be investigated to identify whether or not near-surface interaction can lead to instability where a small disturbance results in a significant motion response (sinkage and/or trim).
- e. To address the performance issues encountered using the SHIPFLOW transverse wave-cut method to determine the submerged body wave resistance coefficient, it is suggested that a more rigorous investigation be completed to identify the effects of the wave-cut method parameters on the predicted result.

REFERENCES

- ACHENBACH, E. 1974. The Effects of Surface Roughness and Tunnel Blockage on the Flow Past Spheres. *Journal of Fluid Mechanics*, Vol. 65, Part 1, pp. 113-124, Great Britain.
- ALLAN, J. F. & CONN, J. F. C. 1950. Effect of Laminar Flow on Ship Models. *Transactions of the Institution of Naval Architects*, Vol. 92, pp. 107-137.
- ALVAREZ, A., BERTRAM, V. & GUALDESI, L. 2009. Hull Hydrodynamic Optimization of Autonomous Underwater Vehicles Operating at Snorkeling Depth. *Ocean Engineering*, 36, pp. 105-112.
- ANDERSON, B., CHAPUIS, M., ERM, L., FUREBY, C., GIACOBELLO, M., HENBEST, S., JONES, D., JONES, M., KUMAR, C., LIEFVENDAHL, M., MANOVSKI, P., NORRISON, D., QUICK, H., SNOWDEN, A., VALIYFF, A., WIDJAJA, R. & WOODYATT, B. 2012. Experimental and Computational Investigation of a Generic Submarine Hull Form. 29th Symposium on Naval Hydrodynamics, Gothenburg, Sweden, 26-31 August.
- BAKER, G.S. & KENT, J.L. 1919. Speed, Dimensions and Form of Cargo Vessels. *Journal of the American Society of Naval Engineers*, 31(2), pp. 494-508.
- BELIBASSAKIS, K. A., GEROSTATHIS, T. P., POLITIS, C. G., KAKLIS, P. D., GINNIS, A. I. & MOURKOIANNIS, D. N. 2009. A Novel BEM-ISOGOMETRIC Method with Applications to the Wavemaking Resistance Problem of Bodies at Constant Speed. 13th Congress of International Maritime Association of Mediterranean. IMAM 2009.
- BRASLOW, A. L. & KNOX, E. C. 1958. Simplified Method for Determination of Critical Height of Distributed Roughness Particles for Boundary-Layer Transition at Mach Numbers from 0 to 5. Langley Aeronautical Laboratory, Langley Field, Virginia, USA.
- BRASLOW, A. L. 1960. Review of the Effect of Distributed Surface Roughness on Boundary-Layer Transition. In: *Aeronautical Fluid Dynamics Paner* (ed.) Advisory Group for Aeronautical Research and Development. London: North Atlantic Treaty Organisation.
- BURCHER, R. & RYDILL, L. 1994. *Concepts in Submarine Design*, Cambridge, United Kingdom, Cambridge University Press.
- COLEMAN, H.W. & STEELE, W.G. 1999. *Experimentation and Uncertainty Analysis for Engineers*. John Wiley & Sons, New York, USA.
- CRETE, P-A. 2013. *CFD Studies on Submarines*. Australian Maritime College, Launceston, Australia.
- CROOK, T. P. 1994. *An Initial Assessment of Free Surface Effects on Submerged Bodies*. MSc Mechanical Engineering, Naval Postgraduate College. USA.

- CYRAN, F. B. 1981. Sting Interference Effects on the Static, Dynamic and Base Pressure Measurements of the Standard Dynamics Model Aircraft at Mach Numbers 0.3 through 1.3. AEDC-TR-81-3, Arnold Engineering Development Centre, Arnold Air Force Station, Tennessee, USA.
- DAVIDSON, K. S. M. 1948. The Use of Turbulence-Producing Devices in Model Experiments. In: HUGHES, G., ed. Fifth International Conference of Ship Superintendents, 1948 London. His Majesty's Stationary Office.
- DAWSON, E., ANDERSON, B., VAN STEEL, S., RENILSON, M. & RANMUTHUGALA, D. 2010. An Experimental Investigation into the Effects of Near-Surface Operation on the Wave-Making Resistance of SSK Type Submarines. Proceedings of MAST 2010, 9-11 November 2010, Rome, pp. 1-8
- DIORIO, D. R. 1995. Forward... From Under the Sea: Historical Perspective and Future Vision of Submarine Littoral Warfare. Newport, Rhode Island, USA: Naval War College.
- DOCTORS, L. & BECK, R. 1987. Convergence Properties of the Neumann-Kelvin Problem for a Submerged Body. *Journal of Ship Research*, 31, pp. 227-234.
- EMMONS, H. W. 1951. The Laminar-Turbulent Transition in a Boundary Layer. *Journal of Aeronautical Sciences*, Vol 18, pp. 490-498.
- FARELL, C. 1973. On the Wave Resistance of a Submerged Spheroid. *Journal of Ship Research*, 17, pp. 1-11.
- FARELL, C. & GÜVEN, O. 1973. On the Experimental Determination of the Resistance Components of a Submerged Spheroid. *Journal of Ship Research*, 17, pp. 72-79.
- FELDMAN, J. 1979. DTNSRDC Revised Standard Submarine Equations of Motion. David W. Taylor Naval Ship Research and Development Centre, Bethesda, Maryland, USA.
- FLOWTECH International A.B. 2012. SHIPFLOW® 4.7 Users Manual. FLOWTECH International, Gothenburg, Sweden.
- FRIEDMAN, N. 1984. *Submarine Design and Development*, Annapolis, Maryland, USA, Naval Institute Press.
- FRIEDMAN, N. 1994. *U.S. Submarines Since 1945*, Annapolis, Maryland, USA, Naval Institute Press.
- FRIEDMAN, N. 1995. *U.S. Submarines Through 1945 An Illustrated Design History*, Annapolis, Maryland, USA, Naval Institute Press.
- GERTLER, M. 1950. Resistance Experiments on a Systematic Series of Streamlined Bodies of Revolution - For Application to the Design of High-Speed

- Submarines. Washington D.C.: Navy Department: The David W. Taylor Model Basin.
- GRANVILLE, P. S. 1976. Elements of the Drag of Underwater Bodies. Bethesda, Maryland, USA: David W. Taylor Naval Ship Research and Development Center.
- GRIFFIN, M. J. 2002. Numerical Prediction of the Maneuvring Characteristics of Submarines Operating Near the Free Surface. PhD in Ocean Engineering, Massachusetts Institute of Technology.
- GROVES, N. C., HUANG, T. T. & CHANG, M. S. 1989. Geometric Characteristics of DARPA SUBOFF Models (DTRC Model Nos. 5470 and 5471). Bethesda, Maryland, USA: David Taylor Research Centre.
- HAMA, F. R. 1957. An Efficient Tripping Device. *Journal of Aeronautical Sciences*, Vol 24, 236-237.
- HAMA, F. R., LONG, J. D. & HEGARTY, J. C. 1957. On Transition from Laminar to Turbulent Flow. *Journal of Applied Physics*, Vol. 28, pp. 388-394.
- HAVELOCK, T. H. 1917. Some Cases of Wave Motion Due to a Submerged Obstacle. *Proceedings, The Royal Society of London*, 93, pp. 520-532.
- HAVELOCK, T. H. 1919. Some Cases of Three-Dimensional Fluid Motion. *Proceedings, The Royal Society of London*, 95, pp. 354-365.
- HAVELOCK, T. H. 1931a. The Wave Resistance of a Spheroid. *Proceedings, The Royal Society of London*, 131, pp. 275-285.
- HAVELOCK, T. H. 1931b. The Wave Resistance of an Ellipsoid. *Proceedings, The Royal Society of London*, 132, pp. 480-486.
- HENDRIX, D., PERCIVAL, S. & NOBLESSE, F. 2001. Practical Hydrodynamic Optimization of a Monohull. *Transactions of the Society of Naval Architects and Marine Engineers*, 109, pp. 173-193.
- HERVEY, J. 1994. *Submarines*, London, Macmillan Publishing Company.
- HESS, J. L. & SMITH, A. M. O. 1964. Calculation of Nonlifting Potential Flow About Arbitrary Three-Dimensional Bodies. *Journal of Ship Research*, 8, pp. 22-44.
- HICKEY, R. I. 1990. Submarine Motion Simulation Including Zero Forward Speed and Propeller Race Effects. Master of Science in Ocean Engineering, Massachusetts Institute of Technology.
- HOERNER, S.F. 1965. *Fluid Dynamic Drag: Practical Information on Aerodynamic Drag and Hydrodynamic Resistance*. Published by the author, Brick Town, New Jersey, USA.

- HONG, Y. S. 1983. Computation of Nonlinear Wave Resistance. Proceedings 2nd DTNSRDC Workshop on Ship Wave-Resistance Computations, D. W. Taylor naval Ship Research and Development Center, Nov 1983, pp. 104-126.
- HUGHES, G. 1954. Friction and Form Resistance in Turbulent Flow and a Proposed Formulation for Use in Model and Ship Correlation. Transactions Institute of Naval Architects, Vol. 96.
- ITTC 1990. ITTC90 - Report of the High-Speed Marine Vehicles Committee.
- ITTC 1999. ITTC - Recommended Procedures and Guidelines: Testing and Extrapolation Methods, General Uncertainty Analysis in EFD Uncertainty Assessment Methodology. 7.5-02-01-01, International Towing Tank Conference.
- ITTC 2002. ITTC - Recommended Procedures and Guidelines: Testing and Extrapolation Methods Resistance Uncertainty Analysis, Example for Resistance Test. 7.5-02-02-02, International Towing Tank Conference.
- JOLIFF, J.V. 1966. Scale Effects on a Particular Submerged Body of Revolution. Naval Engineers Journal, 78(5), pp. 865-876.
- KEY, K. 1965 Verification of Method of Determining the Viscous Drag of a Ship Model. Masters Thesis, The University of Iowa.
- KNAPP, C. F. & ROACHE, P. J. 1968. A Combined Visual and Hot-wire Anemometer Investigation of Boundary-Layer Transition. AIAA Journal, Vol. 6, pp. 29-36.
- KORMILITSIN, Y. N. & KHALIZEV, O. A. 2001. Theory of Submarine Design, Saint-Petersburg, Russia, Saint-Petersburg State Maritime Technical University.
- KOSTYUKOV, A. A. 1959. Theory of Ship Waves and Wave Resistance, Iowa City, Effective Communications Inc.
- KOZLOV, L. F. Year. Investigation of the Boundary Layer Turbulence Stimulation of the Ship Models. In: NAVALE, I.N.P.S.E.E.D.A., ed. 12th International Towing Tank Conference, 1969 Rome.
- LAMB, H. 1913. On Some Cases of Wave Motion on Deep Water. Annali di Matematica, Vol. 21, pp. 237-250.
- LANDWEBER, L. 1951. Discussions of Subject 2, "Skin Friction". Proceedings, 6th International Conference of Ship Tank Superintendents, Washington, USA,
- LARSSON, L. & RAVEN, H. C. 2010. Ship Resistance and Flow, Jersey City, New Jersey, USA, The Society of Naval Architects and Marine Engineers.

- LEWANDOWSKI, E. M. 1994. The Effects of Aspect Ratio, Section Shape, and Reynolds Number on the Lift and Drag of a Series of Model Control Surfaces. Hoboken, New Jersey, USA: Davidson Laboratory, Stevenson Institute of Technology.
- MACKAY, M. 1993. A Review of Sting Support Interference and Some Related Issues for the Marine Dynamic Test Facility (MDTF). St. John's, Newfoundland: Defence Research Establishment Atlantic.
- NEULIST, D. 2011. Experimental Investigation into the Hydrodynamic Characteristics of a Submarine Operating Near the Free Surface. Australian Maritime College: Launceston, Tasmania.
- POLMAR, N. 1963. Atomic Submarines, New Jersey, D. Van Nostrand Company Inc.
- PROHASKA, C. W. 1966. A Simple Method for the Evaluation of Form Factor and Low Wave Speed Resistance, Proceedings 11th International Towing Tank Conference, Tokyo, Japan.
- RAWSON, K.J & TUPPER, E.C. 2001. Basic Ship Theory. Butterworth Heinemann, Oxford, England.
- RISTVEDT, V. G. 1993. The Conventional Submarine Threat in the Littoral Regions. Alabama: Air War College, Air University.
- SCHLICHTING, H. & GERSTEN, K. 1999. Boundary-Layer Theory, Berlin, Springer-Verlag.
- SCHUBAUER, G. B. & KLEBANOFF, P. S. 1955. Contributions on the Mechanics of Boundary-Layer Transition. Washington: National Advisory Committee for Aeronautics.
- TORKELSON, K. O. 2005. Comparative Naval Architecture Analysis of Diesel Submarines. Massachusetts Institute of Technology.
- TZOU, K. T. S. & LANDWEBER, L. 1968. Determination of the Viscous Drag of a Ship Model. Journal of Ship Research, Vol. 12, No. 2, pp. 105-115.
- TZOU, K. T. S. 1969. On the Determination of the Viscous Drag of a Ship Model. PhD, The University of Iowa.
- VAN MANEN, J. D. & VAN OOSSANEN, P. (eds.) 1988. Part II: Resistance, Jersey City, NJ: Society of Naval Architects and Marine Engineers.
- VAN MIERLO, K. J. 2006. Trend Validation of SHIPFLOW Based on the Bare Hull Upright Resistance of the Delft Series. MSc. Delft University of Technology, Delft, the Netherlands.

- VAN STEEL, S. 2010. Investigation into the Effect of Wave Making on a Submarine Approaching the Surface. Australian Maritime College: Launceston, Tasmania.
- WEINBLUM, G., AMTSBERG, H. & BOCK, W. 1950. Tests on Wave Resistance of Immersed Bodies of Revolution. Washington D. C.: The David W. Taylor Model Basin.
- WIGLEY, W.C.S. 1953. Water Forces on Submerged Bodies in Motion. Transactions, Institute of Naval Architects, 95, pp. 268-279.
- WILSON-HAFFENDEN, S. J. 2009. An Investigation into the Wave Making Resistance of a Submarine Travelling Below the Free Surface. Australian Maritime College: Launceston, Tasmania.
- WU, J. & LANDWEBER, L. 1963. Variation of Viscous Drag with Froude Number. Proceedings, 10th International Towing Tank Conference, Teddington, UK.
- YOUNG, A. D. 1989. Boundary Layers, Oxford, England, BSP Professional Books.

APPENDIX A BOUNDARY LAYER TRANSITION INVESTIGATION

BOUNDARY LAYER TRANSITION

The laminar to turbulent transition phenomenon of the boundary layer surrounding a body that is in relative motion continues to be investigated. Schlichting and Gersten (1999) indicate that the transition of the boundary layer surrounding a solid body is highly dependent on the Reynolds number, pressure distribution, body surface roughness and turbulence intensity of the encountered flow.

It is proposed by Young (1989) that in an undisturbed flow field over a curved surface the transition of the boundary layer is initiated by the amplification of unsteady Tollmien-Schlichting waves with possible interaction from Taylor-Görtler vortices. The behaviour of both the Tollmien-Schlichting waves and Taylor-Görtler vortices are dependent on the Reynolds number and surface pressure distribution over the body's surface. Further investigation by Emmons (1951) of flow on a water table, as reported by Young (1989), led to the discovery that the effect of the amplified Tollmien-Schlichting waves results in randomly distributed turbulence spots rather than a uniform span-wise front of turbulence. It was observed that fully turbulent flow did not occur until further downstream, at which point the turbulent spots had enlarged and agglomerated (Figure A-1). It was also observed that the turbulent spots occur in an intermittent manner and an increased rate of generation is influenced by the presence of adverse pressure gradients, turbulence in the external flow and an increased Reynolds number.

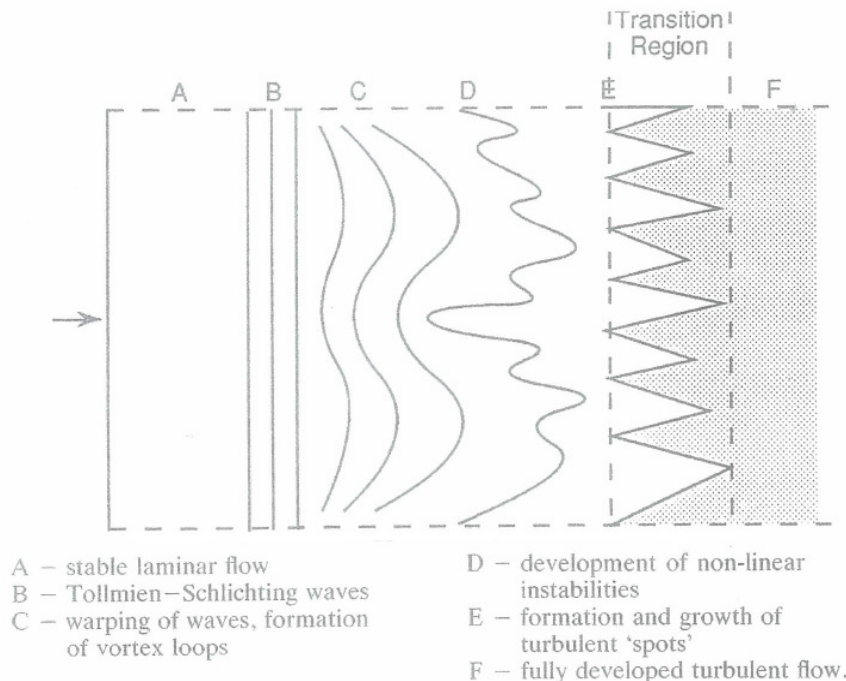


Figure A-1 Suggested stages of the general transition process (Young, 1989)

The work conducted by Knapp and Roache (1968) presented by Schlichting and Gersten (1999) of a visual and hot-wire anemometer investigation of the natural boundary-layer transition of a body of revolution is presented in Figure A-2. The

smoke flow visualisation method used in the investigation illustrates the inception of the Tollmien-Schlichting waves and the progressive transition of the boundary layer, similar in nature to the observations made by Emmons (1951).

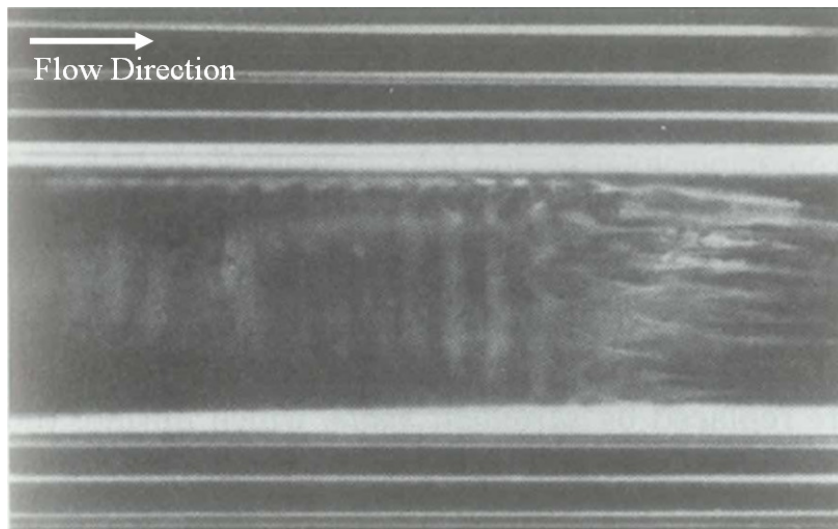


Figure A-2 Flow visualisation of the boundary layer transition for a body of revolution (Schlichting and Gersten, 1999)

Investigations of the boundary layer transition phenomenon of a flat plate at zero incidence to the incoming flow are numerous. As a result, it is commonly accepted that in sub-sonic flows the plate's boundary layer will be laminar for a region starting at the leading edge of the plate and continuing for a distance downstream. At a distance (x) from the leading edge the flow is observed to become turbulent. It is at this location that the critical Reynolds number is reached (Equation A-1). The critical Reynolds number varies for different body geometries and is dependent on the ambient flow conditions (Schlichting and Gersten, 1999).

$$Re_{x\text{ crit}} = \left(\frac{U_{\infty} x}{\nu} \right)_{\text{crit}} \quad \text{Equation A-1}$$

FACTORS AFFECTING TRANSITION

As has been noted, there are several factors that influence the transition behaviour of the boundary layer surrounding a three-dimensional body, the foremost being the Reynolds number. These factors are discussed below:

Pressure Gradient

Unlike a flat plate in a flow with zero incidence, the velocity profiles and the limit of boundary layer stability (critical Reynolds number) of a three-dimensional body differ from one location to another across its surface. The resultant pressure gradient created along the three-dimensional body affects both the point of transition and the occurrence of total boundary layer separation (Schlichting and Gersten, 1999).

Transition is delayed in areas of increasing flow velocity (decreasing pressure) due to the subsequent thinning of the boundary layer. In the case of an adverse pressure gradient, the boundary layer flow is slowed, causing it to thicken and encourage transition. This has the effect of decreasing the critical Reynolds number in the region of a positive pressure gradient and increasing it in the region of a negative pressure gradient. For a bluff ship shaped body in relative motion to its surrounding fluid, a sustained laminar region can originate at the bow (or leading edge) and extend through the favourable pressure gradient only to become susceptible to transition as the adverse gradient is encountered further along the body (Allan and Conn, 1950).

Ambient Turbulence Intensity

The presence of turbulence within the encountered flow can have a destabilising effect on the boundary layer of both two-dimensional (flat plate) and three-dimensional bodies. The transition of a body in a region of zero pressure gradient and with a hydraulically smooth surface is largely dependent on the intensity of the turbulence (or free-stream flow irregularities) and the stability of the laminar boundary layer. If the encountered turbulence is of low intensity and if the boundary layer is stable, it is likely that the flow irregularity will diminish and dissipate. However, if the boundary layer is unstable and/or the turbulence intensity is high there is a possibility that the flow irregularity will propagate and transition will occur (Schlichting and Gersten, 1999).

Surface Roughness

In general terms the surface condition of a body directly affects the transition of the boundary layer. Where all other circumstances are equivalent, a rough surface will promote transition and reduce the Reynolds number at which transition occurs when compared to a smooth surface. The critical parameter of a surface roughness is its height. However, its shape (two-dimensional or three-dimensional) and distribution (single element or multiple elements) also contribute to the behaviour of the transition process. It is important to note that the performance of the surface roughness, its ability to effectively cause boundary layer transition, is influenced by the effects of the ambient turbulence level in the incoming flow and the pressure gradient at the location of the roughness (Schlichting and Gersten, 1999).

The presence of a protuberance (roughness element or excrescence spot) of certain critical size, shape and location on the surface of a body and within its laminar flow region has been found to stimulate the transition of the flow by directly introducing a three-dimensional flow disturbance. The three-dimensional disturbance, combined with the ambient flow turbulence, can in some part bypass the two-dimensional Tollmien-Schlichting stage of the boundary layer transition process (Young, 1989). The net effect of the protuberance is to reduce the critical Reynolds number and shift the location of the boundary layer transition upstream towards the location of the protuberance.

Investigations conducted by Schubauer and Klebanoff (1955) illustrate the resultant characteristic geometry of the turbulent spot generated in the wake of a surface

protuberance on a flat plate (Figure A-3). In the case of Figure A-3 the turbulent spot is initiated by an electric spark formed between an electrode and the plate's surface.

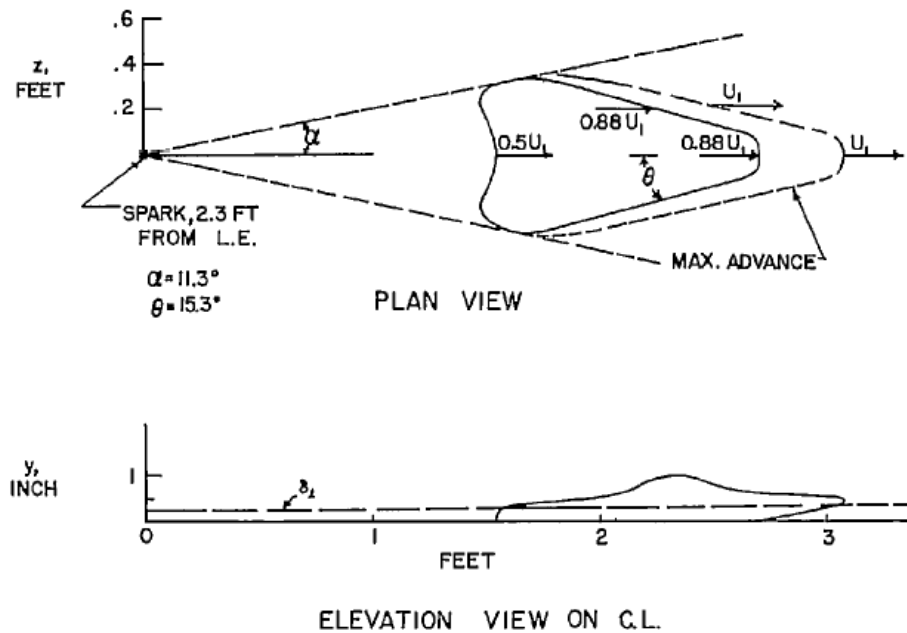


Figure A-3 Developed turbulent spot initiated by a surface protuberance (Schubauer and Klebanoff, 1955)

Through experimental investigation it has been found that there is a critical roughness height (k_{crit1}) below which transition will not occur. As the roughness height increases above k_{crit1} the flow will transition to form a turbulent spot (a discrete region of turbulence) in the wake of the roughness element. The downstream location of the turbulence will move steadily toward the roughness element until a second critical roughness height (k_{crit2}) is reached. At k_{crit2} the transition will occur just behind the roughness element. A critical Reynolds number has been formulated based on the roughness height at which transition occurs (Equation A-2). It is k_{crit2} that is used as an indicator of the required height of a turbulence stimulation device to cause transition at a specific location (Young, 1989).

$$Re_{k_{crit1}} = \left(\frac{U_k k}{\nu} \right)_{crit1} \quad \text{Equation A-2}$$

Braslow (1960) reports that the critical roughness Reynolds number ($Re_{k_{crit1}}$) will increase for particle roughness heights equal to or greater than the thickness of the boundary layer and that in these circumstances the flow condition is no longer equivalent to that upon which the concept of critical roughness height is based. Additionally, Braslow (1960) states that accurate prediction of boundary layer transition due to surface protuberances is dependent on the secondary effects of particle shape and distribution.

TRANSITION OVER A THREE-DIMENSIONAL BODY

A significant experimental investigation into the boundary layer transition of two ogive nosed cylinders, one with a length to diameter ratio of 7.00 and the other of 19.83, is presented by Knapp and Roache (1968). This investigation focused on the boundary layer transition of the cylinders in two pressure gradient conditions: a zero pressure gradient and an adverse pressure gradient.

The experiments were conducted in the non-return wind tunnel at the University of Notre Dame, Indiana. Flow visualisation and hot-wire anemometry was used to observe the boundary layer flow and transition phenomena for both of the pressure gradient conditions and for a natural and forced transition condition. The transition was forced by generating a sound in the tunnel of similar frequency to that of the two-dimensional waves that were observed to occur during transition. Experiments were conducted over a speed range corresponding to $3.16 \times 10^5 \leq Re_L \leq 7.60 \times 10^5$ for the 7.00 cylinder and $5.42 \times 10^5 \leq Re_L \leq 1.30 \times 10^6$ for the 19.83 cylinder, where L is the total length of the cylinder.

Knapp and Roache (1968) were able to record and present a well-defined description of the boundary layer transition phenomenon. In summary, the observed progression from laminar to turbulent flow was found to consist of the formation of sets of two-dimensional (Tollmien-Schlichting) waves on the surface of the cylinder. The waves would travel downstream, amplify and deform in a three-dimensional manner and then form a region of staggered vortex trusses. The vortices would subsequently break down into a turbulent flow region and be followed by the upstream boundary layer returning to a laminar state. This process was observed to recur in a periodic manner. A visual description of the observed transition phenomenon is presented in Figure A-4.

Several important observations and assertions were made by Knapp and Roache (1968) in relation to the occurrence of the transition phenomenon. These are:

- a. The fundamental characteristic of the boundary layer transition phenomenon is independent of the nose geometry.
- b. In an adverse pressure gradient the location of each of the regions moved upstream and the associated flow patterns became exaggerated.
- c. The characteristics of vortex breakdown were observed to differ for the two pressure gradient conditions. In an adverse gradient the vortices were found to shed a small ring from the apex of the vortex, whereas in the zero gradient the vortices remained intact.
- d. The introduced sound source (forced transition) was observed to: increase the definition of the flow topology; move the location of each of the regions upstream; cause the frequency of the two-dimensional waves to eventually lock in to the frequency of the sound; and remove the transition intermittency thereby fixing the location of the defined regions.

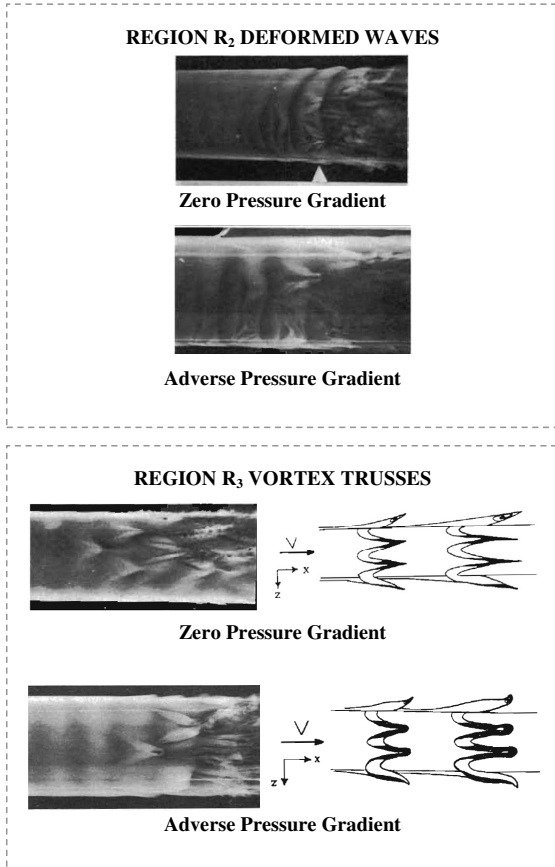
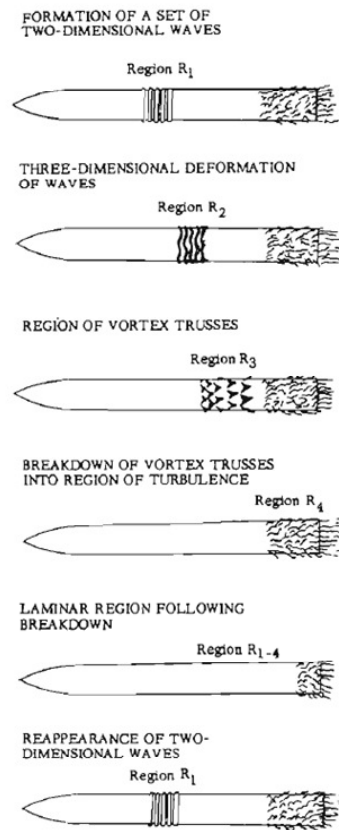


Figure A-4 Temporal evolution of boundary layer transition with smoke flow photography and sketches, adapted from Knapp and Roache (1968)

TURBULENCE STIMULATION DEVICES

Substantial investigation into the design, performance and application of turbulence stimulation devices has been conducted since the late 19th century. This has been driven by the need to address the transition problem in all practical areas of fluid mechanics, in particular aerodynamics and ship hydrodynamics.

Where transition does not occur as a result of the influence of Reynolds number, pressure gradient, general surface roughness or ambient turbulence, it is necessary to use a device to artificially stimulate a turbulent boundary layer. There are several types of transition devices that have been used by experimenters to transition the boundary layer of scale models in both water tanks and wind tunnels. The most effective types are surface mounted protuberances. Of those in use the most common include:

- a. Trip wires: a light gauge wire that is mounted on the surface of the model and perpendicular to the flow. The wire creates a two-dimensional flow disturbance that, with the correct profile height and ambient conditions, will develop into a three-dimensional flow disturbance downstream and promote boundary layer transition.

- b. Cylindrical or hemispherical studs: a span-wise array of discrete roughness elements of either cylindrical or hemispherical profile are affixed to the model's surface perpendicular to the direction of free-stream flow. Each element is able to generate a three-dimensional vortex that promotes boundary layer transition downstream of the array.
- c. Carborundum strips: a span-wise strip of randomly distributed roughness elements (silicon carbide). The particles are adhered with a nominated density to a strip substrate or directly to the model's surface at a nominated width. The strip of carborundum is affixed perpendicular to the direction of the free-stream flow. The bulk effect of the small roughness elements is to generate a coherent turbulent boundary layer downstream of the strip.

The stream-wise location of transition is affected by the two-dimensional versus three-dimensional nature of the stimulation device in combination with free stream velocity. The existence of three-dimensional vortex loops predicates transition from laminar to turbulent flow (Hama et al., 1957). A three-dimensional device, such as studs or spheres, is more direct in producing the vortex loop flow structure illustrated by Knapp and Roache (1968) and therefore transition can occur closer to the device. In the area of ship hydrodynamics it has been identified that three-dimensional stimulation devices are superior to two-dimensional devices due to their ability to directly generate the vortex loops essential for boundary layer transition (ITTC, 1990).

APPENDIX B LOAD CELL AND WAVE PROBE CALIBRATION

The two six-component load cells and four wave probes used in the experiment were systematically calibrated following the Australian Maritime College's standing procedures. The calibration process is described in section 5. The calibration factors determined during the Joubert *L/D* experimental testing program are presented in Table B-1 through Table B-3 below.

Table B-1 AMTI Load Cell Calibration Factors (N/V) and Correlation Coefficient (R^2): F_X and F_Z 5kg calibrated range; F_Y 1kg calibrated range

	Test Date	Fwd F_X	Fwd F_Y	Fwd F_Z	Aft F_X	Aft F_Y	Aft F_Z
Calibration Factor	31/07/2012	-8.2174	-1.0398	7.8117	9.0783	1.1137	8.0406
Correlation Coefficient	31/07/2012	1.000	0.9999	1.000	0.9989	0.9994	0.9998
Calibration Factor	10/08/2012	-8.1901	-1.0342	7.7952	8.8903	1.1062	7.9114
Correlation Coefficient	10/08/2012	1.000	1.000	1.000	0.9994	0.9996	0.9991

Table B-2 Measurement System Signal Conditioning Parameters

Test Date	Fwd F_X	Fwd F_Y	Fwd F_Z	Aft F_X	Aft F_Y	Aft F_Z
SGC Gain	5	10	10	5	10	10
Matronix Gain	2.5	10	10	2.5	10	5
Matronix Filter [kHz]	10	10	10	10	10	10

Table B-3 Wave Probe Calibration Factors (m/V): Calibrated range +/- 100mm; All channels filtered at 10 kHz

Test Date	WP1	WP2	WP3	WP4
03/08/2012	0.0581	0.0280	0.0284	0.0283
04/08/2012	0.0581	0.0279	0.0284	0.0281
06/08/2012	0.0574	0.0278	0.0283	0.0281
07/08/2012	0.0577	0.0280	0.0284	0.0282
08/08/2012	0.0574	0.0279	0.0283	0.0281
09/08/2012	0.0570	0.0276	0.0281	0.0280
10/08/2012	0.0572	0.0277	0.0282	0.0280

APPENDIX C UNCERTAINTY ANALYSIS

A general uncertainty analysis was completed for the total resistance coefficient using the method presented by ITTC (1999) and ITTC (2002). The lift force and trimming moment coefficient data were analysed using the same method. The method specified by the ITTC is equivalent to the error propagation method presented by Coleman and Steele (1999) where bias and precision estimates are determined for the individual independent parameters in the data reduction equation.

TOTAL RESISTANCE COEFFICIENT

The data reduction equation and the partial derivatives are presented in Equation C-1 through Equation C-5. The resultant equation for the uncertainty in C_T is presented in Equation C-6. The bias and precision estimates for the independent variables are presented in Table C-1. The uncertainty estimates for the total resistance coefficient for the Joubert $L/D = 7.30$ model data are presented in Figure C-1 through Figure C-5.

$$C_T = \frac{R_T}{0.5\rho \cdot U^2 \cdot S} \quad \text{Equation C-1}$$

$$\frac{\partial C_T}{\partial R_T} = \frac{1}{0.5\rho \cdot U^2 \cdot S} \quad \text{Equation C-2}$$

$$\frac{\partial C_T}{\partial \rho} = -\frac{R_T}{0.5\rho^2 \cdot U^2 \cdot S} \quad \text{Equation C-3}$$

$$\frac{\partial C_T}{\partial U} = -\frac{2 \cdot R_T}{0.5\rho \cdot U^3 \cdot S} \quad \text{Equation C-4}$$

$$\frac{\partial C_T}{\partial S} = -\frac{R_T}{0.5\rho \cdot U^2 \cdot S^2} \quad \text{Equation C-5}$$

$$U_{C_T} = C_T \cdot \sqrt{\left(\frac{U R_T}{R_T}\right)^2 + \left(-\frac{U \rho}{\rho}\right)^2 + \left(-2 \frac{U U}{U}\right)^2 + \left(-\frac{U S}{S}\right)^2} \quad \text{Equation C-6}$$

Table C-1 Parameter uncertainty estimates

Parameter	Precision	Bias	Uncertainty
R_T [N]	0.014	0.156	0.157
ρ [kg/m ³]	0.000	0.997	0.997
U [m/s]	0.003	0.006	0.007
S [m ₂]	0.000	0.010	0.010

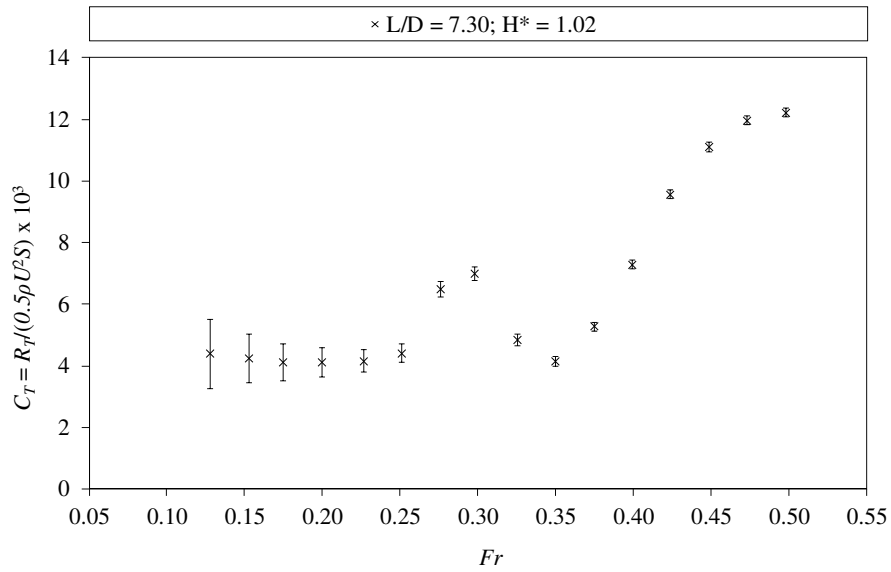


Figure C-1 Joubert $L/D = 7.30$ model at $H^* = 1.02$ total resistance coefficient and experimental uncertainty

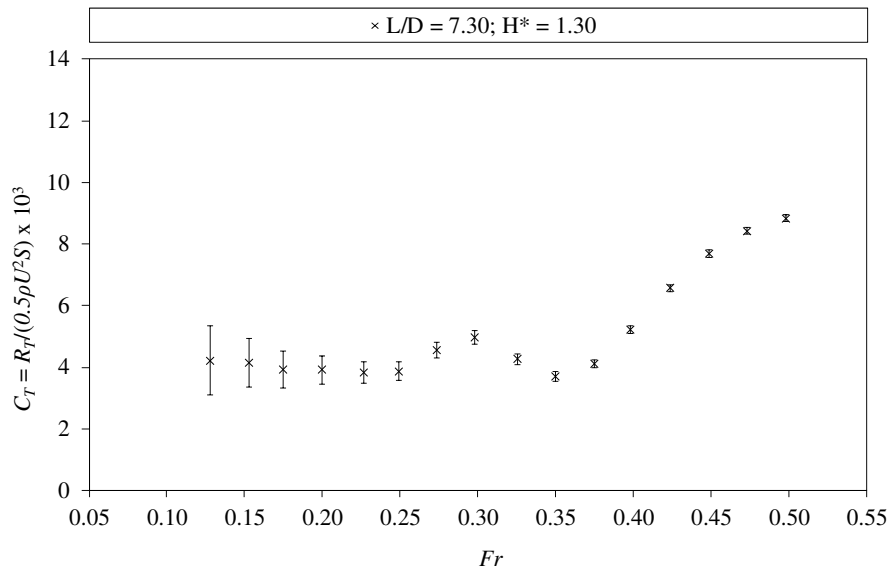


Figure C-2 Joubert $L/D = 7.30$ model at $H^* = 1.30$ total resistance coefficient and experimental uncertainty

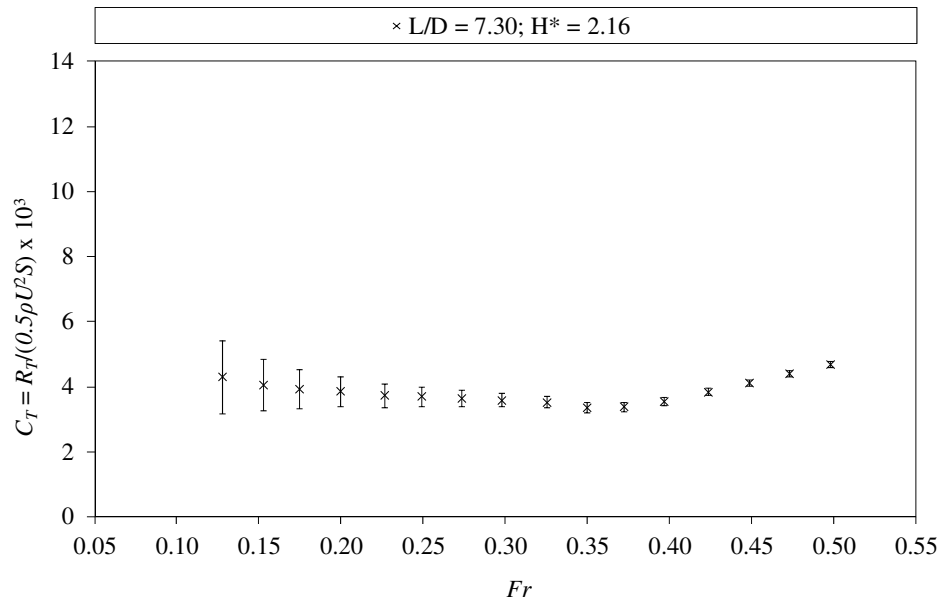


Figure C-3 Joubert $L/D = 7.30$ model at $H^* = 2.16$ total resistance coefficient and experimental uncertainty

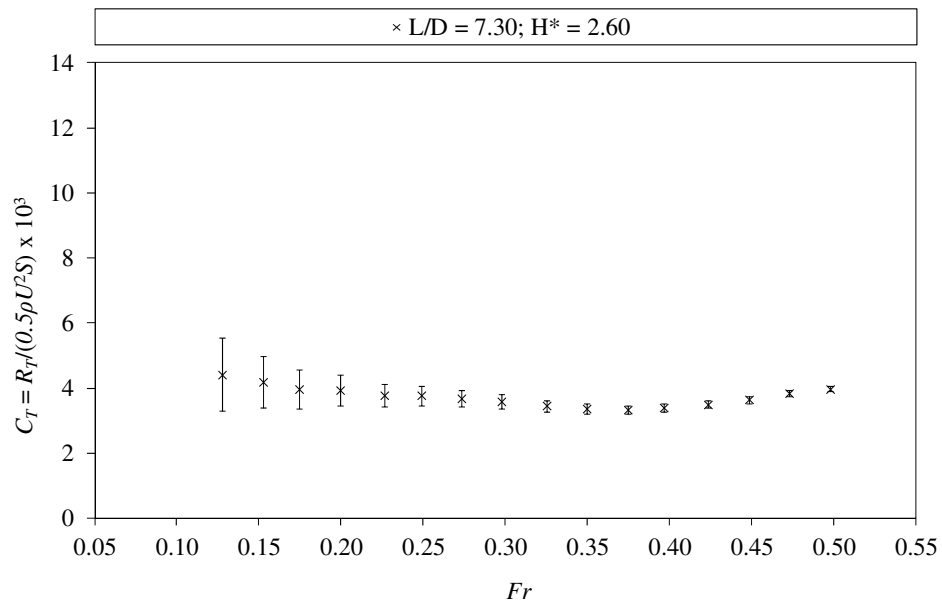


Figure C-4 Joubert $L/D = 7.30$ model at $H^* = 2.60$ total resistance coefficient and experimental uncertainty

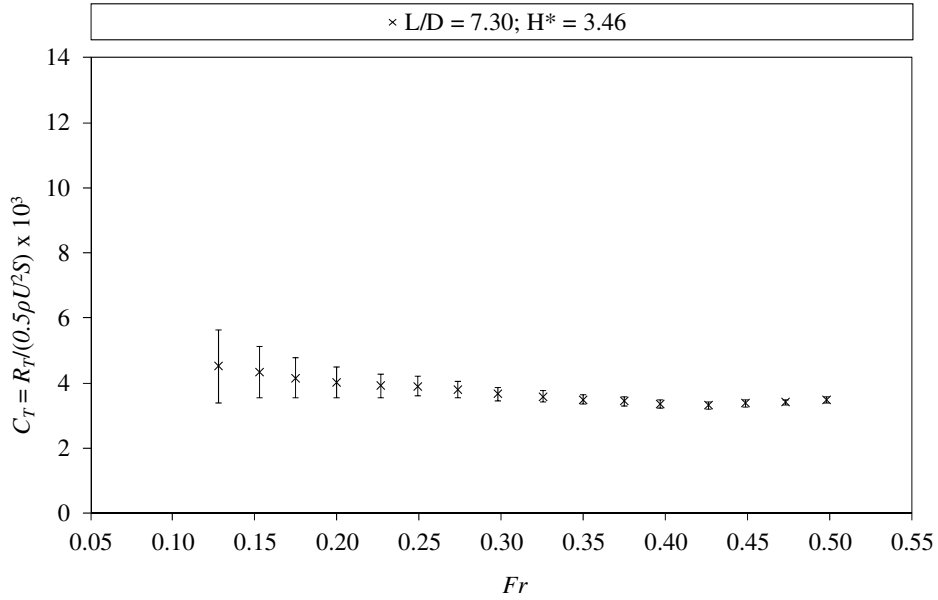


Figure C-5 Joubert $L/D = 7.30$ model at $H^* = 3.46$ total resistance coefficient and experimental uncertainty

LIFT FORCE COEFFICIENT

$$C_L = \frac{F_X}{0.5\rho \cdot U^2 \cdot S} \quad \text{Equation C-7}$$

$$\frac{\partial C_L}{\partial F_X} = \frac{1}{0.5\rho \cdot U^2 \cdot S} \quad \text{Equation C-8}$$

$$\frac{\partial C_L}{\partial \rho} = -\frac{F_X}{0.5\rho^2 \cdot U^2 \cdot S} \quad \text{Equation C-9}$$

$$\frac{\partial C_L}{\partial U} = -\frac{2 \cdot F_X}{0.5\rho \cdot U^3 \cdot S} \quad \text{Equation C-10}$$

$$\frac{\partial C_L}{\partial S} = -\frac{F_X}{0.5\rho \cdot U^2 \cdot S^2} \quad \text{Equation C-11}$$

$$U_{C_L} = C_L \cdot \sqrt{\left(\frac{U_{F_X}}{F_X}\right)^2 + \left(-\frac{U_\rho}{\rho}\right)^2 + \left(-2\frac{U_U}{U}\right)^2 + \left(-\frac{U_S}{S}\right)^2} \quad \text{Equation C-12}$$

Table C-2 Parameter uncertainty estimates

Parameter	Precision	Bias	Uncertainty
F_Z [N]	0.025	0.102	0.105
ρ [kg/m ³]	0.000	0.997	0.997
U [m/s]	0.003	0.006	0.007
S [m ₂]	0.000	0.010	0.010

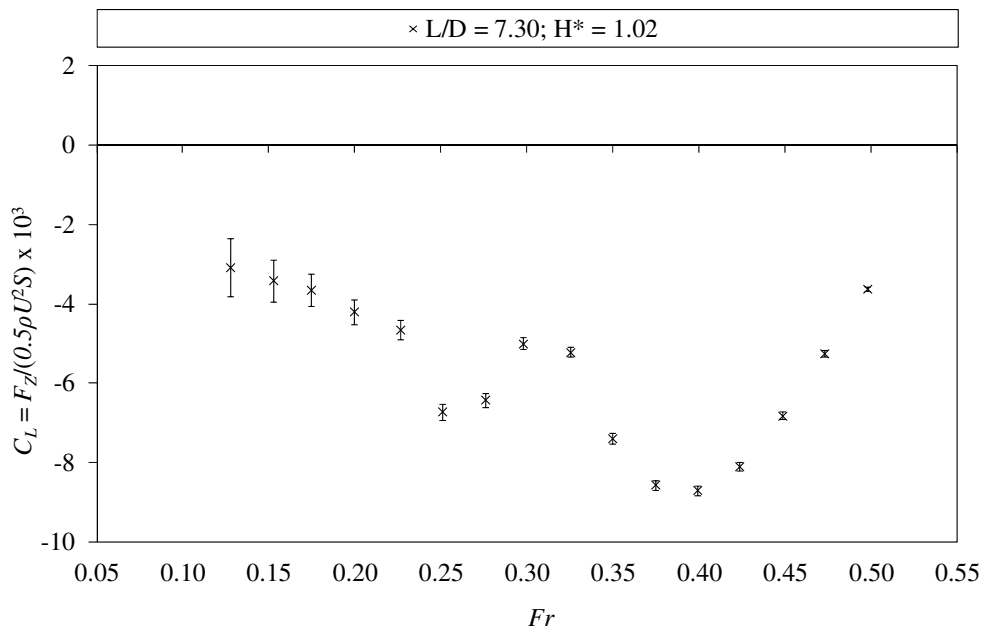


Figure C-6 Joubert $L/D = 7.30$ model at $H^* = 1.02$ lift force coefficient and experimental uncertainty

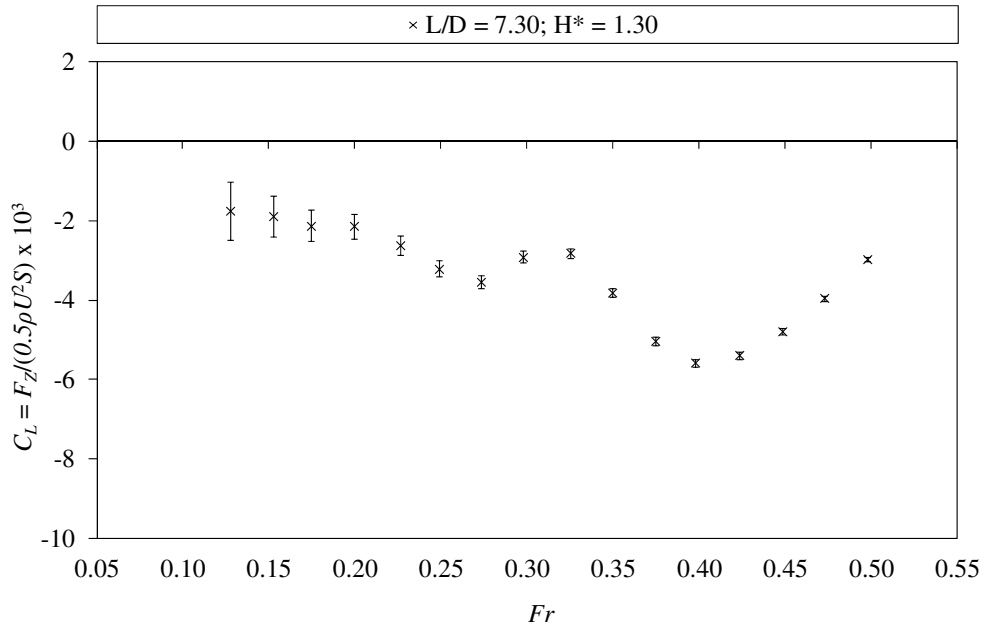


Figure C-7 Joubert $L/D = 7.30$ model at $H^* = 1.30$ lift force coefficient and experimental uncertainty

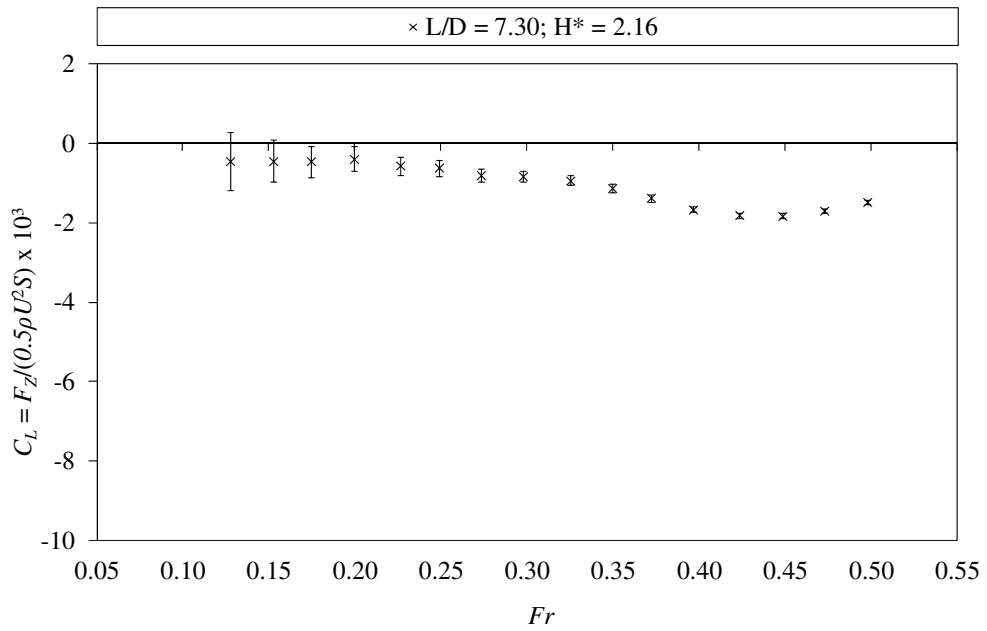


Figure C-8 Joubert $L/D = 7.30$ model at $H^* = 2.16$ lift force coefficient and experimental uncertainty

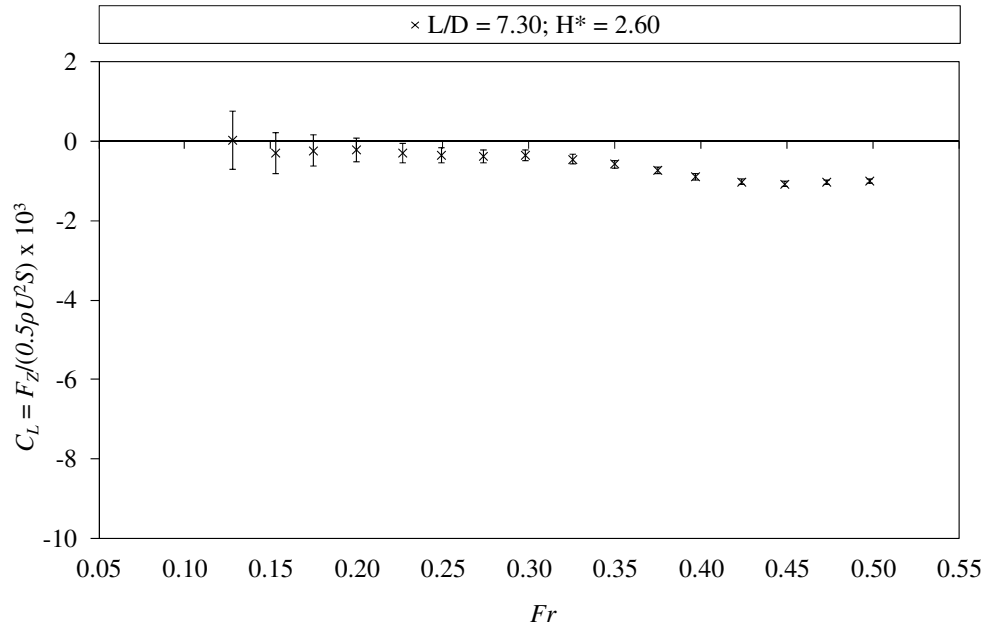


Figure C-9 Joubert $L/D = 7.30$ model at $H^* = 2.60$ lift force coefficient and experimental uncertainty

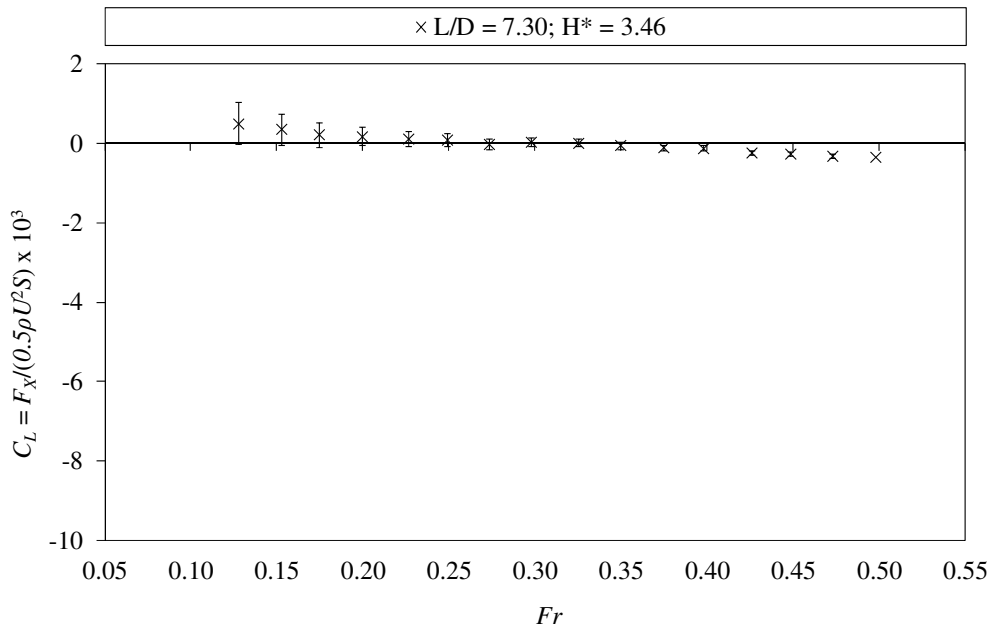


Figure C-10 Joubert $L/D = 7.30$ model at $H^* = 3.46$ lift force coefficient and experimental uncertainty

APPENDIX D SUBOFF RESISTANCE COEFFICIENT DATA

SUBOFF BARE HULL AND HULL AND SAIL CONFIGURATIONS

The total resistance coefficient of the SUBOFF bare hull and SUBOFF hull and sail model configurations are presented in Figure D-1 and Figure D-2 respectively for $1.10 \leq H^* \leq 3.30$. The residuary resistance coefficient data for the two configurations are presented in Figure D-3 and Figure D-4. For both of the hull configurations the results indicate that there is a significant amount of interaction between the model and the free-surface for submergence depths of $H^* < 2.75$ and for speeds greater than $Fr = 0.20$. Despite this observation, it is also apparent that there is still interaction occurring at the mid-tank test depth of $H^* = 3.30$, in particular at Froude numbers greater than $Fr \approx 0.40$ and also at $Fr = 0.30$ where definite local maxima can be identified. At the shallowest submergence depth ($H^* = 1.10$) there are three localised peaks in the resistance coefficient curve. These occur at approximately $Fr = 0.225$, $Fr = 0.30$ and $Fr = 0.50$. In both configurations there are clear trends that indicate that the body and free-surface interaction effects decrease with and increase in submergence depth and/or a decrease in speed.

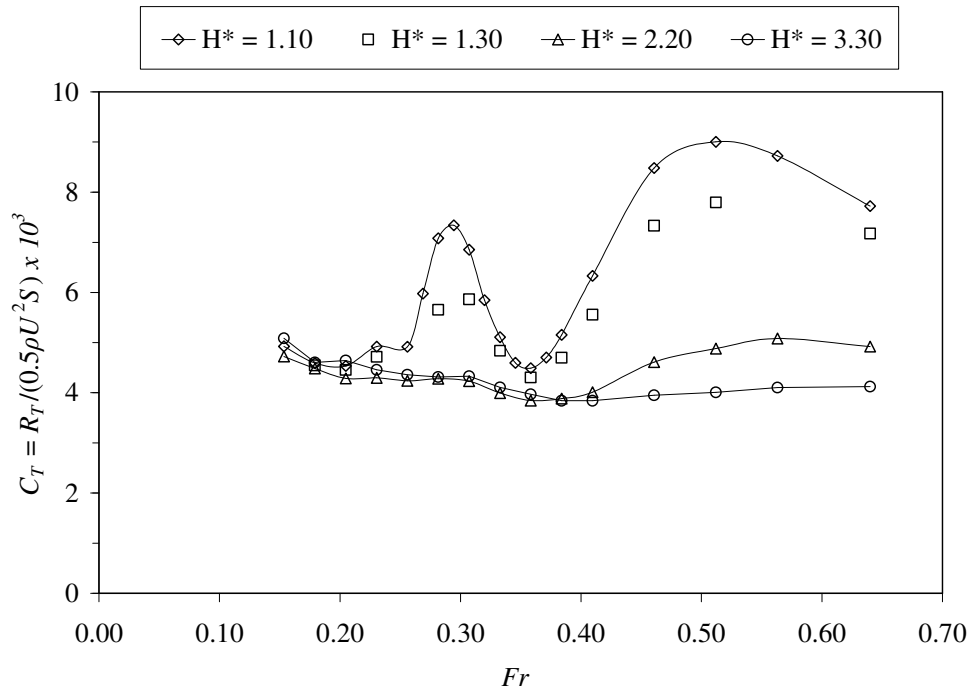
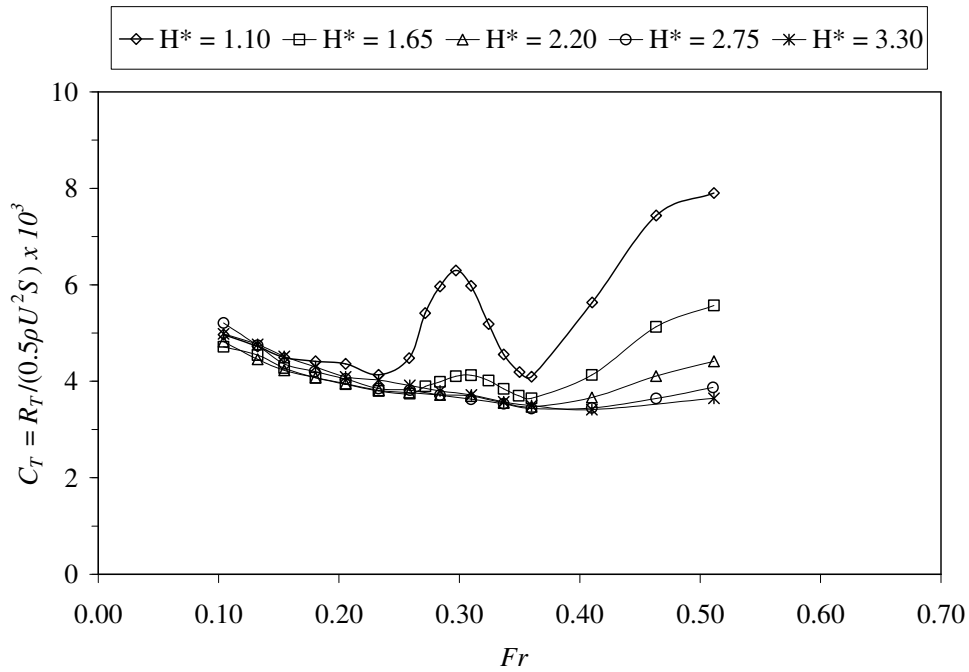
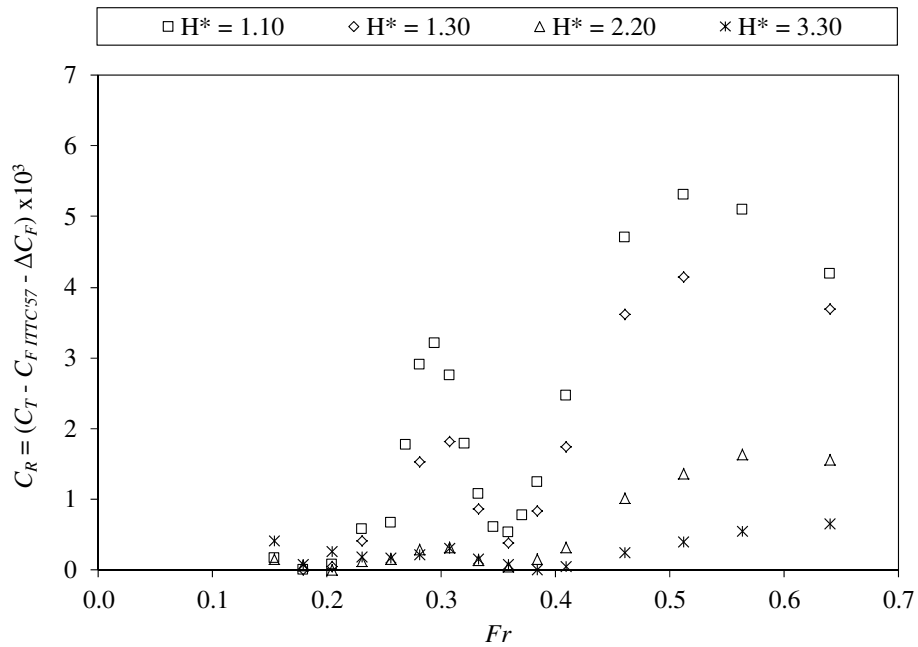


Figure D-1 SUBOFF Bare Hull: Total resistance coefficient (C_T); $0.15 \leq Fr \leq 0.64$



**Figure D-2 SUBOFF Hull & Sail: Total resistance coefficient (C_T);
 $0.10 \leq Fr \leq 0.51$**



**Figure D-3 SUBOFF Bare Hull: Residual resistance coefficient (C_R);
 $0.15 \leq Fr \leq 0.64$**

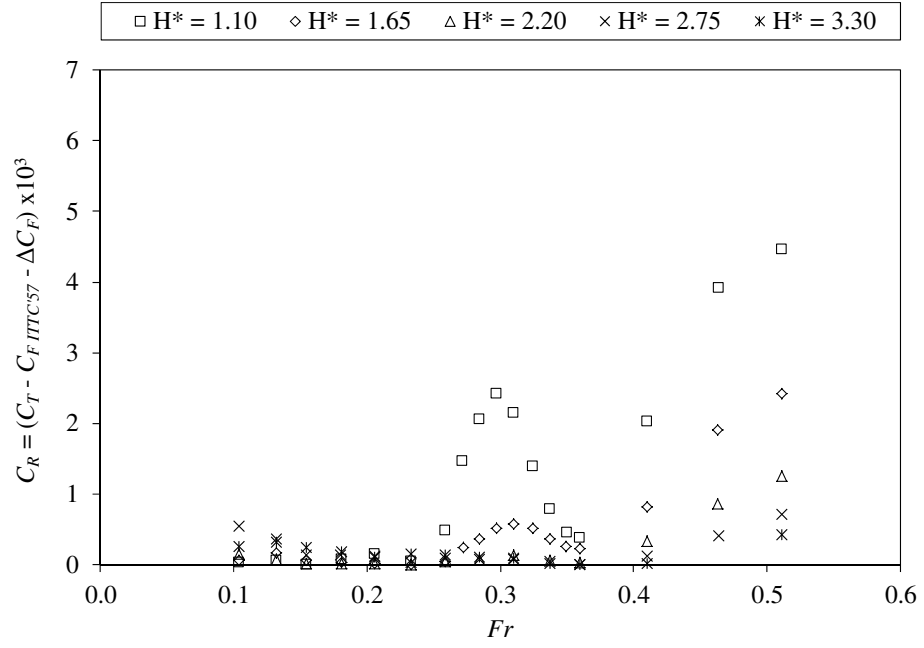


Figure D-4 SUBOFF Hull + Sail: Residual resistance coefficient (C_T); $0.10 \leq Fr \leq 0.51$

APPENDIX E SHIPFLOW RUN FILES

JOUBERT SUBMARINE (HULL ONLY)

```
xflow
  title (titl="Joubert Submarine Hull Only")
  program (xmesh, xpan)
  offsetfile (file = "off_joubert_730", LPP = 1.679, zori = 0.7958)
  hulltype (submarine)
  vship (fn = [0.10], rn = [0.0])
  prtopt (pgeom, pcon, panco, nlterm, bmres, fsres, xyplot, trace)
end

xmesh
  body (grno = 1, offsetgroup = "hull", station = 100, point = 13,
  str2 = 5, df2 = 0.001, dl2 = 0.001)
  free (grno = 2, y2side = 0.0, y4side = -2, xups = -1, xdown = 5,
  point = 40, stau = 20, stam = 20, stad = 80)
end

xpan
  cont (nonlin)
  rela (rfwave = 1)
  conv (epwave = 1.e-5)
  iter (maxit = 100)
  para (nthr = 4)
  wave (numl = 4, lwavec = [-0.1727,-0.3454,-0.5181,-0.6908],
  dxwave = 0.001679)
  twcut (on, xsttwc = 1.0, xentwc = 5.0, statwc = 500, strtwc = 0,
  nvaltw = 100, nwavnu = 20)
end
```

5:1 SPHEROID

```
xflow
  title (title="5:1:1 Spheroid")
  program (xmesh, xpan)
  offsetfile (file = "off_5to1_spheroid", LPP = 1.000, zori = 0.245)
  hulltype (submarine)
  vship (fn = [0.10], rn = [0.0])
  prtopt (pgeom, pcon, panco, nlterm, bmres, fsres, xyplot, trace)
end

xmesh
  body (grno = 1, offsetgroup = "hull", station = 71, point = 13,
  str2 = 5, df2 = 0.001, dl2 = 0.001)
  free (grno = 2, y2side = 0.0, y4side = -2, xups = -1, xdown = 5,
  point = 40, stau = 20, stam = 20, stad = 80)
end

xpan
  cont (nonlin)
  rela (rfwave = 1)
  conv (epwave = 1.e-5)
  iter (maxit = 20)
  para (nthr = 4)
  twcut (on, xsttwc = 1.0, xentwc = 5.0, statwc = 500, strtwc = 0,
  nvaltw = 100, nwavnu = 20)
end
```

SERIES 58 MODEL 4166

```
xflow
  title (title="Model 4166 H* = 1.413")
  program (xmesh, xpan)
  offsetfile (file = "off_4166", LPP = 2.7432, zori = 0.491)
  hulltype (submarine)
  vship (fn = [0.10], rn = [0.0])
  prtopt (pgeom, pcon, panco, nlterm, bmres, fsres, xyplot, trace)
end

xmesh
  body (grno = 1, offsetgroup = "hull", station = 91, point = 13,
  str2 = 5, df2 = 0.001, dl2 = 0.001)
  free (grno = 2, y2side = 0.0, y4side = -2, xups = -1, xdow = 5,
  point = 40, stau = 20, stam = 20, stad = 80)
end

xpan
  cont (nonlin)
  rela (rfwave = 1)
  conv (epwave = 1.e-6)
  iter (maxit = 20)
  para (nthr = 4)
  twcut (on, xsttwc = 1.0, xentwc = 5.0, statwc = 500, strtwc = 0,
  nvaltw = 100, nwavnu = 20)
end
```

RESEARCH PUBLICATIONS

- DAWSON, E., JOHNSON, N., RANMUTHUGALA, D. & BRANDNER, P. (To be submitted in 2014/15). An Investigation into the Effects of Submergence Depth, Forward Speed and Length to Diameter Ratio on Near-Surface Submarine Performance and Wave-Making Characteristics.
- GOURLAY, T. & DAWSON, E. (Submitted October 2014). A Havelock-Source Panel Method for Near-Surface Submarines. *Journal of Ship Research*, Society of Naval Architects and Marine Engineers, Virginia, USA.
- RENILSON, M.R., RANMUTHUGALA, S., DAWSON, E., ANDERSON, B., VAN STEEL, S. & WILSON-HAFFENDEN, S. 2011. Hydrodynamic Design Implications for a Submarine Operating Near the Surface. *Proceedings of Warship 2011: Naval Submarines and UUVs*, 29-30 June, Bath, UK, pp. 1-7 [Refereed Conference]
- DAWSON, E., ANDERSON, B., VAN STEEL, S., RENILSON, M. & RANMUTHUGALA, D. 2010. An Experimental Investigation into the Effects of Near-Surface Operation on the Wave-Making Resistance of SSK Type Submarines. *Proceedings of MAST 2010*, 9-11 November 2010, Rome, pp. 1-8 [Refereed Conference]
- WILSON-HAFFENDEN, S., RENILSON, M., RANMUTHUGALA, D. & DAWSON, E. 2010. An Investigation into the Wavemaking Resistance of a Submarine Travelling Bellow the Free Surface. *Proceedings of PACIFIC 2010*, 27-29 January, Sydney, Australia, pp. 370-379